

AD 680235

AD

USAAVLABS TECHNICAL REPORT 68-50B

SMALL GAS TURBINE ENGINE COMPONENT TECHNOLOGY - TURBINE VOLUME II PHASE II SUMMARY REPORT

By

W. Franklin
J. Neilbron
S. Moskowitz

August 1968

**U. S. ARMY AVIATION MATERIEL LABORATORIES
FORT EUSTIS, VIRGINIA**

**CONTRACT DA 44-177-AMC-182 (T)
CURTISS-WRIGHT CORPORATION
WOOD-RIDGE, NEW JERSEY**

*This document has been approved
for public release and sale; its
distribution is unlimited.*



Reproduced by the
CLEARINGHOUSE
for Federal Scientific & Technical
Information Springfield Va. 22151

224



DEPARTMENT OF THE ARMY
U. S. ARMY AVIATION MATERIEL LABORATORIES
FORT EUSTIS, VIRGINIA 23604

Appropriate technical personnel have reviewed this report and concur with the conclusions contained herein.

The findings and recommendations outlined herein will be taken into consideration in the planning of future programs for turbines and turbine engines.

TASK 1G162203D14413
Contract DA 44-177-AMC-182(T)
USAAVLABS Technical Report 68-50B
August 1968

**SMALL GAS TURBINE ENGINE COMPONENT TECHNOLOGY -
TURBINE
VOLUME II
PHASE II SUMMARY REPORT**

By

W. Franklin
J. Heilbron
S. Moskowitz

Prepared By

Curtiss-Wright Corporation
Wood-Ridge, New Jersey

for

U.S. ARMY AVIATION MATERIEL LABORATORIES
FORT EUSTIS, VIRGINIA

This document has been approved
for public release and sale; its
distribution is unlimited.

SUMMARY

This report details the manufacture and presents the results of a test evaluation of a complete high-temperature transpiration-air-cooled small axial turbine stage, the aerothermal and mechanical design of which is described in Volume I. The turbine size and work objective of 140 Btu per pound were established to make it suitable for use in a gas generator having a single-stage turbine driving a compressor of 8 to 10 pressure ratio and a weight flow capacity of 4 pounds per second.

The complete turbine stage was tested for a total of 100.83 hours, which included 2 hours at an average turbine inlet temperature of about 2500°F, with a local peak temperature of 3140°F. All blading, both stator and rotor, was in excellent condition after exposure to these conditions. The stator cascade rig was tested for a total of 87.92 hours, which included 1.17 hours at 2650°F average gas temperature, with a peak of 3340°F. Again, posttest condition of the blading was excellent. In both the cascade tests and the complete stage tests, measured temperatures of the stator spars and ancillary hot-section hardware verified the efficacy of the thermal design and transpiration cooling as applied to small-size blading. Two failures occurred during testing of the complete stage. In each case the failure was traced to the connecting shaft between turbine and gearbox.

Included in the performance test program was the warm air aerodynamic evaluation of the full-stage turbine component over a range of correction rotor speed, N/\sqrt{T} (60 percent to 110 percent of design), stage pressure ratio (1.4 to 3.2), and blade row cooling airflow (0 percent to 10 percent). In addition, aerodynamic testing of the stator row in the cascade rig established the effects of cooling airflow (0 to 13 percent) on performance over a range of pressure ratios (1.5 to 2.6) for this low-aspect-ratio transpiration-cooled blade design. Whereas the addition of transpiration cooling airflow over the range tested produced extremely small effects on row aerodynamic performance, the significant effects classically associated with low aspect ratio and those due to the particular selection of blade profile were observed.

The design goals, test goals, and test accomplishments compare as follows:

	<u>Design Goal</u>	<u>Test Goals</u>	<u>Test Accomplishments</u>
Work	140 Btu/lb	133 Btu/lb	133 Btu/lb
Turbine Inlet Temperature	2500°F	2298° F	2500°F
η Tot - Tot	89%	88%	71%
Wa	4 lb/sec	3.01 lb/sec	2.44 lb/sec
Wa Rotor	3% - 5%	5% at 2420°F	4.98% at 2446°F
Wa Stator	3% - 5%	-	5.23% at 2471°F

A stage design with substantially higher efficiency can be provided based on (1) test data analysis which suggests a revised blade profile in combination with (2) a shortened blade chord which is now possible through technological developments in manufacturing and materials, which were not available when this design was conceived, without compromise to the structural and thermal requirements.

Prior to the turbine evaluation, the fuel vaporizing annular combustor was tested for 137.83 hours at an average exit temperature up to 2500°F to establish the burner performance and temperature profiles and to develop operating characteristics that were consistent with the cooled turbine requirements.

In addition, the manufacturing processes were established to fabricate an integrally welded air-cooled turbine rotor assembly by utilizing electron beam welding for the blade-to-disc attachment.

FOREWORD

The work reported herein is in partial fulfillment of Contract DA 44-177-AMC-182(T), which was conducted for the U.S. Army Aviation Materiel Laboratories, Fort Eustis, Virginia, under the technical direction of Mr. E. Johnson. It represents the completion of the accomplishments during Phase II of the contract, and includes the fabrication and test evaluation of the combustor, the stator cascade, and the complete turbine stage. The aerodynamic and mechanical design and the preliminary test evaluation of the turbine are described in Volume I - Phase I Summary Report.

The guidance of Mr. J. White of the Aeronautical Propulsion Division of the U.S. Army AVLABS is gratefully acknowledged.

Mr. T. Schober, Manager, Small Gas Turbine Engine Program, Mr. S. Moskowitz, Manager, Turbine Component Technology and Mr. W. Franklin, Project Engineer were the principal investigators.

Engineering contributions provided by Dr. G. Provenzale, Messrs. R. Gigon, S. Thirumalaisamy and overall guidance provided by Mr. S. Lombardo are gratefully acknowledged.

BLANK PAGE

TABLE OF CONTENTS

	<u>Page</u>
SUMMARY	111
FOREWORD	v
LIST OF ILLUSTRATIONS	ix
LIST OF TABLES	xv
LIST OF SYMBOLS	xvii
1.0 INTRODUCTION	1
2.0 DETAIL DESIGN - TURBINE COMPONENT	3
2.1 Stator Vane	3
2.2 Rotor Blade	4
2.3 Rotor Blade and Disc Assembly	4
3.0 FABRICATION	13
3.1 Turbine Component	13
3.1.1 Blade Fabrication	13
3.1.2 Rotor Blade and Disc Assembly	18
3.2 Turbine Test Rig	29
4.0 TEST PROGRAM	65
4.1 Combustor Testing	65
4.1.1 Combustor Performance	67
4.1.2 Combustor Durability and Modifications	71
4.2 Cascade Testing	111
4.2.1 Turbine Temperatures	111
4.2.2 Cooling Airflow and Leakage Characteristics	111
4.2.3 Aerodynamic Performance	113
4.2.4 Instrumentation	114
4.2.5 Stator Durability	115
4.3 Turbine Component Testing	118
4.3.1 Rotor Blade Cooling Airflow and Leakage Characteristics	145

	<u>Page</u>
4.3.2 Aerodynamic Performance	145
4.3.3 Durability	148
4.3.4 Test Equipment	155
CONCLUSIONS	182
RECOMMENDATIONS	184
APPENDIX, TEST PROGRAM SUMMARY	185
DISTRIBUTION	197

LIST OF ILLUSTRATIONS

<u>Figure</u>		<u>Page</u>
1	Turbine Component Basic Arrangement	5
2	Vane Turbine Assembly	7
3	Blade Turbine Rotor Assembly	9
4	Blade and Disc Turbine Rotor Assembly	11
5	Stator Vane Casting	31
6	Turbine Rotor Blade Strut	32
7	Airfoil Sections and Stator Strut	33
8	Airfoil Sections and Rotor Strut	34
9	Stator Vane Welding Fixture - Assembled	35
10	Stator Vane Welding Fixture - Disassembled	36
11	Turbine Stator Vane Assembly	37
12	Stator Vane Welded Assembly	38
13	Stator Vane Welded Assembly	39
14	Rotor Blade Welding Fixture - Disassembled	40
15	Turbine Rotor Blade Welded Assembly	41
16	Airfoil Cross Section Etched to Show Land Welds	42
17	EB Weld on Middle Land Concave Side	43
18	EB Weld on Trailing-Edge Land Convex Side	44
19	Weld Bead Machined Flush Prior to Aging - Leading-Edge Side	45
20	Turbine Rotor Disc and Shaft Casting	46
21	Rotor Disc Cooling Air Impeller Vanes and Ceramic Core . .	47
22	Turbine Rotor Disc and Shaft Rough Machining	48
23	Turbine Rotor Assembly	49

LIST OF ILLUSTRATIONS (Continued)

<u>Figure</u>		<u>Page</u>
24	Blade Disc Weld Specimen	50
25	Blade-to-Disc Welding Process Sequence	51
26	Weld Root from Blade-to-Disc Weld Specimen Showing Full Penetration	52
27	Slope-In and Slope-Out Sequence	53
28	View of Blade-to-Disc Weldment Showing Blade Interface Extensions	54
29(a)	Turbine Rotor Blade-to-Disc Weld Fixture - Original . . .	55
29(b)	Turbine Rotor Blade-to-Disc Weld Fixture - Revised . . .	56
30	Blade-to-Disc Weld Attachment Trials	57
31	Turbine Rotor EB Weld Joint Revised Design for Controlled Penetration	58
32	Turbine Blade-to-Disc Weld Penetration Trials	59
33	Turbine Blade-to-Disc Weld Penetration Trials	60
34	Weld Bead Machined Flush Prior to Aging - Trailing-Edge Side	61
35	Turbine Blade Material Comparison	62
36	Hardness Survey of Cast Inconel 718 Disc EB Welded to Inconel 713	63
37	Photomicrograph of Inconel and 713 LC Weld - 100x Magnification. Turbine Blade-to-Disc Weld Attachment Trial - Alternate Material	64
38	Inlet Support	72
39	Combustor Headplate	73
40	Combustor Outer Liner	74
41	Combustor Inner Liner	75
42	Partial Stator and Support Assembly	76

LIST OF ILLUSTRATIONS (Continued)

<u>Figure</u>		<u>Page</u>
43	Labyrinth Seal Assembly	77
44	Turbine Support - Rear View	78
45	Bearing Retainer - Front	79
46	Turbine Exhaust Housing - Front View	80
47	Turbine Shroud Filled With Nicroseal	81
48	Actual Assembly Measurements - Rotor Build 5	82
49	Turbine Rig Complete Assembly - Rear View	83
50	Vaporizer - No Dams	84
51	Annular Vaporizer With Axial Dams	85
52	Vaporizer With Circumferential Dam	86
53	Combustor Pressure Drop Characteristic	87
54	Combustor Pressure Drop Characteristic	88
55	Total Pressure Loss During Burning	89
56	Combustor Efficiency	90
57	Combustor Ignition Characteristic	91
58	Radial Exit Temperature Profile	92
59	Circumferential Exit Temperature Profile	93
60	Circumferential Exit Temperature Profile	94
61	Circumferential Exit Temperature Profile	95
62	Circumferential Exit Temperature Profile	96
63	Circumferential Exit Temperature Profile	97
64	Circumferential Exit Temperature Profile	98
65	Circumferential Exit Temperature Profile	99
66	Circumferential Exit Temperature Profile	100

LIST OF ILLUSTRATIONS (Continued)

<u>Figure</u>		<u>Page</u>
67	Vaporizer Airflow - Calibration Curve	101
68	Combustor Rig Assembly	102
69	Inner Liner, Posttest	103
70	Outer Liner, Posttest	104
71	Inner Liner Schematic - Temperature Paint Evaluation . . .	105
72	Outer Liner Schematic - Temperature Paint Evaluation . . .	106
73	Combustor Inner Liner	107
74	Combustor Liner - Side View	108
75	Combustor Outer Liner	109
76	Combustor Headplate	110
77	Turbine Gas and Blade Metal Temperature Distribution . . .	119
78	Turbine Stator Cooling Flow Characteristics	120
79	Welded Stator Assembly - Front View	121
80	Turbine Stator Vane - Individual Channel Flow	122
81	Stator Blade Cooling Airflow Single Blades	123
82	Stator Mid-Height Cascade Test Results	124
83	Stator Cascade Test Results	125
84	Stator Cascade Test Results	126
85	Stator Cascade Test Results	127
86	Typical Mid-Height Data Trace - 0 Percent Cooling Air . .	128
87	Typical Mid-Height Data Trace - 4 Percent Cooling Air . .	129
88	Typical Mid-Height Data Trace - 8 Percent Cooling Air . .	130
89	Ratio of Average to Mid-Height Stator Loss Coefficient . .	131
90	Turbine Stator and Combustor Cooling Air Deflectors . . .	132

LIST OF ILLUSTRATIONS (Continued)

<u>Figure</u>		<u>Page</u>
91	Stator Cascade Test Results	133
92	Stator Cascade Test Results	134
93	Rig Cross Section - Stator Instrumentation	135
94	Second Welded Stator Assembly - Rear View Showing Static Pressure Instrumentation	136
95	Stator Inlet Pressure Instrumentation	137
96	Survey Instrument Showing Fixed Kiel Probes on Rotating Ring	138
97	Driving Mechanism for 18-Element Survey Instrument	139
98	Liner and Support Rework	141
99	Outer Stator Plenum Flow Characteristic	143
100	Turbine Rotor Blade - Channel Flow Characteristics for Ambient External Conditions	160
101	Turbine Rotor Blade - Total Flow Characteristics for Ambient External Conditions - Single Blade	161
102	Turbine Rotor Cooling Airflow Characteristics - Rotor Build 5	162
103	Turbine Performance Test Results	163
103(a)	Universal Turbine Map - Comparison of Estimated and Test Performance	164
103(b)	Estimated Overall Turbine Performance Map	165
103(c)	Test Overall Turbine Performance Map	166
104	Comparison of Design With Test Vector Diagram	167
105	Stator Loss Coefficient and Efficiency Versus Aspect Ratio	168
106	Comparison Between Present USAAVLABS Turbine and Recommended Modified Design	169
107	Gas and Metal Temperatures During Test - Rotor Build 5	171

LIST OF ILLUSTRATIONS (Continued)

<u>Figure</u>		<u>Page</u>
108	Pressures and Airflow Values During Test - Rotor Build 5 .	173
109	Turbine Rotor	175
110	Turbine Stator	176
111	Turbine Rotor and Stator	177
112	Turbine Rotor Blade Skin Temperature Leading-Edge Pressure Side Channel	178
113	Airflow Path Through Shroud Support Assembly	179
114	Test Cell Installation - Rear View	180
115	Rig Control Panel	181
116	Rig Instrumentation Panel	181
117	Interconnecting Shaft ID	193
118	Interconnecting Shaft ID	193
119	Gearbox Input Shaft Spline End After Test - Rotor Build 5	194
120	Turbine Rotor After Test - Rotor Build 5	195
121	Interconnecting Shaft Details After Tests - Rotor Build 2B	196

LIST OF TABLES

<u>Table</u>		<u>Page</u>
I	Nominal Chemical Composition of Blading and Airfoil Materials	14
II	Porous Mesh Tensile Properties	16
III	Weld Parameters	20
IV	Weld Parameters	23
V	Rotor Welding Sequence	25
VI	Interblade Crack Lengths	27
VII	Alternate Blade-to-Disc Materials Tensile Test Data Inconel 713 LC Blade and Inconel 718 Disc	28
VIII	Combustor Test Accomplishments	65
IX	Combustor Vaporizer Characteristics	66
X	Configuration Characteristics and Performance	68
XI	Combustor Airflow Distribution - Design Values Versus Test Values	70
XII	Stator and Rotor Hot Test Times	115
XIII	Comparison of Design and Actual Stator Blade Temperatures	116
XIV	Turbine Stator Sealing Configurations	117
XV	Program Test Summary	144
XVI	Improved Design and Estimated Performance	148
XVII	Accumulated Time at Temperature	149
XVIII	Design Versus Test Metal Temperatures	149
XIX	Design Versus Test Metal Temperatures	150
XX	Airfoil Mesh Material Properties	152
XXI	Airfoil Leading-Edge Pressure Side Panel Temperatures . .	152
XXII	Airfoil Data Through Shroud	154

<u>Table</u>		<u>Page</u>
XXIII	Combustor Test Chronology	185
XXIV	Stator Test Summary	188
XXV	Full-Stage Rig Test Summary	189

LIST OF SYMBOLS

A_t	Stator throat area
b	Blade axial chord
h	Blade height
M_{2i}	Ideal Mach number defined by $P_{S_2}/P_{T_0} = \left(1 + \frac{\gamma-1}{2} M_{2i}^2\right)^{\frac{-\gamma}{\gamma-1}}$
N	RPM of engine
P_S	Static pressure
P_T	Absolute total pressure
P_{T_R}	Relative total pressure
R_1	Stator pressure recovery at stator exit given by P_{T_1}/P_{T_0}
R_2	Stator pressure recovery at rotor inlet given by P_{T_2}/P_{T_0}
T_T	Total temperature
U	Wheel, peripheral speed
W	Weight flow
W_c	Total cooling weight flow
η_1	Stator blade efficiency at stator exit given by $\left[1 - \left(P_{S_1}/P_{T_1}\right)^{\frac{\gamma-1}{\gamma}}\right] / \left[1 - \left(P_{S_1}/P_{T_0}\right)^{\frac{\gamma-1}{\gamma}}\right]$

η_2 Stator blade efficiency at rotor inlet given by

$$\left[1 - \left(P_{S_2} / P_{T_2} \right) \frac{\gamma - 1}{\gamma} \right] / \left[1 - \left(P_{S_2} / P_{T_0} \right) \frac{\gamma - 1}{\gamma} \right]$$

η_T Turbine efficiency given by

$$\left[\Delta H_T / C_P W_2 T_{T_2} \right] / \left[1 - \left(P_{T_4} / P_{T_0} \right) \frac{\gamma - 1}{\gamma} \right]$$

ϕ Flow coefficient given by

$$\left(\frac{W_2 \sqrt{T_{T_2}}}{P_{T_0} A_t} \right) / \sqrt{\frac{\gamma}{R}} M_{2i} \left(1 + \frac{\gamma - 1}{2} M_{2i}^2 \right)^{-\frac{\gamma + 1}{2(\gamma - 1)}} \text{ for } M_{2i} < 1$$

$$\left(\frac{W_2 \sqrt{T_{T_2}}}{P_{T_0} A_t} \right) / \sqrt{\frac{\gamma}{R}} \left(\frac{\gamma + 1}{2} \right)^{-\frac{\gamma + 1}{2(\gamma - 1)}} \text{ for } M_{2i} \geq 1$$

W_1 Stator loss coefficient at stator exit given by

$$P_{T_0} - P_{T_1} / P_{T_0} - P_{S_1}$$

W_2 Stator loss coefficient at rotor inlet given by

$$P_{T_0} - P_{T_2} / P_{T_0} - P_{S_2}$$

W_4 Rotor loss coefficient at constant radius given by

$$P_{T_{R_2}} - P_{T_{R_4}} / P_{T_{R_2}} - P_{S_4}$$

SUBSCRIPTS

0	Stator inlet
1	Stator exit
2	Rotor inlet
4	Rotor exit

		<u>Units</u>
T_L	Local temperature	°F, °R
T_4	Combustor exit temperature	°F, °R
T_4	Average combustor exit temperature	°F, °R
V_{AX}	Axial velocity	Feet per second
V_w	Whirl velocity	Feet per second
V_R	Relative velocity	Feet per second
U	Wheel velocity	Feet per second
M_{VR}	Relative Mach No.	Mach No.
V	Absolute velocity	Feet per second
M_v	Absolute Mach No.	Mach No.

BLANK PAGE

1.0 INTRODUCTION

A key element in the improvement of the specific horsepower output of small gas turbine engines is the ability of the turbine component to operate efficiently at significantly higher inlet temperatures. By the use of transpiration cooling applied to the hot and highly stressed components, the turbine can be operated at inlet temperatures well above the 1600° to 1800°F limit of uncooled gas turbines. Successful operation of the turbine at inlet temperatures up to 2650°F has been demonstrated under this program using transpiration cooling applied to both the stator and rotor blades. This achievement provides the potential of obtaining twice the specific horsepower output of current uncooled high-performance small gas turbine engines despite the somewhat lower stage efficiency that must be accepted as compared to high performance non-cooled turbines.

One of the more important aspects to be considered in the mechanical design of an advanced high-temperature turbine is the selection of the blade cooling method. This is so because the fundamental thermal characteristics of a blade - (1) average metal temperature, (2) chordwise temperature gradients, (3) sensitivity to gas temperature gradients, (4) sensitivity to gas temperature profiles, and (5) amount of coolant required - are functions of the cooling method selected and turbine inlet temperature.

On the basis of theoretical, experimental, and practical investigations, the transpiration cooling method was selected as the optimum choice for the development effort described herein. The major reasons for making this selection are described as follows. Transpiration is theoretically the most efficient and most effective air cooling method under all conditions of laminar and turbulent flow heat transfer. Transpiration-cooled turbine blades require less coolant flow than any other type of air-cooled blades above a given turbine inlet temperature (TIT); the superiority of transpiration cooling is further increased as the turbine inlet gas temperature is raised to still higher temperatures.

The chordwise metal temperature gradients present in transpiration blade structures are small due to the uniform coolant distribution that can be achieved in a homogeneous transpiration material as opposed to the isolated injection that is inherent in other film cooling methods.

Blade design and construction permit flexibility in distributing and controlling the airflow by the use of metering orifices to feed discrete coolant channels and porous airfoil sections of different permeabilities. Orifices may be easily revised to tailor coolant flows to the needs of local blade areas. Discrete sections of the porous airfoil may be removed and replaced by electron beam welding. This is an important development tool as well as a significant service consideration.

Transpiration blades have the capability of accepting wide ranges in positive and negative incidence angles with no detrimental thermal effects at the leading edge. The coolant flow and the leading-edge temperature are

practically insensitive to a shifting stagnation point on stator or rotor leading edges. This feature is particularly important in the consideration of high-temperature, variable-geometry turbine designs. Also, engine and cascade tests have indicated that turbine performance is not affected significantly by changing transpiration cooling airflows over a wide range (Figures 82, 91, 103).

Thus, the transpiration air cooling technology utilized in this program was based on background experience of theoretical analysis and of test engine and component operation in the regime up to 3000°F turbine inlet temperature for blade heights from .5 to 5.0 inches which apply to engine designs from 4 to 600 pounds per second airflow.

Volume I of this report describes the work carried out under Phase I of the contract: the design, analysis, and preliminary evaluation of the complete transpiration-air-cooled turbine stage rig. The rig parts were detailed and fabricated as outlined in Volume I with only minor changes for ease in manufacture. As a result of the stator cascade evaluation performed in Phase I, the full round stator assembly was modified to incorporate positive sealing features to minimize leakage of the stator cooling air.

This volume describes the work carried out under Phase II of this program, which consisted of the manufacture and rig test evaluation of the complete turbine stage, including the combustor. While the long-lead-time items like blades and rotor disc castings were being fabricated, testing was initiated on the combustor section. Next, stator testing was carried out while the rotor blade-to-disc welding technique was being perfected. Finally, the fully assembled complete turbine stage tests were undertaken. Warm air aerodynamic performance data were obtained first, and then the high turbine inlet temperature capability was demonstrated. A detailed discussion of these various phases of this program and the test results and analysis are presented in the following sections of this report.

2.0 DETAIL DESIGN - TURBINE COMPONENT

A complete preliminary design of the turbine component was carried out under the Phase I portion of this program. A final detailed design was carried out during the Phase II portion of the program.

The only major change that occurred between the original preliminary design and the final design was that the turbine's design direction of rotation was reversed. This was done so that the turbine's rotation would match the direction of rotation of the compressor which was being developed as part of the same gas generator. To accomplish this change, the final drawings were detailed as mirror images of the original layouts where applicable. All the aerodynamic and mechanical design work was still valid for the reverse rotation. The turbine now rotates clockwise as viewed from the rear. A presentation of the turbine component basic arrangement is shown in Figure 1.

2.1 STATOR VANE

Only minor changes in detail were made between the stator vane design of Phase I and the final design of Phase II. The changes were made to simplify manufacture and did not compromise the mechanical design. The mating shelf surfaces for the inner and outer shelves were circular arcs and initially had individual centers. A common center was used in actual manufacture. This changed the shelf thickness slightly but made it possible to use only one setup for machining both inner and outer shelf sealing surfaces. This is change B in Figure 2.

The spar section was changed slightly to allow removal of the wax casting die. The direction of withdrawal was revised to avoid contact with the curved shelf. The surface near the lands had to be modified also so that there was always a slight draft angle in the direction of die withdrawal. This change affected only the internal spar and had no effect on the external airfoil shape.

Casting stock allowance was specified at .020 inch to .030 inch above the outside shelf surfaces. During subsequent casting trials, it was found that this tolerance had to be increased to .060 inch so that shelf positioning would be assured. The airfoil section of the spar is precision cast to final dimensions (within $\pm .003$ inch), and machining was not required.

The use of the cast trunnions to position the blade for subsequent machining resulted in a uniform orientation of the blades in the final assembly. Subsequent welding of the blades into an assembly was required as testing progressed. The locating lugs required initially proved to be valuable in positioning the blades during this subsequent operation.

Further details of the welded assembly are discussed in Section 4.2.1. Also discussed in that section are the initial changes made to the shelf sealing surfaces to minimize the interblade leakage.

2.2 ROTOR BLADE

The detailed design of the rotor blade followed the Phase I design with slight modifications for ease in manufacturing. The blades were made in several width-of-butt sizes to make possible snug fitting of the blades on the rotor disc. The butt design included a hollow plenum for the cooling air. To prevent movement of the ceramic core which provided the plenum in the blade casting process (later leached out) two radials 1/8 inch holes were allowed in the butt inner face to accommodate two fixed core stabilizing pins. The holes became unnecessary because an alternate method was found for holding the core while making the wax casting. The method consisted of using two removable pins to hold the core in place during the wax casting and then removing the pins and patching holes in the wax mold.

The air inlet groove at the butt was enlarged to prevent the possibility of the root of the blade-to-disc butt weld from closing off the air passage. This design was again changed for the second rotor and is discussed in detail in Section 3.1. The only other change from the original design was the modification to the leading-edge pressure side cooling orifice configuration, which is also discussed in Section 3.1.

Figure 3 shows the essential features of the detailed drawing. As with the stator vane, the casting stock allowance of .030 inch was exceeded and resulted in increased machining for stock removal. The airfoil section of the spar was precision cast to finished dimensions (within $\pm .003$ inch), and machining was not required.

2.3 ROTOR BLADE AND DISC ASSEMBLY

The detailed drawing of the complete rotor assembly is shown in Figure 4. The end of the shaft was not bored through, but this option was available if required for routing out of instrumentation lines. The disc-to-blade joint was modified to match the blade changes mentioned in the previous section.

The main design effort in making the final detailed drawing of the rotor assembly was directed to establishing a method of dimensioning which would locate the blades on the disc so that when the weld crowns were removed and the front and rear faces were machined, the walls of the hollow blade butt would be of approximately equal thickness. This was accomplished by establishing one reference plane for the disc from which all dimensions were given and then adjusting the dimensions to within the tolerance band to which the blade butt walls had been made.

Balancing of the rotor was required to be within .001 ounce-inch.

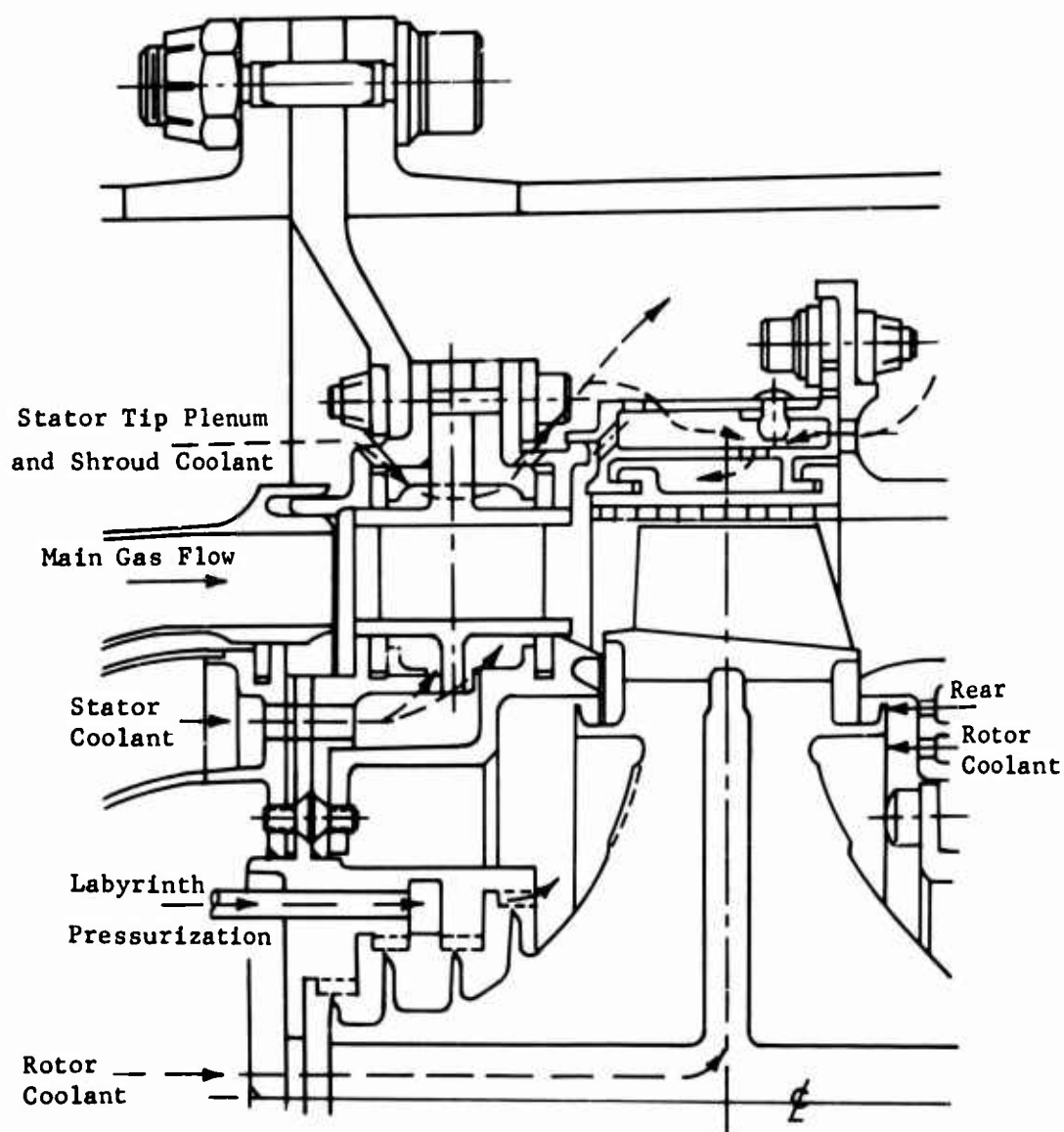


Figure 1. Turbine Component Basic Arrangement.

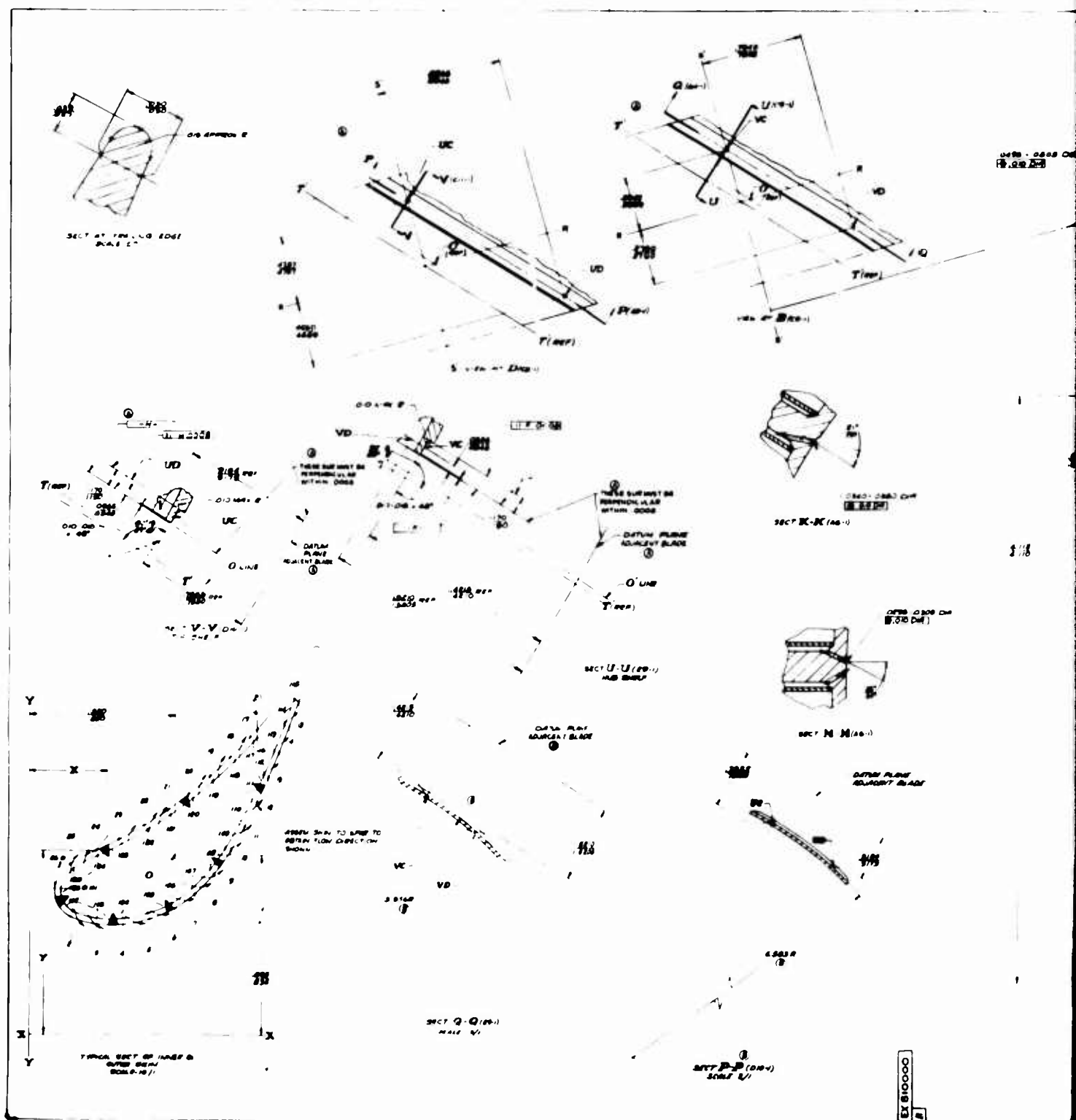
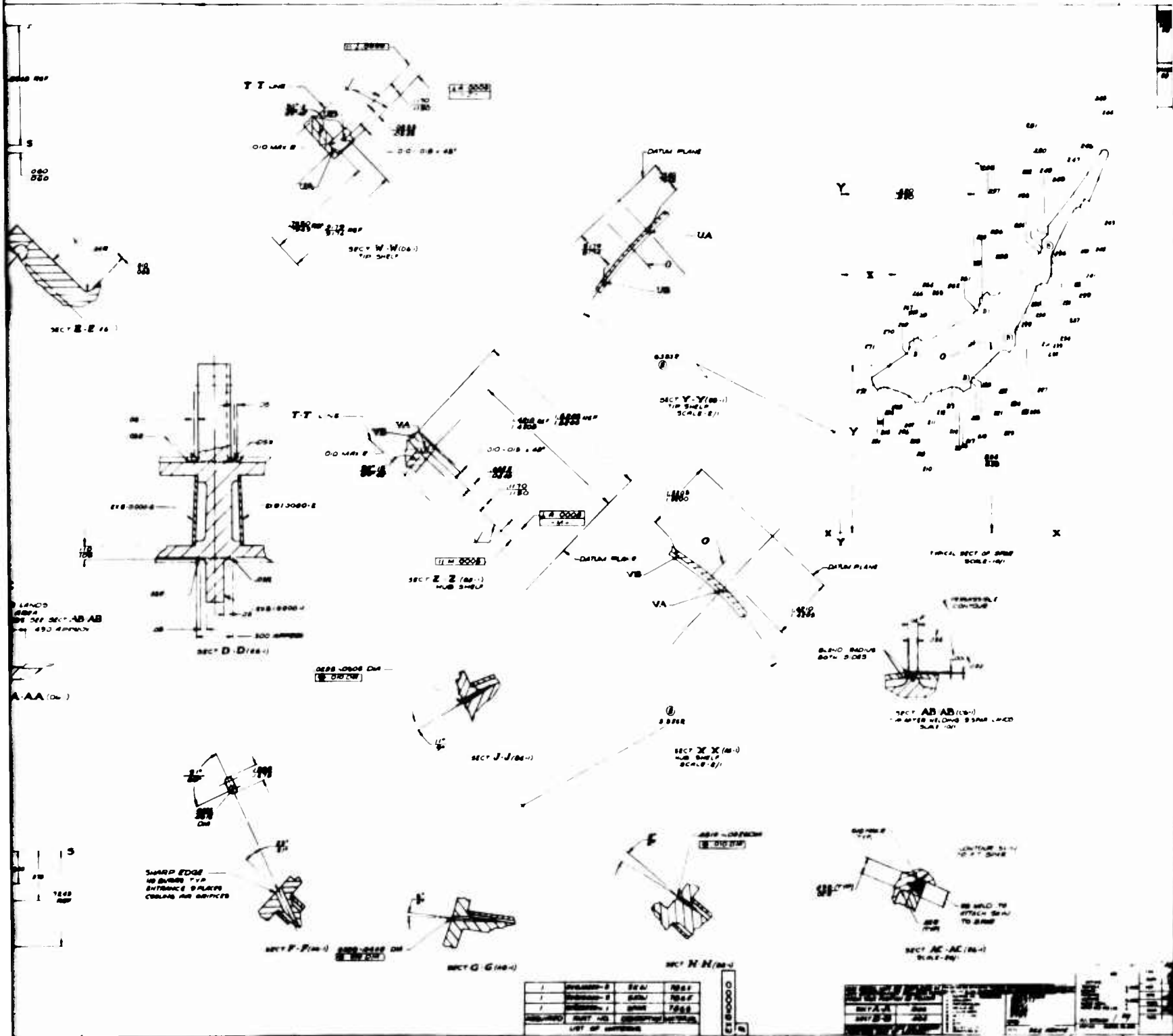
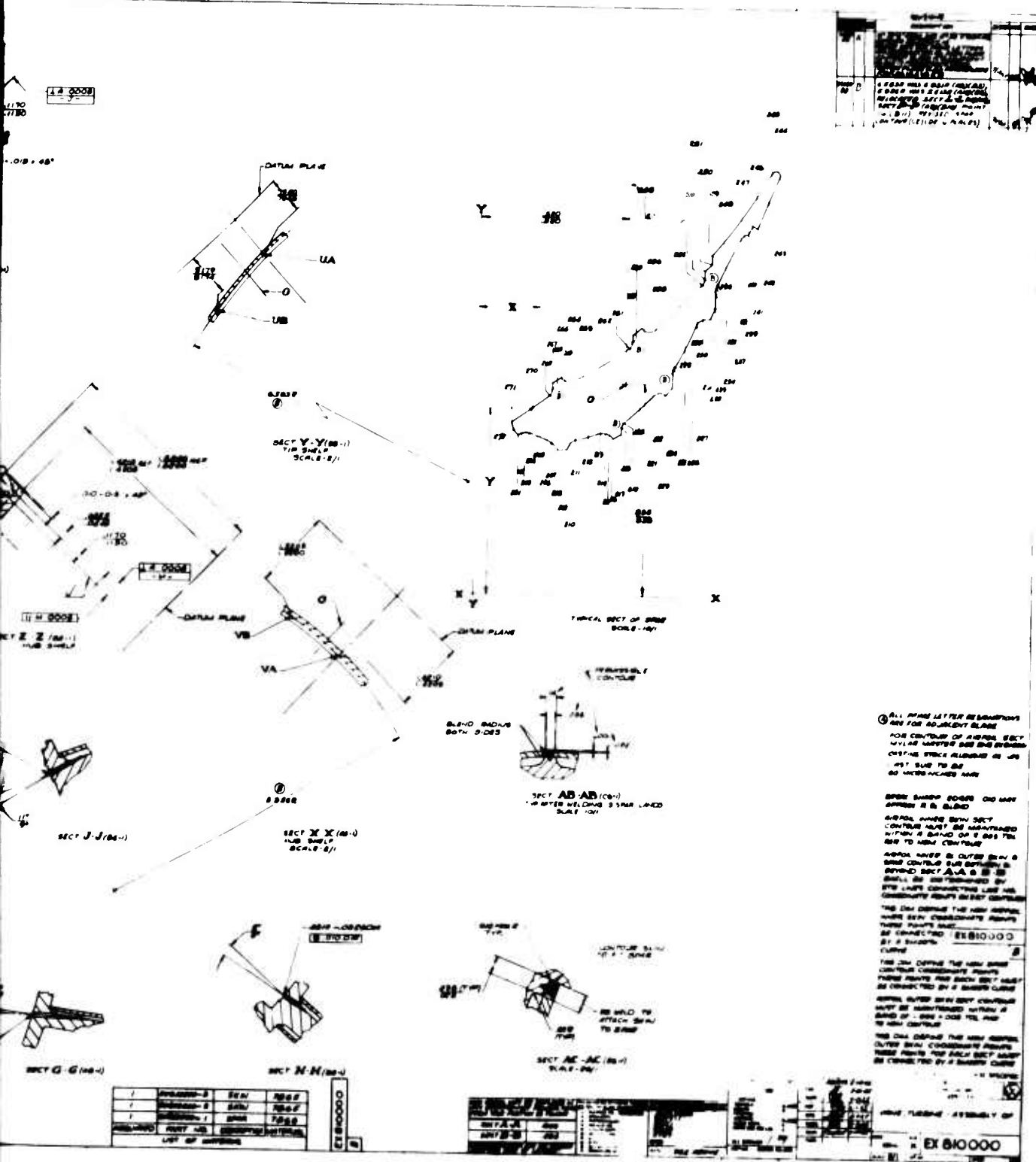


Figure 2. Vane Turbine Assembly.

A

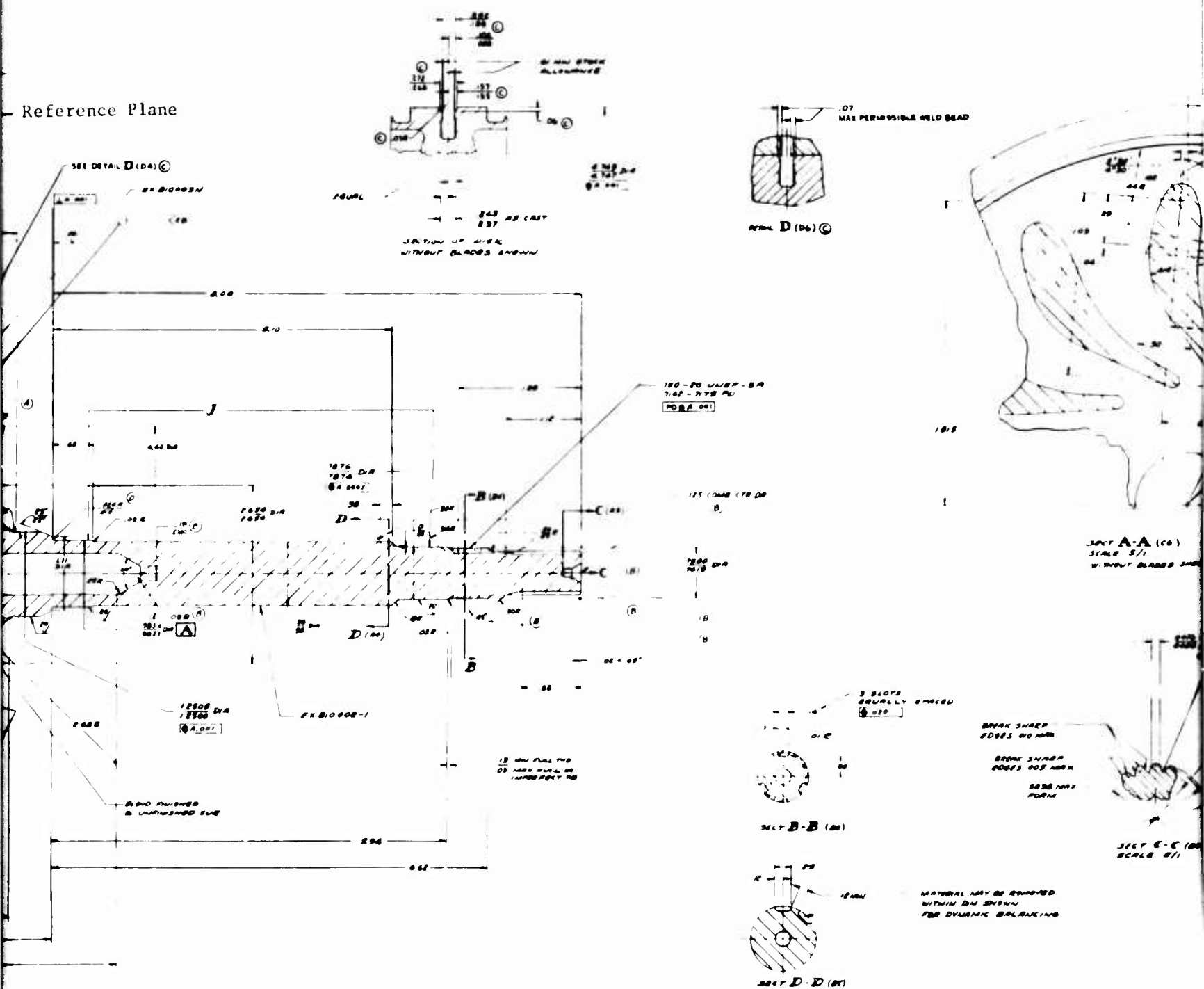


C



iD

Reference Plane



EX 810002 E

B

3.0 FABRICATION

3.1 TURBINE COMPONENT

3.1.1 Blade Fabrication

The fabrication techniques and experience gained on the larger transpiration cooled blades of earlier Curtiss-Wright turbine programs were applicable to a large extent to the small blading of the USAAVLABS turbine component program. In the course of continuous materials research and study, properties of many strut and porous mesh airfoil materials have been evaluated as well as their suitability for joining into a composite structure by electron beam (EB) welding. Among the strut materials evaluated were HS31, cast and wrought René 41, MAR-M 302, MAR-M 322, IN 100, Nimonic 115, Inconel 700, and Inconel 713 low carbon (LC). Airfoil materials included N-155, Hastelloy X, and Nichrome V Cb for various wire diameters, airfoil (wall) thicknesses, and mesh weaves (wound and woven).

Examination of the mechanical and physical properties and the weldability of these materials led to a choice of cast Inconel 713 LC for the stator vane struts and MAR-M 302 for the rotor struts. Selection of MAR-M 302 was made for the rotor struts based on early success in achieving weld compatibility of this material with cast Inconel 718, the disc material whereas difficulties were anticipated in welding Inconel 713 to Inconel 718. Subsequent explorations in welding Inconel 713 and Inconel 718 (described later in the report) indicate that welding parameters have essentially been resolved. The chemical composition of the materials selected for the turbine blading fabrication for the test program is shown in Table I. The airfoil material originally selected was N-155 wound mesh, nominally .020 inch thick and made into .0035-inch-by-.0065-inch wire ribbon. Based on continuing metallurgical test evaluation Nichrome V Cb was later chosen as the airfoil mesh material because of its superior ductility and oxidation resistance, as compared to N-155, after long term exposure to temperatures of 1300° to 1600°F. Stators having airfoils made from both mesh materials were fabricated and used in tests in this program.

During these earlier programs, it was recognized that although weld compatibility existed between the porous mesh and the solid strut, it was necessary to gain basic knowledge pertaining to the applicability and flexibility of electron beam welding as used in the blade fabrication. It was felt that the electron beam weld joint would be sensitive to such variables as airfoil-to-strut fit-up, mesh cleanliness, beam incidence, and welding parameters such as beam current, power density, weld speed, etc. In addition, the requirements imposed by the complex blade design were demanding and included narrow land (joint) width, ability to follow the helical twist of the blade contour, and desire to have a smooth airfoil surface. Since each of these conditions could be satisfied only by a precisely defined and optimized welding schedule, an extensive material processes research program was conducted at Curtiss-Wright. The basic parametric information

TABLE I
NOMINAL CHEMICAL COMPOSITION OF BLADING AND AIRFOIL MATERIALS

	C	N	Mn	Si	Cr	Ni	Fe	Cb	Ti	Al	W	Co	Mo	B	Zr	Ta
Blading Materials																
Inconel 713 LC	.05	-	-	-	12.0	Bal	-	2.0*	.6	5.9	-	-	4.5	.010	.10	-
MAR-M 302	.85	-	-	-	21.5	-	-	-	-	-	10.0	Bal	-	.005	.20	9.0
Airfoil Materials																
N-155	.12	.15	1.5	1.0	21.0	20.0	Bal	1.0*	-	-	2.5	20.0	3.0	-	-	-
Nichrome	.025 Max.	-	.50 Max.	1.2	19.5	75 Min.	1.0 Min.	1.0 Min.	-	-	-	1.0 Max.	-	-	-	-
* Cb + Ta																

from this study was utilized to define the welding schedule for the materials and blade mechanical design of this turbine program.*

In all, five material combinations were investigated as follows: for stator vanes, Inconel 713 LC as strut material in combination with N-155 and Nichrome V Cb airfoil mesh materials; for rotor blades, MAR-M 302 and Inconel 713 LC as strut materials in combination with Nichrome V Cb airfoil mesh material; for rotor strut-to-disc attachment materials, MAR-M 302 and Inconel 713 LC as strut materials with Inconel 718 as disc material.

The following paragraphs describe the blade fabrication and manufacturing process development conducted during this program to provide the blading for the turbine component rig testing.

Strut

The load-carrying member of the stator - the stator strut - was precision cast of high-strength Inconel 713 LC (Figure 5). The inner and outer gas shelves were cast integral with the stator strut. The airfoil section, including spanwise cooling air channels and weld lands, was finish cast to final dimensions and required no machining. Only the sealing surfaces on the shelves where platforms of each vane intersected and the antitorque locating lugs were subsequently ground to the finished dimensions.

The rotor-blade load-carrying member - the strut - was precision cast of MAR-M 302 (Figure 6). The strut casting incorporates an integral cast inner gas shelf and cooling air plenum. The airfoil section, including the spanwise cooling air channels and weld lands, was cast to finish dimensions and required no further machining. Only the shelf sealing surfaces (Figure 6) and the surface mating with the rotor disc were ground to finish dimensions. The outside diameter trunnion used for fixturing was machined-off prior to welding.

In the case of both the stator and the rotor, the cooling air orifices which feed the spanwise channels from the plenum beneath the inner shelf were made by the electrical discharge machining process in order to ensure close sizing of the small-diameter orifices (to within .001 inch tolerance) for closely controlled metering of the cooling air.



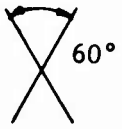
Airfoil.

The porous mesh airfoil which is an integral part of the transpiration cooling concept forms the appropriate aerodynamic shape of the gas passage. The porous mesh airfoil is formed from flat sheet wire mesh. The mesh is made as follows:

*Development of Techniques for Electron Beam Welding of WTF60 Transpirationally Cooled Turbine Blade - WAD P423-14, Contract AF33(657)-15787, Wood-Ridge, New Jersey, Curtiss-Wright Corporation, April 1966

1. The .005-inch diameter is extruded into a rectangular cross section (.0035 inch x .0065 inch).
2. The wire ribbon is wound on a mandrel.
3. The wound mesh is then swaged to the desired permeability and thickness.
4. The wires of the mesh are diffusion bonded to form a coherent structure.

The mechanical properties of the porous airfoil material are a function of the mechanical properties of the alloy of which the wire is made as well as density, wire diameter, weave intersection angle, and direction of loading. For Nichrome V Cb alloy and .023-inch mesh thickness, the properties shown in Table II were obtained in an Instron uniaxial tensile test at 1200°F.

TABLE II POROUS MESH TENSILE PROPERTIES				
Direction of Load		Ultimate Tensile Strength (ksi)	.2 Percent Yield Strength (ksi)	Elongation (percent)
Wire Intersection Angle		16.3	12.2	6.7
Wire Intersection Angle		30.0	19.0	5.3

Earlier tests on N-155 wire in the temperature range of 1300° to 1600°F revealed embrittlement because of overaging; they also showed reduced oxidation resistance. On the other hand, Nichrome V Cb showed no appreciable overaging in this temperature range and demonstrated greater oxidation resistance. Thus, the material selected as first choice for this program was Nichrome V Cb. However, because a considerable amount of high-temperature transpiration-cooled blade testing had been successfully accomplished with the N-155 alloy, several stator vanes were made which incorporated N-155 airfoils to establish a metallurgical reference point when operated in the same temperature environment as the Nichrome V Cb airfoils.

Since the porous mesh airfoil is not normally a load-carrying element, no advantage was taken of the anisotropic strength characteristic of the mesh. Instead, another mesh characteristic was utilized beneficially. The cooling air leaves the surface of the mesh all in one direction at a 30-degree angle to the surface. This was utilized to ensure ejection of the cooling air in the same direction as the gas flow. It was felt that this would

tend to minimize aerodynamic losses and improve the cooling effectiveness. Thus, the mesh material was tested for flow direction and appropriately oriented during the fit-up for welding to the strut so that discharge of cooling air (C/A) was in the direction of the gas flow.

The tooling for forming the airfoil mesh consisted of two nonpermanent molds which duplicated the pressure and suction side airfoil of the strut. The flat sheet mesh is drawn over these molds. The final forming step consisted of matching each airfoil mesh with the individual strut to which it would be welded. Figures 7 and 8 show typical formed airfoil sections for the stator and rotor blades.

Blade Welding

The welding required on the blades included the following:

1. Airfoil to strut lands
2. Convex to concave airfoil sections to leading edge land
3. Airfoil to trailing edge
4. Airfoil to shoulder at the inner and outer gas shelves

A description of the requirements and techniques involved is presented in Volume I. The airfoil to strut welding was accomplished in a 150 KVA Hamilton-Zeiss electron beam welding machine. The following paragraphs summarize the fixturing and welding effort.

Stator Vane Welding

The clamping fixture used for airfoil welding consisted of a rigid frame to hold the vane in proper orientation. Free floating sectional clamps at the convex surface, concave surface, and leading edge held the mesh airfoil in firm contact with the lands. The mesh was then fused to the land by electron beam welding. Slots in the frame and in the floating clamps allowed passage of the electron beam. A line was scribed on the mesh to aid in aligning the beam over the land.

Figures 9 and 10 show the vane welding fixture. The vane with the fitted skin is clamped in the fixture, and this complete assembly then rotates on a circle offset from the center line of the trunnion. The gear rotating the vane is in turn driven by a rack gear. The speed of rotation of the vane is governed by the linear motion of the rack. A cam is used to drive the rack and impart varying rotational speed to the vane during welding. Two additional cams imparted variable horizontal and vertical motion to the vane being welded. All three cams are driven in sequence by a single motor inside the vacuum chamber and integral with the fixture. The purposes of the fixture motion are to maintain the work at the point of and normal to the electron beam and to maintain constant welding speed.

The completed stator vanes are shown in Figure 11. The shelf land joint required the use of .015-inch Hastelloy X filler wire to produce a flush surface. A typically excellent joint of the Inconel 713 strut material and Nichrome V Cb mesh is shown in Figure 12. A welded vane with N-155 mesh is shown in Figure 13.

Rotor Blade Welding

Welding of rotor blades followed procedures similar to those of the stator vanes with a similar welding fixture designed with movements for alignment of the land under the beam. Figure 14 presents the fixture.

A typical rotor blade assembly is shown in Figure 15. The land weld penetration was excellent. Figure 16 shows an etched cross section of the electron beam welded turbine rotor blade. Figure 17 is an enlarged view of the middle land weld on the concave side. The trailing-edge land weld on the convex side is shown in Figure 18. The required flush weld surface was achieved without filler wire by making a second low-beam power cosmetic pass following the initial fusion pass.

In addition to demonstrating primary manufacturing techniques for transpiration cooled blades which were applicable to the small blade size, certain repair techniques were also demonstrated. Procedures were utilized for removing discrepant mesh panels and replacing them with new panels. This was accomplished not only on separate individual blades but also on rotor blades which were already welded on the rotor disc as part of the complete rotor assembly. Figure 19 shows test rig rotor assembly no. 2 that had all of the leading edge pressure side panels removed and replaced with new ones while the blades were attached to the complete rotor assembly. Welding in the complete rotor assembly prevented aligning of the electron beam normal to the work surface. Nevertheless, weld penetration, weld width, and beam positioning were carried out to within acceptable limits. This demonstrated the adaptability of the electron beam welding process for attaching transpiration cooled airfoil mesh material onto blade struts that are integrally cast with the disc.

3.1.2 Rotor Blade and Disc Assembly

Rotor Disc and Shaft

The rotor disc and shaft was a one-piece precision casting of Inconel 718 (Figure 20). Cooling air vanes were integrally cast between the front and rear halves of the disc as shown in the cross section of Figure 21. The ceramic core used in the wax mold is also shown. After casting, the core was leached out leaving well-defined and smooth cooling vanes. The casting was then rough machined as shown in Figure 22. Prior to welding-on of the rotor blades, the disc outside diameter was machined to the finished dimension. The blades were then fitted to this surface for welding. After welding of the blades to the disc, the assembly was heat treated and then the entire rotor assembly was completed by finish machining the labyrinth fins, blade tips, bearing journals, and drive splines. Finally, the center

cooling air passage through the shaft center was bored to dimension. The finish machined rotor assembly is shown in Figure 23. This figure shows the leading-edge pressure side panels after replacement on the completed rotor assembly by electron beam welding.

Blade-to-Disc Welding

The joining of transpiration cooled rotor blades to a cast rotor disc was accomplished by following a three-phase program: (1) development of a sample joint configuration which satisfies the design and stress requirements; (2) welding of a structure which simulates the component conditions and permits proof-testing of the weld parameters, check-out of welding fixtures, and establishment of a fabrication sequence; and (3) welding of the test rig hardware. This approach was followed and is now described in detail.

Sample Joint Configurations

Welding parameters were developed on a flat, straight joint which consisted of a cast Inconel 718 plate to simulate the disc and a machined MAR-M 302 simulated blade butt. The weld root bead protrusion was about .070 inch, and a recess was later specified at the inside of the joint to accommodate this weld root bead. This recess was intended to minimize protrusion of the weld root and thus avoid blockage of the cooling air passages.

Welding of Simulated Blade-Hub Assembly

Electron beam welding of thick sections requires special considerations. Backup material may be used on the penetration (root) side of the weld, or a heavy section may be welded from both sides with the two welds joining in the center of the joint. Another technique often used is to design a joint with a backup lip which contains the weld penetration. The above techniques normally require accessibility to the root of the weld for machining away the backup material or weld bead. In the actual turbine wheel design the rim consists of two 1/2-inch-thick sections separated by a .2-inch gap accommodating the rotor cooling vane height (Figure 22). With the blades electron beam welded to the rim, the backs of the 1/2-inch sections become inaccessible after welding. Since none of the above-mentioned conventional electron beam welding techniques could be applied because of design geometry of the part, a technique was developed whereby the weld was made from one side of the double joint with high beam power input and high weld speed. With this technique, as the forward section was welded the beam was "jumped" across the gap, penetrating about one-third of the thickness of the other section. The resultant weld root protrusion was about .060 inch to .070 inch and reasonably uniform. The final step was to complete the weld from the opposite side with partial penetration of the section sufficient to fuse with the weld made during the first pass.

Initially, weld samples to evaluate the face and root weld geometry were performed on single thickness disc samples. Subsequently, rotor blade butt samples were successfully welded to spaced discs, simulating the actual

configuration of the blade-disc assembly. The technique proved effective, as shown in Figure 24 and Figure 26. The disc front side was welded with beam gun at 3 inches from the disc surface. The rear side was welded 10 inches from the disc surface. This distance was dictated by the length of the turbine shaft. The blade-to-disc welding process is described in Figure 25. The weld parameters established for the first rotor assembly are shown in Table III.

TABLE III
WELD PARAMETERS

Weld Type	Kilovolts	Milliamps	Inches	Focus	Gun-to-Work
			Per Minute		Distance, Inches
Tack Pass	18	180	150	Sharp	3 and 10
Fusion Pass	30	380	75	Sharp	3
Fusion Pass	30	390	60	Sharp	10

X-ray inspection and sectioning of the weld areas verified the soundness of the welds. The simulated assembly was cut through the annulus for a visual inspection of the weld root which is shown in Figure 26. The weld root made at both the 3-inch and the 10-inch beam focal lengths was uniform and metallurgically sound.

A satisfactory circumferential weld overlap technique was developed and used in this application. The parameters and dimensions of the power slope sequences were established on 5-inch blocks of Inconel 718. An accelerating voltage of 8 kilovolts was selected for the starting as well as the decay setting. The refined sequence is shown in Figure 27.

Rotor Blade and Disc Welding - First Rotor

For rotor assembly no. 1, the transpirationally cooled rotor blades were electron beam welded to the disc in a welding fixture in which each blade was located and restrained by a three-fingered shelf clamp which was adjusted from the outside diameter of the fixture by a single clamping screw. The weld parameters, weld sequence, and techniques used were those previously proven successful on simulated rotor assemblies. The fixture is illustrated in Figure 29 (a).

Inspection after blade-to-disc welding revealed that both welds contained blade interface extensions, i.e., radial cracks extending into the weld from the blade-to-blade interfaces (Figure 28). The maximum length of these cracks was approximately .150 inch. The cracks were routed out and manually tungsten arc inert gas shield (TIG) weld-filled with Inconel 718 wire prior to the aging heat treatment.

Since no interface crack extensions were experienced on the welded simulated rotor assemblies, it was important to determine the difference between the two assemblies in terms of physical variables and to obtain a remedy for this condition. The major differences between the actual and simulated blades were: (1) the actual blade shelves were canted 15 degrees to axial, while the simulated blades were straight; and (2) the actual blades had a .002 inch to .003 inch sidewall shoulder to allow butting to each other at the disc surface and clearance for expansion at the gas shelf surface, whereas the sample pieces butted each other all along their radial joint.

It was determined that the major cause of interblade crack extensions was the ability of the blades to move with respect to each other during welding - a phenomenon attributed to the expansion and shrinkage forces associated with the welding process. Therefore, the welding fixture was redesigned to provide for a three-point shelf clamp, providing individual adjustment of pressure on the shelf of each blade assembled to the disc illustrated in Figure 29 (b). The new fixture was evaluated by welding a trial rotor assembly. The rotor was divided into three 120-degree segments, each segment being utilized to evaluate a different welding technique. On one segment, an improvement was observed using the same welding parameters as those on the first welded turbine assembly. Nevertheless, some cracking was still evident, although it was smaller and less frequent.

Another approach proved successful. With blades assembled, fixtured, and electron beam tack welded to the hub, all blade interfaces on a 120-degree segment were TIG welded together using Inconel 718 filler wire. This eliminated the blade interfaces and provided a single butt joint. A subsequent full power electron beam fusion weld was completely crack free.

The final electron beam fusion weld was made with the beam in the vertical (3-inch focal length) position and also slanted at 15 degrees to the vertical (4-1/2-inch focal length). Slanting of the gun at 15 degrees simulated an alternate to the 10-inch focal length setup for the shaft side of the rotor assembly. Equally sound welds were achieved with both electron beam gun positions. Figure 30 shows two locations on the trial welded assembly prior to machining. There are no interface crack extensions into the electron beam fusion weld where TIG tacks were used, as illustrated by View B. The half-moon represents the TIG weld tacks prior to the circumferential electron beam weld pass. View A of Figure 30 shows the interblade extensions into the weld but not into the disc where TIG tacking was not used.

The results of these trials indicated that the modified fixturing in association with the TIG tack welds minimized the occurrence of interblade extensions.

Repair welding techniques were also evaluated on the trial rotor assembly. It was shown that it is possible to repair interblade extensions by either TIG welding, localized electron beam welding, or continuous electron beam welding. Inconel 718 filler metal was used for all three methods.

Post-Weld Heat Treat Aging Cycle of Disc and Blades

Tests were conducted to determine the response of a welded cast Inconel 718 to MAR-M 302 joint to the thermal cycling experienced during the heat treat aging required for the Inconel 718 material. The possibility existed that the welding stresses and additional stresses caused by the dilatometric change due to phase transformation during aging would promote crack extensions at the blade-to-hub weld joint.

Test specimens were machined from electron beam weldments of 1/2-inch-thick Inconel 718 and MAR-M 302 plates. Two test groups were notched .025 inch deep with a .003-inch notch radius in the following locations: (1) the middle of the weld and (2) the heat-affected zone adjacent to MAR-M 302. The specimens were tested in a stress-rupture machine under constant loads simulating stresses of at least 50 percent of the yield stress of MAR-M 302 (which is the weaker of the two alloys) and at temperatures simulating: (1) the normal aging temperature cycle for Inconel 718 (6.2 hours to 1325°F) and (2) a rapid cycle (1.0 hour to 1325°F). The results of the tests indicate that the normal or rapid aging cycle did not affect the composite Inconel 718-MAR-M 302 weld joint. No cracks could be induced at the root of the notch under the simulated thermal and loading cycles. Although these tests did not duplicate the exact stress conditions of the blade-to-hub weld, they indicate that the notch in the weld joints between Inconel 718 and MAR-M 302 is stable. The heat treat sequence established for use after welding was as follows:

1. Place rotor in muffle and purge with argon.
2. Heat rotor to 900°F at 200°F per hour. Equalize at 900°F for 30 minutes.
3. Heat rotor to 1325°F as rapidly as possible. Hold 8 hours.
4. Lower temperature to 1150°F. Hold for a total aging cycle of 18 hours.
5. Remove muffle from furnace and cool in air.

Posttest Weld Revisions

Posttest inspection by destructive analysis of the first test rotor assembly revealed the existence of three additional problem areas meriting further study prior to welding the second test rotor assembly. These problem areas were as follows:

1. Varying height of penetration bead and residual splatter.
2. Incomplete penetration of one of the dual weld joints.
3. Lack of an adequate nondestructive weld inspection technique.

To resolve the interrelated problems of underbead variation and residual splatter, the following criteria were established:

1. The electron beam should decay within the metal thickness, and the weld spike should terminate within a band width of .125 inch from the inside face of the joint.
2. The joint geometry design should feature a low stress concentration configuration at the weld bead root.
3. The weld spike should exhibit minimum taper from top to bottom.

The joint design selected is sketched in Figure 31. The mating surface to be welded is represented by the .375-inch dimension. A .062-inch groove, distributed equally between the blade and the hub, provides a transition having low stress concentration. The view (a) of Figure 32 shows a joint with an unfilled .062-inch groove. Indications of the beam jumping the groove can be seen. The view (b) of Figure 32 shows insufficient penetration into the Inconel 718 wire filling the groove. The view (a) and view (b) of Figure 33 show good penetration with the 3-inch and 10-inch distance of the gun to the work respectively.

Thus, the revised electron beam weld joint satisfied the above criteria. The termination of the weld bead within the joint positively eliminated the problems of varying underbead height and splatter onto the hub internal walls. The shorter fusion line (.375 inch instead of .50 inch) enhanced the reliability of fusing the joint completely. The parameters established for the new joint are shown in Table IV.

TABLE IV WELD PARAMETERS		
	Front	Rear
Gun-to-work distance (inches)	3	10
Accelerating voltage (kilovolts)	29	29
Beam current (milliamps)	250	250
Welding speed (inches per minute)	60	55
Focus current dial setting	495	375

Rotor Blade and Disc Welding - Second Rotor

The welding sequence tabulated in Table V, which proved successful on a simulated rotor, was followed in welding the rotating test rotor. This procedure resulted in satisfactory results on the disc front side. However, during the full power pass on the shaft-side weld, an arc-out occurred at blade location 16 (Figure 34). A second arc-out was experienced at blade location 72. The arc-outs caused local craters. Examination of

the rotor revealed that the Viton A pressure pads between the blade shelf and blade fixture clamping screws had overtemperatured and possibly had outgassed. This would explain the severity of the arc-out. The craters were repaired by TIG weld filling with Hastelloy X wire. The surface repair shown at blade 61 was made to fill a hole made for inspection of the weld and not to repair an arc-out crater.

The weld bead surface on the disc shaft side was ground off to within .010 inch of final dimension for inspection (Figure 34). The lower portion of the photograph shows the hairline cracks of the as-machined surface. The upper portion shows the cracks as exaggerated by etching.

Prior to heat treatment, the weld cracks pictured in Figure 34 were measured. The crack lengths are tabulated in Table VI. Crack progression was not observed after the heat treatment.

Listed also in Table VI is the crack length after build 5. Although the turbine operated at steady-state rotor speeds up to 50,000 rpm (100 percent design) and sustained overspeeds to about 70,000 rpm, these cracks did not progress beyond the weld at the disc rim. Cracks averaged an increase of .011 inch.

Alternate Materials Evaluation

Inconel 713 LC is superior in strength properties to MAR-M 302; hence, it was considered as a candidate strut material for future use in the rotor blade application. There had been considerable experience in welding transpiration cooled porous mesh material to Inconel 713 LC in the stator vane fabrication. However, its weld compatibility with the Inconel 718 disc material required evaluation. An initial study of this combination was described in Volume I. Continued study during the Phase II period showed that a sound weld was possible. This was demonstrated on .5-inch-thick sections. Further efforts were directed at obtaining structural properties test data. Figure 35 shows the published values of allowable stress versus temperature, showing the superiority of Inconel 713 LC over MAR-M 302 in yield strength and stress rupture.

Tensile specimens were machined from approximately 1/2-inch-thick welded plates of cast Inconel 718 disc material and Inconel 713 LC blade material. The plates were aged at 1325°F for 8 hours after welding, furnace cooled to 1150°F, held there for 8 hours, and then air cooled. Mechanical test results of the specimens are presented in Table VII.

Figure 36 is the result of a hardness check taken across the weld in the as-welded and aged condition. Figure 37 shows photomicrographs (100 X magnification) of this weld before and after aging.

Although further weld parameter investigations are required, the Inconel 713 LC appears to be an attractive candidate material for incorporation into the welded rotor blade-to-disc construction.

TABLE V
ROTOR WELDING SEQUENCE

<u>Operation</u>	<u>Description</u>
1	Tack weld Inconel 718 filler wire into .062-inch groove.
2	Fit blades to hub.
3	Ultrasonic clean.
4	Align hub to fixture.
5	Assemble blades and fixture clamping head.
6	Align fixture under electron beam gun, shaft end down.
7	Weld pass, low power electron beam at 3-inch gun-to-work distance.
8	Invert fixture and align under electron beam gun.
9	Weld pass, low power electron beam at 10-inch gun-to-work distance.

<u>Low Power Weld Parameters</u>	<u>Gun-to-Work Distance</u>	
	<u>3 Inches</u>	<u>10 Inches</u>
Accelerating voltage, kilovolts	18	20
Beam current, milliamps	115	150
Travel speed, inches per minute	54	54
Focus current, dial setting	77	458

10	Remove rotor from fixture.
11	Rout and TIG plug blade-blade-hub interfaces.
12	Flush grind tacks at weld joint and relocate and scribe weld joints, both sides.
13	Ultrasonic clean.
14	Refixture and align under gun, shaft end down.
15	Weld pass, full power at 3-inch gun-to-work distance.
16	Invert fixture and align.
17	Weld pass, full power at 10-inch gun-to-work distance.

TABLE V - Continued

<u>Operation</u>		<u>Description</u>	
<u>Full Power Weld Parameters</u>		<u>Gun-to-Work Distance</u>	
		<u>3 Inches</u>	<u>10 Inches</u>
Accelerating voltage, kilovolts		29	30
Beam current, milliamps		255	264
Travel speed, inches per minute		57	57
Focus current, dial setting		495	368
18	Visually inspect.		
19	Machine shaft-side weld bead flush.		
20	Repair defects with TIG welding and Hastelloy X filler wire.		
21	Visually inspect-measure crack lengths.		
22	Ultrasonic clean.		
23	Heat treat.		
24	Inspect.		

TABLE VI
INTERBLADE CRACK LENGTHS - SHAFT SIDE

Indication Identification	Initial Crack Length (inches)	Crack Length After Build 5 (inches)
A	.148	.150
B	.165	.190
C	.185	.190
D	.131	.150
E	.174	.190
F	.110	.210
G	.185	.180
H	.070	.150
I	.155	.210
J	.153	.150
K	.165	.200
L	.204	.190
M	.186	.200
N	.180	.100
O	.175	.200
P	.177	.190
Q	.175	.190
R	.170	.140
S	.190	.200
T	.187	.180
U	.186	.210
V	.190	.130
W	.175	.200

TABLE VII ALTERNATE BLADE-TO-DISC MATERIALS TENSILE TEST DATA INCONEL 713 LC BLADE AND INCONEL 718 DISC						
Spec. No.	Test Temp (°F)	Ultimate Tensile Strength (ksi)	.2 Percent Yield Strength (ksi)	Elongation (percent)	Reduction of Area (percent)	Weld Efficiency (Percent Yield Strength of Inconel 713)
49-1	RT	133.6	114.3	10.5	12.3	Inconel 718 base metal 100+
-2	RT	133.2	114.7	11.0	27.5	Inconel 718 base metal
-3	700	117.0	104.2	6.5	18.3	Inconel 713 base metal 100
-4	700	126.4	110.7	7.0	17.1	Inconel 718 base metal
-5	700	124.9	105.8	11.0	32.1	Inconel 718 base metal
50-1	850	123.5	97.1	8.0	29.0	Inconel 713 base metal 99
-2	850	118.1	99.2	6.0	20.3	Inconel 718 base metal
-3	850	131.2	117.3	7.0	18.9	Inconel 718 base metal
-4	1000	124.7	105.9	7.0	9.0	Inconel 718 base metal 98
-5	1000	122.4	102.4	8.0	13.9	Inconel 718 base metal
-6	1000	113.1	97.8	6.0	25.8	Inconel 718 base metal

3.2 TURBINE TEST RIG

The parts fabricated in this portion of the program were designed and are fully discussed in Volume I. The figures in this section show the major parts. A brief discussion is presented on each component with appropriate comments concerning any fabrication difficulty or design change.

Figure 38 shows the inlet support for the test rig. This unit was bolted to the test equipment ducting through which preheated air to 610°F from a direct fired burner was provided. The struts in this support provided the cooling air passages to supply the rotor and stator cooling air systems and the rotor front labyrinth seal balancing air pressure. In addition, stator and rotor system instrumentation was routed through these struts. This resulted in pressure losses which restricted testing. Increased passage sizes are possible within the existing strut envelope and are recommended in future testing.

Figures 39, 40, and 41 present the combustor headplate, outer liner, and inner liner respectively. All liner parts are made of Hastelloy X. Initially, rivets were used to attach the cooling air deflectors to the liners. However, after the initial hot testing, deflector locations were found to be satisfactory and were therefore welded in place.

Figure 42 shows the stator assembly with part of the blades removed in order to show the relationship of the various support rings. The slots of the forward inner and outer rings were precision ground. The blades of the final assembly fitted snugly in the mating slots. The assembly procedure consisted of placing the blades in the outer ring and then sliding the inner ring in place. The slots acted as radial splines and held the inner supports and attaching labyrinth seal assembly in good concentricity.

The labyrinth seal assembly is shown in Figure 43. The pilot surface at the large flange was machined eccentric as required so that the labyrinth fins were concentric with the mating rotor seal. In the last rotor assembly, the pilot was eliminated in favor of two dowels to locate the labyrinth concentric to the rotor.

The turbine support was made from nodular cast iron and is shown in Figure 44.

The roller bearing retainer (Figure 45) is a welded assembly which cantilevers the bearing off the pilot and clamping face. This provides a soft mounting and a desirable low spring rate for the forward bearing.

The turbine exhaust housing shown in Figure 46 is a Hastelloy X welded and machined assembly.

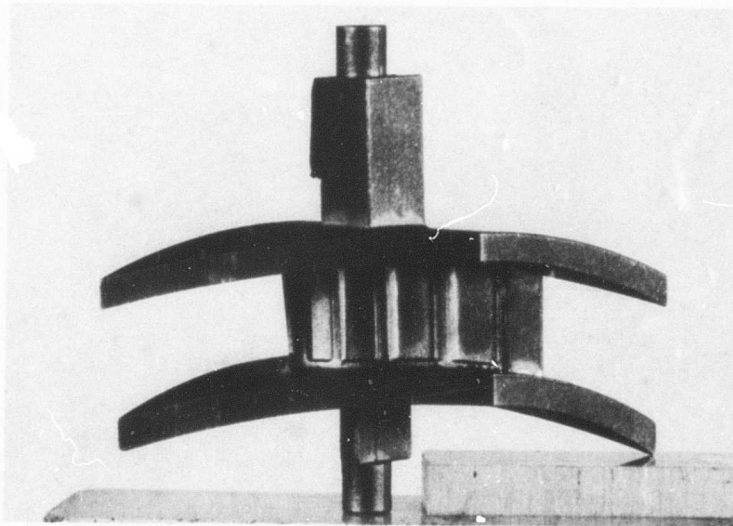
The final turbine shroud configuration is shown in Figure 47. The shroud segments are made by brazing the Hastelloy X honeycomb ribbon material to the shroud ring. The segments are then held in their assembled position, and the inner diameter is ground to size. The honeycomb was filled with

"Microseal", a heat-resistant, low-density, nickel-chrome alloy. It is rub-tolerant because of its low density which allowed it to be compressed. Because of its low density, it also acts as an insulator transmitting less heat than a comparable solid metal shroud.

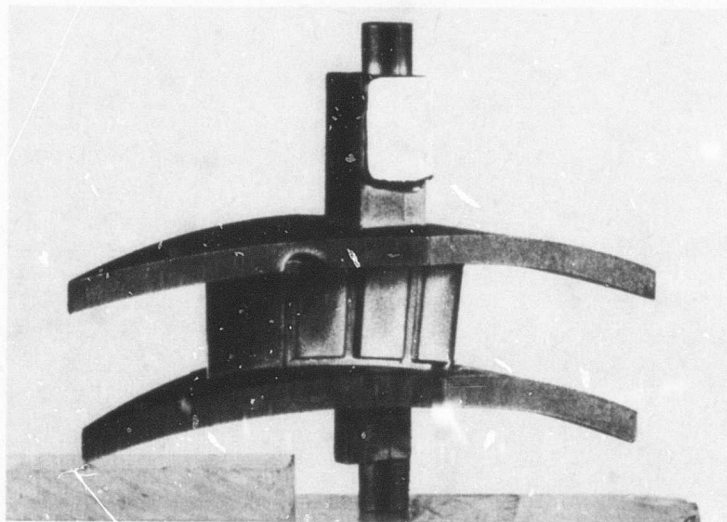
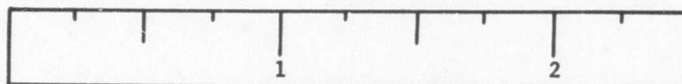
The filler proved entirely satisfactory for the high temperature tests.

The rig was assembled using the actual fits and dimensions shown in Figure 48.

Figure 49 shows the side and rear external views of the complete rig.

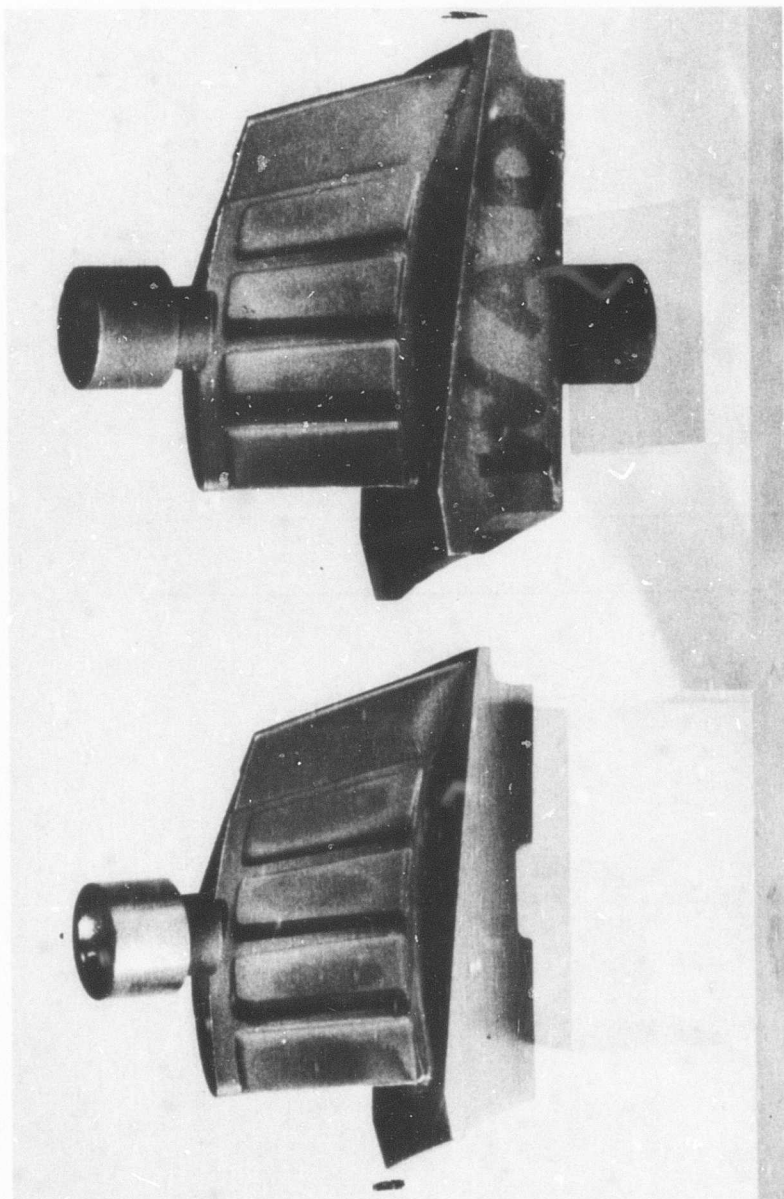


Suction Side



Pressure Side

Figure 5. Stator Vane Casting.



As Cast

Machined

Figure 6. Turbine Rotor Blade Strut.

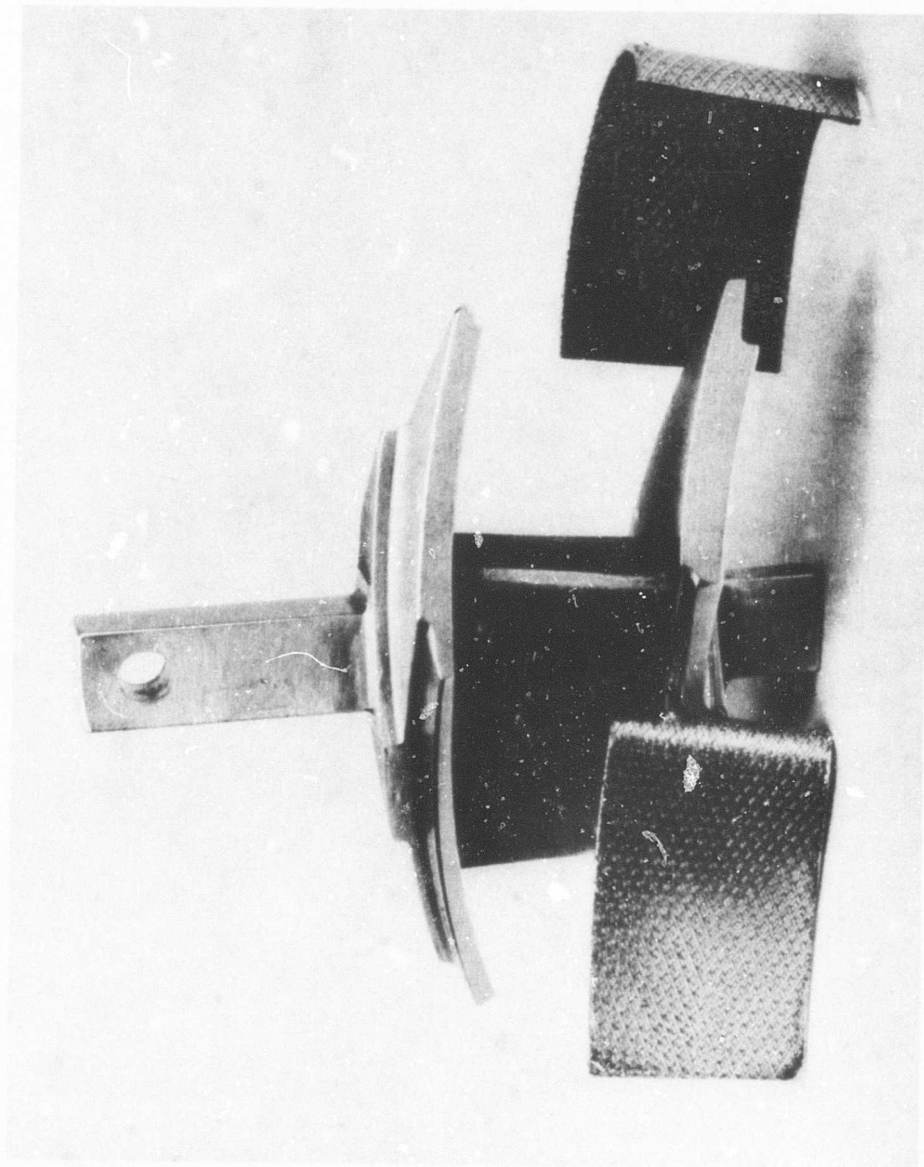


Figure 7. Airfoil Sections and Stator Strut.

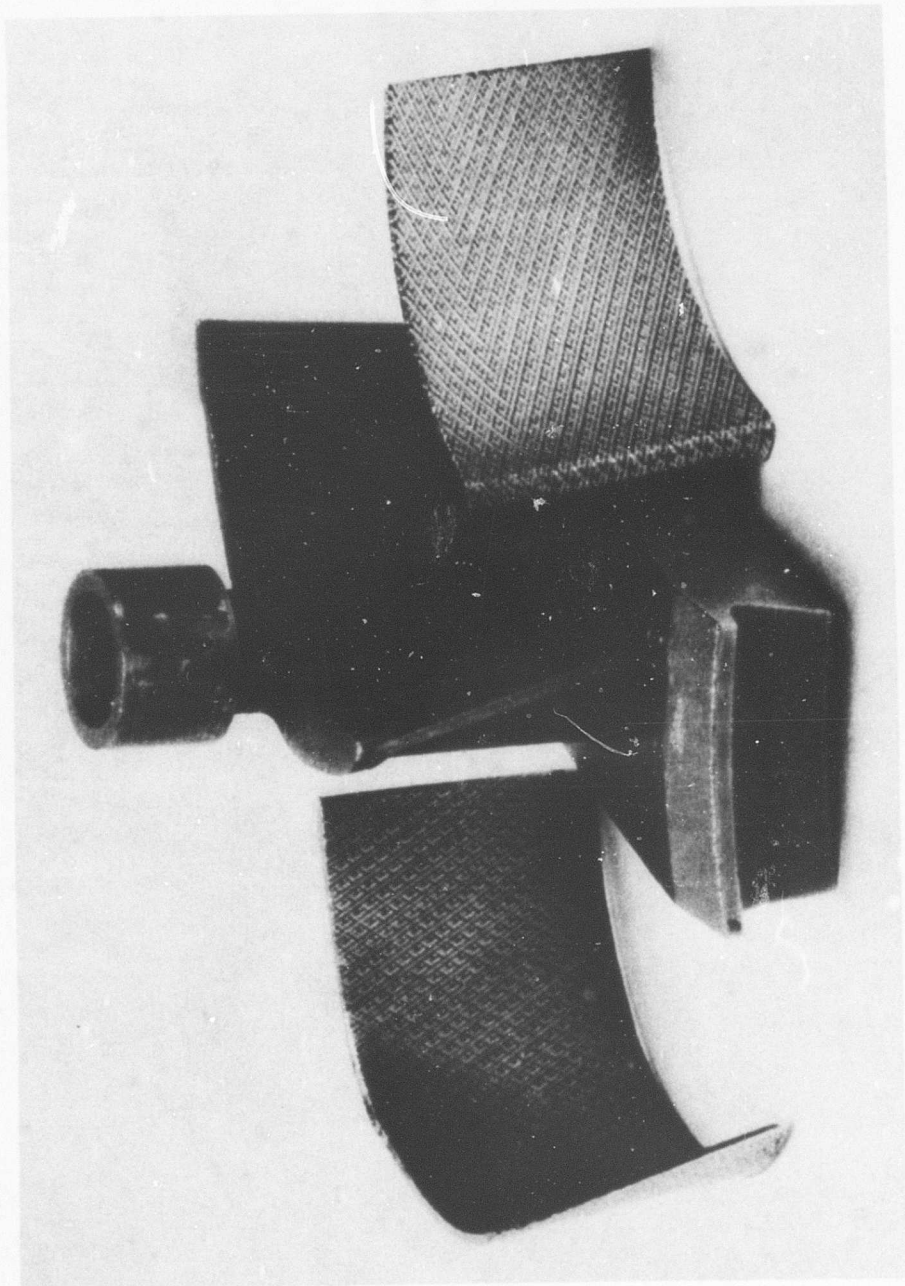


Figure 8. Airfoil Sections and Rotor Struts.

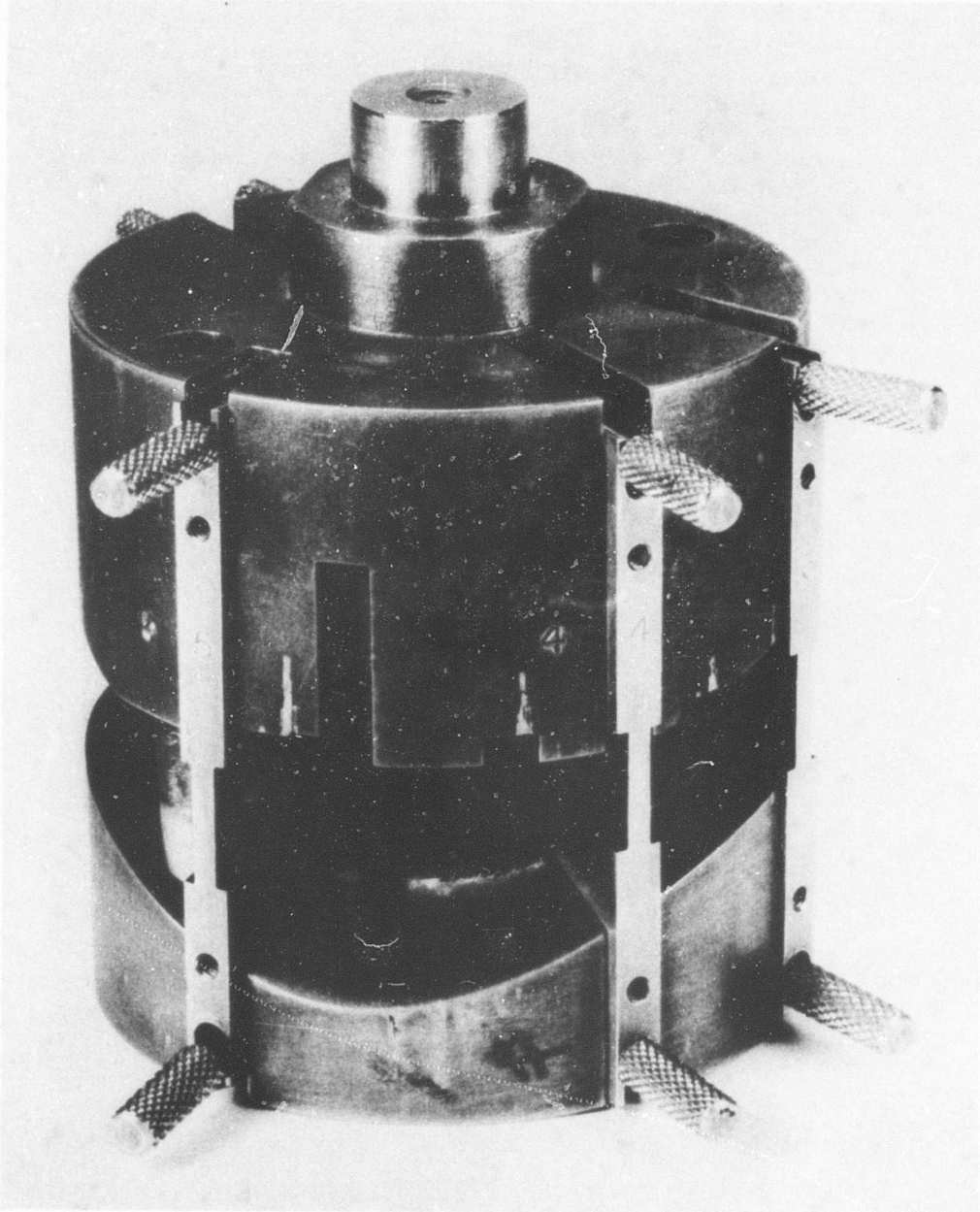


Figure 9. Stator Vane Welding Fixture - Assembled.

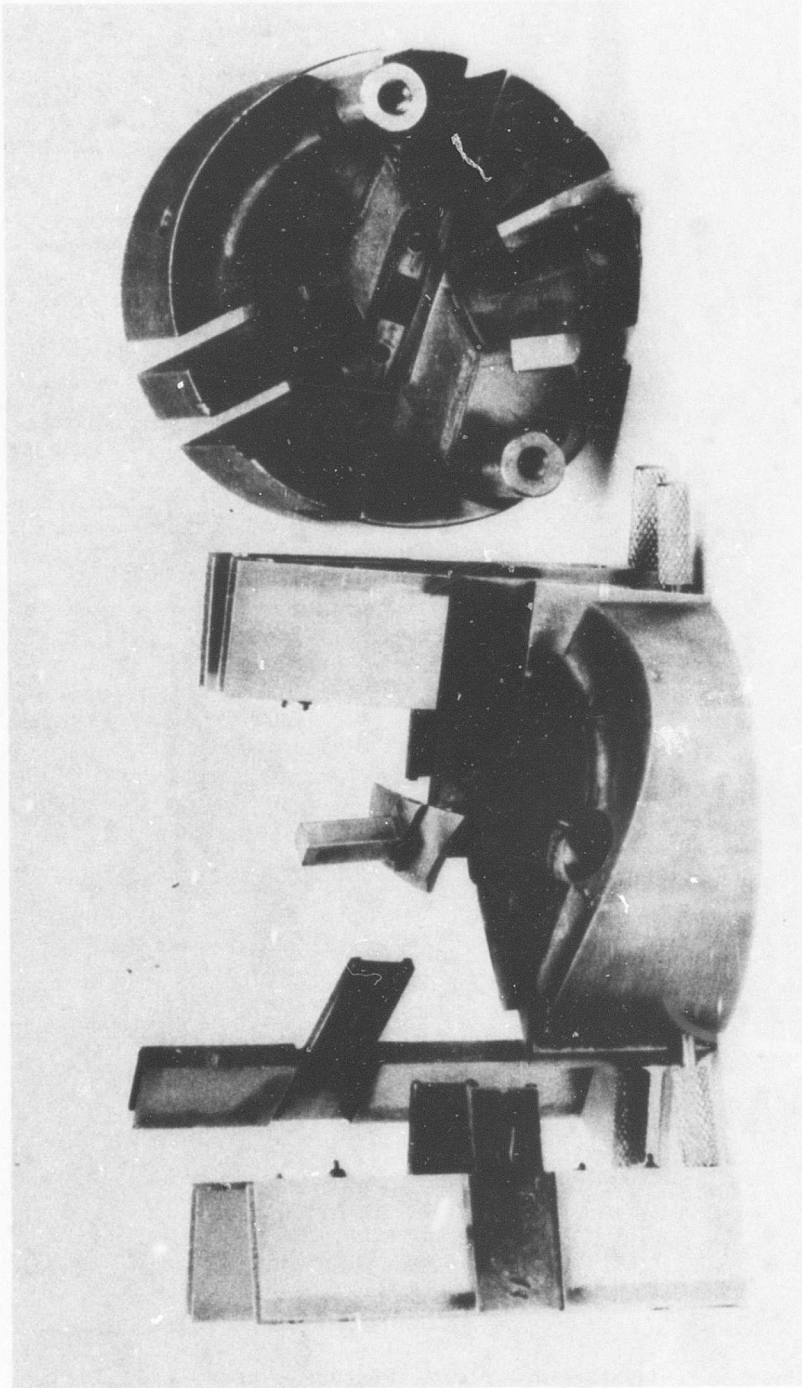


Figure 10. Stator Vane Welding Fixture - Disassembled.

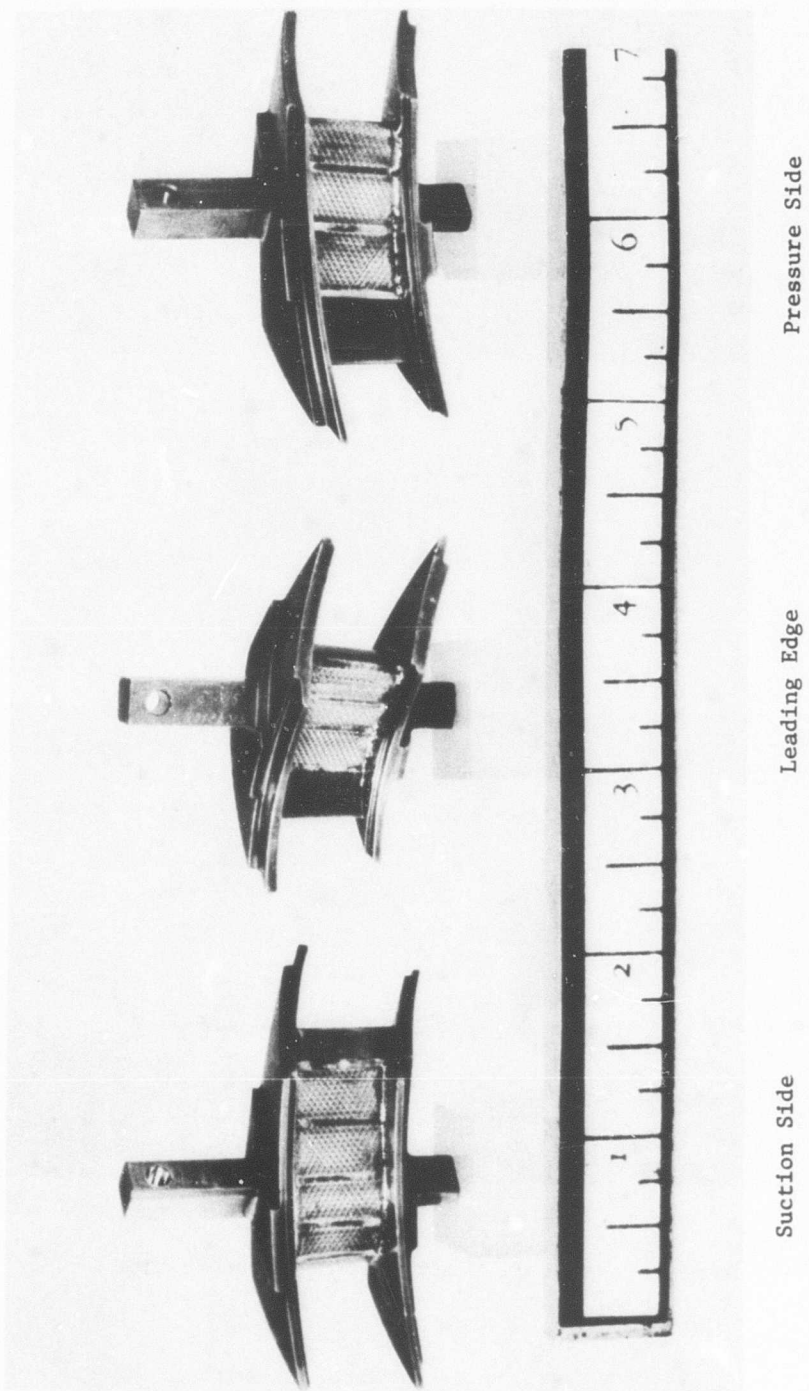
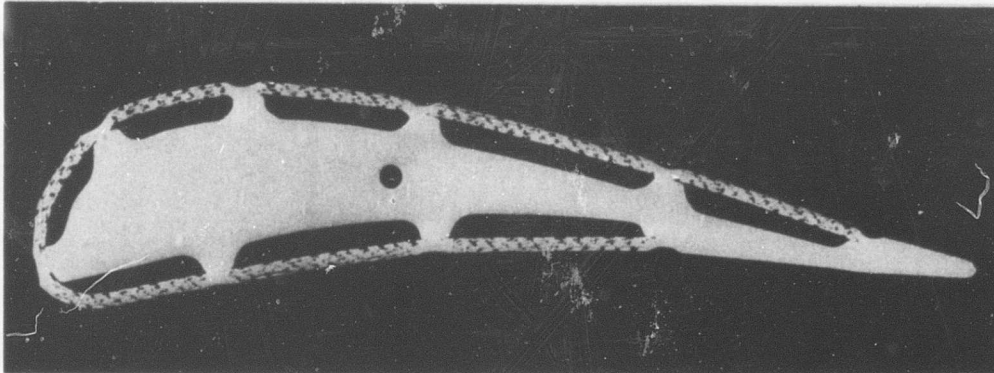
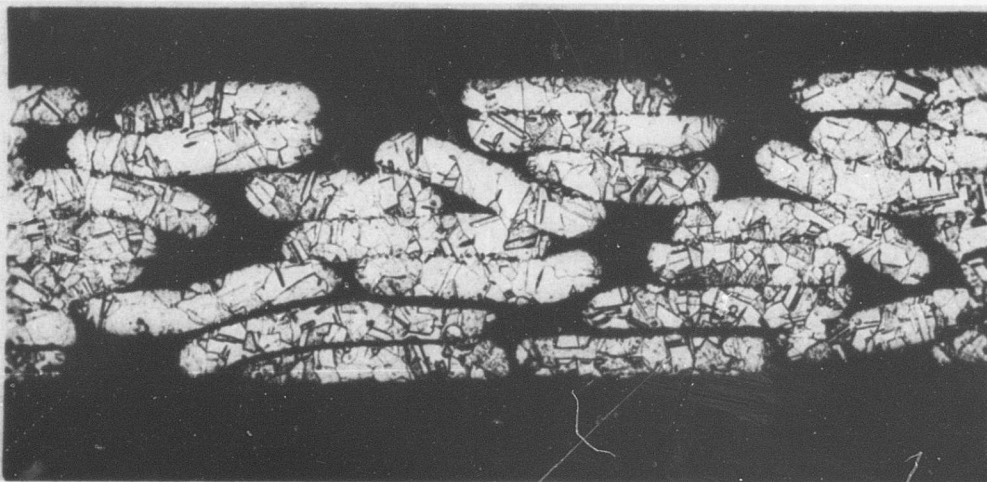


Figure 11. Turbine Stator Vane Assembly.



Mag. 5X

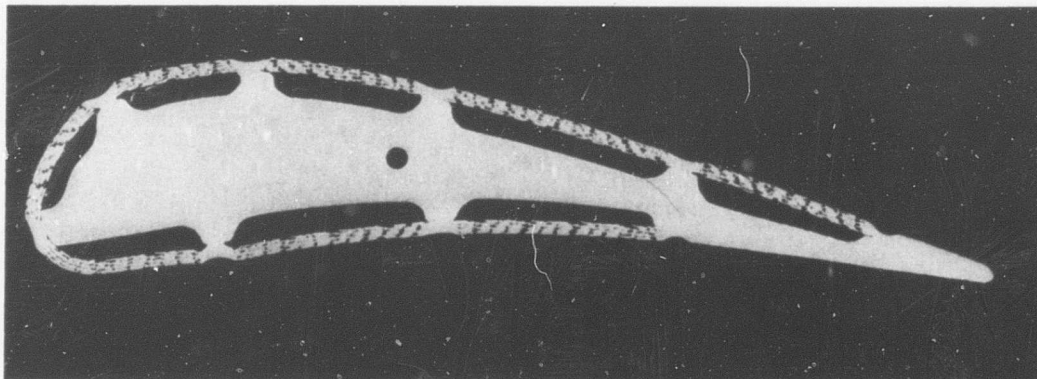
(a) Vane Cross Section - As Polished



Mag. 100X

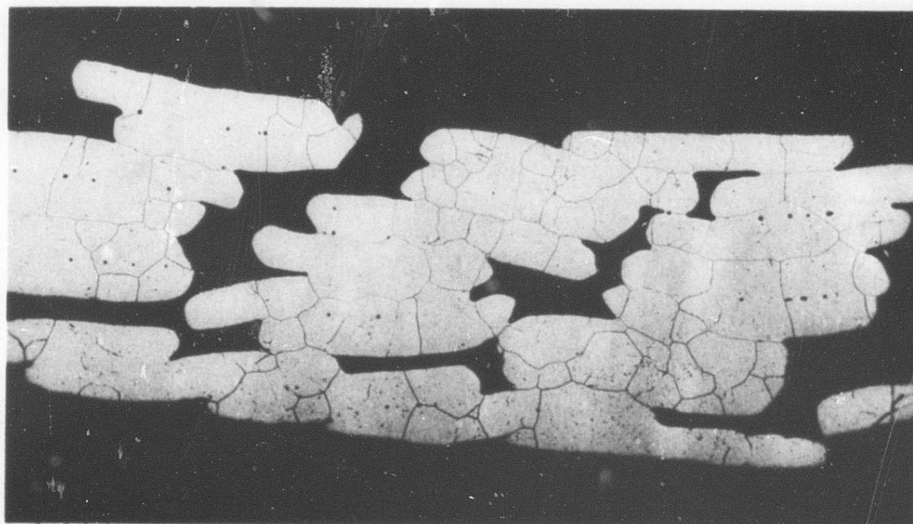
(b) Nichrome V Cb Airfoil Section at LE Pressure Side

Figure 12. Stator Vane Welded Assembly.



Mag. 5X

(a) Vane Cross Section - As Polished



Mag. 100X

(b) N155 Airfoil Section at LE Pressure Side

Figure 13. Stator Vane Welded Assembly.

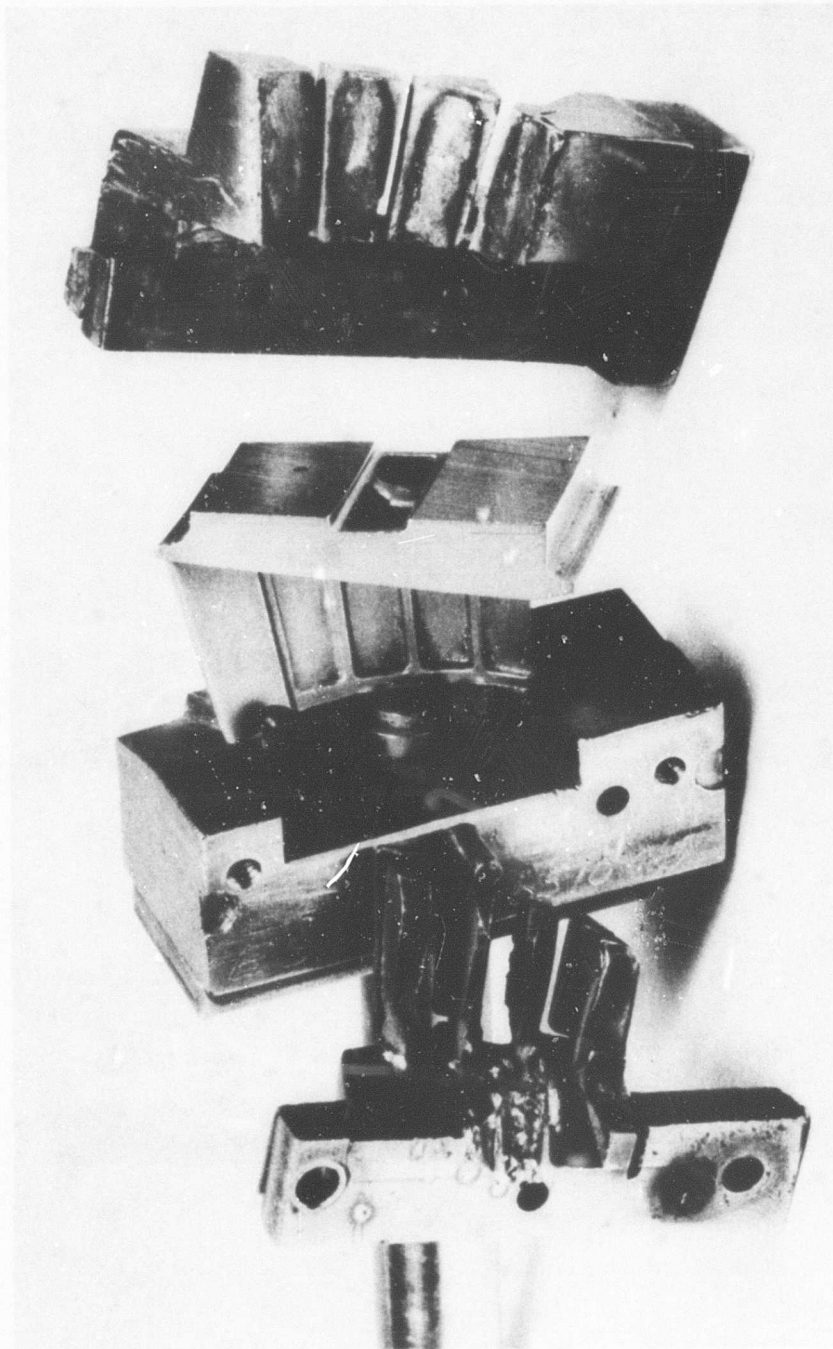
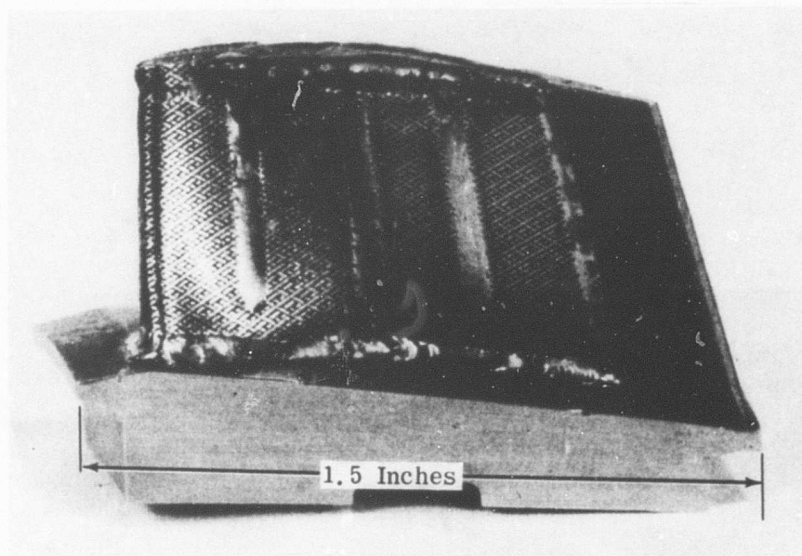
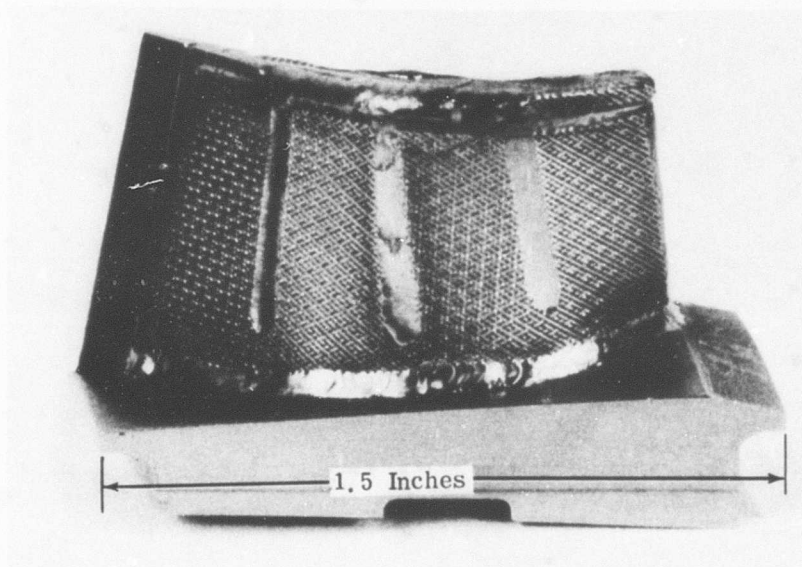


Figure 14. Rotor Blade Welding Fixture - Disassembled.

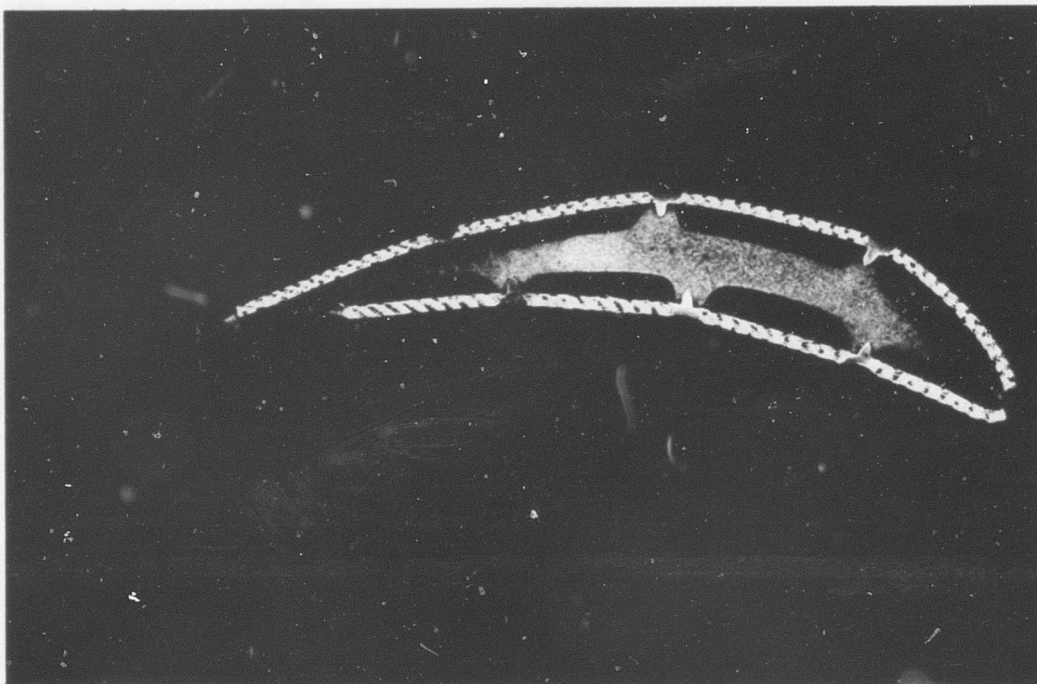


Suction Side



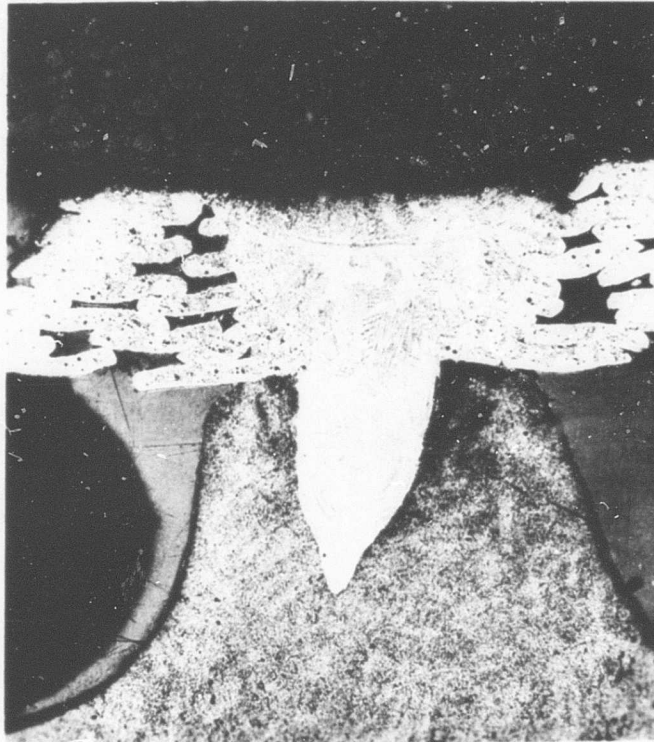
Pressure Side

Figure 15. Turbine Rotor Blade Welded Assembly.



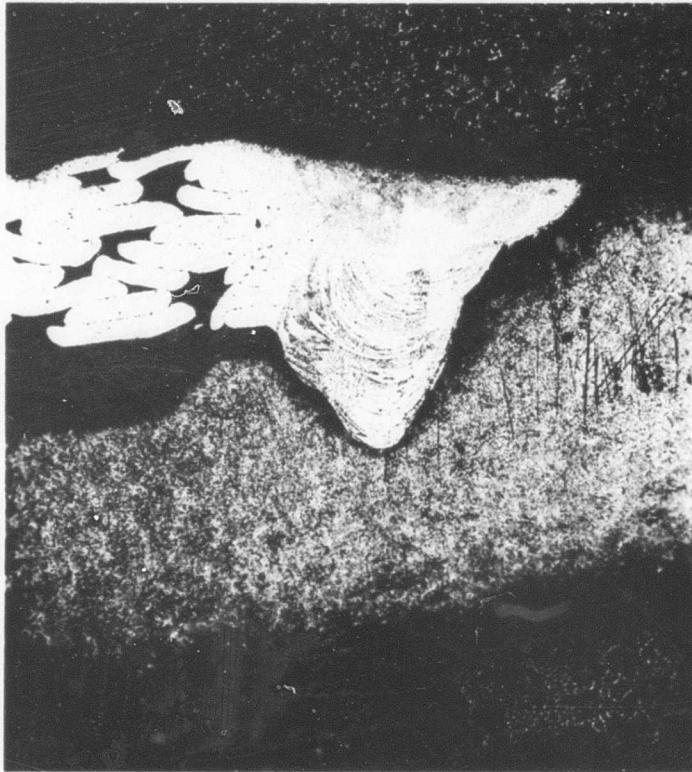
Approx 3x

Figure 16. Airfoil Cross Section Etched to Show Land Welds.



Approx 75x

Figure 17. EB Weld on Middle Land Concave Side.



Approx 75x

Figure 18. EB Weld at Trailing-Edge Land Convex Side.

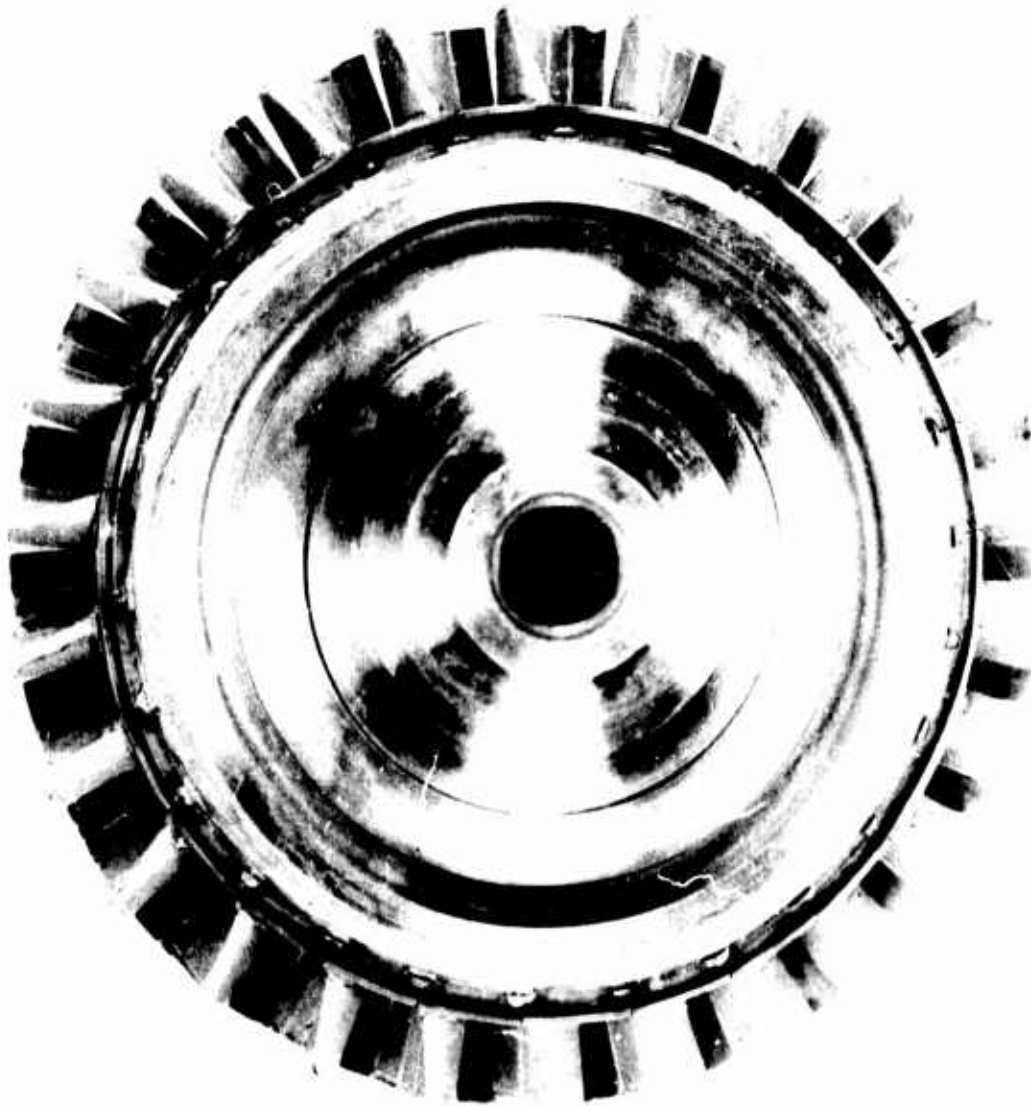


Figure 19. Weld Bead Machined Flush Prior To Aging - Leading-Edge Side.

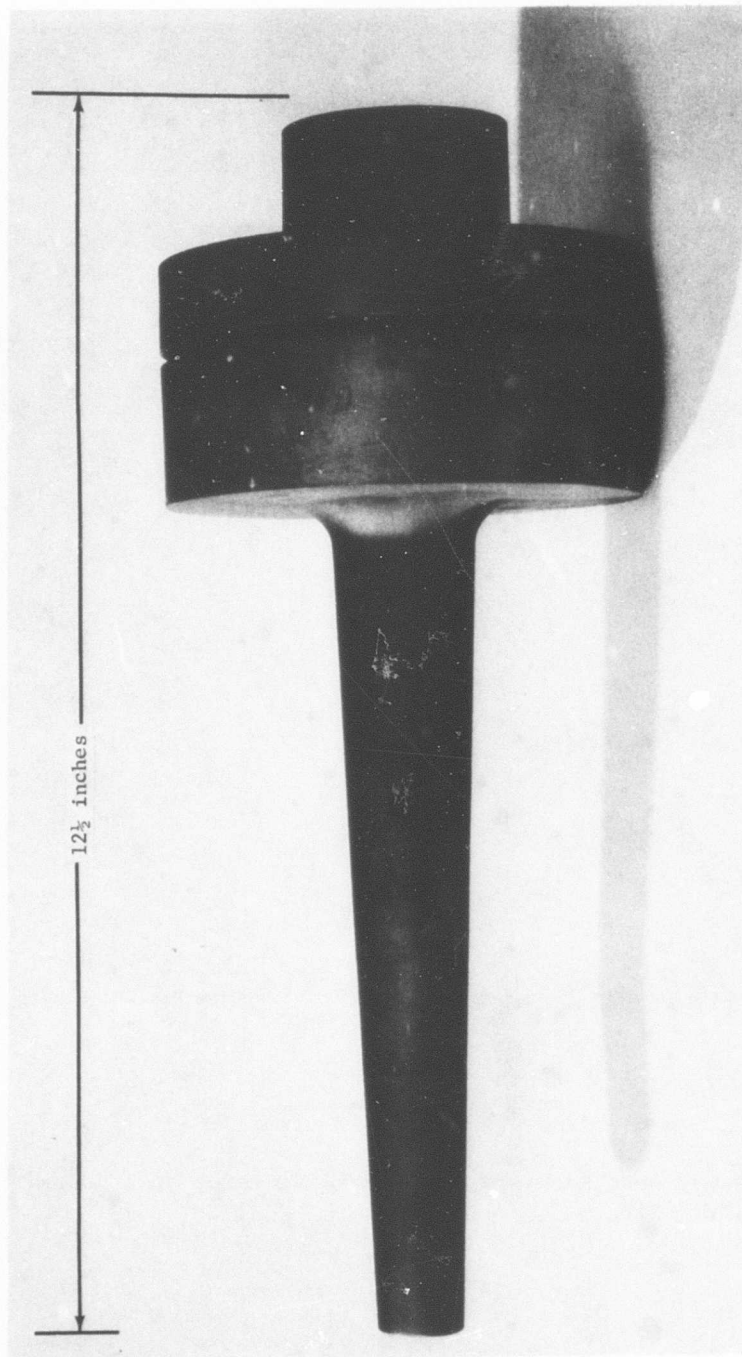


Figure 20. Turbine Rotor Disc and Shaft Casting.

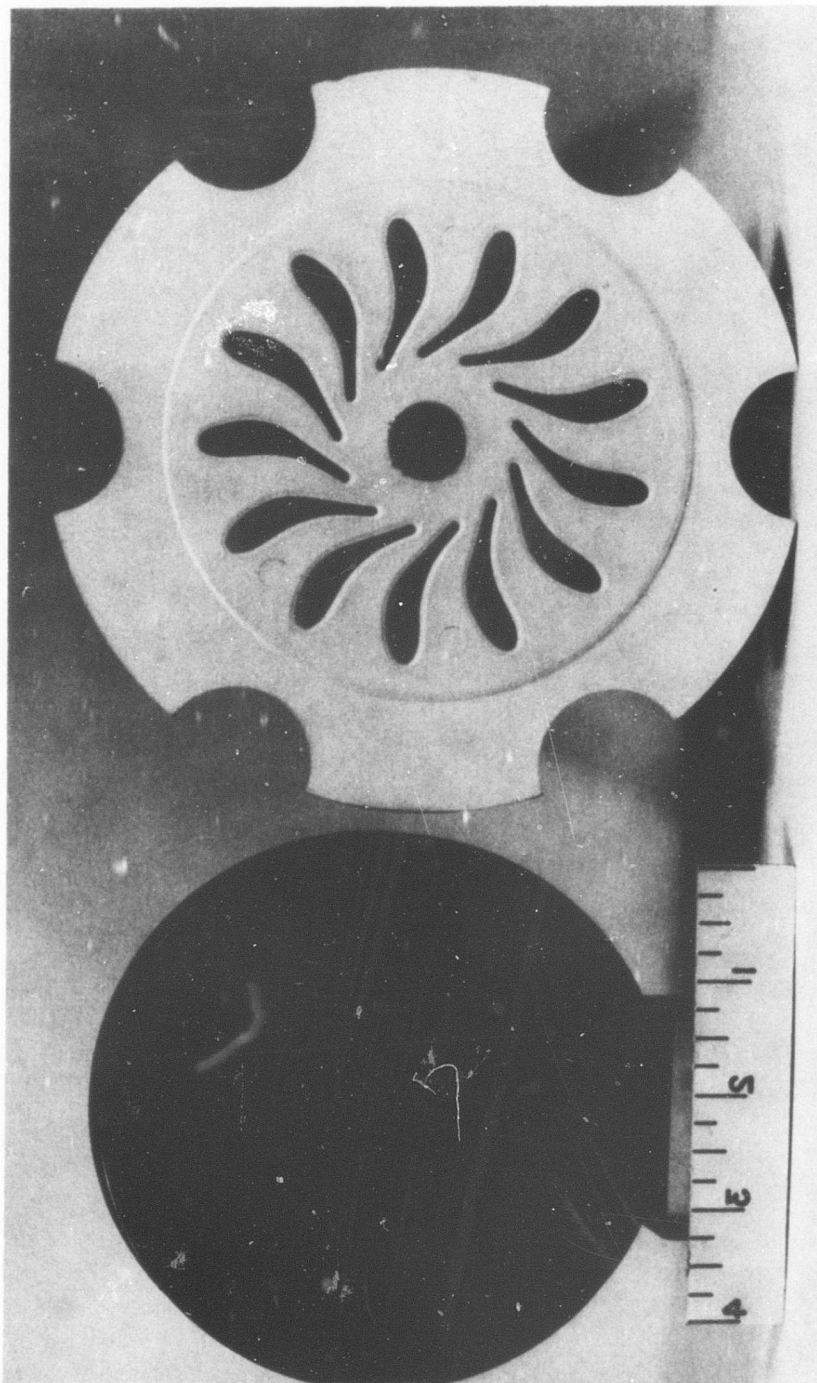


Figure 21. Rotor Disc Cooling Air Impeller Vanes and Ceramic Core.

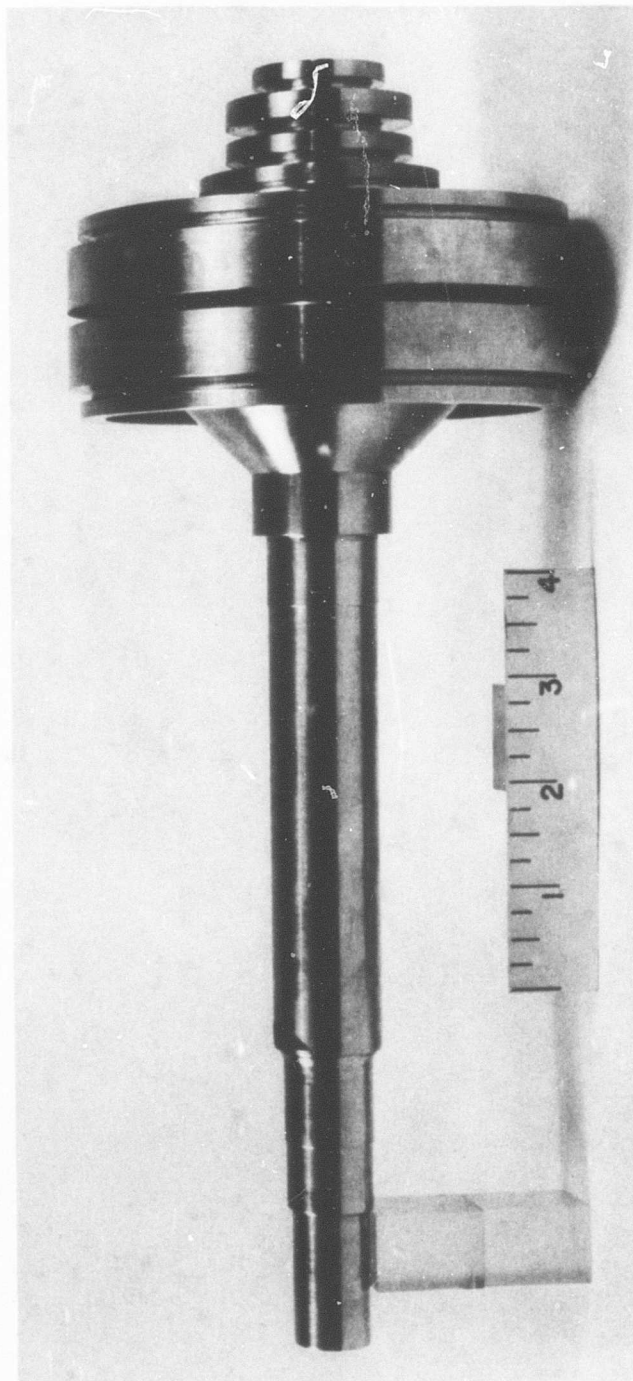


Figure 22. Turbine Rotor Disc Shaft Rough Machining.

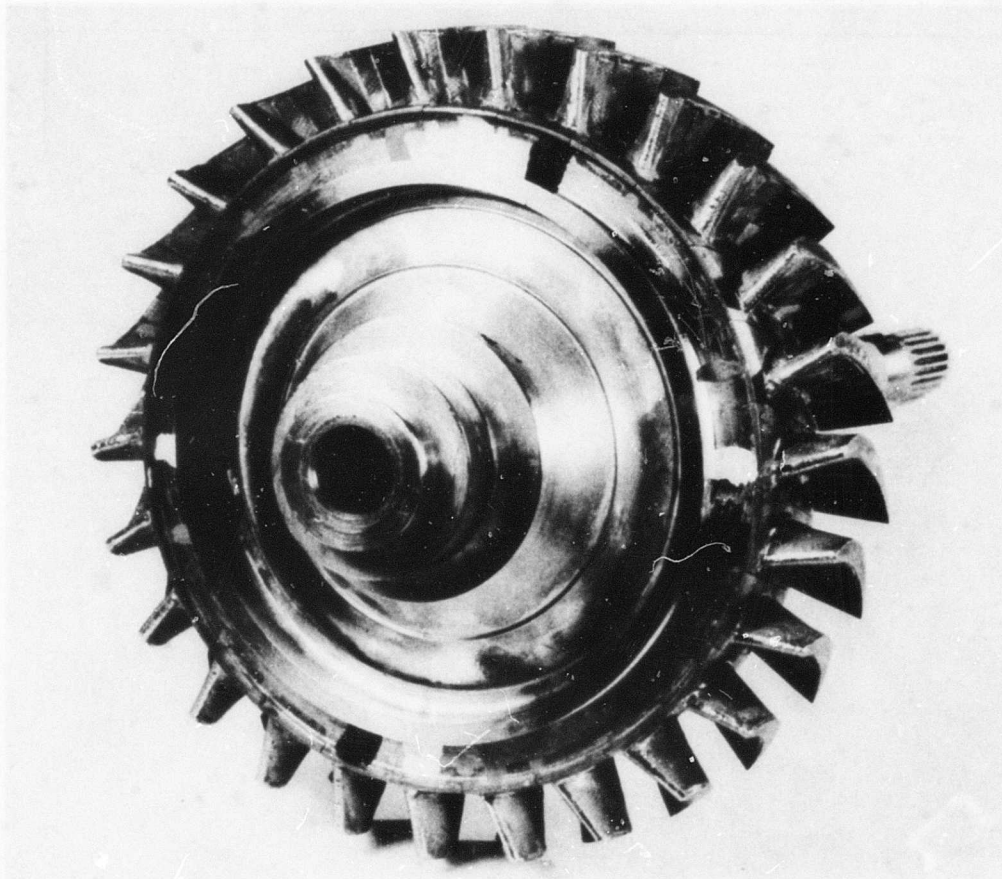


Figure 23. Turbine Rotor Assembly.

(This Figure Shows the Leading-Edge Pressure Side Panels After Replacement on the Completed Rotor Assembly by Electron Beam Welding.)

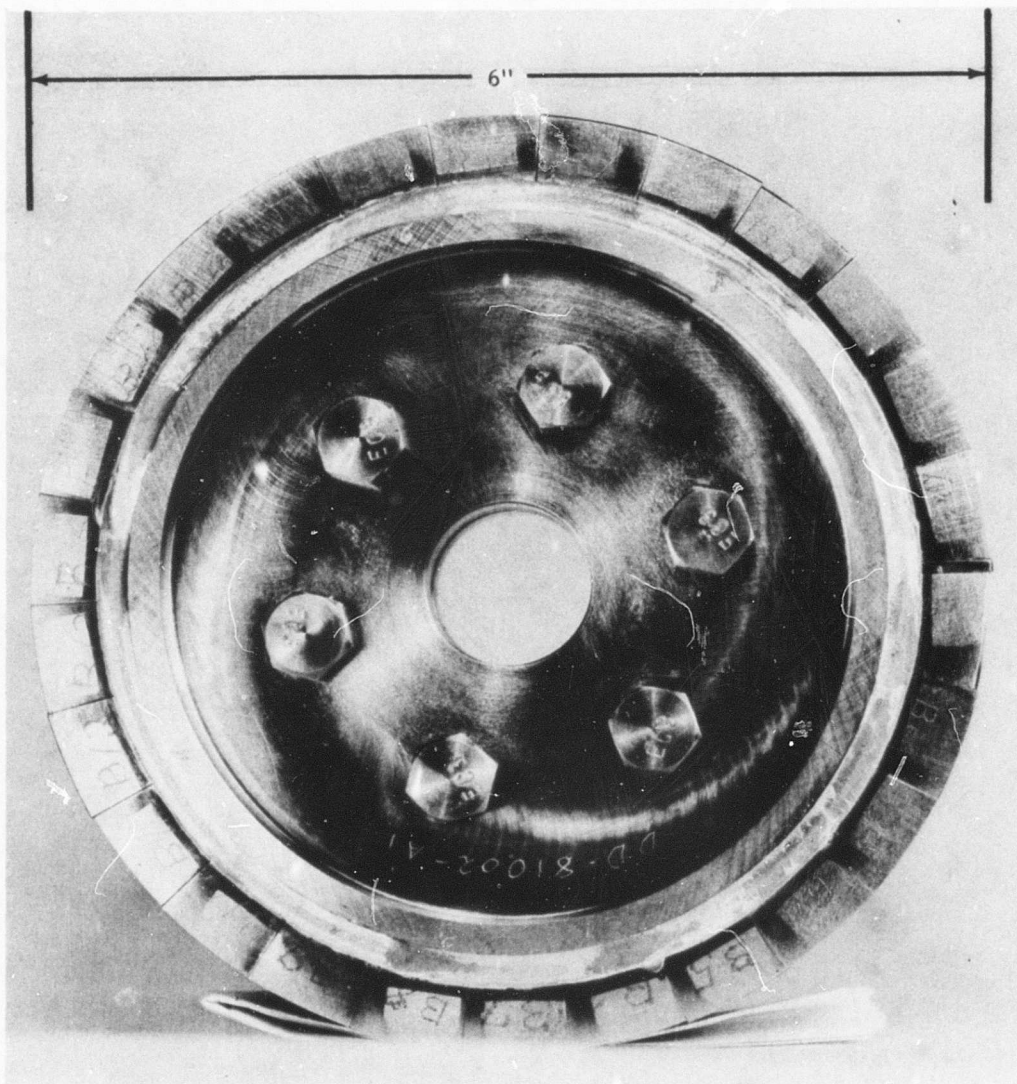


Figure 24. Blade Disc Weld Specimen.

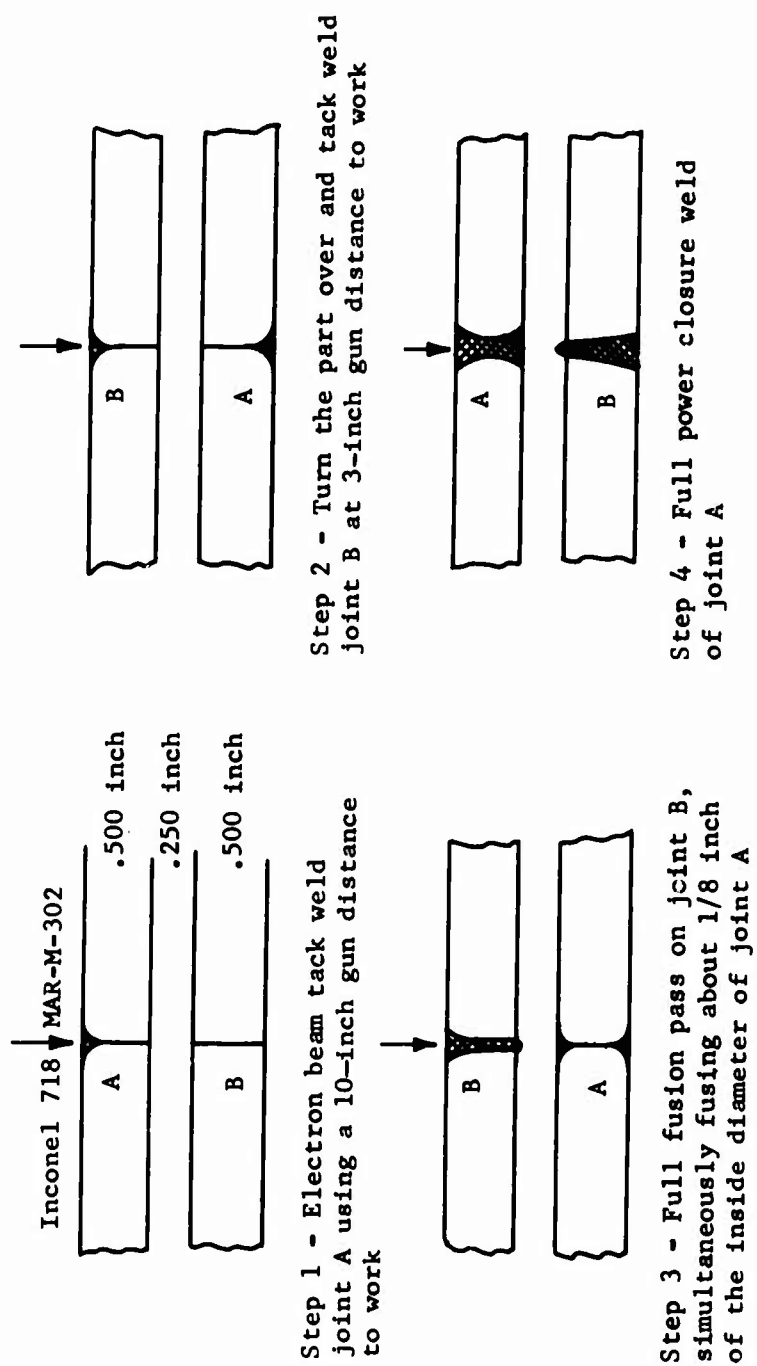


Figure 25. Blade-to-Disc Welding Process Sequence.

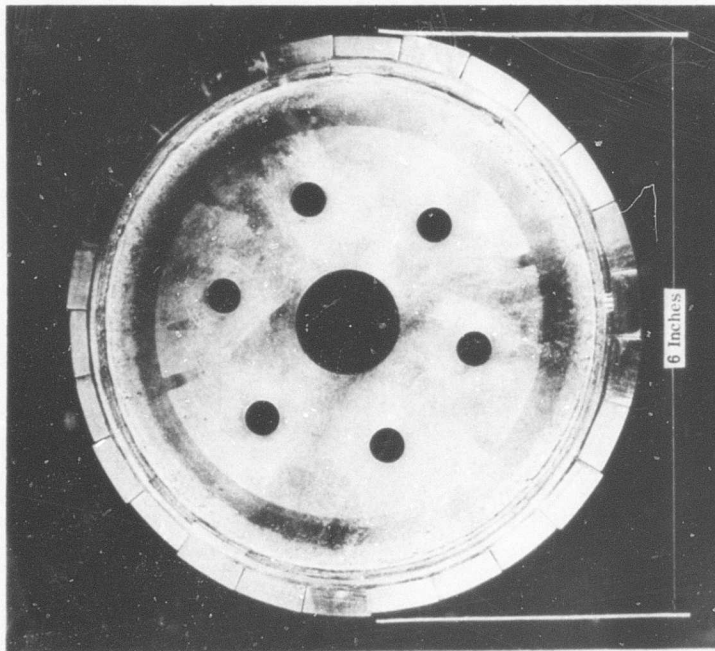
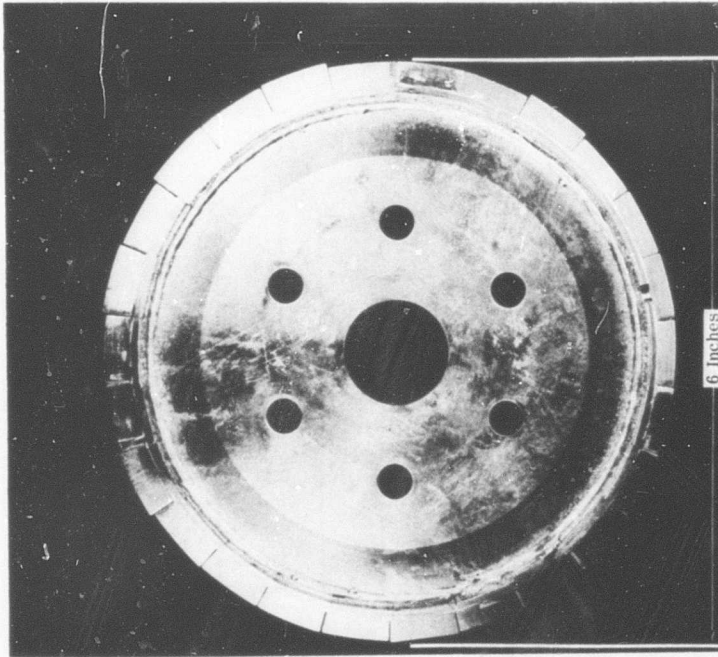


Figure 26. Weld Root From Blade-to-Disc Weld Specimen Showing Full Penetration.

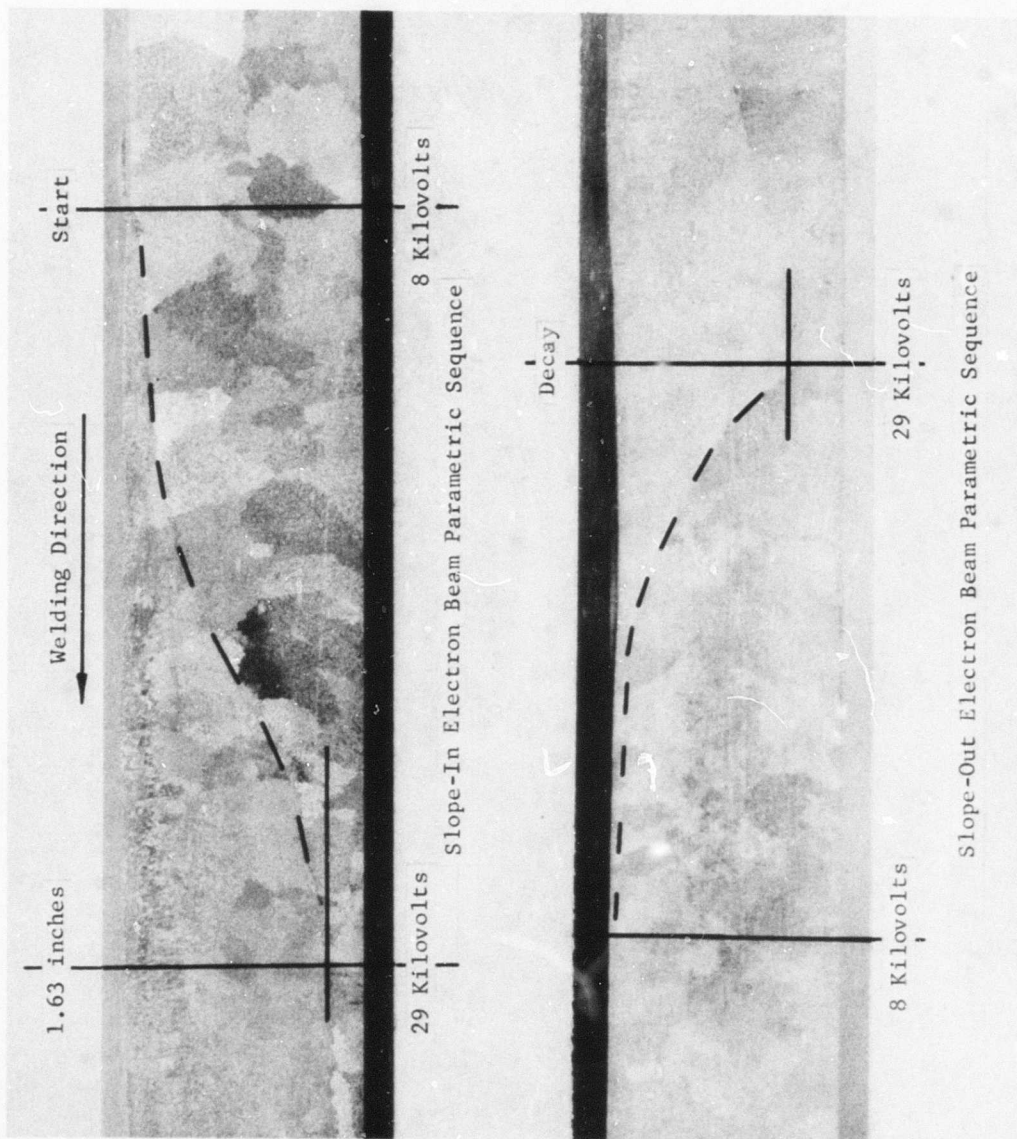


Figure 27. Slope-In and Slope-Out Sequence.

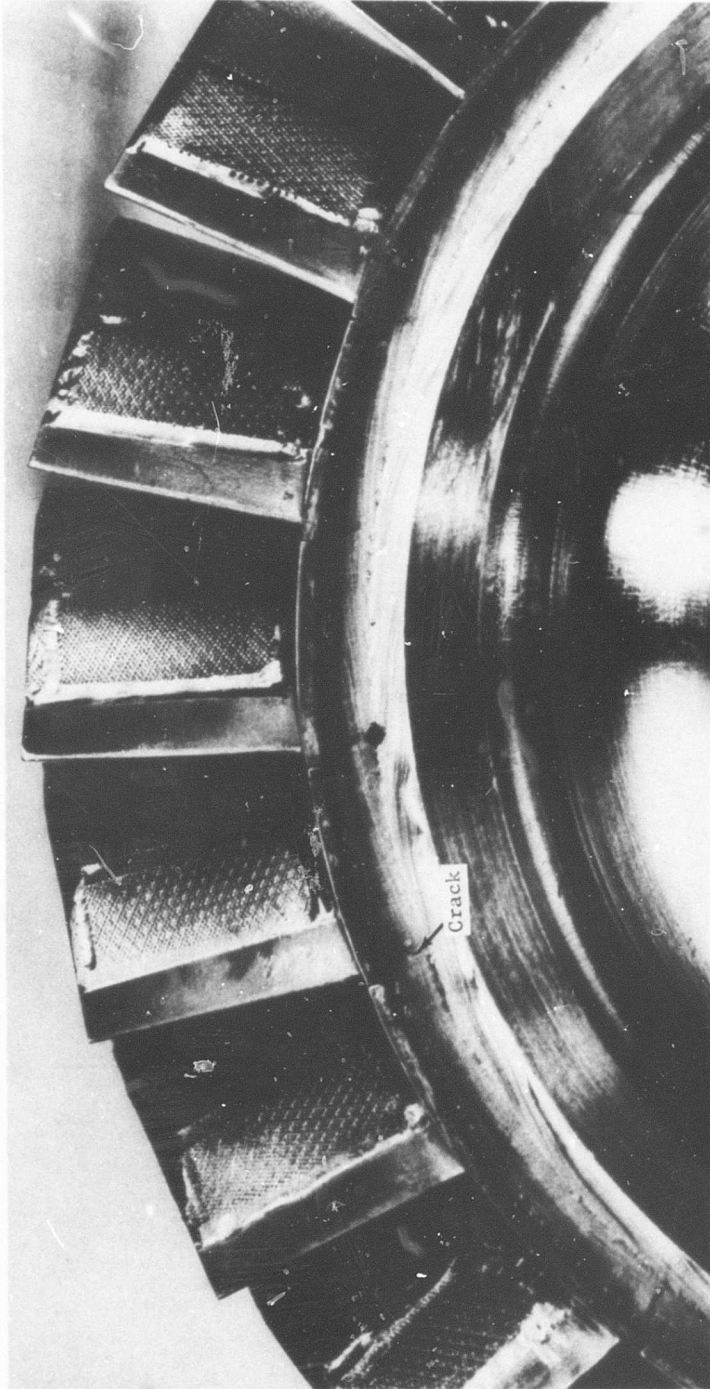


Figure 28. View of Blade-to-Disc Weldment Showing Blade Interface Extensions.

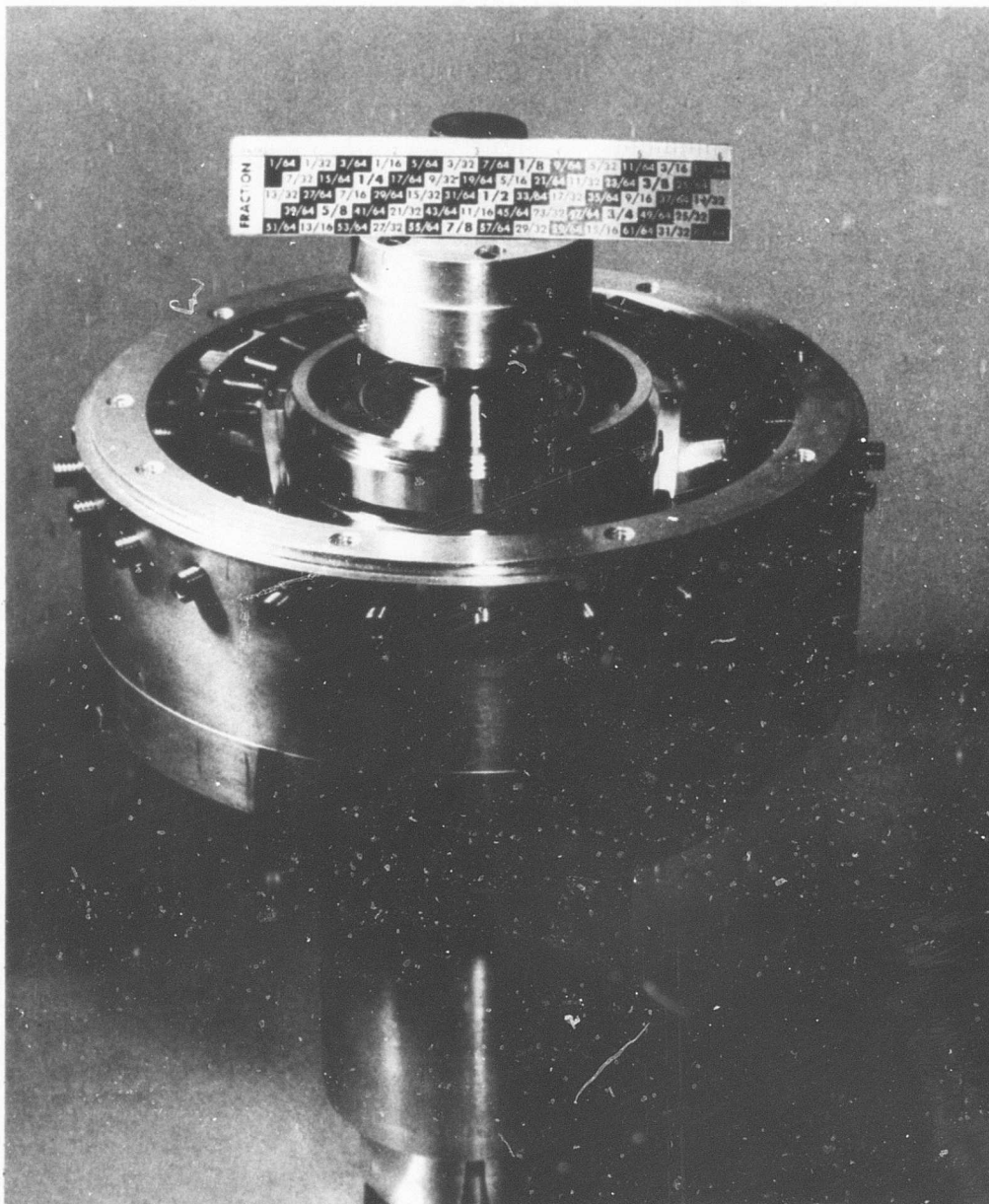


Figure 29(a). Turbine Rotor Blade-To-Disc Weld Fixture - Original.

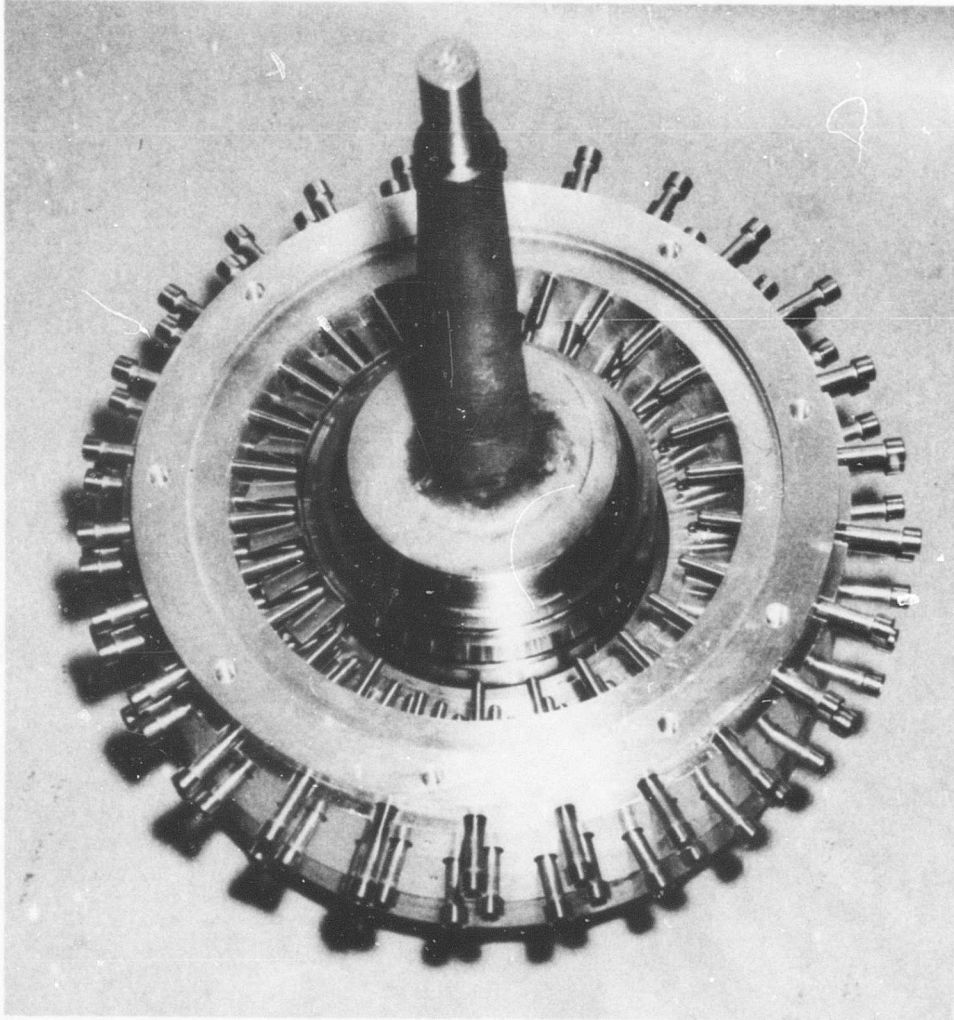
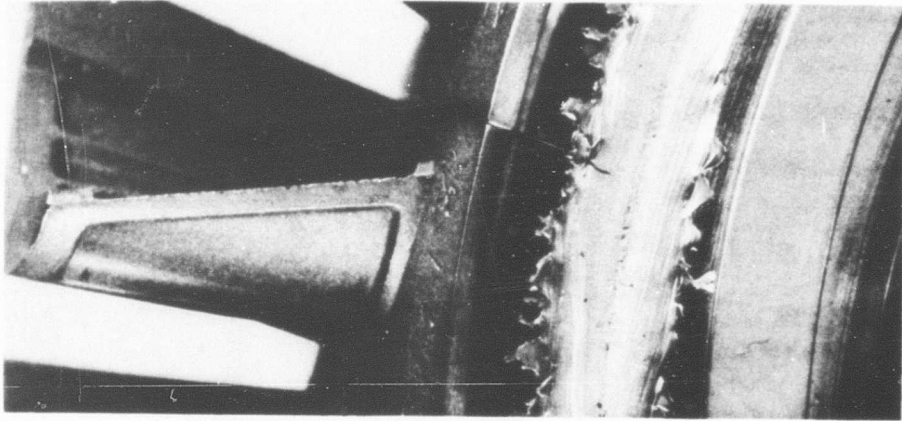
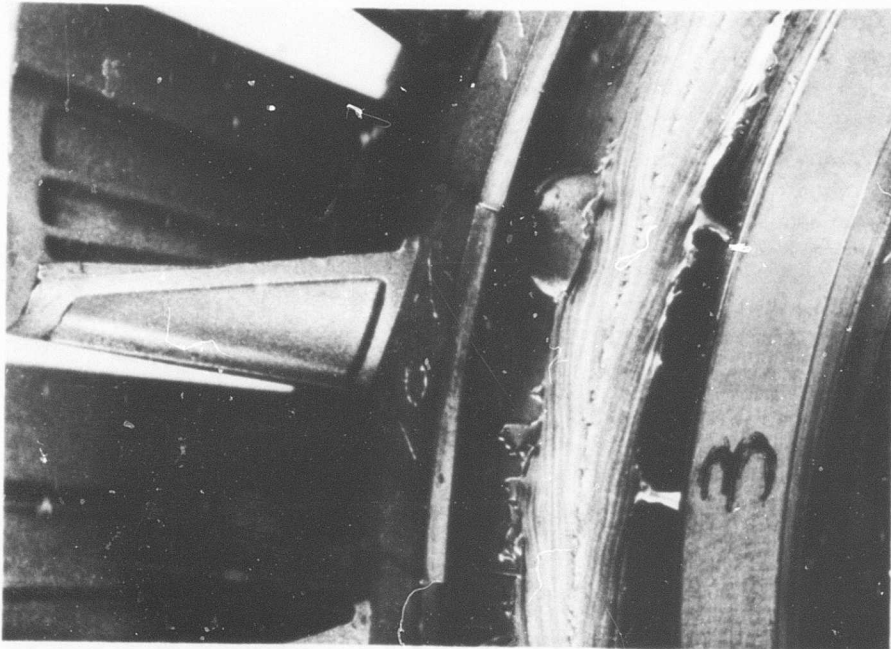


Figure 29(b). Turbine Rotor Blade-To-Disc Weld Fixture - Revised.



View A



View B

Figure 30. Blade-to-Disc Weld Attachment Trials.

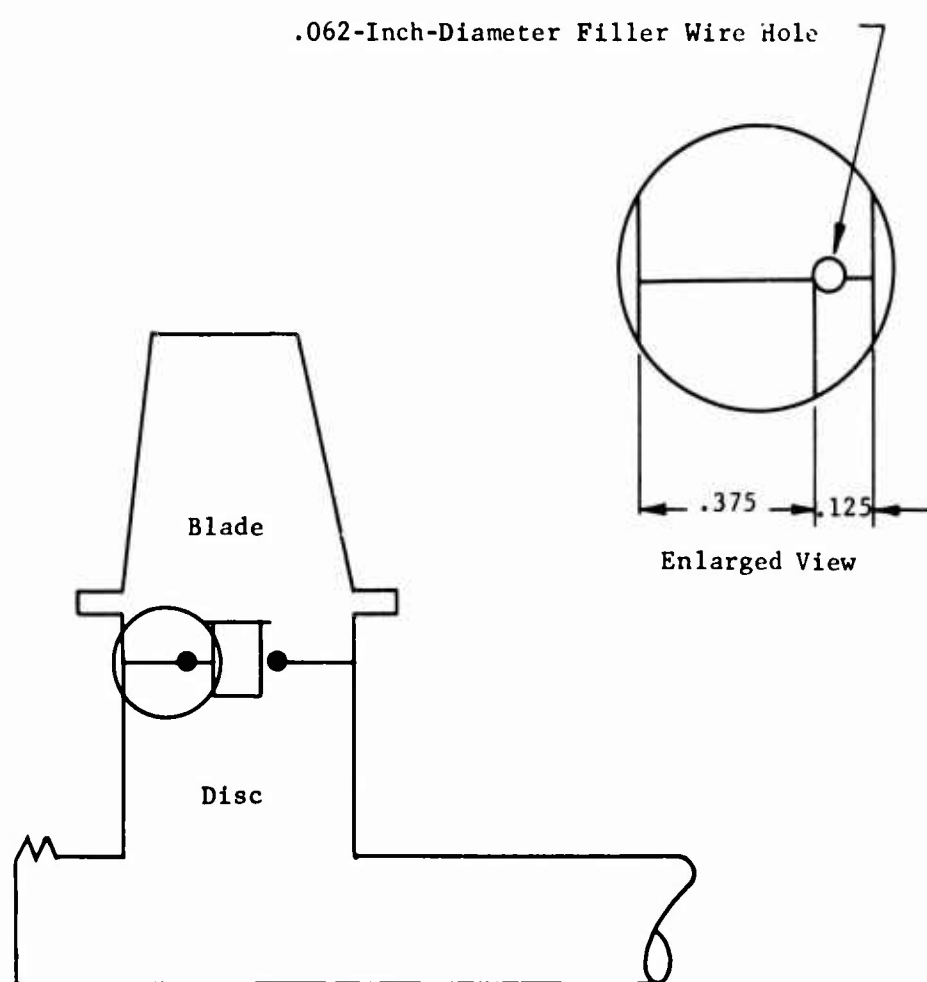
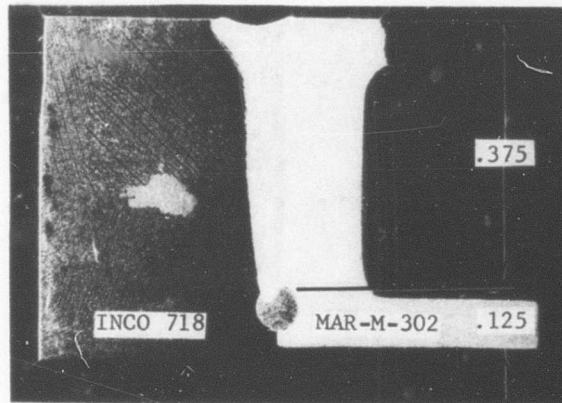
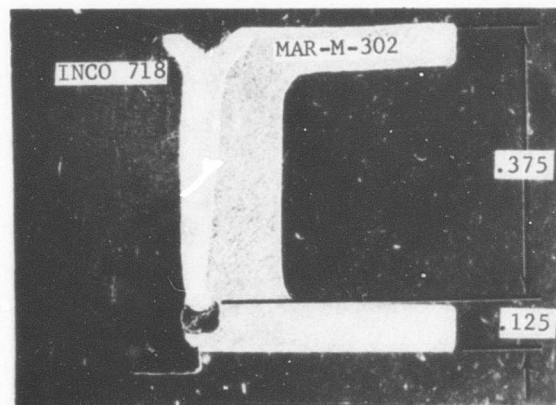


Figure 31. Turbine Rotor EB Weld Joint Revised Design for Controlled Penetration.

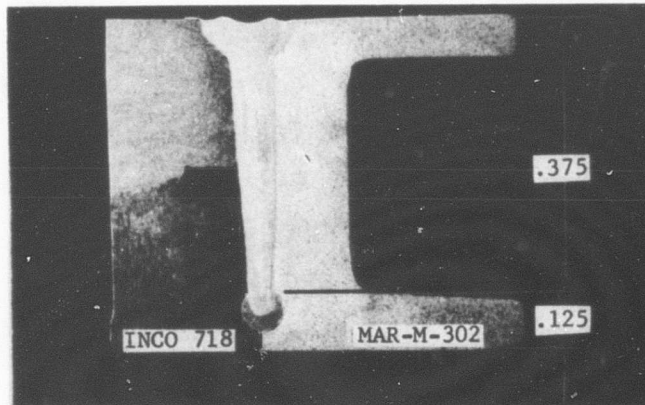


(a) 3-Inch EB Gun Height - .062-Inch Open Groove Beam Focus on Surface

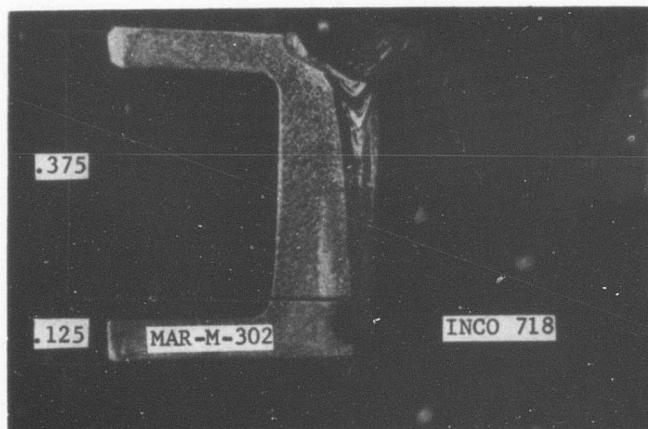


(b) 3-Inch EB Gun Height - Inconel 718 Wire Filled Groove Beam Focused on Surface - .023-Inch Weld Penetration Into Filler Wire

Figure 32. Turbine Blade-to-Disc Weld Penetration Trials.

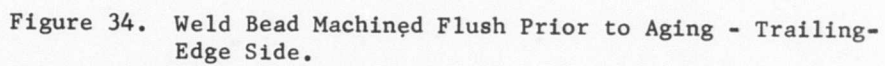


(a) 3-Inch EB Gun Height - Inconel 718 Wire Filled Groove Beam Focused on Surface - .036-Inch Weld Penetration Into Filler Wire



(b) 10-Inch EB Gun Height - Inconel 718 Wire Filled Groove Beam Focused .125-Inch Above Surface

Figure 33. Turbine Blade-To-Disc Weld Penetration Trials.



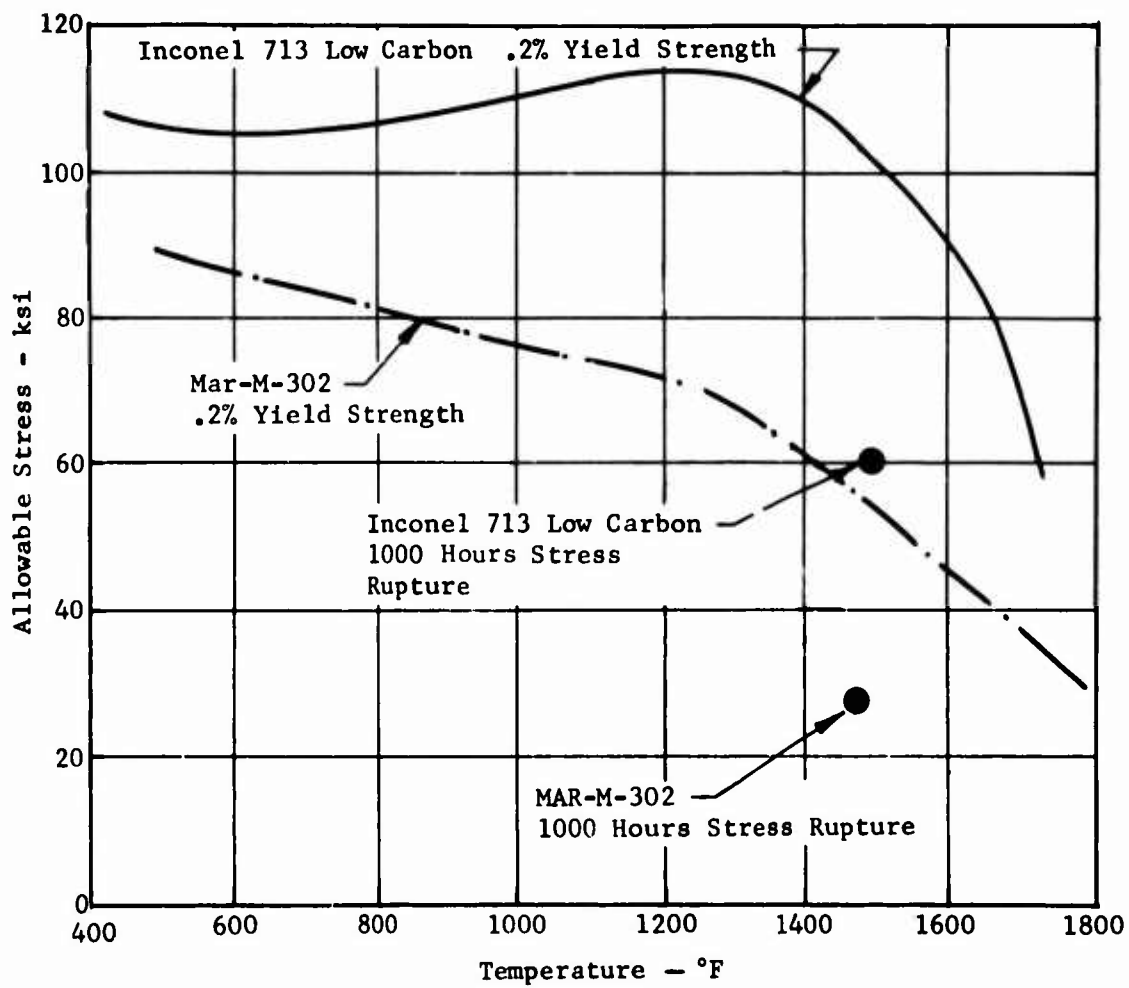


Figure 35. Turbine Blade Material Comparison.

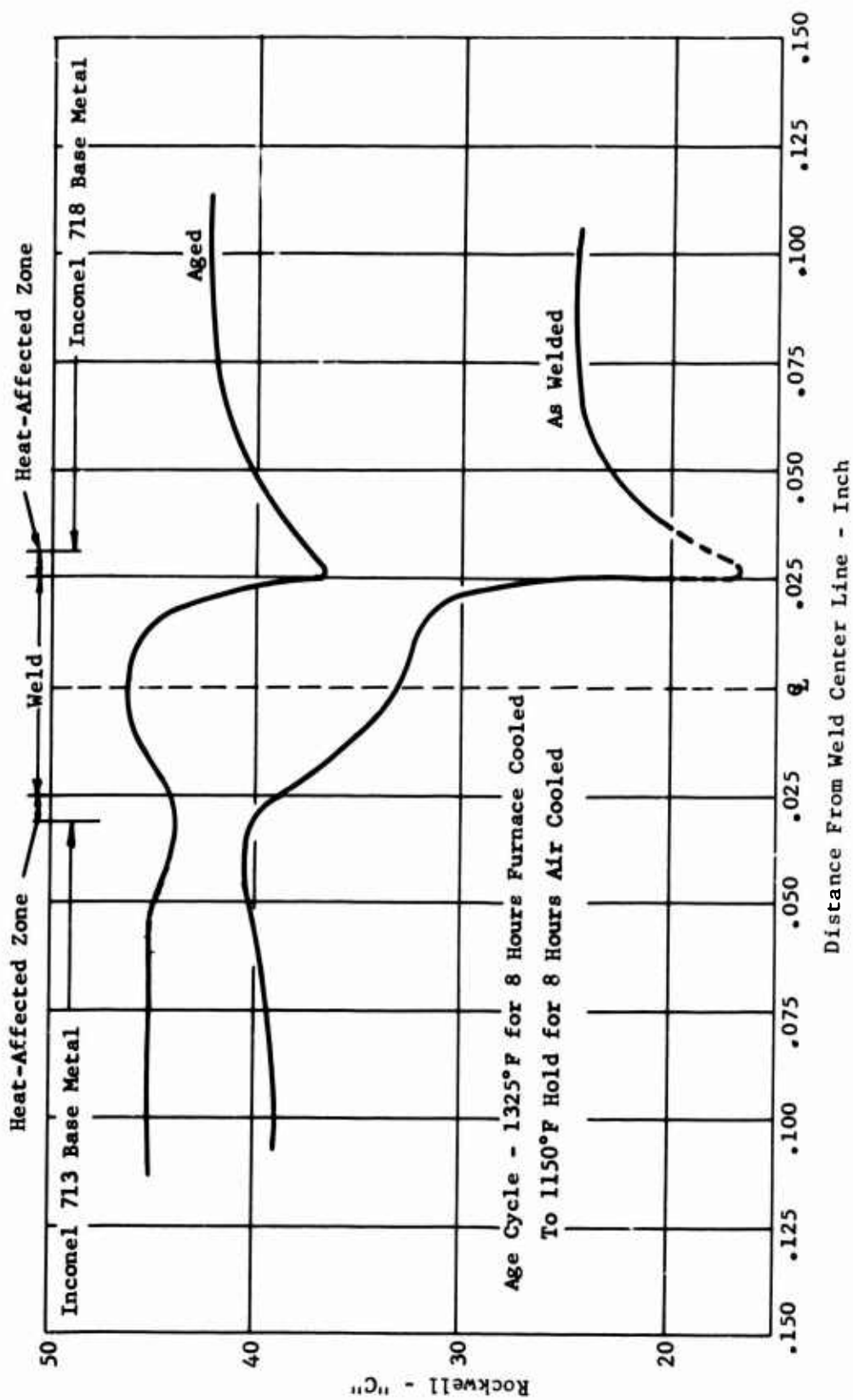


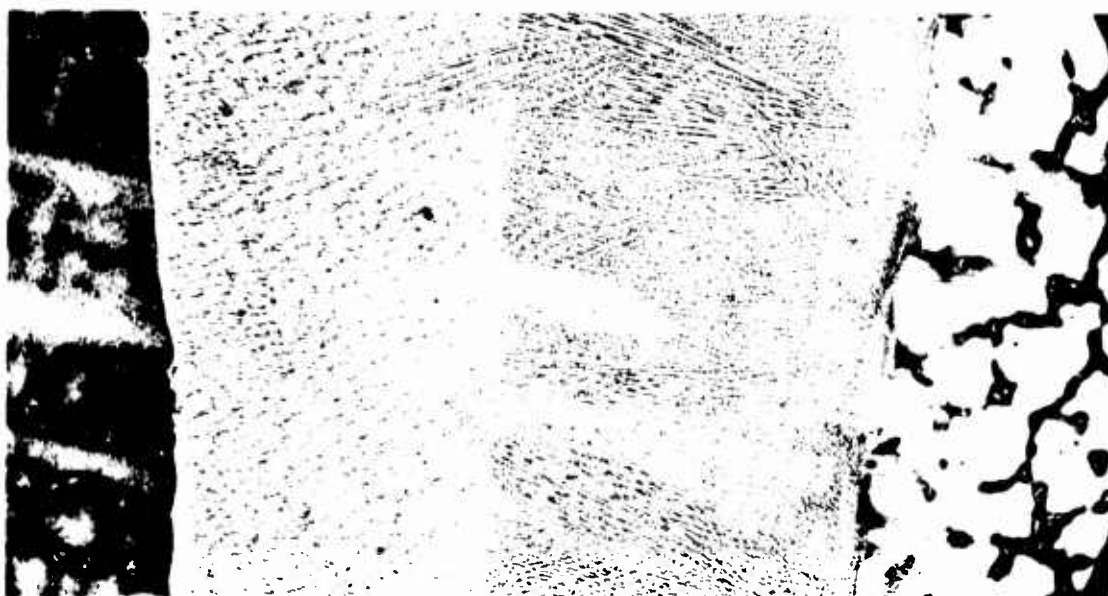
Figure 36. Hardness Survey of Cast Inconel 718 Disc EB Welded to Inconel 713.



Inconel 718

As Welded

Inconel 713 LC



Inconel 718

Aged

Inconel 713 LC

Figure 37. Photomicrograph of Inconel and 713 LC Weld -
100x Magnification. Turbine Blade-to-Disc
Weld Attachment Trail - Alternate Material.

4.0 TEST PROGRAM

A series of test programs were carried out under the contract to demonstrate the mechanical and feasibility characteristics of the rig components to determine their performance and to verify the engineering analyses used in their design. Combustor atmospheric discharge testing up to an average temperature of 2500°F was carried out to establish temperature profiles and performance acceptable for turbine testing. Hot turbine vane cascade testing up to 2650°F was carried out to establish blade cooling characteristics and aerodynamic performance. Tests of the complete turbine component were carried out to establish the aerodynamic performance and establish the mechanical characteristics under hot operating conditions. The following sections present detail descriptions of the tests and the results.

4.1 COMBUSTOR TESTING

Combustor testing was directed toward accomplishing a two-fold goal: high performance and good durability. Both of these goals were met to an acceptable level prior to initiating the combined test of combustor and stator cascade. The accomplishments shown in Table VIII show the high level of performance and durability obtained.

TABLE VIII COMBUSTOR TEST ACCOMPLISHMENTS			
	Item	Goal	Accomplishment
<u>Performance</u>			
1	Combustor pressure loss at $F/A = .032$, percent (2500°F point)	3	3.67
2	Combustor efficiency, percent	99	99
3	Mean radial to average temperature ratio T_1/T_4 , °R/°R	1.061	1.061
4	Maximum local to average temperature ratio T_{Lmax}/T_4 , °R/°R	1.135	1.170
5	Maximum average temperature, °F	2580	2650
6	Inlet conditions at 1070°R temperature		
	Total pressure, inches Hg A	178.5	178.5
	Combustor weight flow, pound per second	2.89	2.89
<u>Durability</u>			
1	Hours between 2400° - 2650°F	1.0	2.0
2	Hours between 2200° - 2400°F	4.0	4.5
3	Hours between 1600° - 2200°F	5.0	25.08
4	Total time, hours	25.0	137.83

Total time on the combustor includes the time listed in Table VIII plus the times on the stator and rotor tests.

For convenience, an annotated test summary is presented in Table XXIII showing the tests conducted in a chronological order.

A substantial period of the program was devoted to combustor test evaluation in order to meet the requirements for durability as well as the specifications for temperature distribution and profiles. Whereas the combustor liner aerothermal and mechanical design was straightforward, configuration and operation of the fuel vaporizer were immediately recognized as the key elements to achieving these goals. A series of vaporizer configurations including variations on the number of fuel injection points, the location of injection points, and the type of fuel vaporizer dam or baffle were tested.

A simplified description of the various combustor vaporizer configurations tested is presented in Table IX.

TABLE IX COMBUSTOR VAPORIZER CONFIGURATIONS				
Configuration No.	No. of Fuel Injection Points	Location of Fuel Injection Points with Respect to Primary Air	No. and Type of Fuel Dam	Primary Airflow Direction
1	2	Upstream	0	Swirl
2	2	Downstream	0	Swirl
3 Figure 50	2	Inline	0	Swirl
4 Figure 51	2	Downstream	4-Axial	Swirl
5	4	Downstream	0	Swirl
6	2	Downstream	0	Swirl
7	4	Downstream	4-Axial	Swirl
8 Figure 52	4	Downstream	1-Circumferential	Swirl

Configuration 8 was further modified by having all the fuel injection points sized to close tolerance of each other and by making all the fuel feed lines of identical size and shape. The final combustor configuration also included an upstream air straightening screen. The location of the diluent slot was moved forward but then was returned to its originally designed position. The cooling air deflectors had the downstream orifice holes enlarged and were welded in place. They were also segmented and dimpled to prevent collapsing and restriction of the cooling film. Details of the modifications will be discussed in the following section.

4.1.1 Combustor Performance

Combustor Pressure Loss

The combustor cold flow pressure loss (shown in Figure 53) is 2.9 percent as against the 3 percent design target for hot operation. This curve shows the percent pressure loss versus the inlet airflow parameter. Figure 54 shows the pressure loss in terms of the combustor exit static pressure and airflow and is useful in determining stator upstream pressure during cascade and rotor performance tests by measuring static pressures rather than using total pressure probes that could break and cause turbine damage.

The pressure drop due to heat addition is small due to the extremely low reference velocity of this combustor. Figure 55 shows an extrapolated value of 3.67 percent versus 3 percent for design.

Combustor Efficiency

Combustor efficiency versus fuel-air (F/A) ratio is shown on Figure 56. The lean limit of stable burning was recorded as low as .002 F/A. The scatter of points on the curve from the exit temperature thermocouples used in the efficiency calculation is to be expected where limited durability at the higher F/A ratios was exhibited by the instrumentation. Nevertheless, the majority of data indicates high combustion efficiency, and a value of 99 percent was approximated as a realistic average value.

Figure 57 shows the ignition characteristic of the combustor. Note that ignition is fairly insensitive to pressure and the weight flow parameter.

Radial Exit Temperature Profile

The combustor exit temperature profile was obtained by using three thermocouples spaced at points of equal area along the radius and free to circumferentially traverse the full exit annulus. The full 360-degree traverse required 2 minutes to allow sufficient time for thermocouple response. The temperature readings for each radial location were recorded on a strip chart showing temperature versus angular position. An average temperature for each trace was obtained by using a planimeter to obtain the area and by dividing by the appropriate scale factor. This average value in °R is the T_L referred to in the temperature ratio expressions. The average of all three is the T_0 value. The $T_{L_{max}}$ is the maximum peak of each trace.

Figure 58 is a typical radial profile of $T_{L_{max}} / T_0$ and T_L / T_0 shown against the design goal. As can be seen, the mean radial to average temperature ratio T_L / T_0 reached the target value of 1.061. The $T_{L_{max}} / T_0$ value fell above the target, indicating higher peaks than anticipated. This maximum

local to average temperature ratio can best be discussed by studying the circumferential temperature profiles in the following section.

Circumferential Temperature Profile

The combustor exit temperature profile shown in Figure 59 represents the best level attained with the final combustor configuration. The maximum local to average temperature ratio, $T_{L_{max}} / T_0$, was 1.17 at a .030 F/A

ratio, whereas the goal was 1.135 at a .032 F/A ratio. The value attained is well within the present turbine cooling capability and was considered to be adequate for subsequent stator and rotor testing.

Figure 60 shows the profile obtained with four-point fuel injection without any fuel spreading dams. The $T_{L_{max}} / T_0$ ratio for this configuration was

1.18 at a .030 F/A ratio. Figures 59 and 60 can be compared directly since the data were taken at the same F/A ratio. As can be seen from the comparison, the final configuration with the circumferential dam was superior ($T_{L_{max}} / T_0$ of 1.17 versus 1.18). These two configurations were closest to

each other in temperature profile; all the other configurations tried were noticeably inferior. Figures 61, 62, and 63 compare the best of the other candidate configurations at the same F/A ratio. A brief summary of the above figures is shown in Table X.

TABLE X
CONFIGURATION CHARACTERISTICS AND PERFORMANCE

Figure No.	Configuration No.	Configuration	F/A	$T_{L_{max}} / T_0$, °R/°R
59	8	4-pt. injection - circumferential dam	.030	1.170
60	5	4-pt. injection - no dam	.030	1.180
61	8	4-pt. injection - circumferential dam	.020	1.125
62	7	4-pt. injection - 4 axial dams	.020	1.195
63	4	2-pt. injection - 4 axial dams	.020	1.252

In the attempt to optimize the final configuration, variations of hardware relationships were tried. The temperature pattern remained essentially as shown in Figure 61 regardless of the angular orientation of the headplate, outer liner, inner liner, inlet support housing, or outer liner exit support plate (stator support plate). There was a shift in pattern when the entire rig was shifted or when just the vaporizer was shifted. Figure 64 shows the exit profile with the vaporizer shifted 180 degrees and may be compared directly with Figure 61. As can be seen, the profile has shifted approximately 90 degrees. The sensitivity of the temperature profile to the vaporizer positioning indicates an area for further study and possible improvement. Also, additional fuel injection points can assure full distribution of fuel in the vaporizer annulus.

The combustor that was used for the last hot stator test and the rotor program was assembled and tested for documentation of the exit temperature profile. The profile obtained in Figure 65 at a .0284 F/A ratio was essentially the same as that of Figure 59 at a .030 F/A ratio except for an additional peak at the 320-degree position. The peak persisted even at the higher F/A ratio point of .0307. The resulting maximum to average temperature ratio $T_{L_{max}} / T_0$ was 1.23. Rather than continue further combustor in-

vestigations on these variations in profile, it was decided to perform the stator and rotor tests with the more severe profile, thus testing turbine durability at more penalizing conditions. Subsequent testing justified this course of action since the blades showed no effect from the higher than design local gas temperature.

Figure 66 shows the persistence of the extra temperature peak at the 320-degree angular location. This traverse was made at 410°F combustor inlet temperature rather than 610°F, so that the exit temperature would still be low enough to prevent damage to the exit thermocouples. It is interesting to note that the temperature peak at the 90-degree angular location results in the same temperature ratio as obtained in previous tests with this configuration (Configuration No. 8).

To determine the amount of swirl that takes place from the point of fuel injection to the exit of the combustor, flow from one injection point was stopped and the resulting cold spot was noted in the exit profile. The swirl angle when using a full open annulus and axial dams is 240 degrees. With the circumferential dam, the annulus is closed down, and the resulting swirl angle of 190 degrees indicates a velocity increase in the primary air.

Combustor Airflow Distribution

To experimentally determine the amount of airflow to the various portions of the combustor, first, all the openings were taped over except for the primary air passage through the vaporizer. Figure 67 shows the pressure drop versus airflow for the vaporizer at design inlet temperature and pressure. Next, the tape covering the other combustor openings was removed and the test was repeated. By measuring the pressure drop in the vicinity of

each of the remaining openings, and having measured the opening areas, air-flow was calculated. The vaporizer flow was measured separately because the passage geometry prevented use of a predictable discharge coefficient.

Table XI compares design air partition against that computed from the cold flow data. Examination of the table indicates an increase in film cooling air over the design value. However, since this increase of approximately 10 percent was at the expense of dilution air and not primary zone air, development of the combustor could proceed without liner geometry changes. Dilution air and film cooling air can be adjusted as a refinement to the exit profile to minimize the presence of hot spots as testing indicates.

TABLE XI COMBUSTOR AIRFLOW DISTRIBUTION - DESIGN VALUES VERSUS TEST VALUES		
	Design Percent	Test Percent
Outer Liner Passage - Total	53.03	50.47
Dilution Slots - Total	31.67	22.16
Film Cooling - Total	21.36	28.31
1st Film Cooling Annulus	5.54	7.91
2nd Film Cooling Annulus	4.15	5.43
3rd Film Cooling Annulus	4.15	5.43
4th Film Cooling Annulus	5.88	7.85
5th Film Cooling Annulus	1.64	1.69
Inner Liner - Total	6.30	10.02
1st Film Cooling Annulus	1.56	3.28
2nd Film Cooling Annulus	1.21	2.39
3rd Film Cooling Annulus	1.63	2.40
4th Film Cooling Annulus	0.87	0.87
5th Film Cooling Annulus	1.04	1.08
Vaporizer Headplate - Total	40.67	39.49
Vaporizer	13.67	14.29
Primary Air Cups - Slots	25.09	23.42
Primary Air Cups - Anti-Carbon Holes	0.96	0.89
Headplate Anti-Carbon Holes	0.96	0.89

4.1.2 Combustor Durability and Modifications

After completing the initial airflow checks and establishing a configuration for stable combustion, effort was concentrated on evaluating liner durability. Figure 68 shows the combustor assembly with temperature paint and thermocouples installed. Figures 69 and 70 show the inner and outer liner after testing to an F/A ratio of .030. Figures 71 and 72 translate a portion of this temperature paint to a schematic of the liners for easy study. It is to be noted that the figures represent liners that were re-worked as compared to the initial design as follows:

1. The outer liner's last downstream row of cooling holes were enlarged from .047 inch diameter to .082 inch diameter.
2. The inner liner's last two downstream rows of cooling holes were enlarged from .034 inch diameter to .060 inch diameter on the fourth row and .037 inch diameter to .065 inch diameter on the last row.
3. All cooling air deflectors were dimpled at about a 1-inch circumferential spacing to prevent them from closing below .015 inch. The deflectors were also split at about a 2-inch circumferential spacing to avoid buckling. Finally they were welded at the leading edge rather than riveted to prevent local separation from the liners.
4. The first upstream row of cooling holes on the inner liner was displaced aft by .125 inch, and the inner beveled corners of the shell near these holes were rounded. In this way the cooling holes were moved out of a stagnant area of the first bend in the flow passage.

Subsequent testing of the combustor during the hot stator cascade tests over a wide range of combustor exit gas temperatures, including 1.17 hours at 2650°F, verified the excellent durability characteristics of the combustor. Furthermore, during the entire hot turbine stage test (except for the final half hour on test rotor no. 2), the combustor continued in excellent condition as observed by periodic borescope inspection of the rig. During the final 30 minutes, the fuel vaporizer radial positioning screws had all unthreaded, which permitted misalignment of the vaporizer concentricity. Since fuel distribution is substantially affected by the annular area formed by the vaporizer, it was no surprise to find local burned areas on the combustor inner liner (Figure 73). However, it was noted that the circumferential locations of these hot spots were not coincident with the locations of peak gas temperatures measured during the combustor test evaluation. This substantiates that the condition of the inner liner was a result of secondary damage and does not reflect upon liner durability. Figures 74, 75, and 76 show the excellent condition of the outer liner and headplate after the same second turbine stage hot test including 2 hours at 2400°-2500°F.

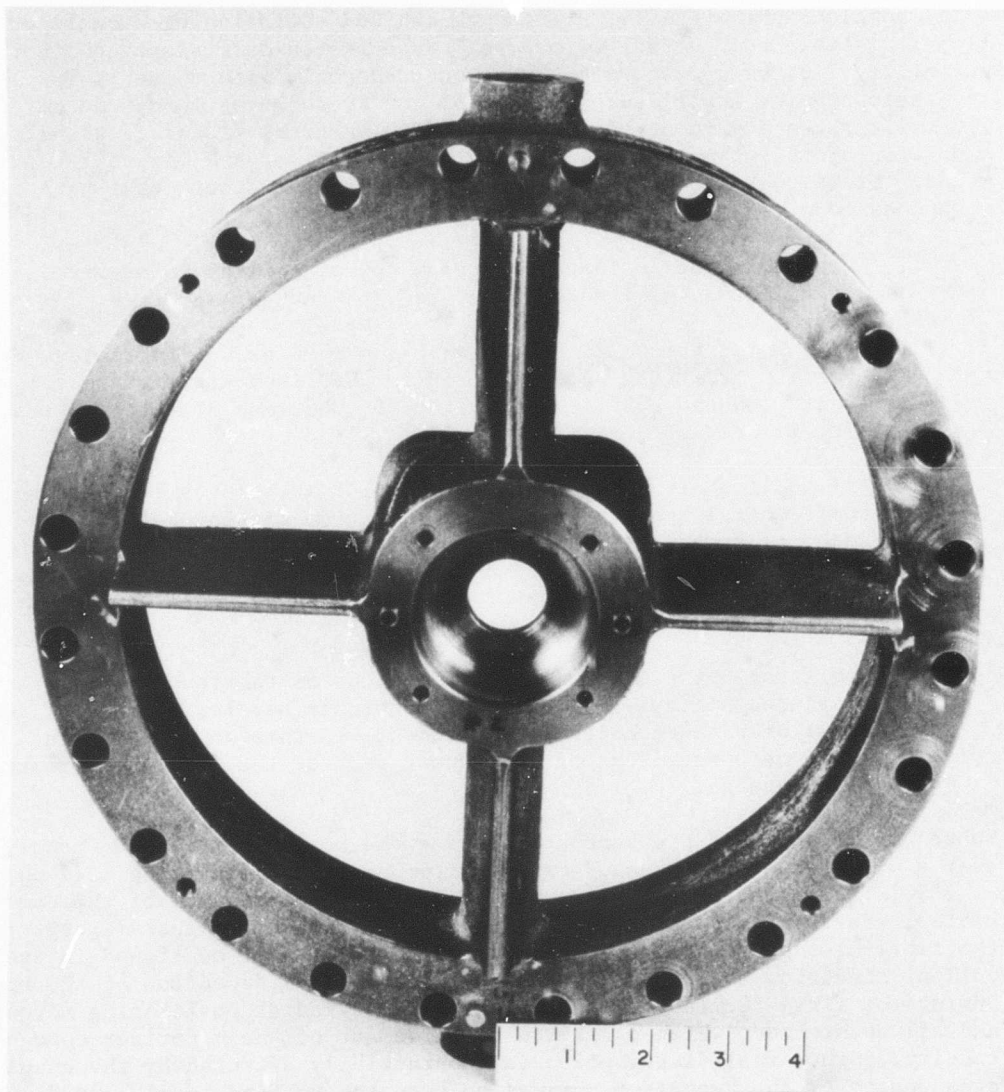


Figure 38. Inlet Support.

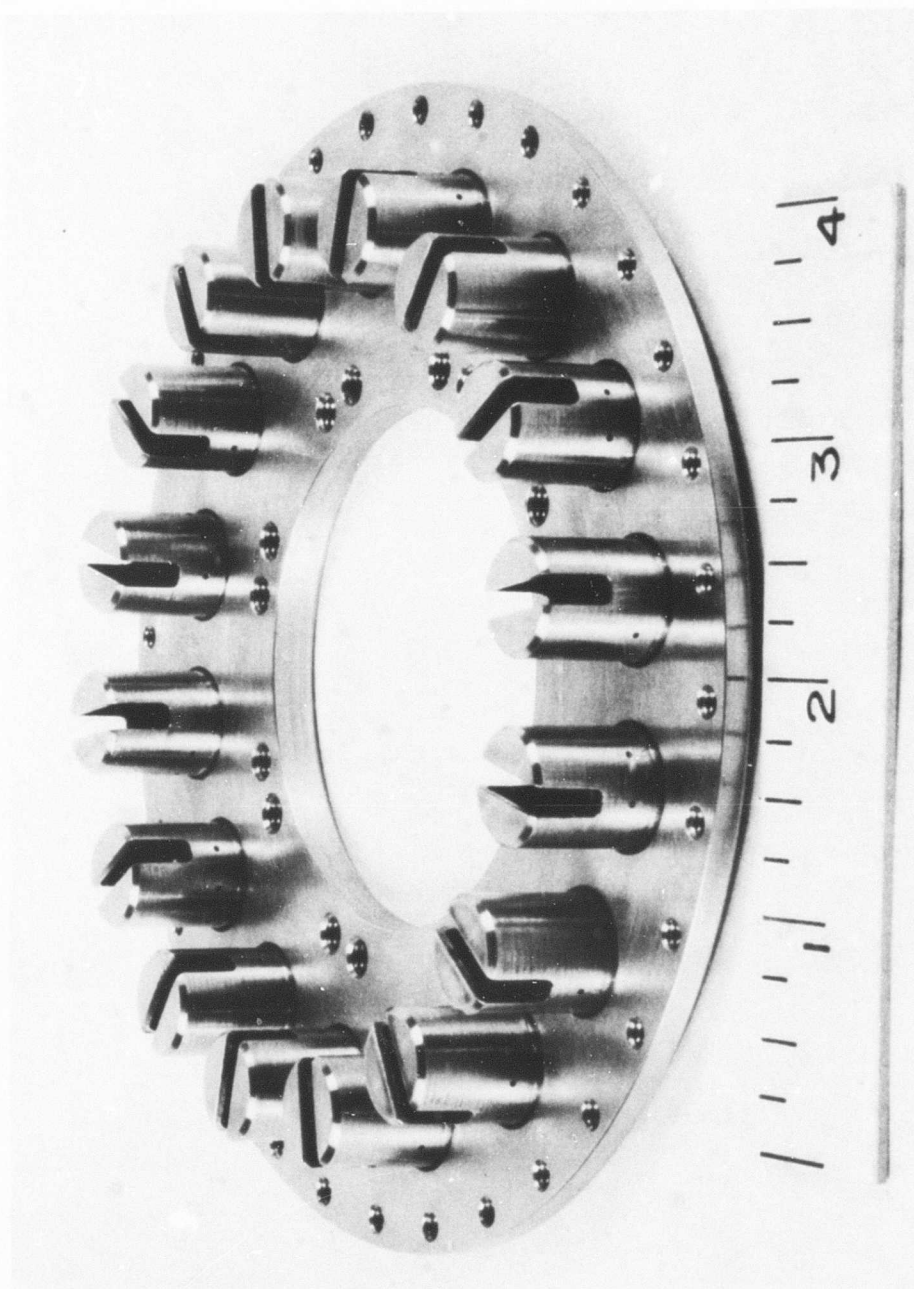


Figure 39. Combustor Headplate.

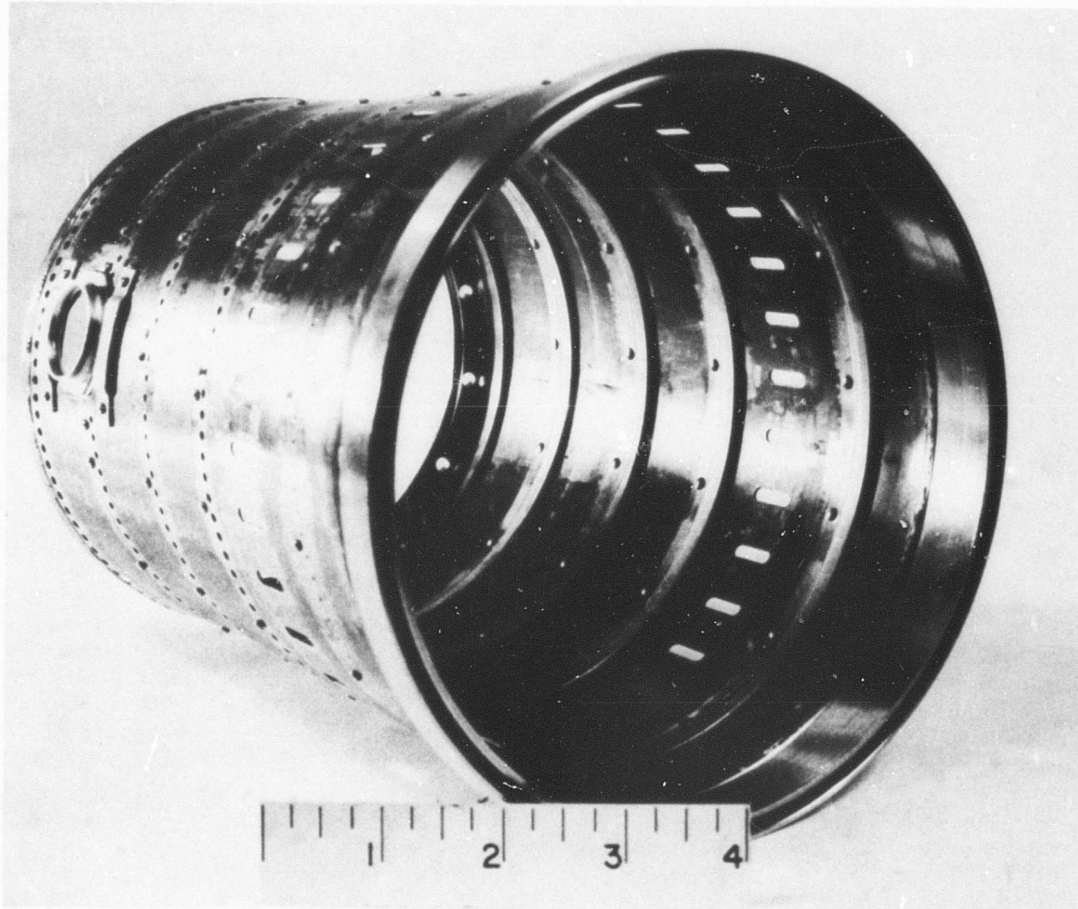


Figure 40. Combustor Outer Liner.



Figure 41. Combustor Inner Liner.

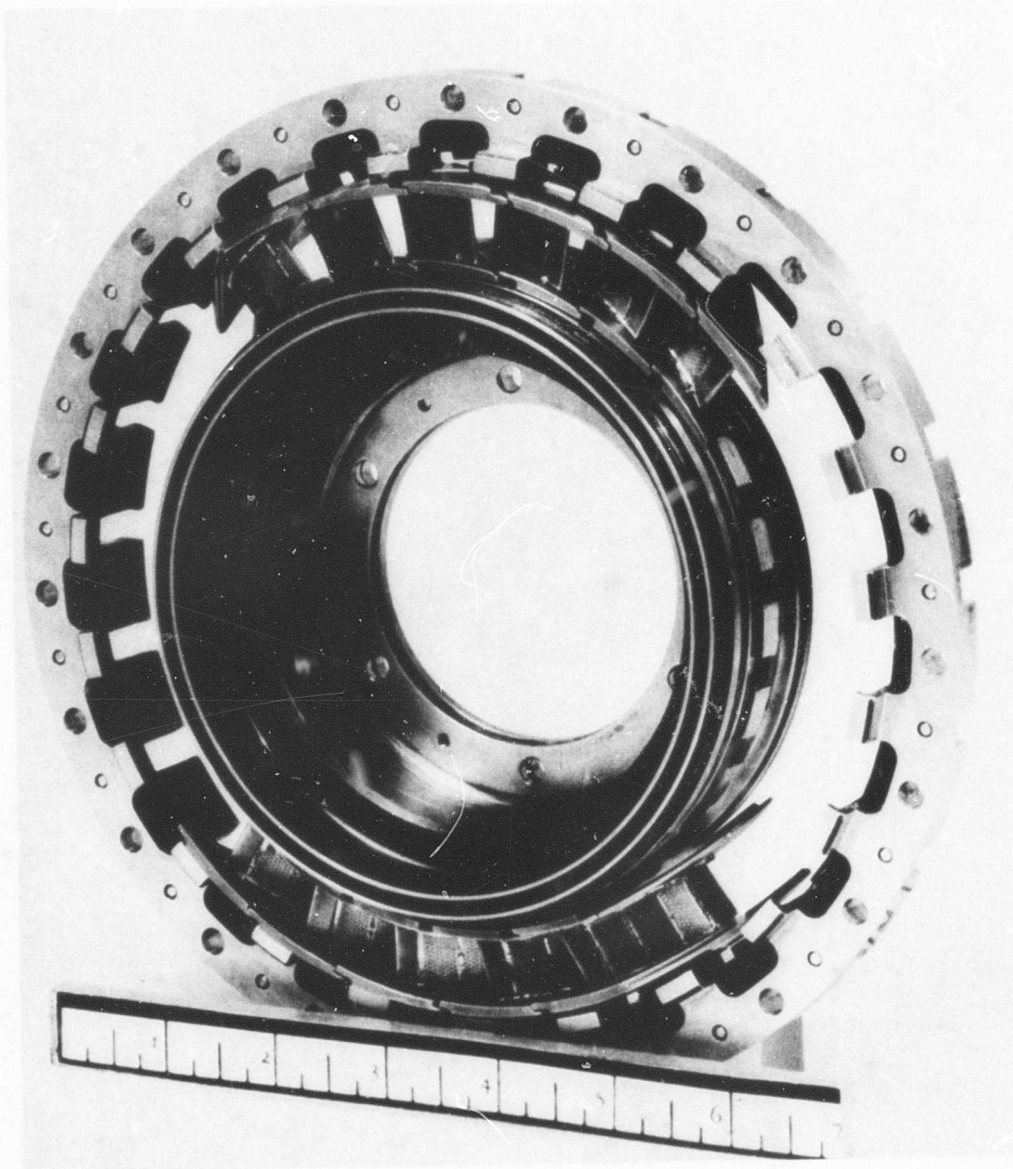


Figure 42. Partial Stator and Support Assembly.

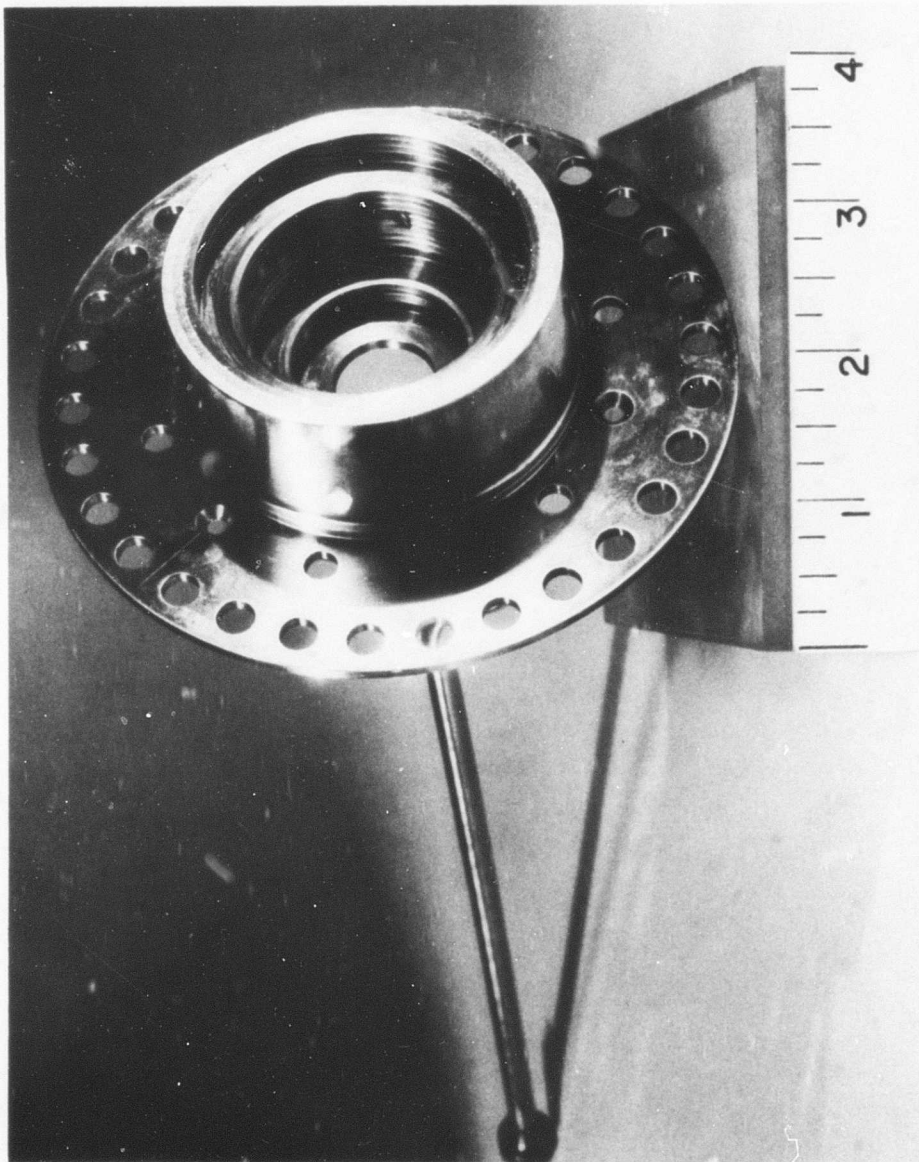


Figure 43. Labyrinth Seal Assembly.

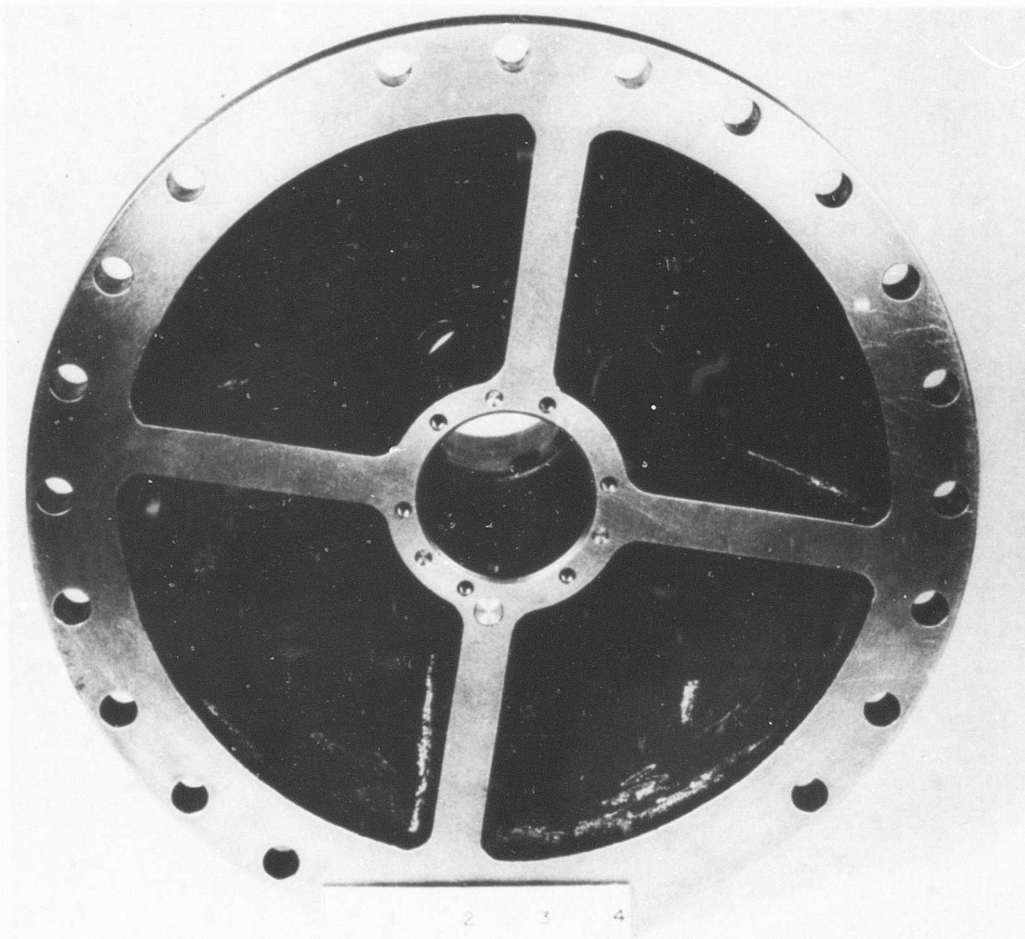


Figure 44. Turbine Support - Rear View.

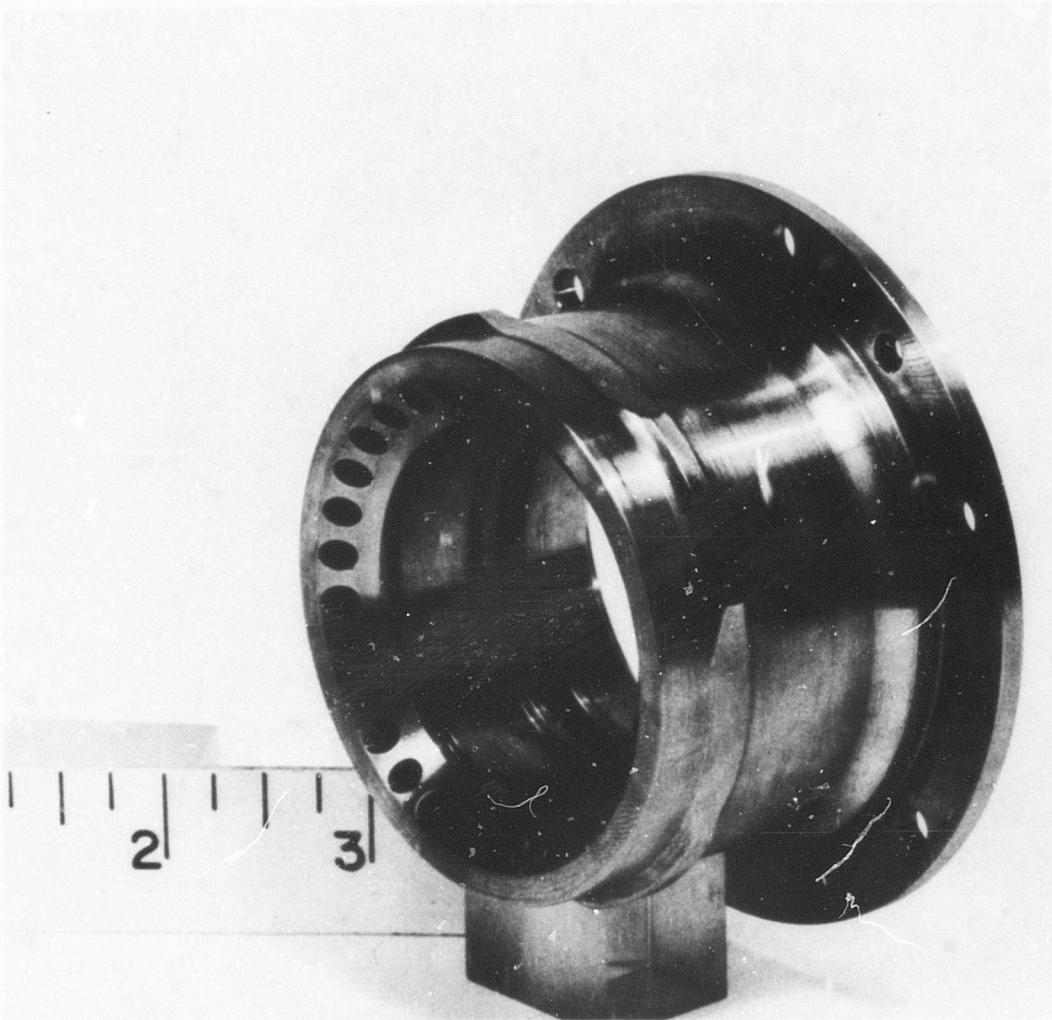


Figure 45. Bearing Retainer - Front.

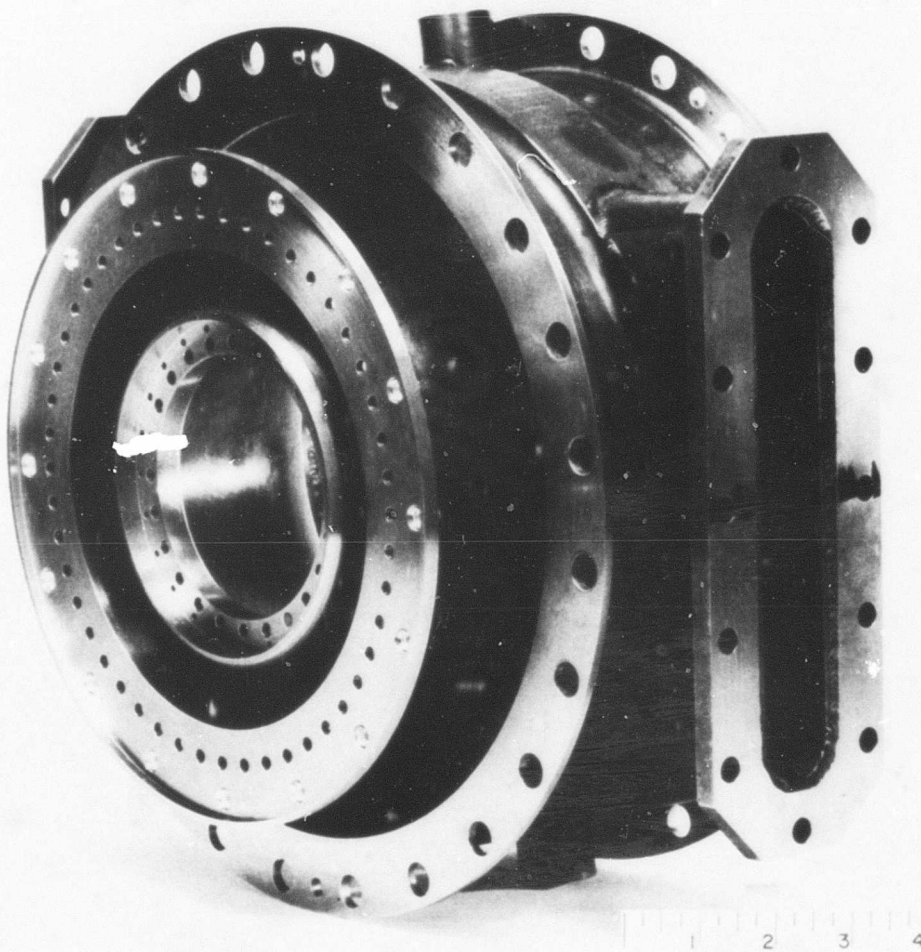


Figure 46. Turbine Exhaust Housing - Front View.

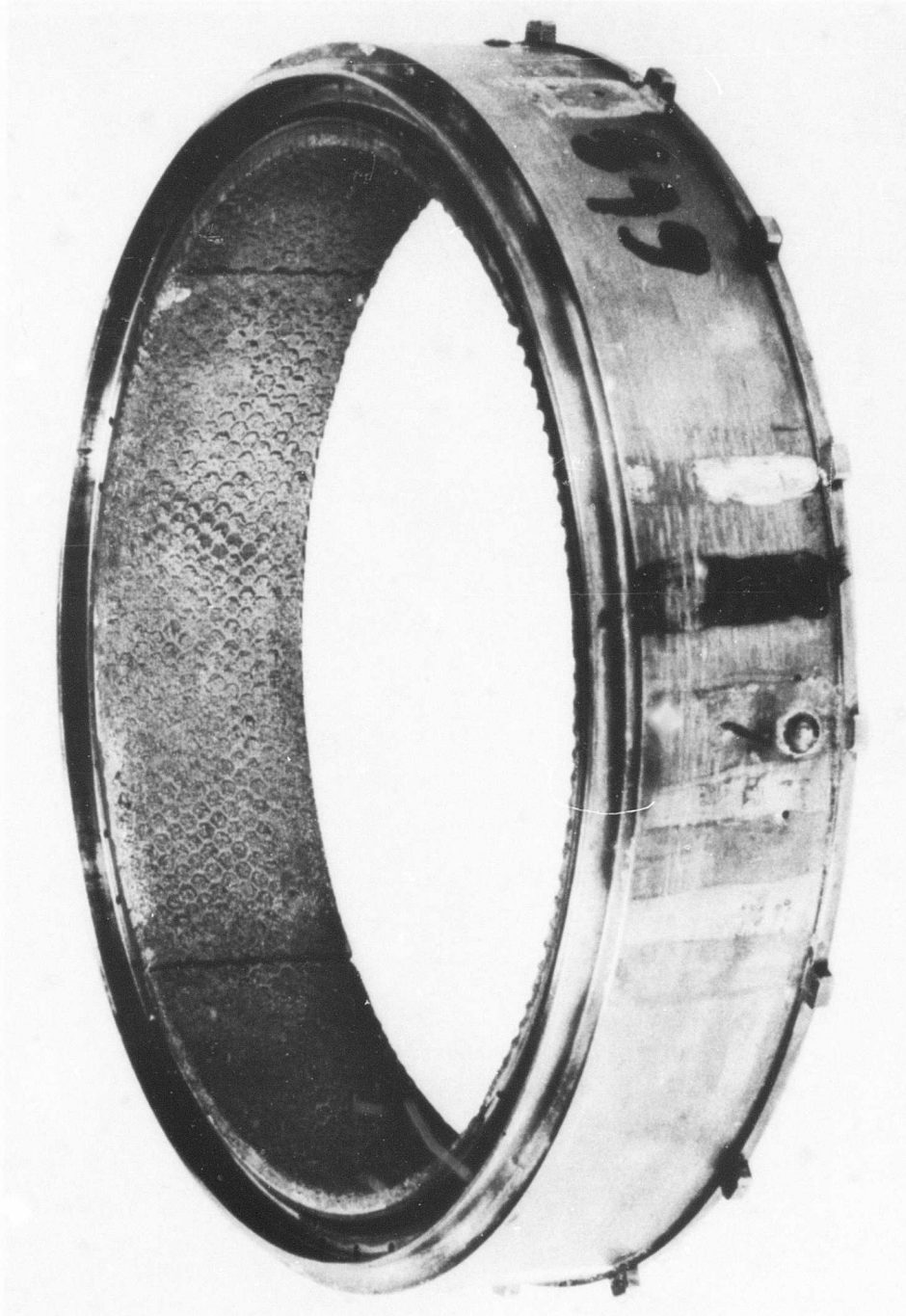


Figure 47. Turbine Shroud Filled With Microseal.

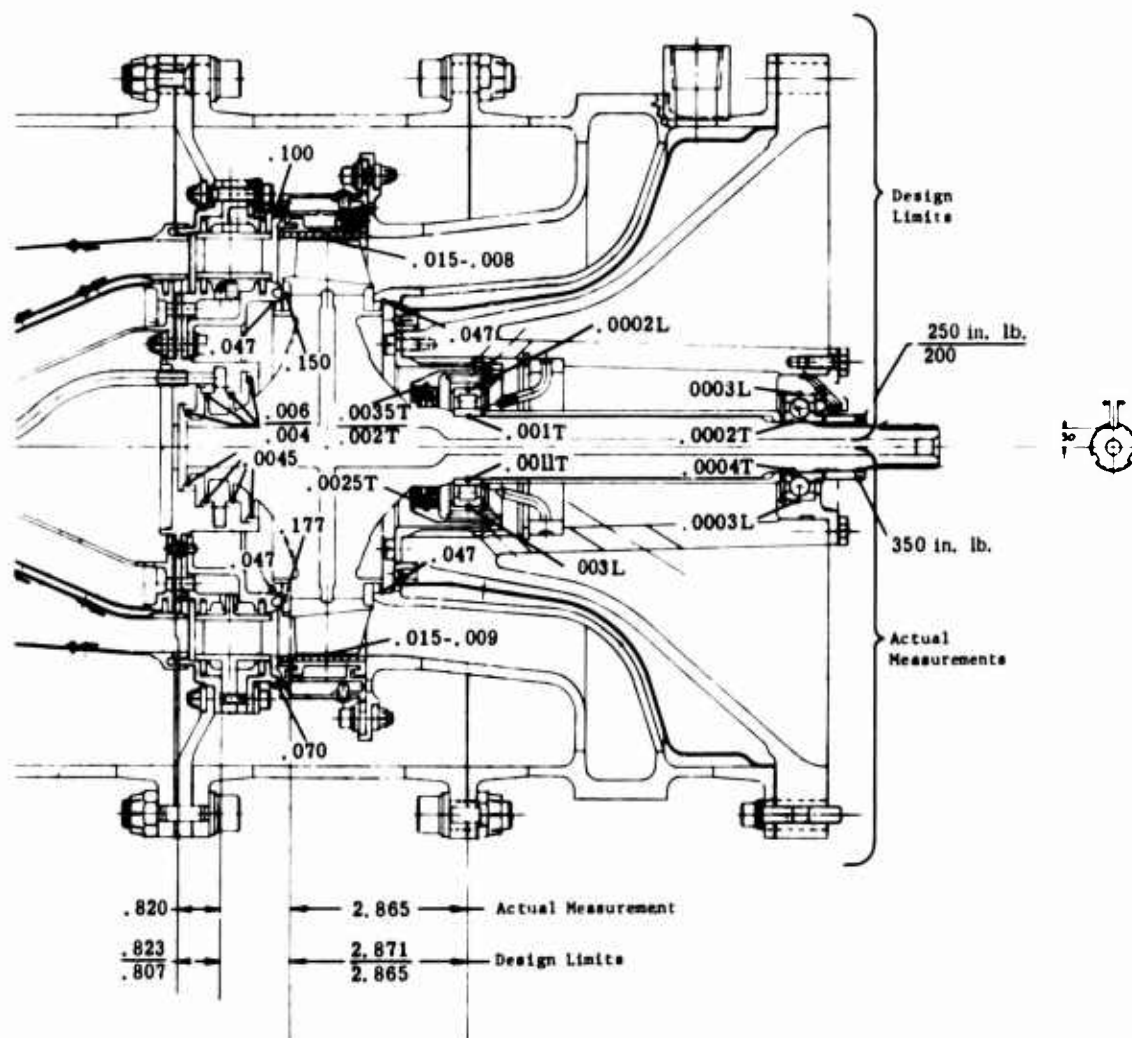


Figure 48. Actual Assembly Measurements - Rotor Build 5.

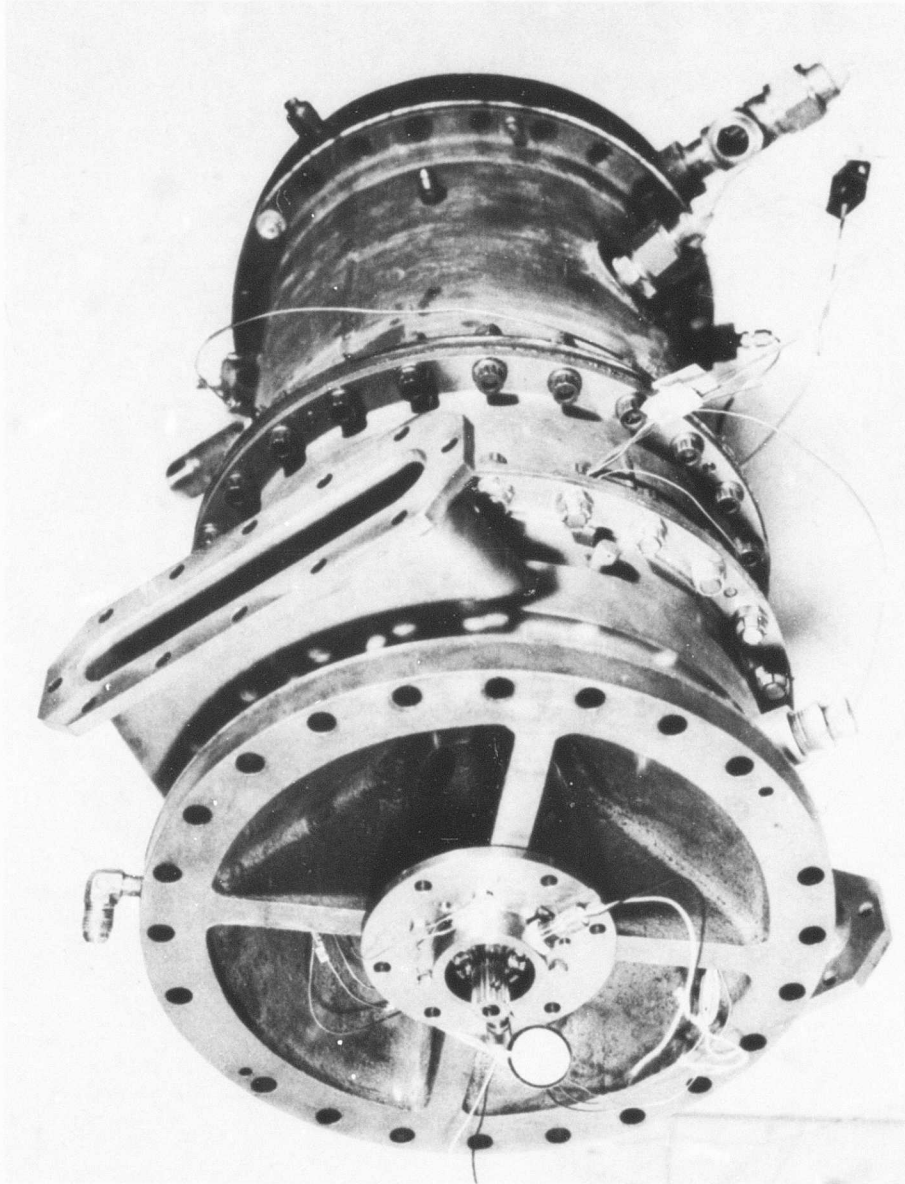


Figure 49. Turbine Rig Complete Assembly - Rear View.

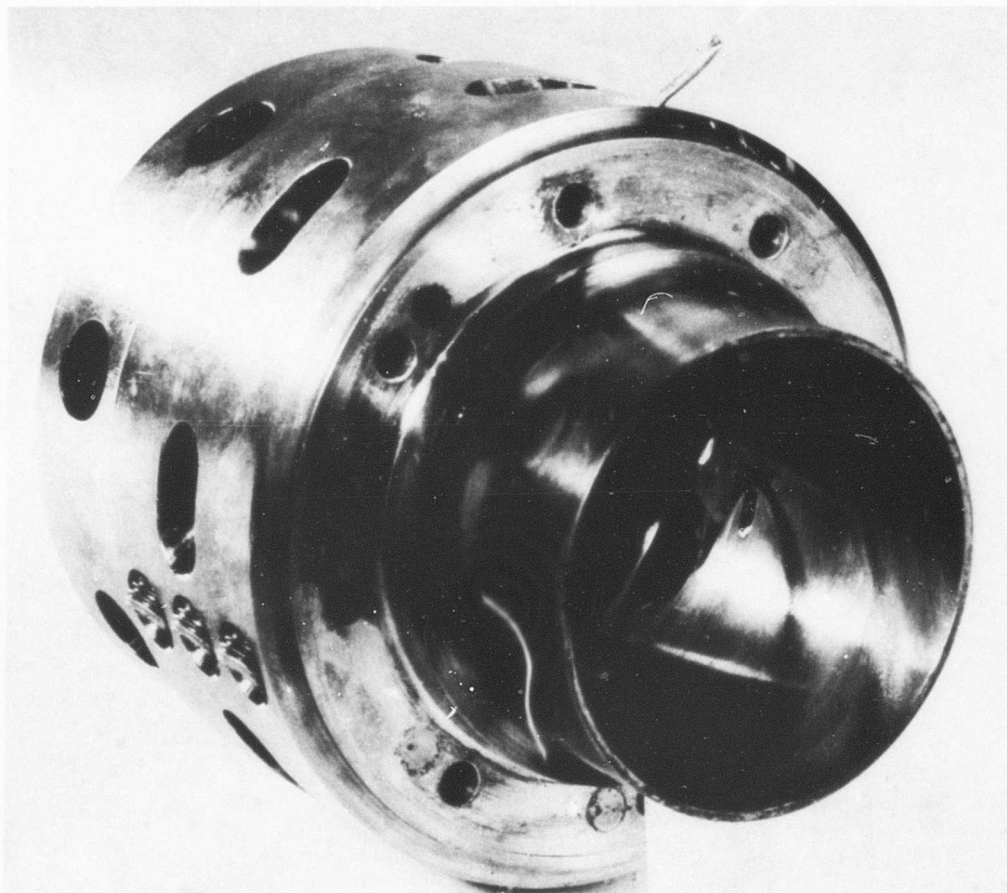


Figure 50. Vaporizer - No Dams.

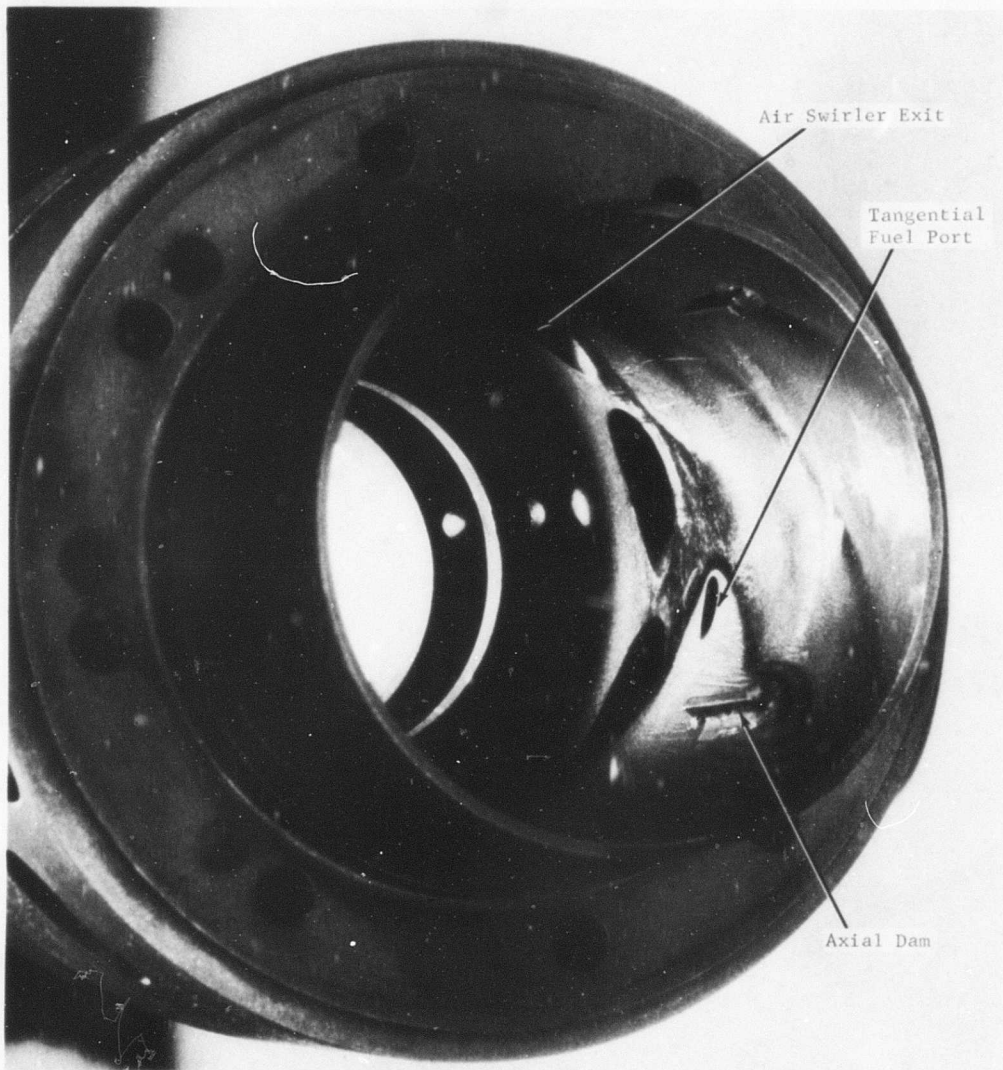


Figure 51. Annular Vaporizer With Axial Dams.

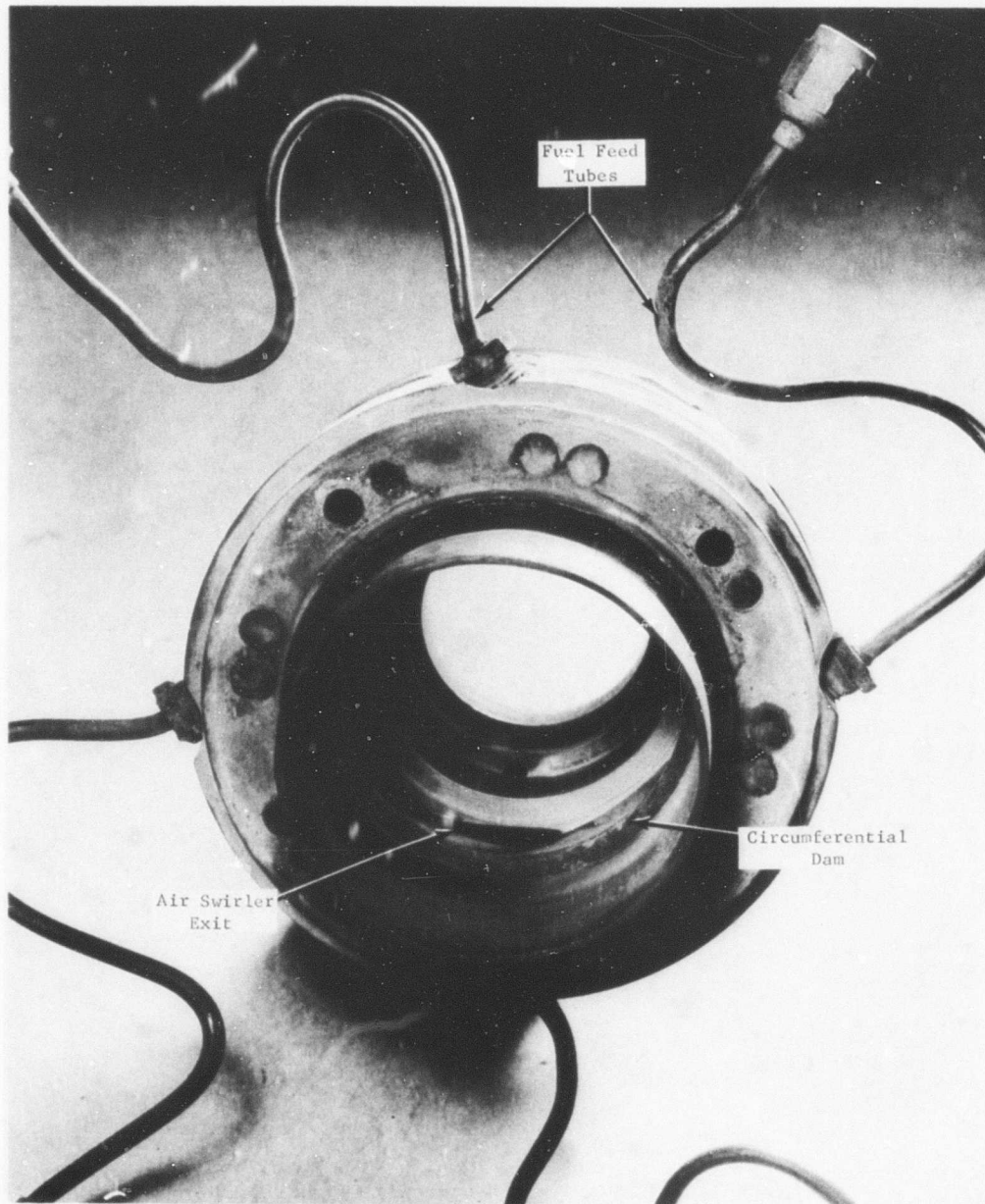


Figure 52. Vaporizer With Circumferential Dam.

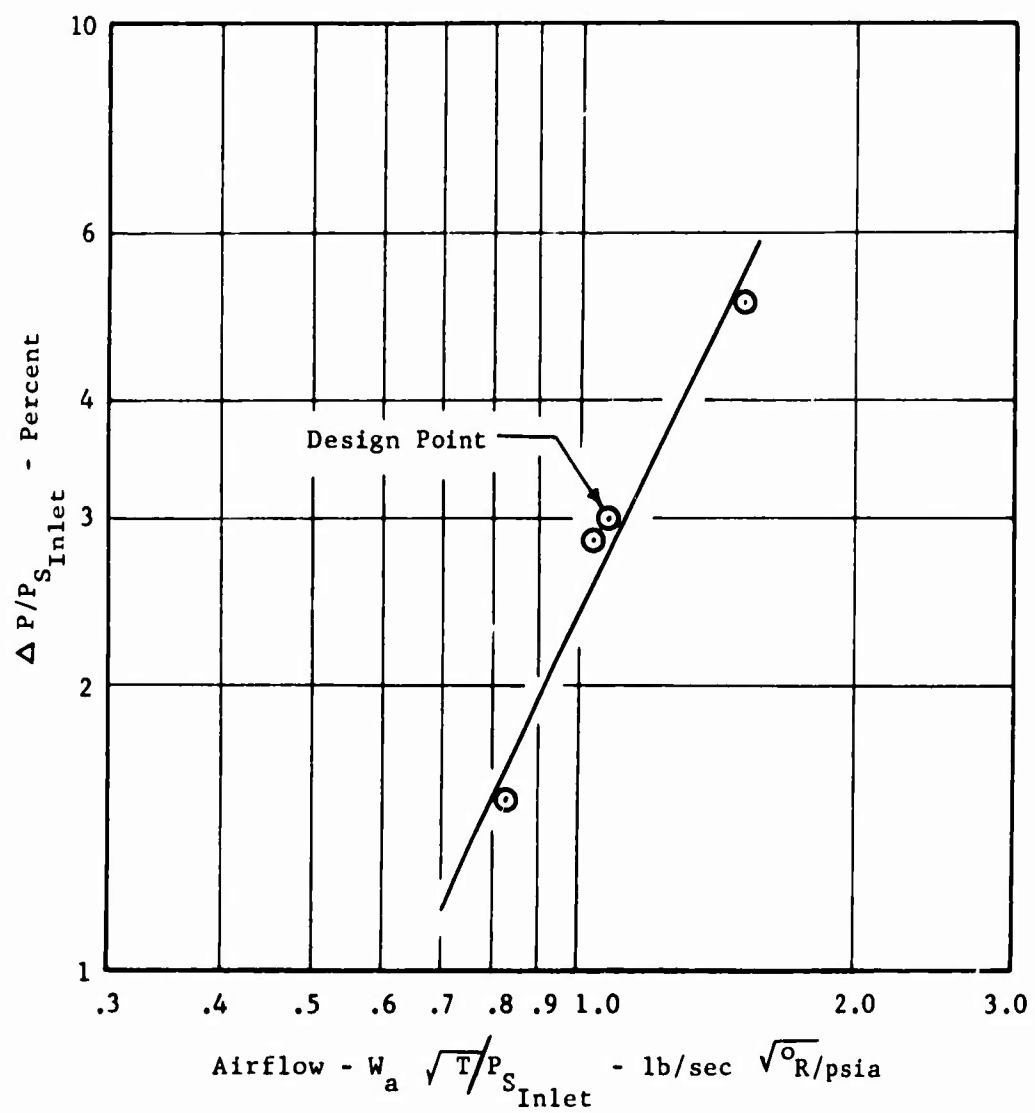


Figure 53. Combustor Pressure Drop Characteristic.

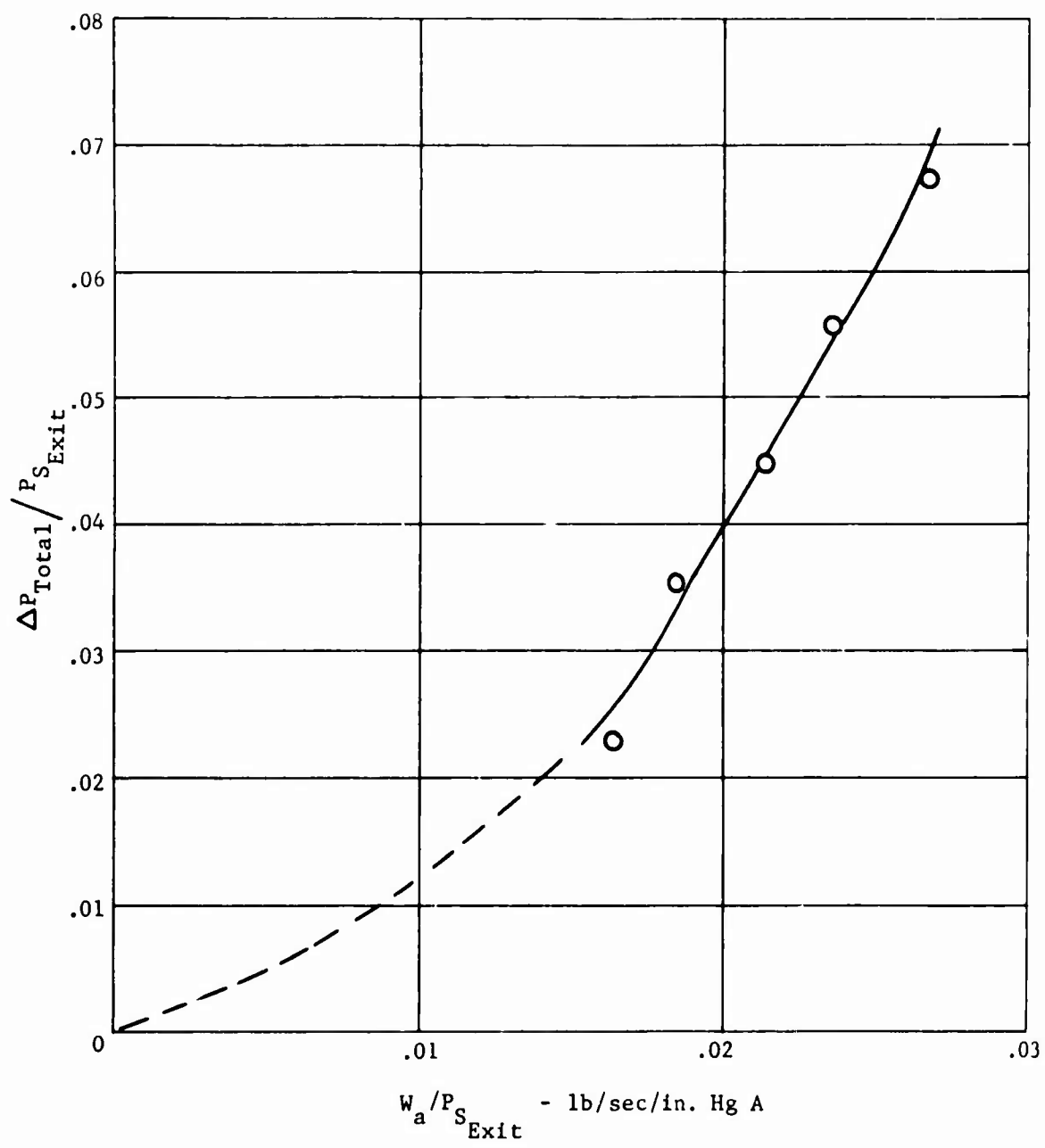


Figure 54. Combustor Pressure Drop Characteristic.

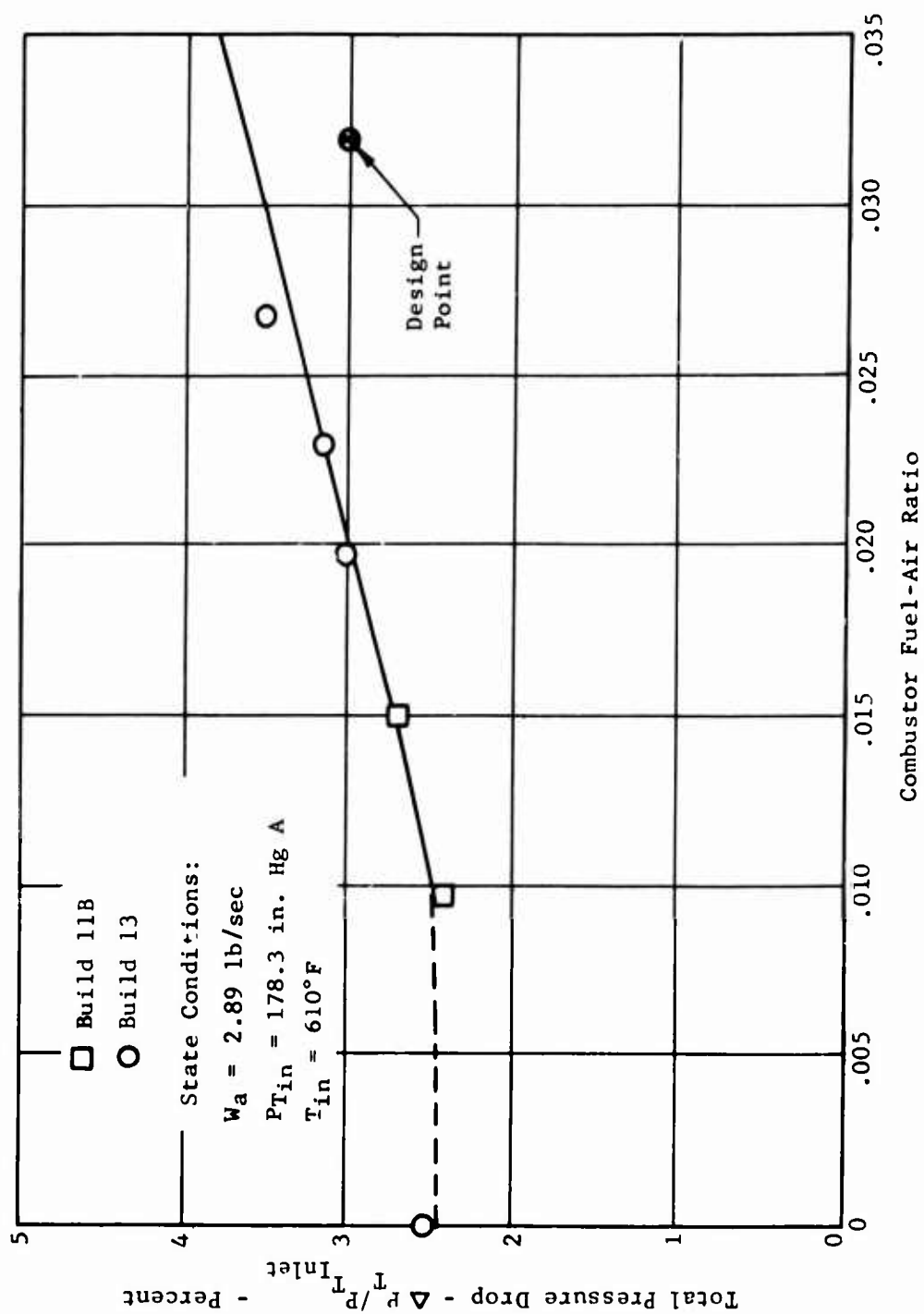
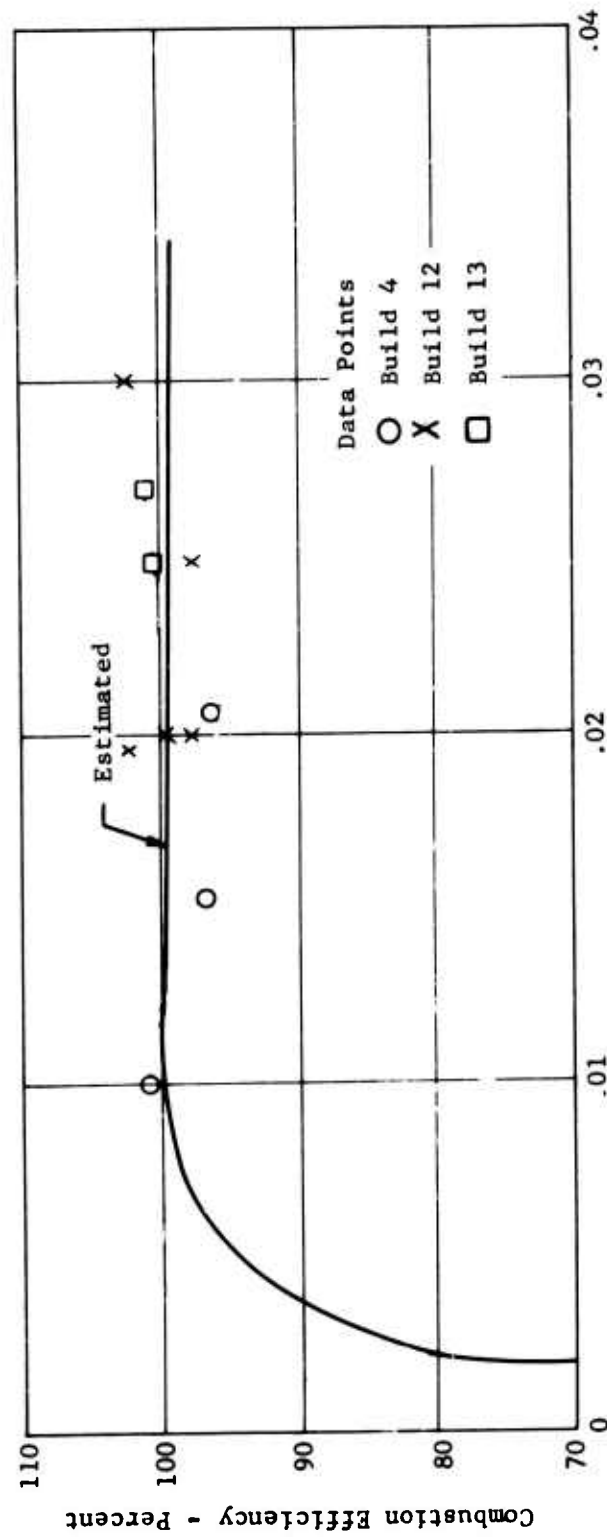


Figure 55. Total Pressure Loss During Burning.



Fuel-Air Ratio - F/A

Figure 56. Combustor Efficiency.

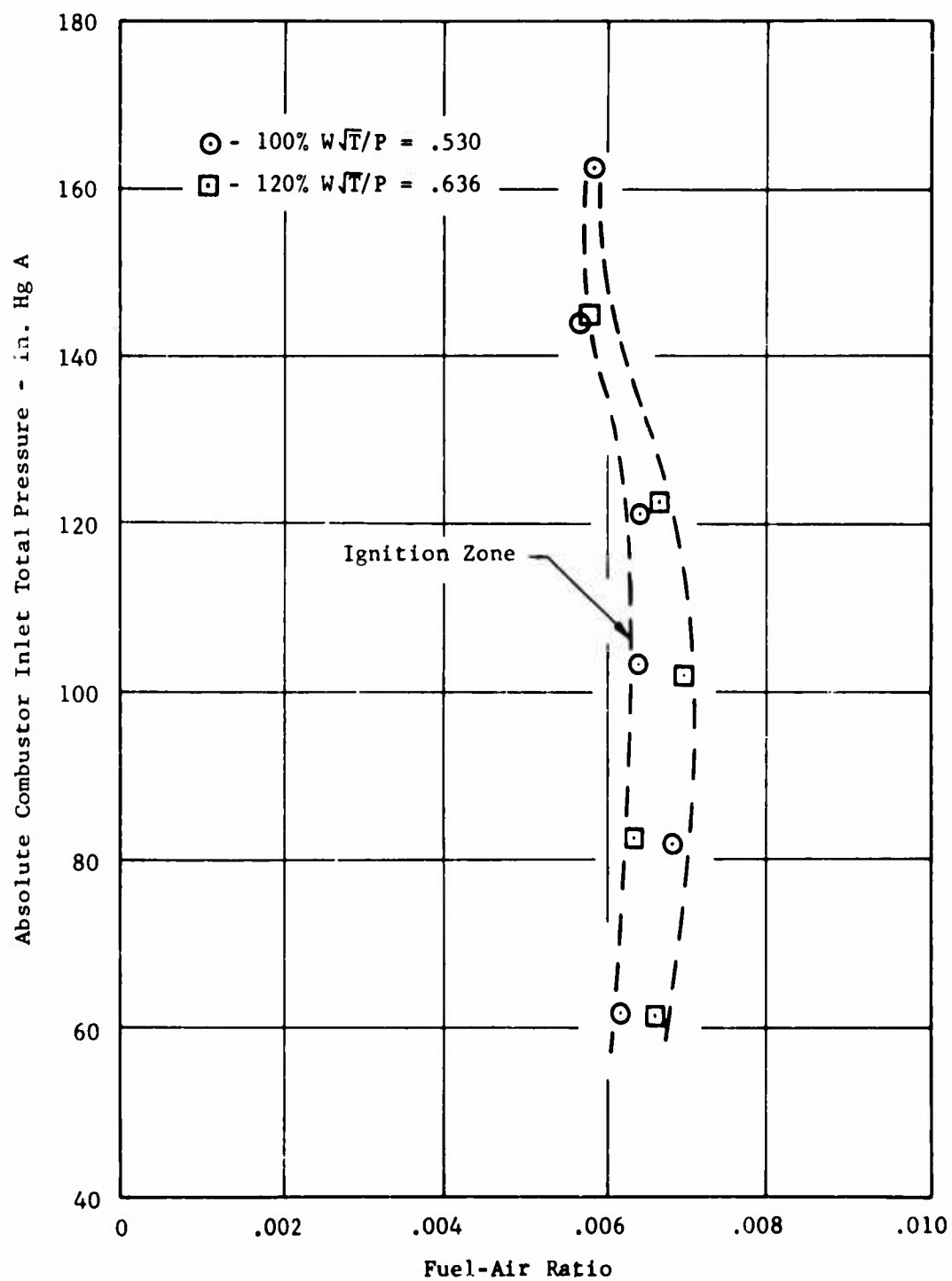


Figure 57. Combustor Ignition Characteristic.

Build 9404-1-14
6-22-66, F/A = .019

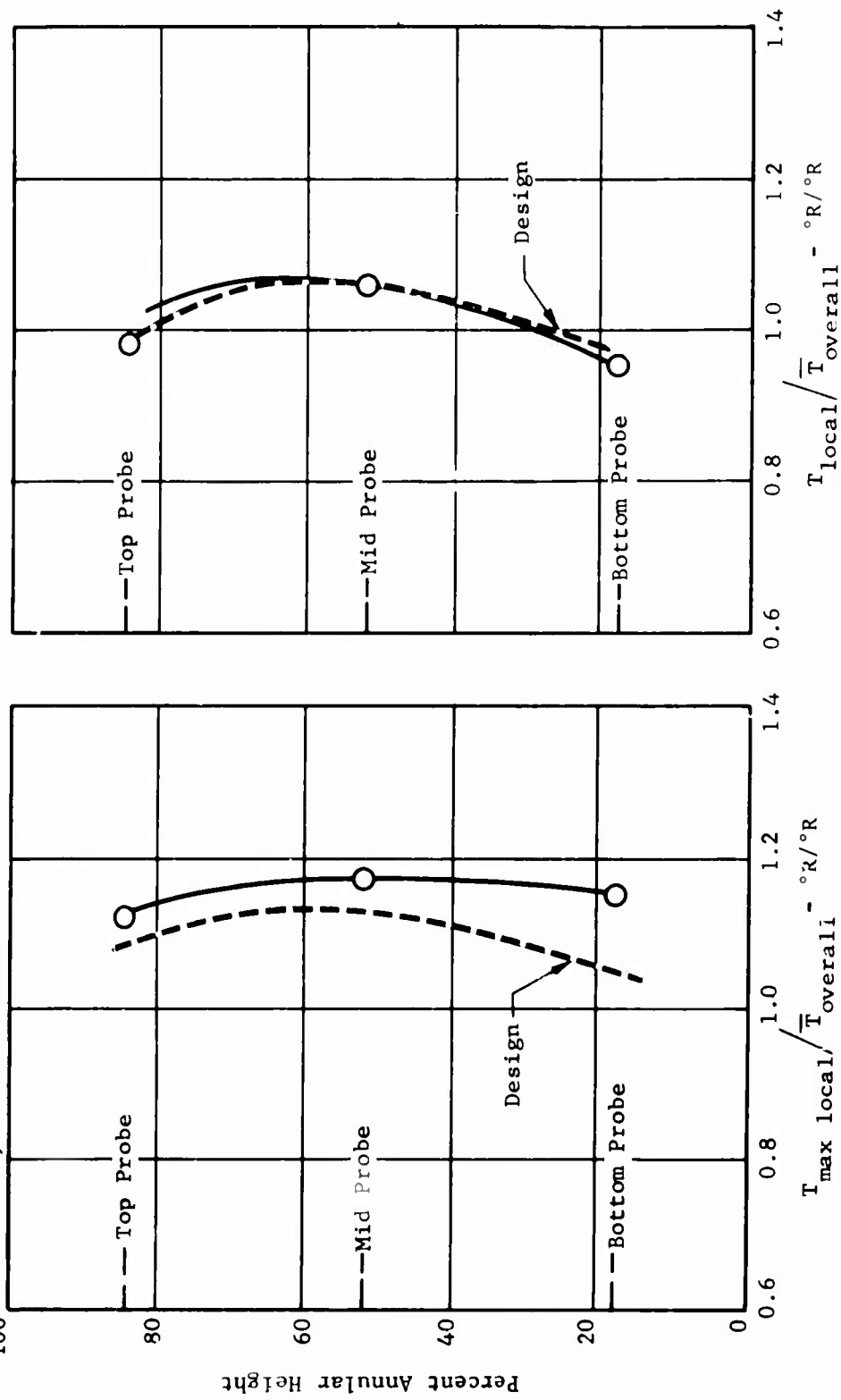


Figure 58. Radial Exit Temperature Profile.

Config. No. 8, Data Pages 7
Build 9404-1-12
F/A = .030

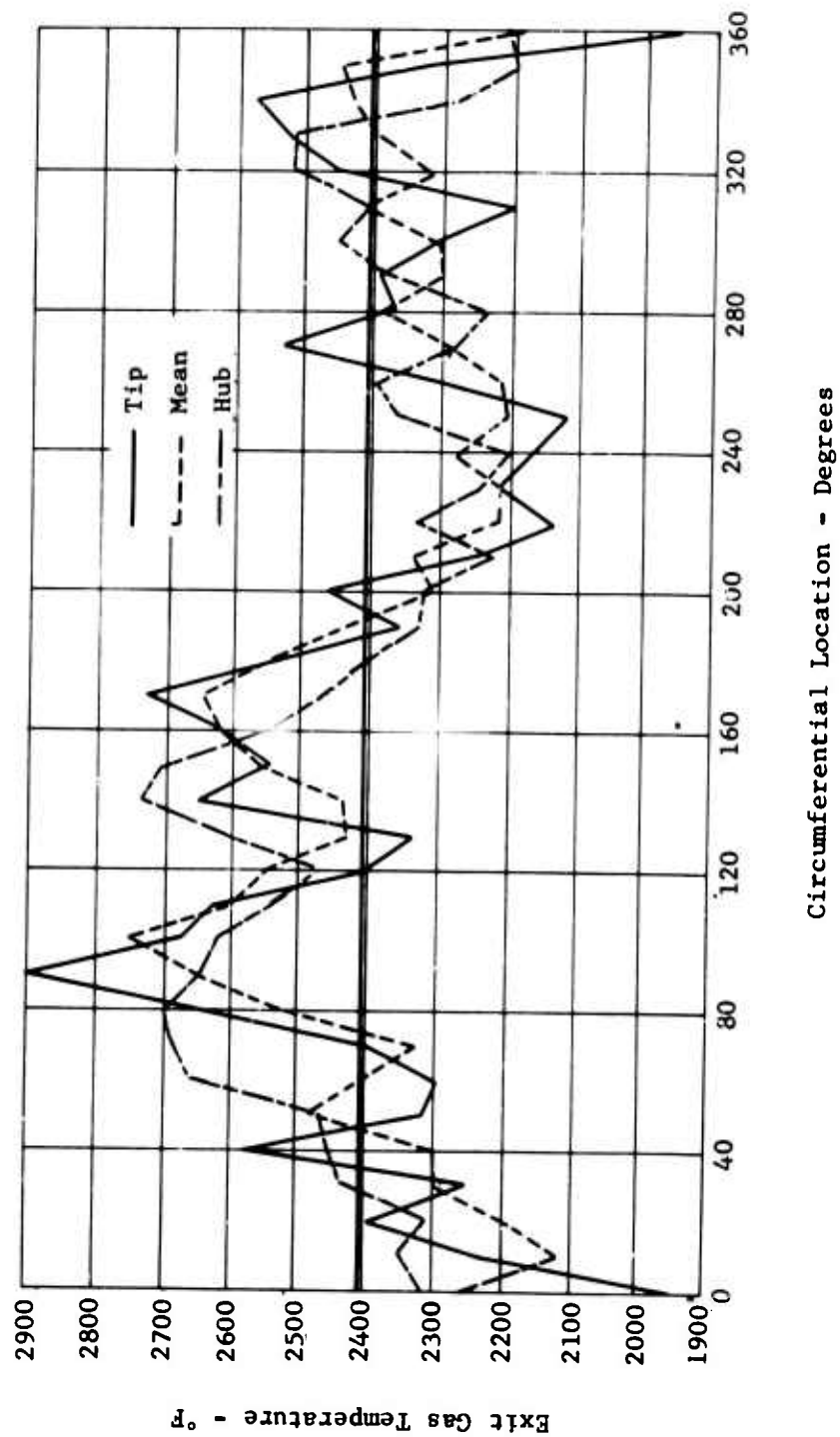


Figure 59. Circumferential Exit Temperature Profile.

Config. No. 5
 Build 9404-1-16
 F/A = .030

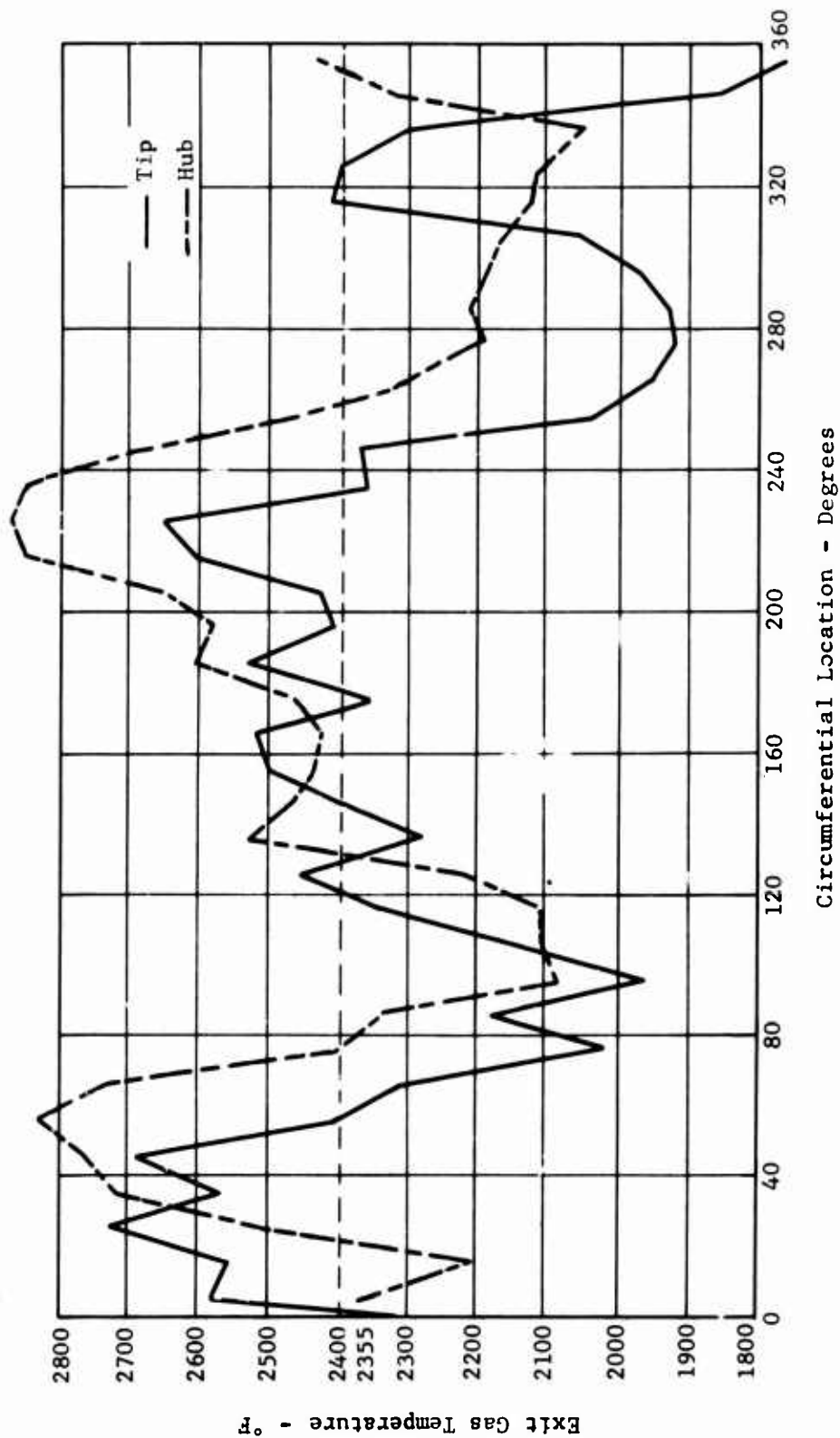


Figure 60. Circumferential Exit Temperature Profile.

Config. No. 8, Data Point 24
 Build 9404-1-12
 F/A = .020

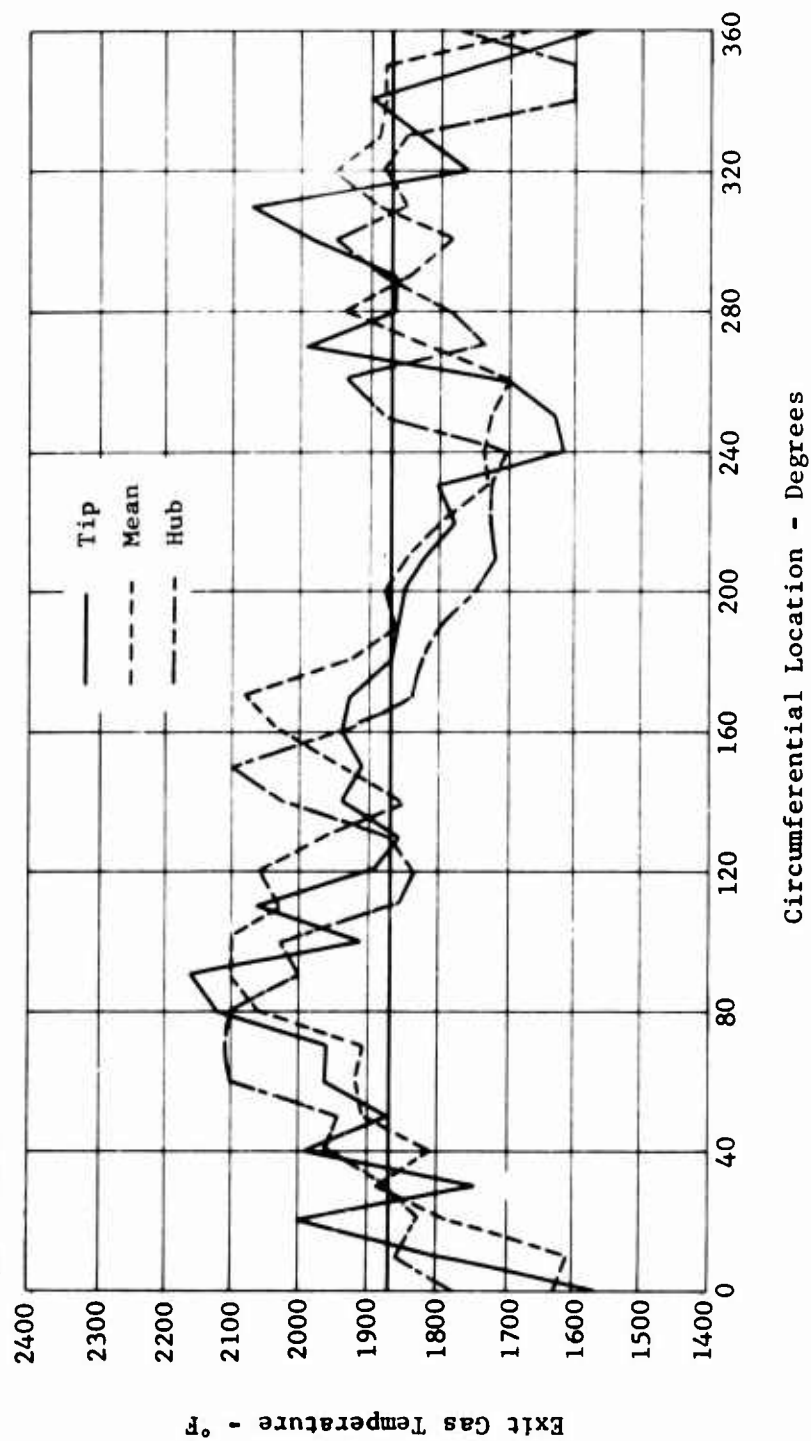


Figure 61. Circumferential Exit Temperature Profile.

Config. No. 7, Data Point 16
 Build 9404-1-9
 F/A = .020

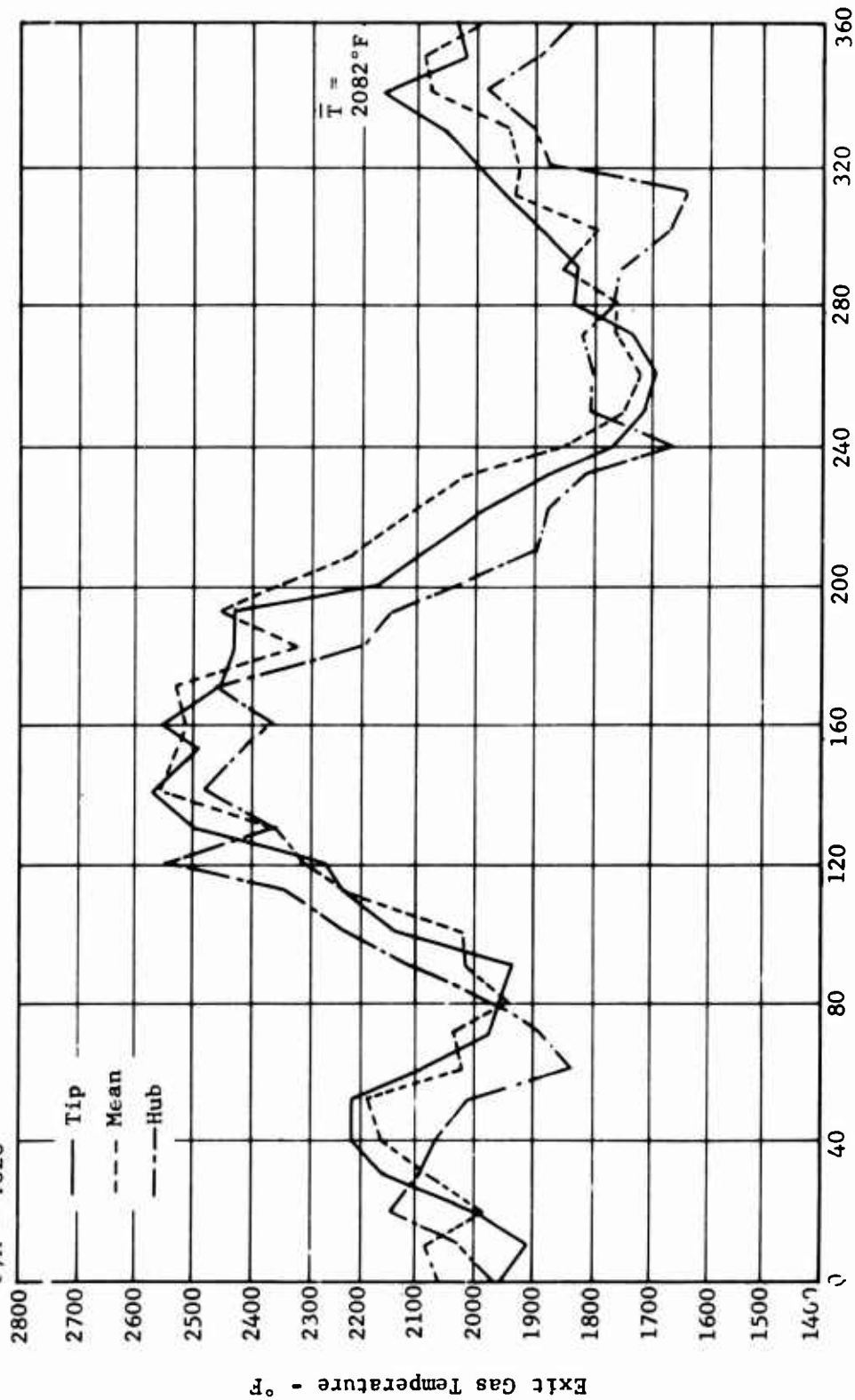


Figure 62. Circumferential Exit Temperature Profile.

Config. No.4, Data Point 2
 Build 9404-1-8
 F/A = .0199

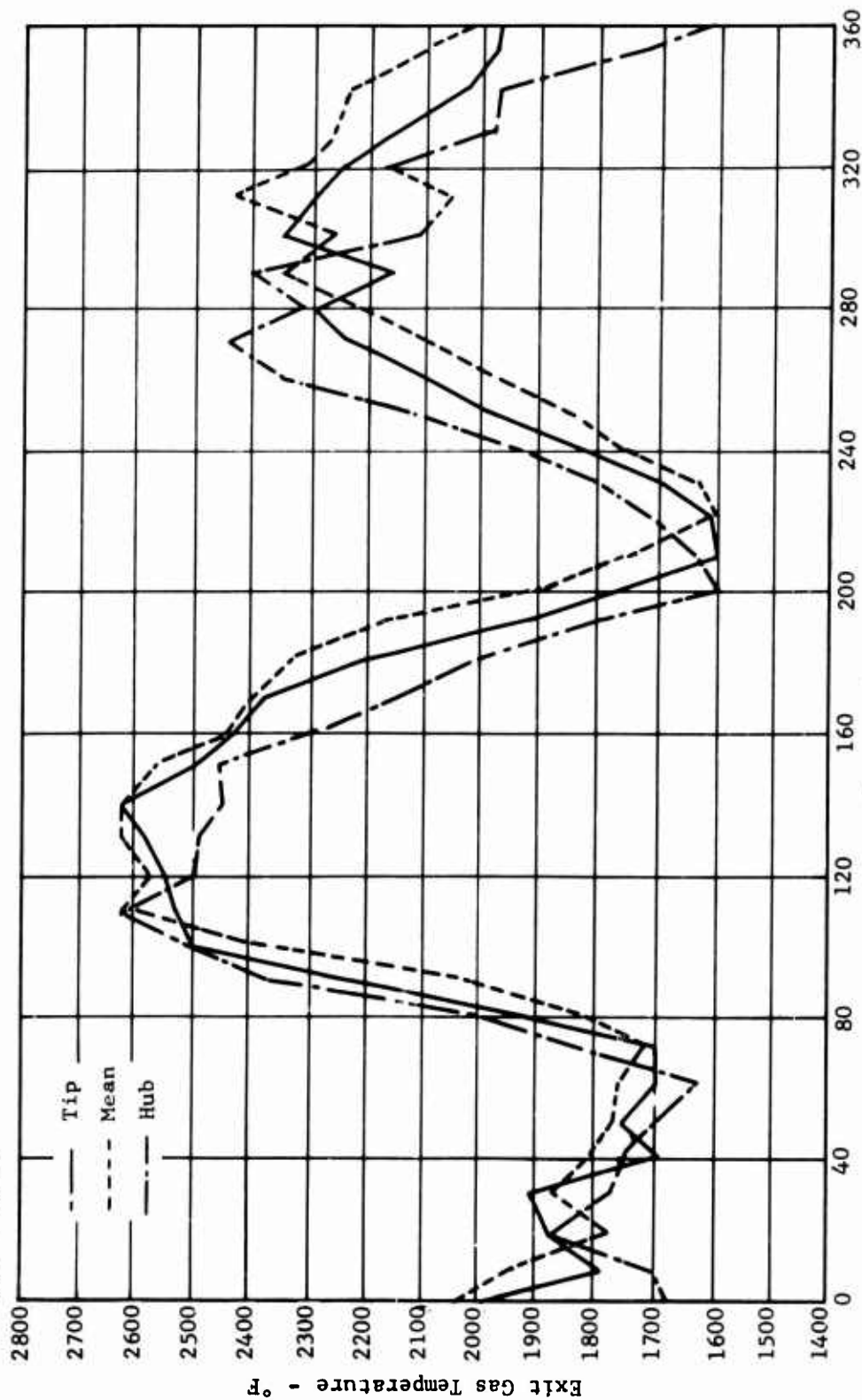


Figure 63. Circumferential Exit Temperature Profile.

Config. No. 8, Data Point 19
Build 9404-1-12
F/A = .0197
Inverted Vaporizer

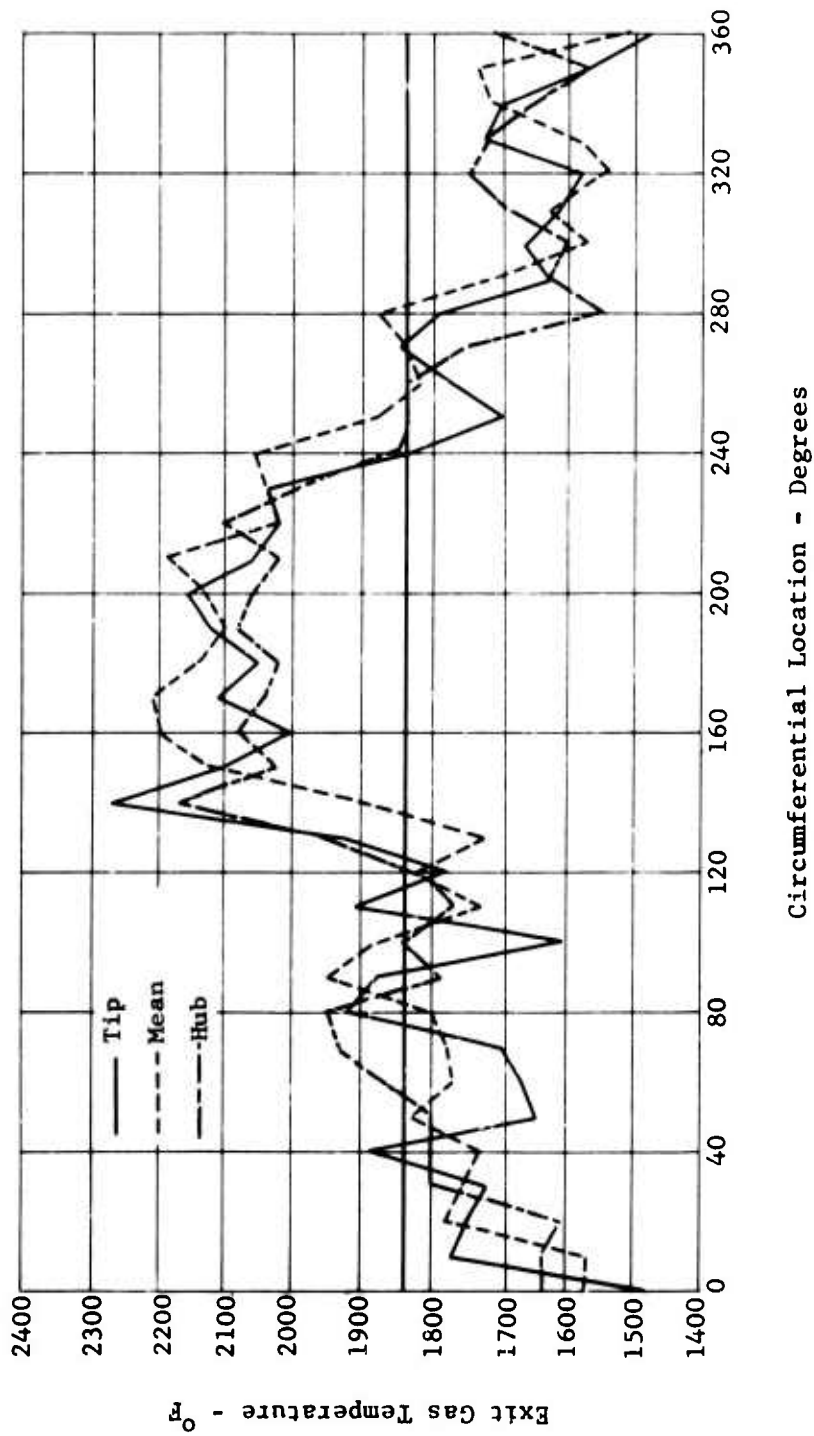


Figure 64. Circumferential Exit Temperature Profile.

Config. No 8, Data Point 7
 Build 9504-1-16
 F/A = .0284

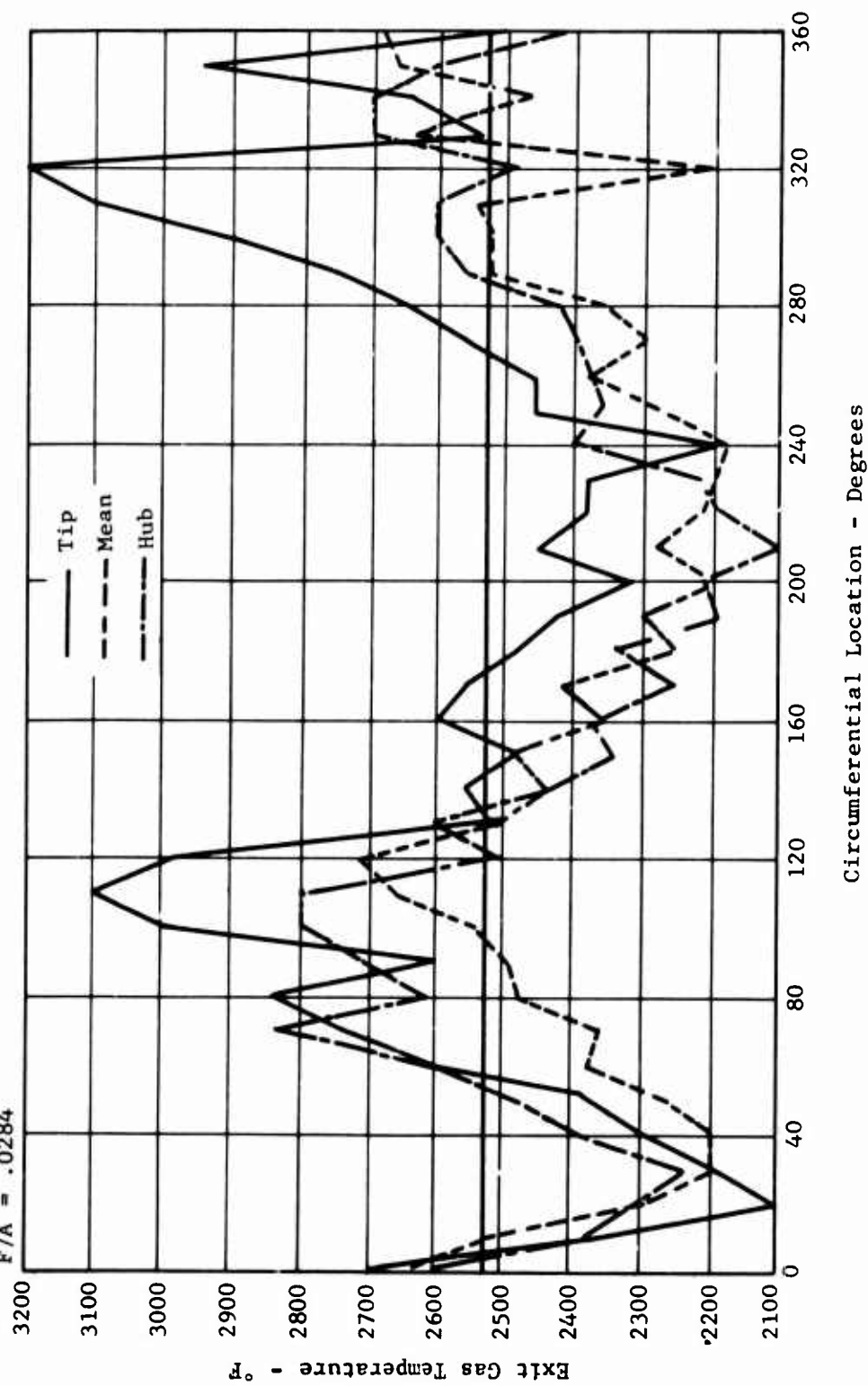


Figure 65. Circumferential Exit Temperature Profile.

Config. No. 8, Data Point 9
 Build 9404-1-16
 F/A = .0307

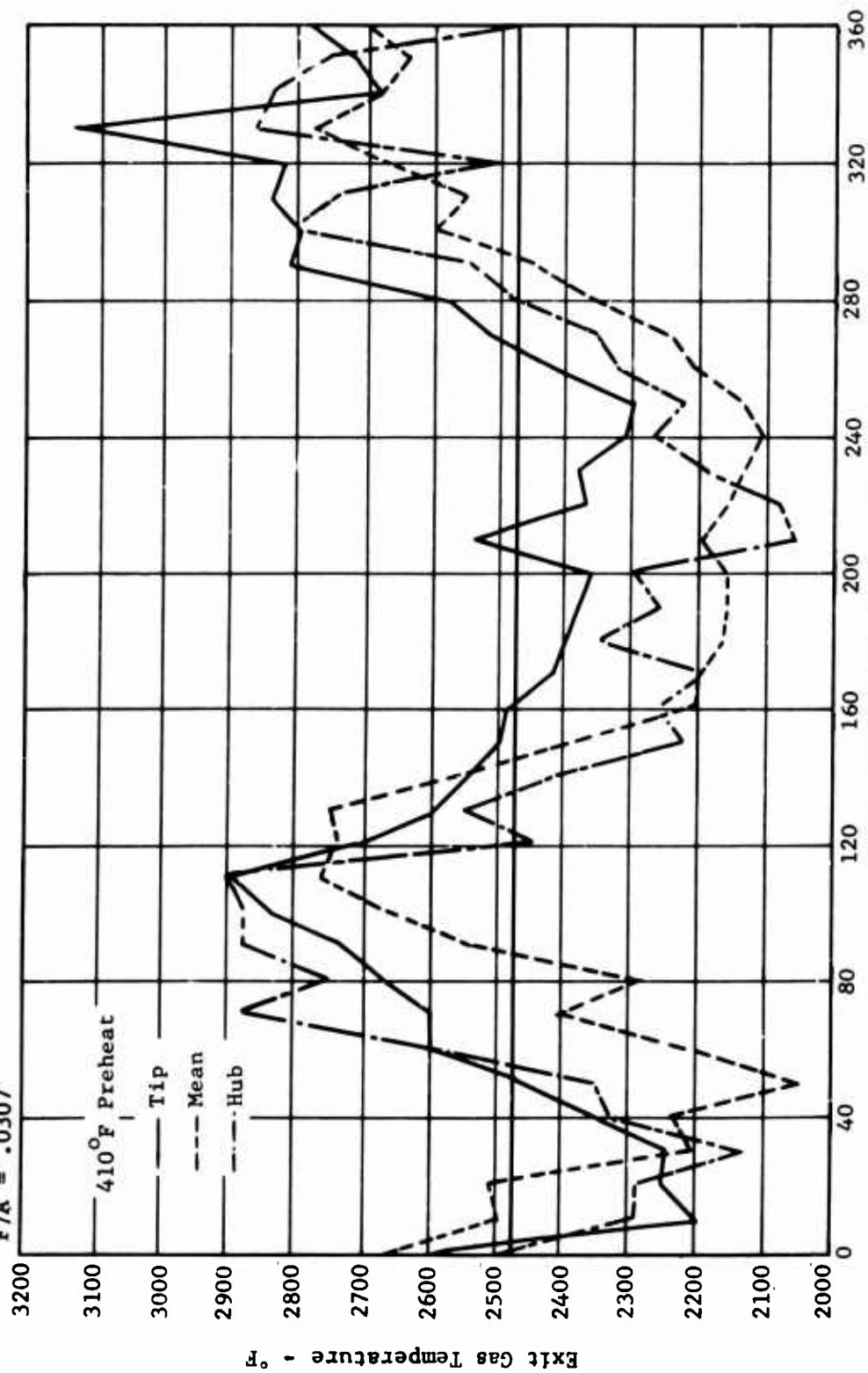


Figure 66. Circumferential Exit Temperature Profile.

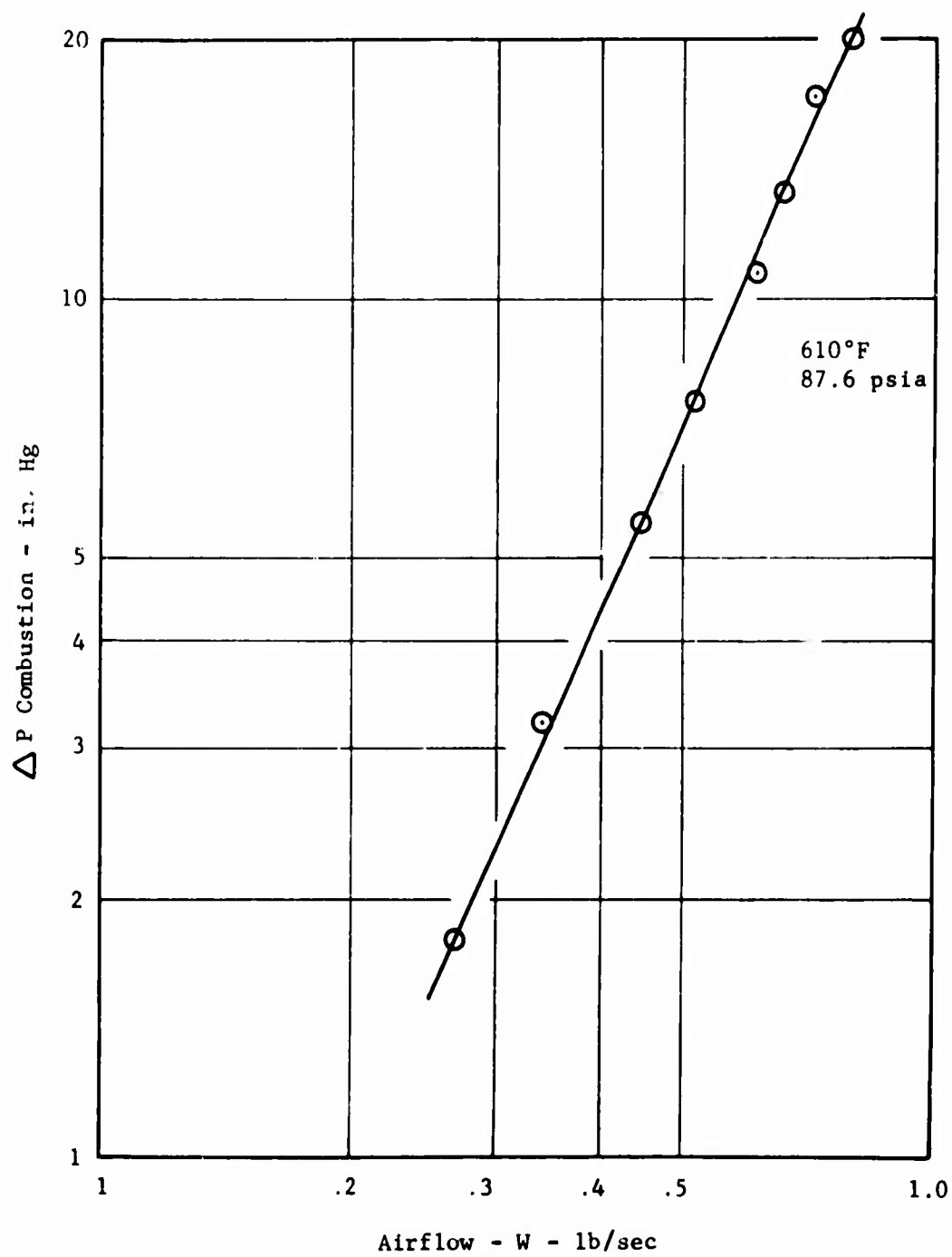


Figure 67. Vaporizer Calibration Curve.

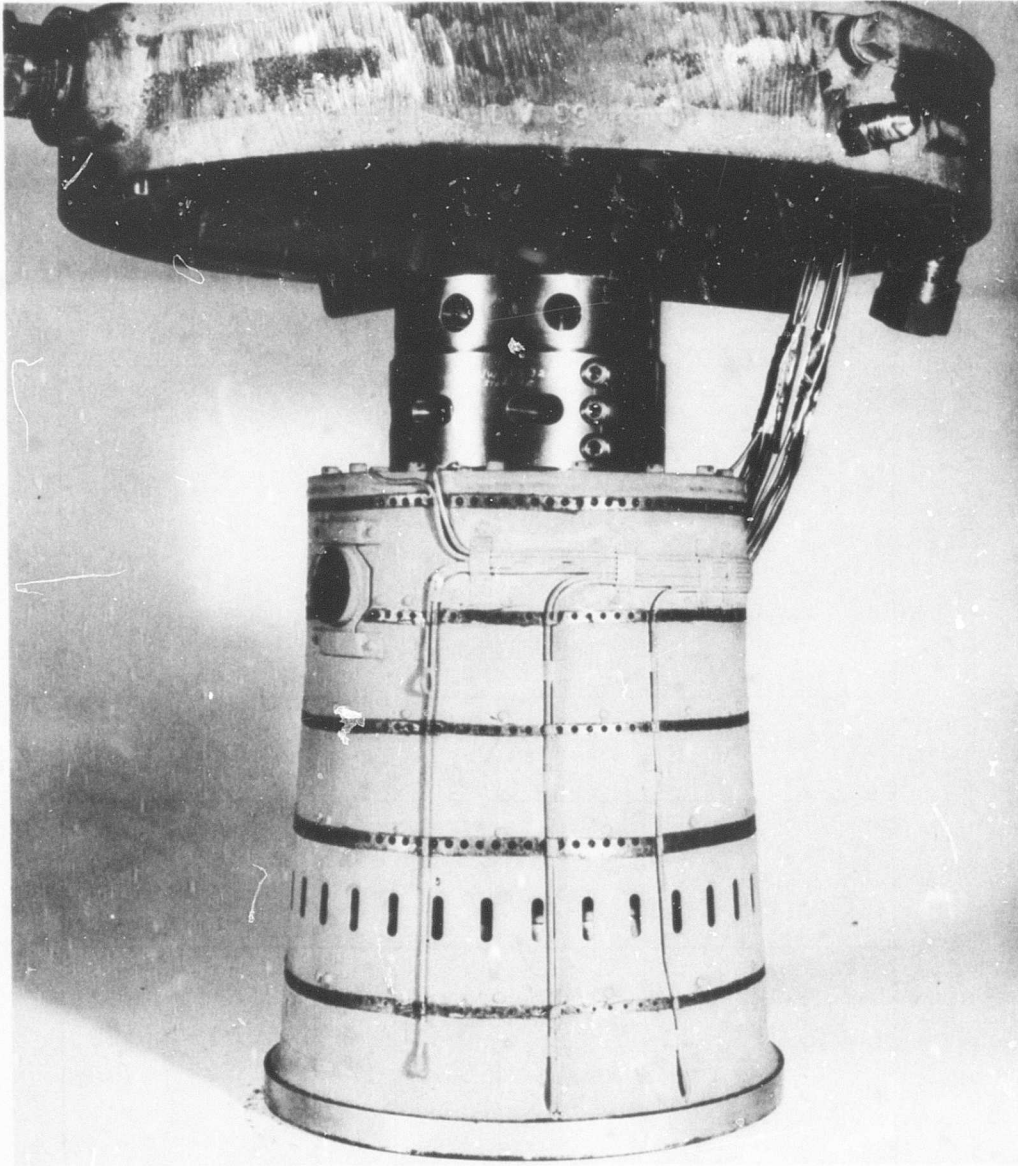


Figure 68. Combustor Rig Assembly.

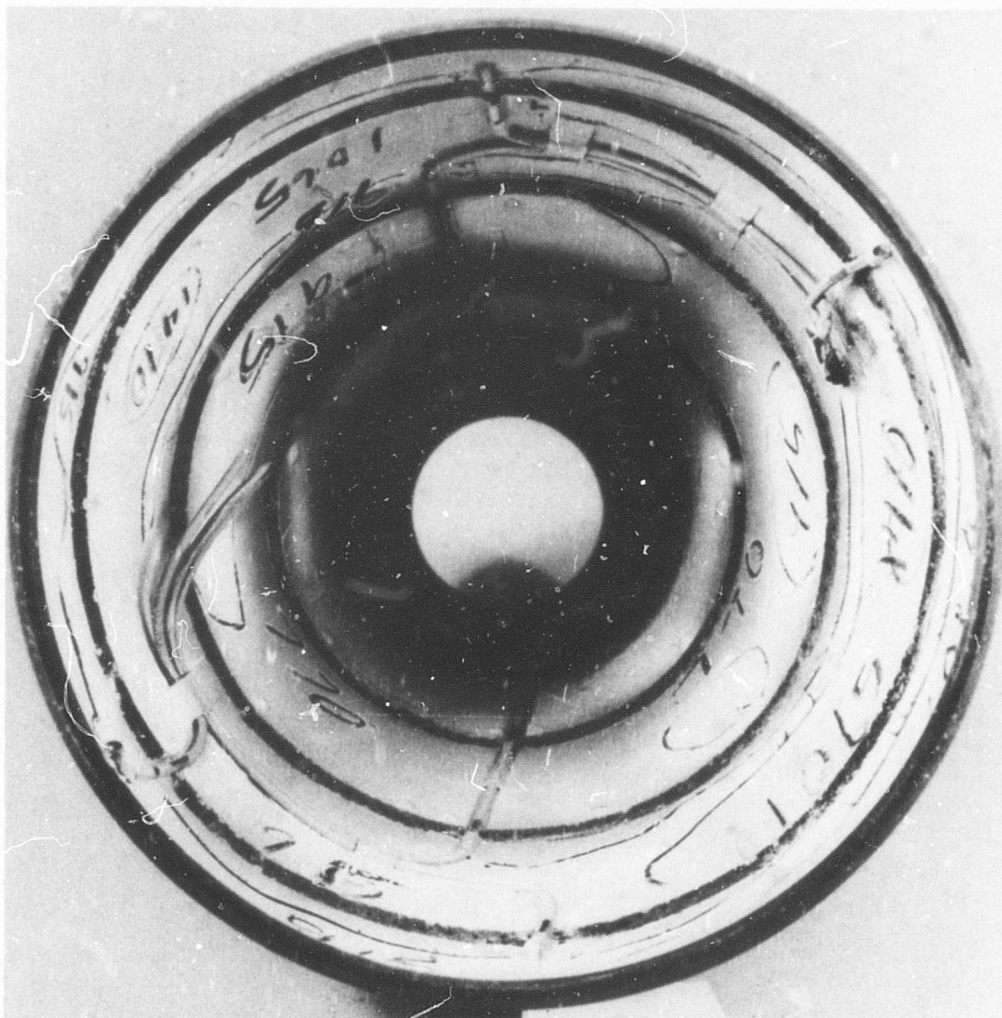


Figure 69. Inner Liner, Posttest.

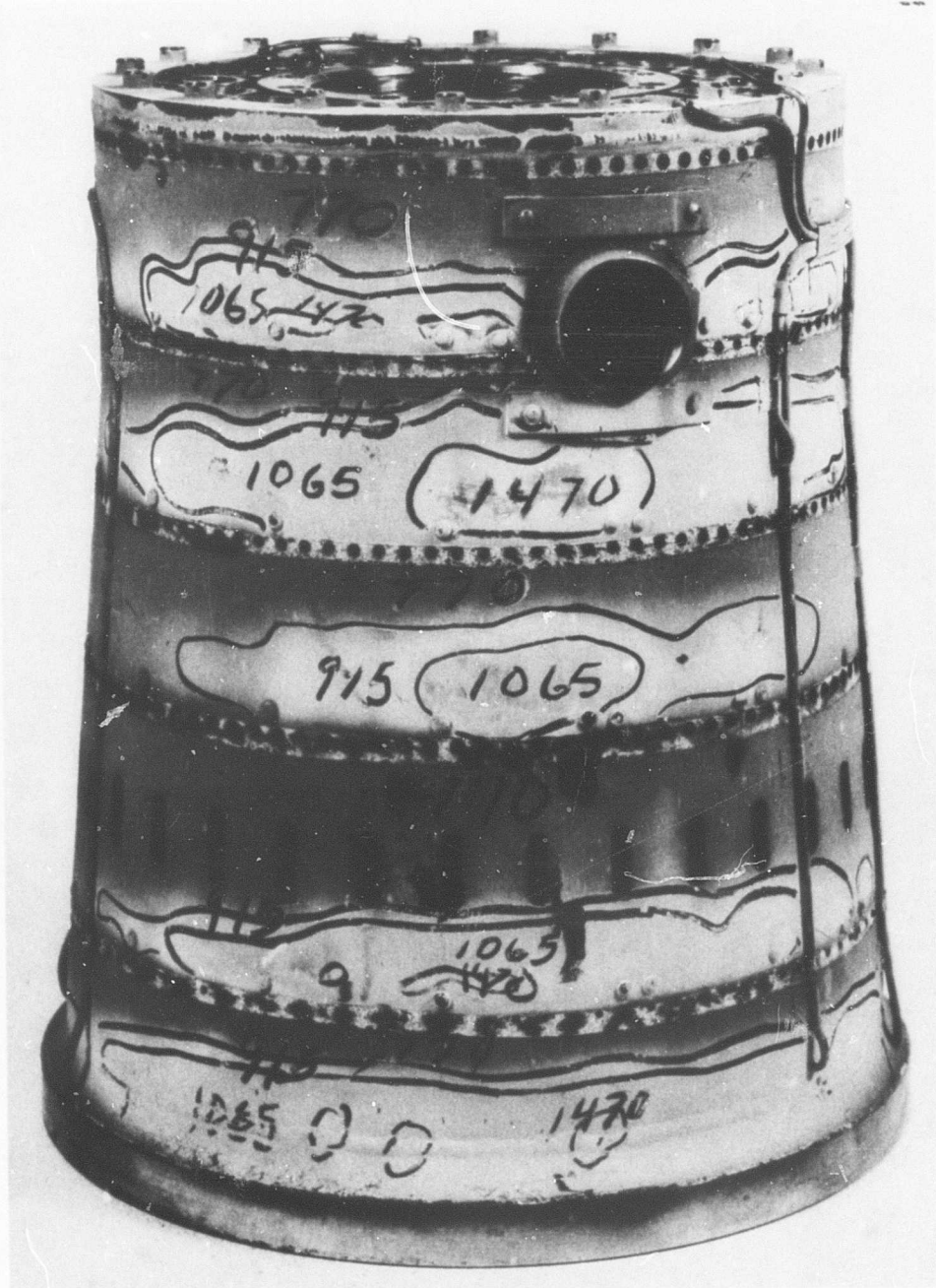


Figure 70. Outer Liner, Posttest

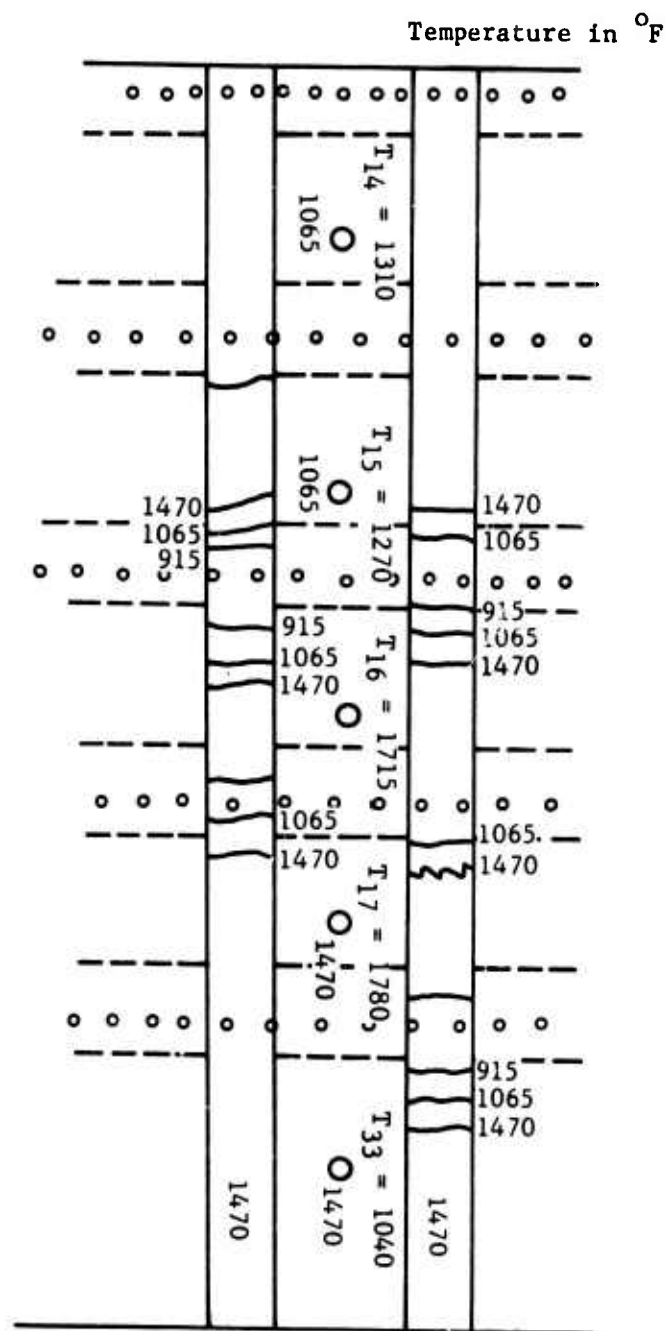


Figure 71. Outer Liner Schematic - Temperature Paint Evaluation.

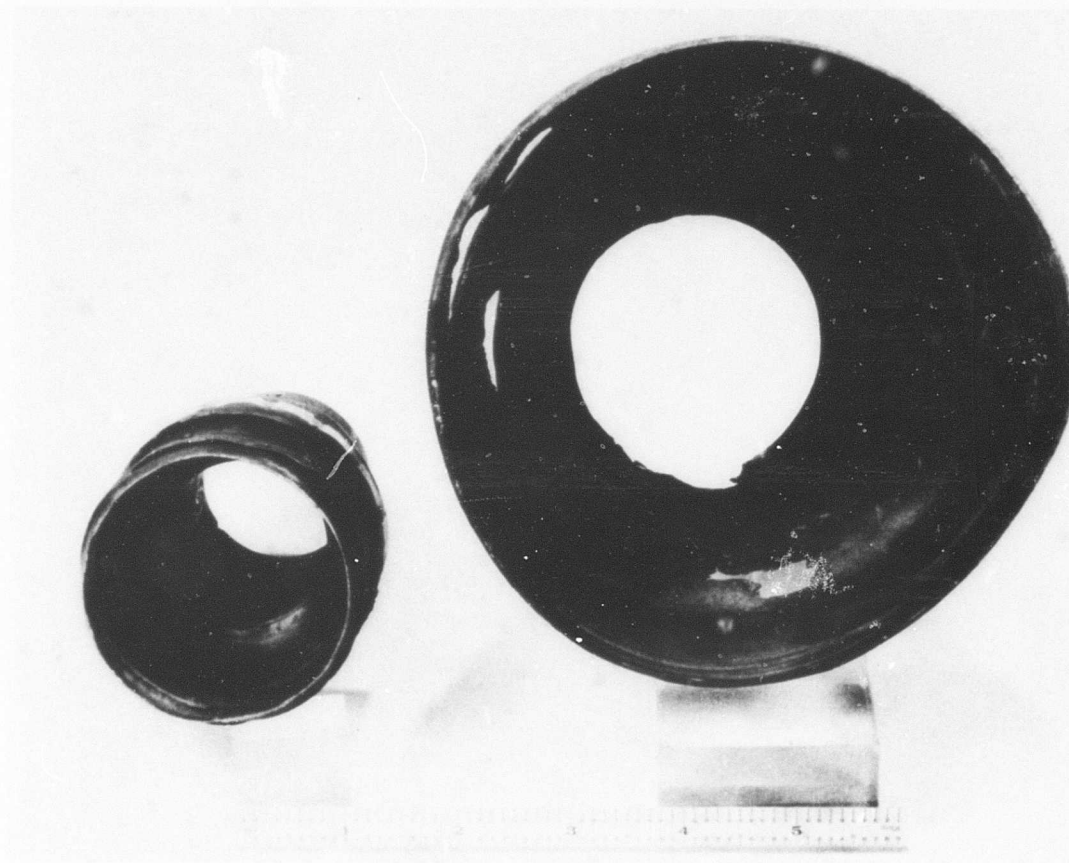


Figure 73. Combustor Inner Liner.

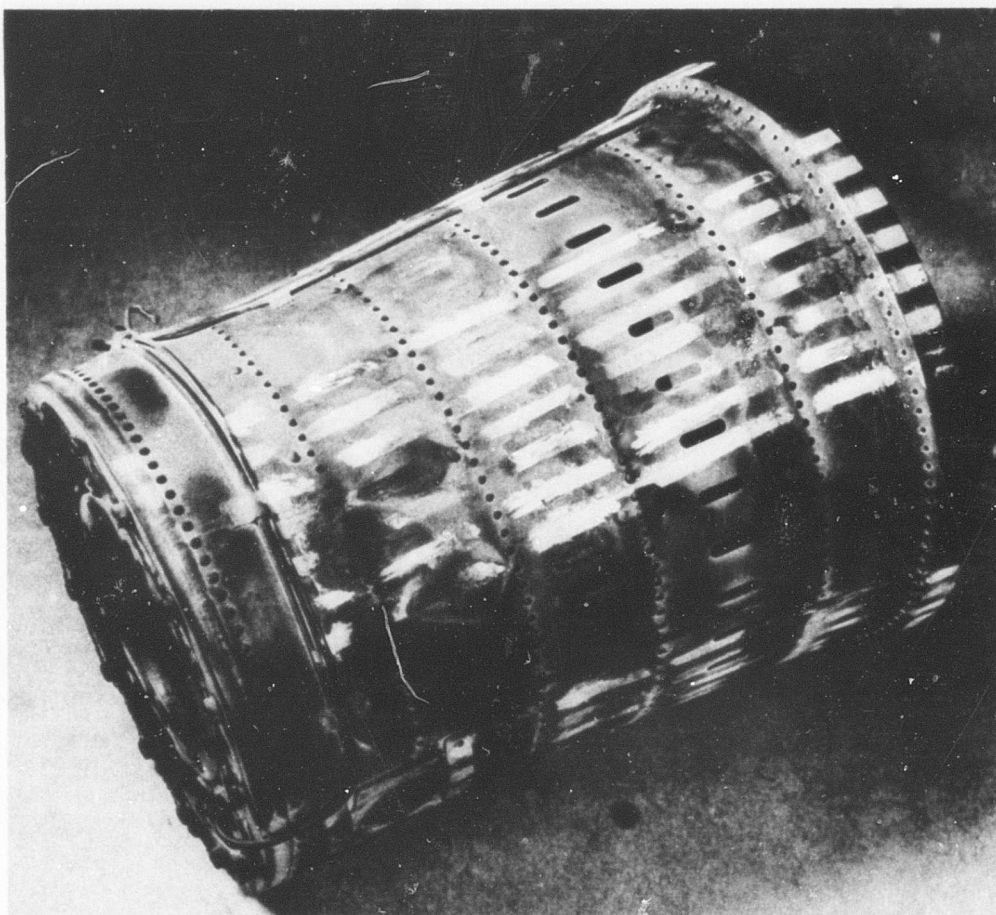


Figure 74. Combustor Liner - Side View.

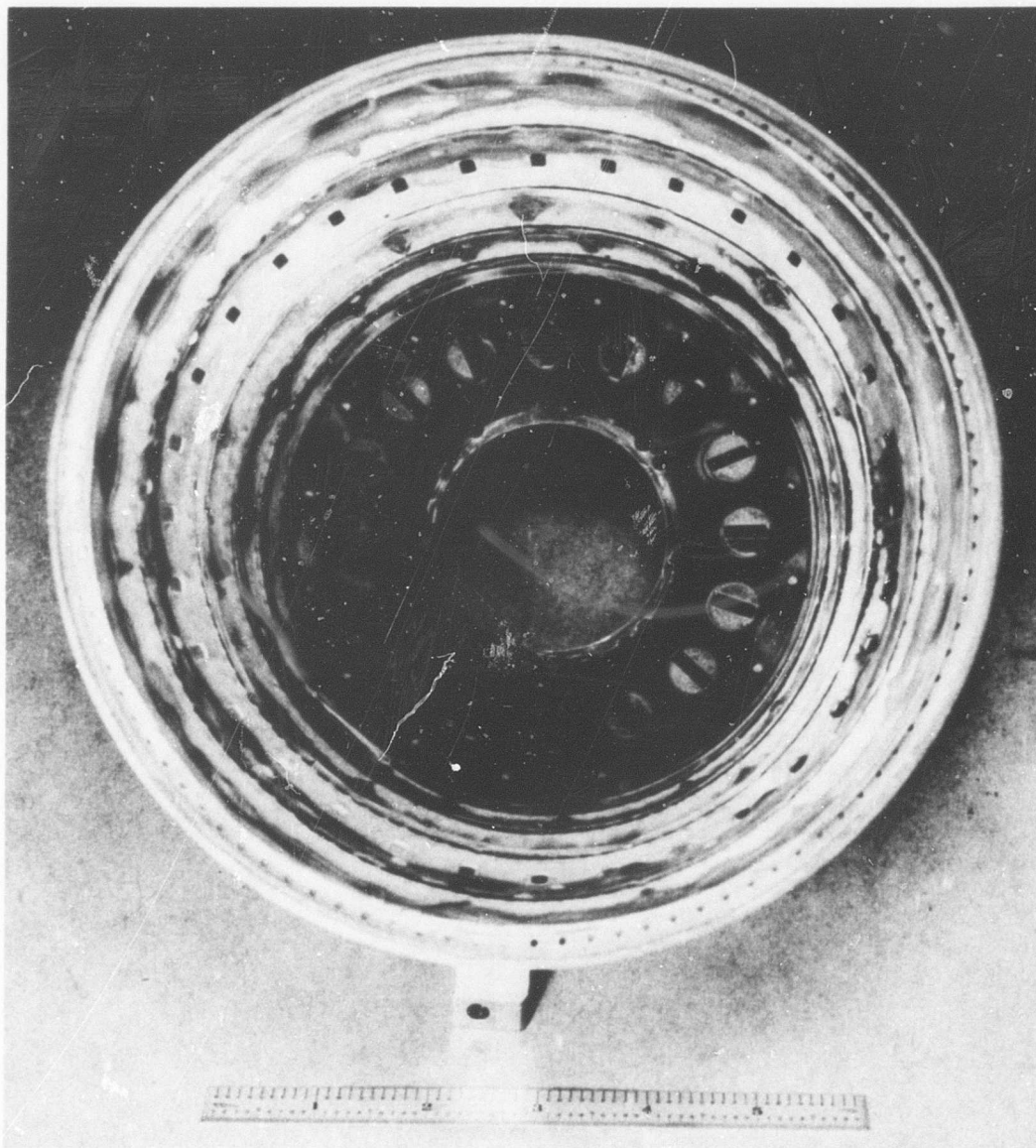


Figure 75. Combustor Outer Liner.



Figure 76. Combustor Headplate.

4.2 CASCADE TESTING

The objective for cascade testing this high temperature turbine stator was to evaluate the design in the following critical areas:

1. Determine stator blade metal temperatures when operated at design inlet conditions.
2. Determine cooling airflow distribution to the blades.
3. Determine the aerodynamic performance of the low aspect ratio transpiration cooled blades.
4. Determine durability of the blades and their associated housings, supports, shrouds, etc.

The cascade rig utilized for this program was the same hardware, including combustor, annular stator assembly, and exhaust duct used in the full-stage component rig; a spool piece and rotating probe section were substituted for the rotor section. Hot testing was conducted up to an average turbine inlet temperature of 2650°F with local temperatures in excess of 3300°F.

4.2.1 Turbine Temperatures

Figure 77 is a plot of the turbine inlet gas temperature and shows the location of the instrumented blades. The temperature profile shown was obtained during combustor testing. Since the combustor configuration did not change, the profile should not change. However, the fuel-air ratio run during the cascade testing was increased and the temperature scale was adjusted upward 100°F to locate the average fuel-air ratio for the profile coincident with the average as run. The position of the instrumented blades is included to show the effect of gas temperature on metal temperature. As can be seen, the maximum measured temperature was 1375°F at the blade trailing edge. This is well below the design value of 1550°F.

Table XIII compares two high temperature points of Build 6 and a high temperature point from the rotor test with respect to design values. The stator test run with successively higher coolant temperatures indicated that running the full turbine stage at the design point was feasible. The rotor point very nearly matched design requirements. Although the maximum gas temperature during the rotor test was 200 degrees higher than design, the maximum metal temperature was only 25 degrees higher. Blade condition after test was good, which also verifies the margin of safety of the design and the potential for high durability (Figure 77).

4.2.2 Cooling Airflow and Leakage Characteristics

The stator assembly was initially designed with removable blades to facilitate rework or replacement of blades for the experimental test rig. However, this configuration inherently created a serious leakage problem at the blade shelves. After the initial series of hot tests in which several

blade shelf seal arrangements were evaluated, the blade condition was found to be excellent. Since there was no need for modifications to the cooling flow distribution, the stator's shelves were butt welded together to form an integral assembly, thus eliminating the need for interblade shelf seals. The sealing evaluations are summarized in the following paragraphs.

Figure 78 presents the stator assembly cooling airflow characteristic as obtained from bench test flow checks. The design curve was established by individually flowing each blade from the assembly with all leakage paths sealed.

Table XIV summarizes the stator assembly configurations for sealing the interblade surfaces and the cooling air supply plenum at the base of the stator vanes. The data shown were obtained from bench flow checks. Data at 20 inch Hg plenum pressure are presented to demonstrate the evolution of sealing improvements with each configuration change. Category 1 initially incorporated a loosely woven Inconel ribbon for interblade seals. A 25 percent leakage reduction was effected through the addition of a high temperature resin filler material in the low solidity mesh. Further (12 percent) reduction in leakage was observed with the use of a more densely woven Inconel mesh seal. The cooling air supply plenum at the stator vane base used piston ring radial seals. Viton A seals were substituted for the ring seals for the low temperature (aerodynamic) cascade testing. A 53 percent reduction in leakage was shown for that configuration and indicated that the leakage was apparently split evenly between the interblade and the plenum joints. Category 2 utilizing Vitrium fiber glass stranded seal at both joints, showed further reduction (about 24 percent - 38 percent) in leakage from the Build 1 configuration.

Category 3 incorporates the integrally welded stator assembly which provides:

1. Butt welded blade shelves which preclude interblade leakage.
2. Axial fiber glass seals for the plenum.

This provided reduction in leakage of 61 percent - 86 percent as compared with the best of Category 2. This welded configuration (Figure 79) was successfully used for the final stator high temperature tests on the stator cascade and the full-stage rig.

Figure 80 shows the typical test results of a bench flow test performed on individual blades. The curves show the flow characteristics of each coolant flow passage. Variations from the design value are attributed to tolerances in machining the cooling air metering orifice size and/or local variation in mesh permeability. Figure 81 shows the total blade flow characteristics. All blades tested plotted within 10 percent of the design curve.

4.2.3 Aerodynamic Performance

Initial aerodynamic cascade tests were confined to performance measurement at the mid-height radius of the blades. The resulting relatively high performance of the stator was inconsistent with the level of performance measured in the turbine full-stage rig. Further cascade surveys were made at nine radial locations covering the full 360-degree circumference in the turbine annulus.

Figure 82 shows the stator cascade performance at mid-height incorporating both the initial and the later test results. Figures 83, 84, and 85 show the blade performance at the nine radial locations when the cascade was operated at three different pressure ratios and cooling airflow percentages.

Figures 86, 87, and 88 are actual data traces obtained at the mid-height location as the probe surveyed 360 degrees circumferentially in the annulus at the rotor inlet plane. The traces show the difference between stator inlet total pressure and stator outlet pressure or loss in total pressure between inlet and outlet. The loss area was integrated and the average ΔP_T loss was obtained. The ΔP_T loss for 0 percent, 4 percent, and 8 percent cooling air is 2.3, 2.5, and 2.4 inches of mercury respectively. Since the inlet pressure to the stator was constant, the ΔP_T loss is a measure of the blade row efficiency; it can be seen that cooling air has little effect on mid-height blade performance. The width of each peak or valley is essentially the same, indicating that additional cooling air does not cause increased width of wake; hence, no significant increase in wake mixing losses and no separation effects.

The cascade data were integrated as indicated above for each pressure ratio at each radius and for each percentage cooling air.

It is evident from Figures 83, 84, and 85 that the performance deteriorates very rapidly from mean radius towards the hub, resulting in average loss coefficients twice as high as those at mean radius. This was true over a range of pressure ratios as shown in Figure 89. Combustor liner cooling air deflectors, shown in Figure 90, were suspected of contributing adversely to the root performance of the stator, in addition to producing some flow restriction. To determine the effects of these deflectors, complete radial surveys were conducted in two different builds, one with and one without the deflectors installed.

Figures 84 and 85 show that the deflectors did not have any measurable effect on stator performance.

Figure 91 presents the variation of stator performance with cooling flows at tip (90 percent height from internal diameter), mean (50 percent blade height), and hub (10 percent height from internal diameter) as well as the area averaged performance. The effect of cooling flow is shown to be insignificant at tip and mean with noticeable effect at the hub. The

variation of performance with pressure ratio is shown in Figure 92. The efficiency is essentially constant at tip and mean but again decreases at hub with increasing pressure ratio. These results indicate that the effect of cooling flow on loss coefficient and flow coefficient is very small when the flow is not separated as at tip and mean. This is consistent with other transpiration blade cascade tests. The hub deficiency indicates strong secondary flows from tip to hub, resulting in the accumulation of cores of low energy boundary-layer flow at the hub and consequent flow separation. The separation could also have been aggravated by the adverse hub streamline curvature when the flow becomes unguided along the overhang portion of the suction side of the hub as shown in Figure 90. It was concluded that the low level of stator performance degraded the entire stage performance.

4.2.4 Instrumentation

For the stator vane cascade aerodynamic evaluation, instrumentation was installed to allow for evaluation of the loss coefficient. The coefficient was determined .050 and .550 inch downstream of the trailing edge (TE), the latter being the rotor blade leading-edge plane. Inner and outer diameter wall static taps were installed in each of these planes (Figures 93 and 94).

Inlet total pressures were measured by two fixed 3-element rakes and one fixed 9-element rake; the 3-element rakes were 120 degrees apart with the 9-element probe at the top (Figure 95). The 9-element rake had probe heads .020 inch from the inner and outer wall with .020 inch radial space between probes to detect any boundary effect on the inlet profile.

Outlet total pressures were measured by 18 Kiel probes (9 at each plane) mounted on a ring which could rotate 360 degrees (Figure 96). The 9 probes are radially positioned at equidistance (.053 inch) to cover the .536-inch annulus height and are circumferentially located at equiangular(s) position.

The heads of the Kiel probes were fixed and set at design outlet gas angle. The gas deviations were not large, and Kiel probes yield true pressure readings when aligned to ± 20 degrees with the flow. Figure 97 shows the driving mechanism and an early 6-element survey instrument.

Transducers reading pressure differential supplied an electrical signal to an X-Y plotter providing a continuous plot of pressure difference for each of the 18 outlet total pressure probes versus the full 360-degree circumferential travel.

A self-balancing yaw probe was used to make qualitative checks of the 18 probe survey instrument. This probe was fixed in a circumferential location (30 degrees) but could traverse in and out radially from root to tip.

4.2.5 Stator Durability

Stator testing consisted of eight builds and tests. Of these, four were with the main burner in operation. An annotated test summary is presented in the Appendix (Table XXV). Builds 1, 2, 7, and 8 were aerodynamic evaluations. Builds 3, 4, and 5 were directed at seal development to obtain adequate blade sealing. Build 6 was the final evaluation of cooling air and thermal design.

The hot test times at various turbine inlet temperatures are listed below. In addition to the time during stator testing, a listing must be made for the time accumulated during rotor testing. Both of these times and the totals are shown in Table XII. Condition of the stator blades after the full-stage hot testing is shown in Section 4.3.2.

TABLE XII STATOR AND ROTOR HOT TEST TIMES			
Turbine Inlet Temperature Range (avg) - °F	Hours		
	Stator	Rotor	Total
1000 - 1600	9.83	8.75	18.58
1600 - 2200	11.50	5.42	16.92
2200 - 2400	2.92	4.33	7.25
2400 - 2650	1.17	2.00	3.17

Because of the combustor exit temperature ratio, T_{\max}/T_0 , of 1.23, some of the blades were above the average temperatures listed. Since the profile peaks around the 90-degree circumferential location, blades in that vicinity were instrumented for strut temperatures. These measured strut temperatures never exceeded design, even though design maximum value was based on a temperature ratio of 1.135. Figure 77 shows the gas temperature and metal temperatures at maximum conditions as related to design during Build 6, which was the final hot stator test to evaluate stator durability. Table XIII compares the design and actual stator blade metal temperatures for Builds 5 and 6 at specific locations on the blade.

Modifications for Improved Cooling

The major damage that occurred during hot cascade testing was the burning of the outer shelf. To prevent this, further cooling air was introduced around the periphery of the stator inlet by means of one hundred .070-inch diameter holes as shown in Figure 98. This increase in cooling flow was only 2 percent of the total liner and had negligible effect on the overall combustor airflow distribution.

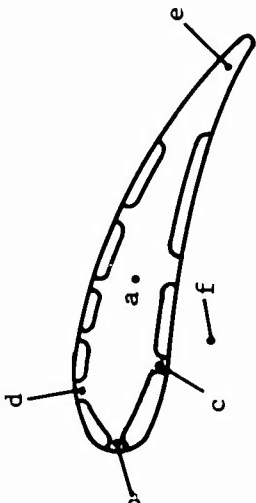
TABLE XIII COMPARISON OF DESIGN AND ACTUAL STATOR BLADE TEMPERATURES				
Point	Stator Build 6 Point 12	Stator Build 6 Point 13	Rotor Build 5 Point 12	Design
Average TIT - °F	2650	2460	2585	2580
Max TIT at 90 degrees - °F	3270	3040	3190	2980
Max TIT - °F	3365	3132	3285	2980
Percent Stator Coolant Flow	11.2	9.7	6.5	6.2
Average Coolant Temp - °F	166	343	580	610
Metal Temperatures - °F				
a. Spar	640 - 575	740 - 675	855	1220
b. Leading-Edge Land	810	860	1100E	1540
c. First Pressure Side Land	545	690	920E	1240
d. First Suction Side Land	1065 - 835	855 - 675	1075E	1290
e. Trailing Edge	1375 - 1140	1325 - 1135	1525 - 1300	1550
f. Outer Shelf	1240 - 1150	1240 - 875	1050	1350
				
E = estimated				

TABLE XIV TURBINE STATOR SEALING CONFIGURATIONS										
Category	Description	Build No.	Seal Configuration Interblade	Plenum	Percent Leakage Flow = Total -Design (at Ambient External Pressure) Plenum Pressure					
					20 inch	30 inch	40 inch			
					Hg	Hg	Hg			
1	Individual stator blades with spring-loaded ring seals - Inconel mesh seals		Low solidity mesh	Piston Ring	140					
			Low solidity mesh with filler	Piston Ring	105					
		1	High solidity mesh	Piston Ring	92					
2	Individual stator blades with spring-loaded ring seals - fiber glass mesh seals (Vitrinum)	2	High solidity mesh	Viton A Ring Seal	43					
		3-4	Vitrinum	Vitrinum	70	78				
		5-6	Vitrinum	Vitrinum	57	71				
3	Welded stator assembly with axial ring seal	7-8	Welded	Vitrinum	22	25	30			
		Rotor Build 3	Welded	Vitrinum	8	13	17			

The testing revealed another requirement: the need to seal the outer shelf of the stators. Good sealing was required to ensure that the combustor inlet air (610°F) is bled for stator shelf cooling and to prevent influx of hot combustion gas into the cooling flow. The outer diameter seals were developed in the following sequence:

1. Solid piston ring-type seals.
2. Solid piston ring-type seals backed by expander springs.
3. Ground piston ring-type seals with expander springs and grooves filled with Inconel mesh or fiber glass Vitrium packing.
4. Beveled solid rings with Inconel mesh and Vitrium.

Figure 99 shows the optimum flow possible using Viton A seals (for low temperature operation only) and the best hot configuration, viz., Inconel mesh seals and rings as in item 4.

Transpiration Skin Configurations

Two types of transpiration skins were evaluated, N-155 and Nichrome V Cb material. From previous tests, the Nichrome V Cb skin was considered to have superior high temperature oxidation resistance and ductility. Testing on these two materials was continued into Phase II in an attempt to corroborate the previous observations and to accumulate comparative data.

During the complete stage high temperature demonstration run as well as during the hot stator cascade testing, blades of the two skin materials were evaluated side by side. No visible difference was noted in the appearance of these blades. Consequently, the controlled laboratory tests became the main criterion of oxidation resistance and ductility. Therefore, the Nichrome V Cb material would be the candidate material used for any future transpiration skin material.

4.3 TURBINE COMPONENT TESTING

A transpiration cooled, single stage, axial flow turbine was designed having the following characteristics: inlet temperature of 2500°F, high work (140 Btu/per pound), and low airflow (4 pounds per second). The complete aerodynamic design criteria are set forth in Volume I and were used for the Phase II final design of the turbine component. Whereas the turbine was designed to demonstrate the feasibility of operating a high work transpiration cooled turbine blade design at 2500°F gas temperature, some compromise to the blade aerodynamics was effected to ensure safe operating margins for cooling and stress. Furthermore, thorough consideration was given to the fabrication aspects of this small blade design in order to be consistent with the level of transpiration cooled blade manufacturing technology available at the time. Thus, the turbine aerodynamic testing was

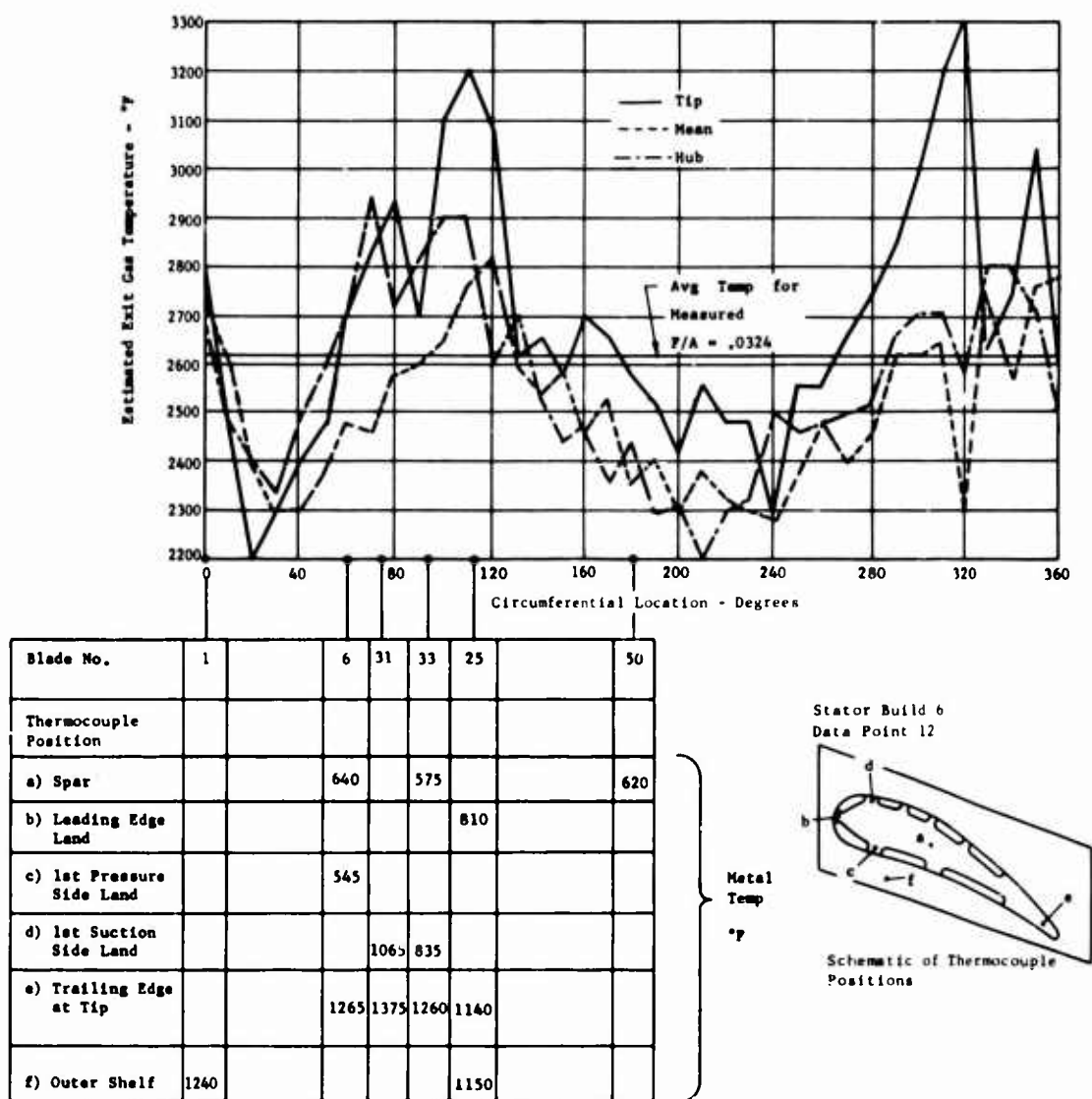


Figure 77. Turbine Gas and Blade Metal Temperature Distribution.

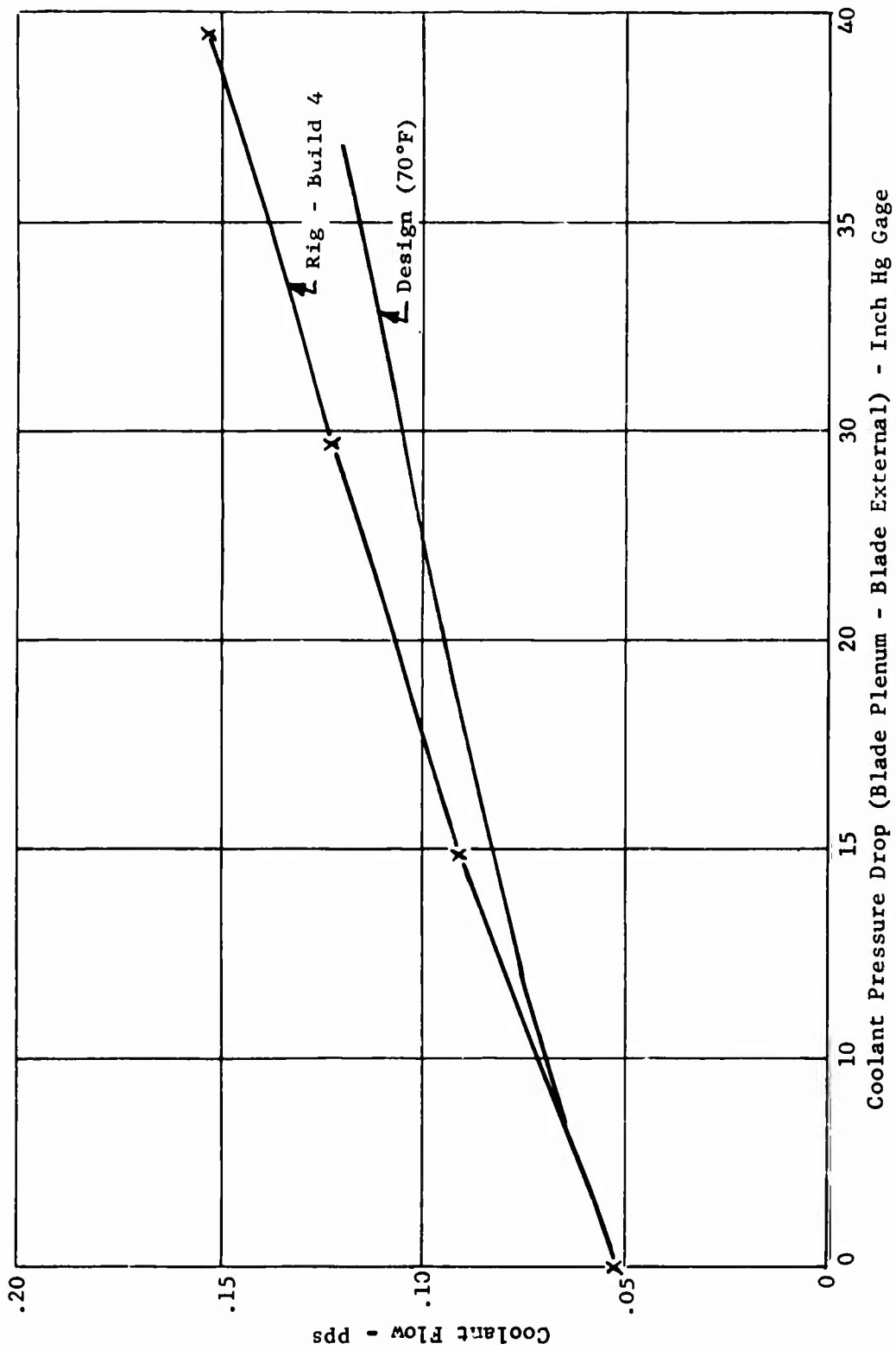


Figure 78. Turbine Stator Cooling Flow Characteristics.

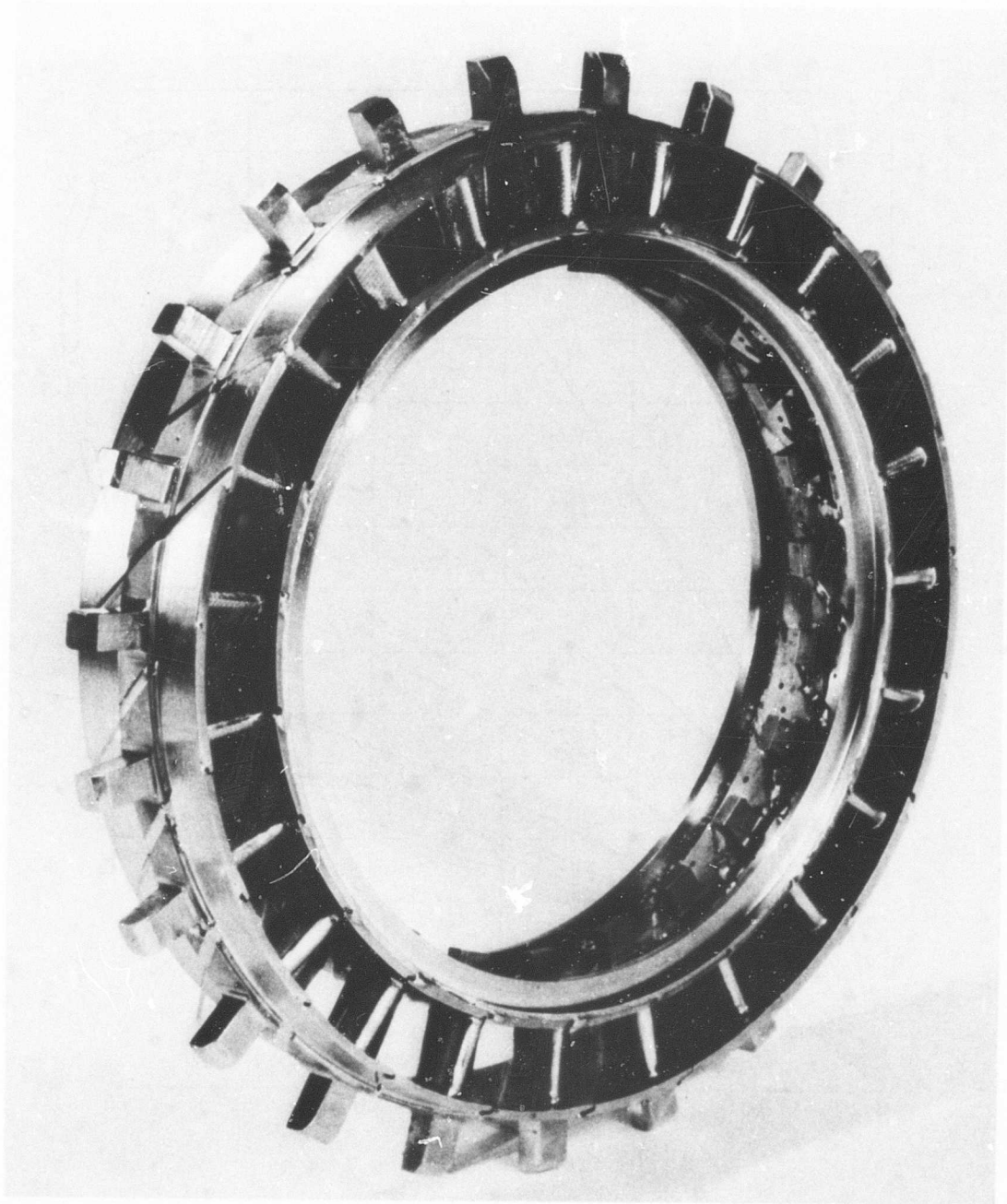


Figure 79. Welded Stator Assembly - Front View.

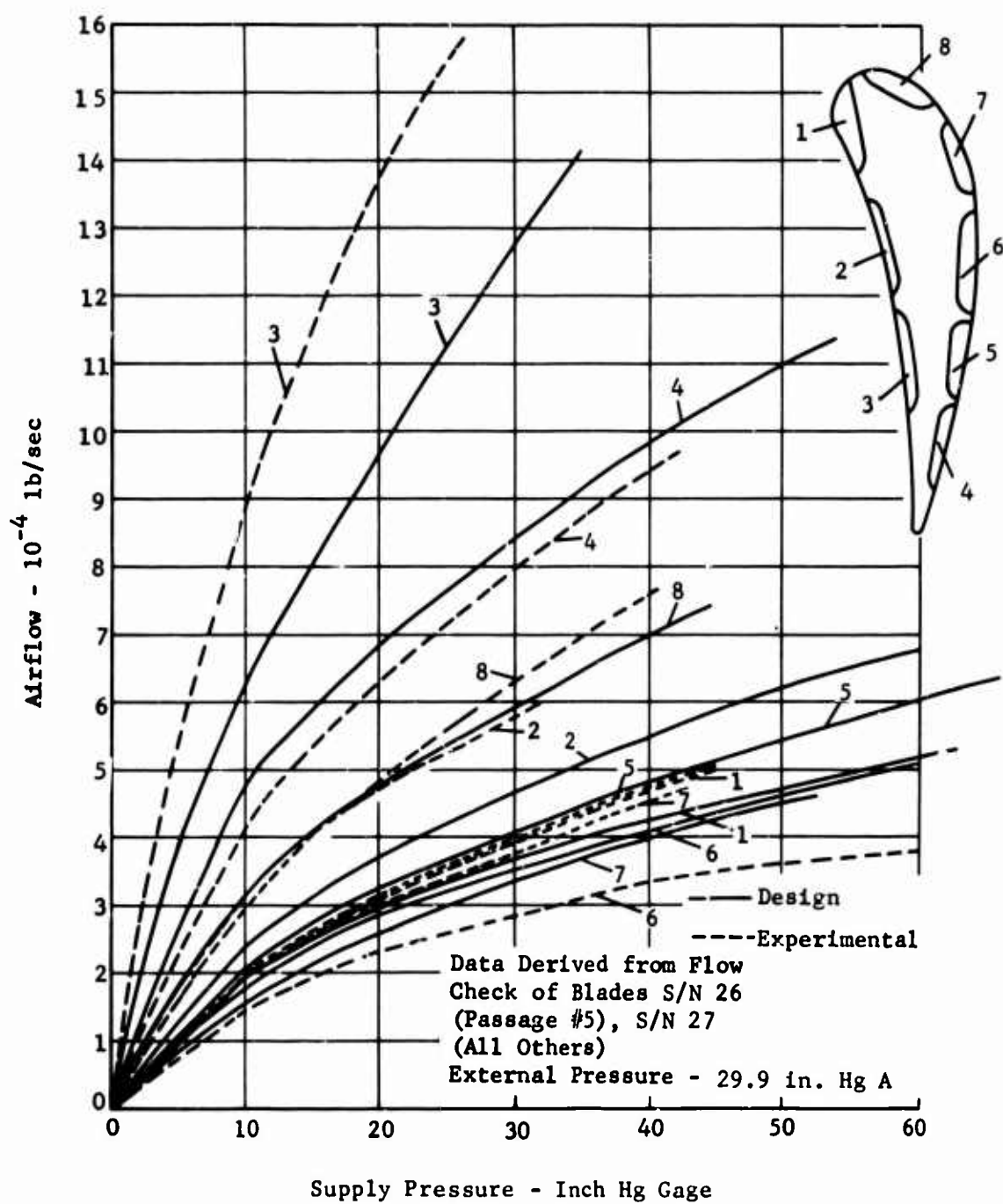


Figure 80. Turbine Stator Vane - Individual Channel Flow.

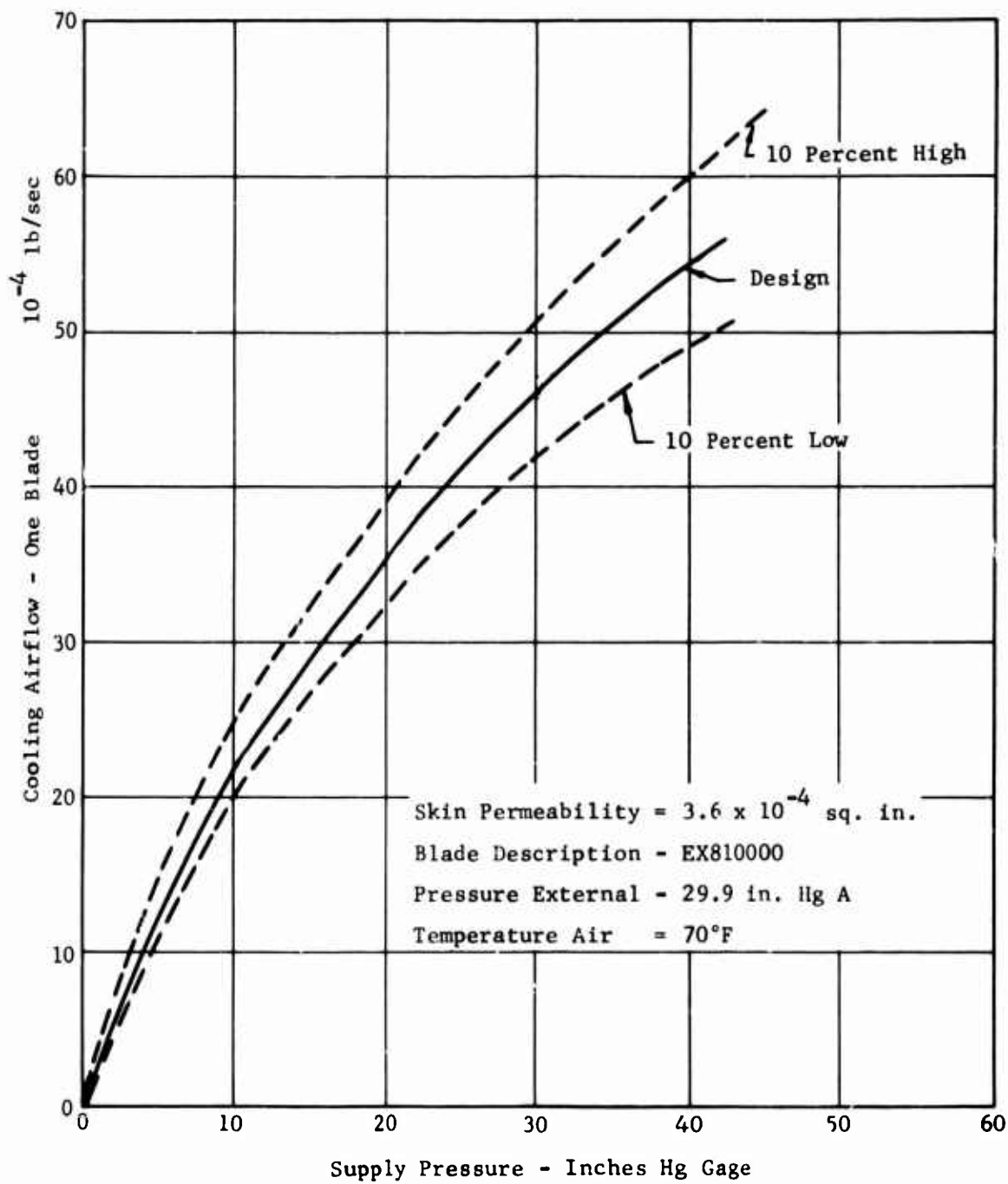


Figure 81. Stator Blade Cooling Airflow Single Blades.

Rigs 9404-2,Builds 2,6,7,8

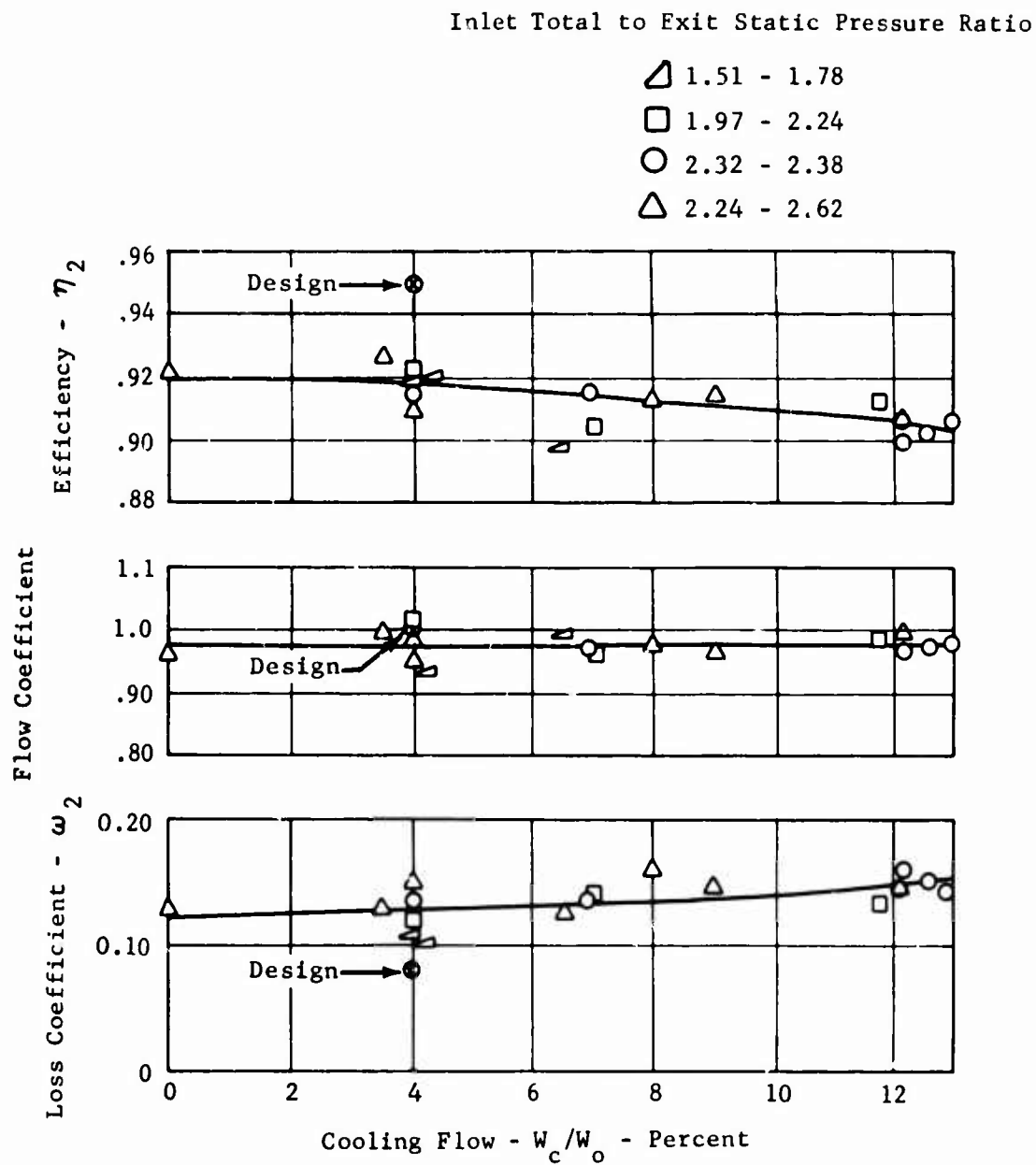


Figure 82. Stator Mid-Height Cascade Test Results.

Rig 9404-2-7 With Cooling Air Deflectors

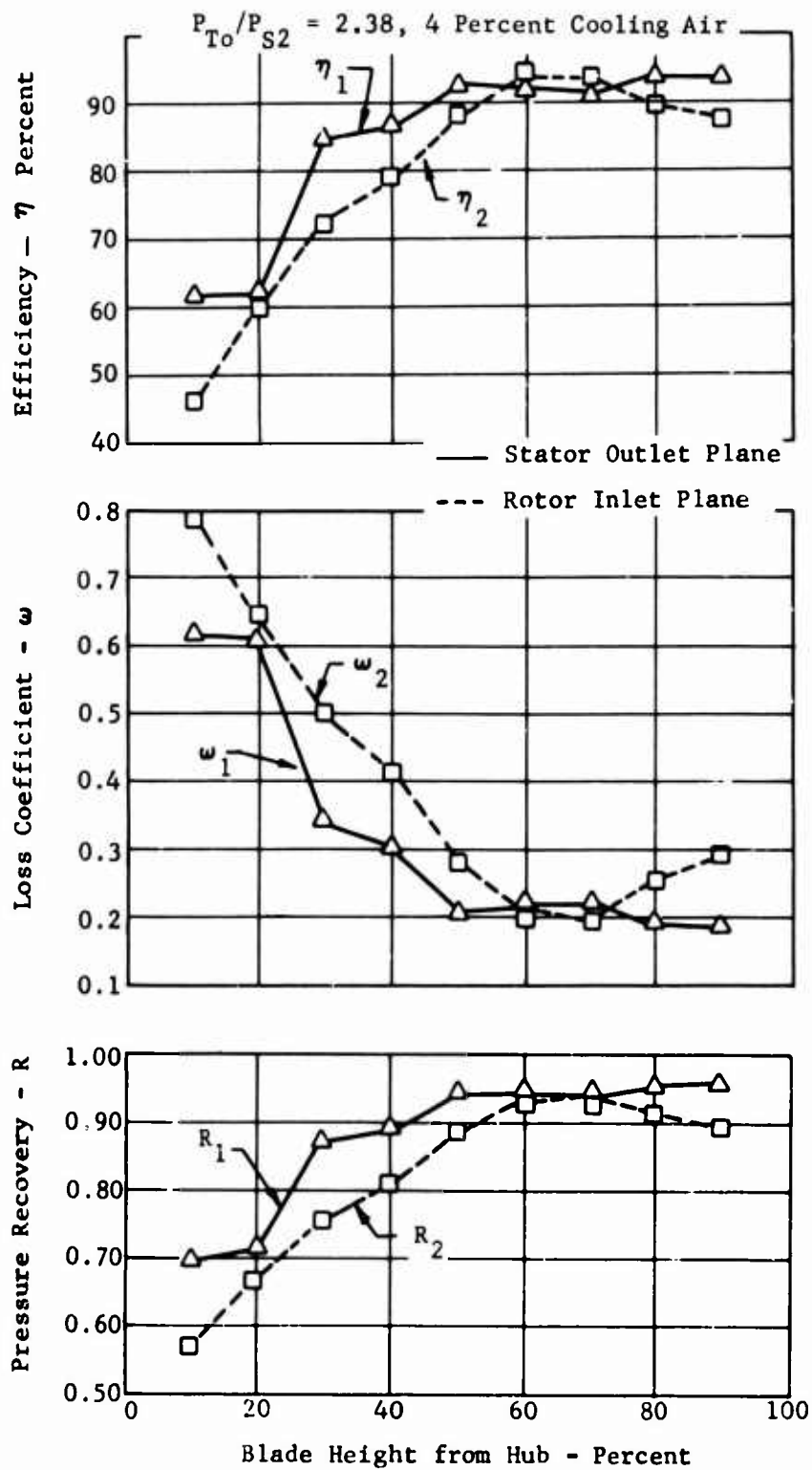


Figure 83. Stator Cascade Test Results.

Rig 9404-2-7 With Cooling Air Deflectors

$P_{T1}/P_{S2} = 2.42$, 9 Percent Cooling Air

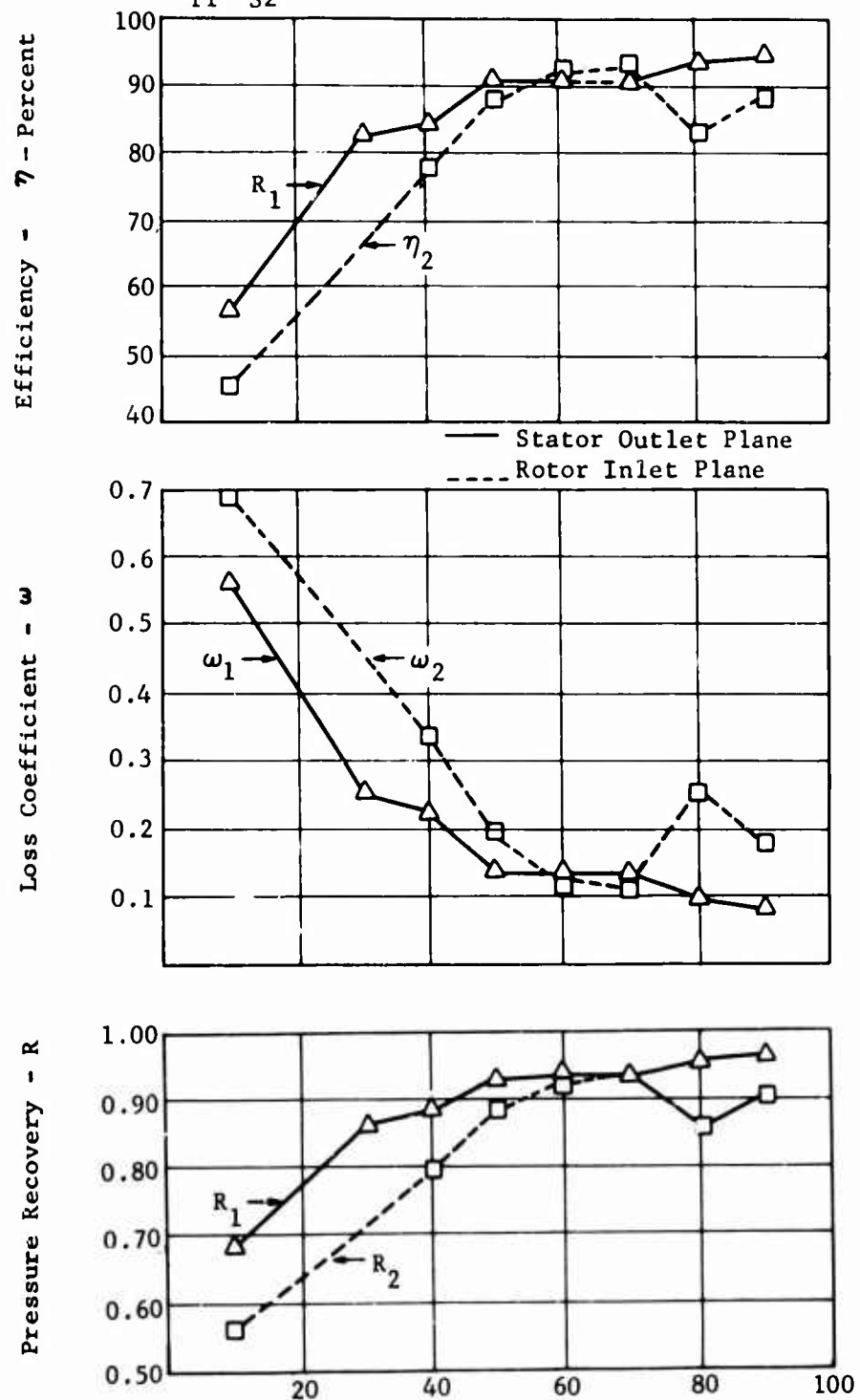


Figure 84. Stator Cascade Test Results.

Rig 9404-2-8 Without Cooling Air Deflectors

$P_{To}/P_{S2} = 2.62$, 8 Percent Cooling Air

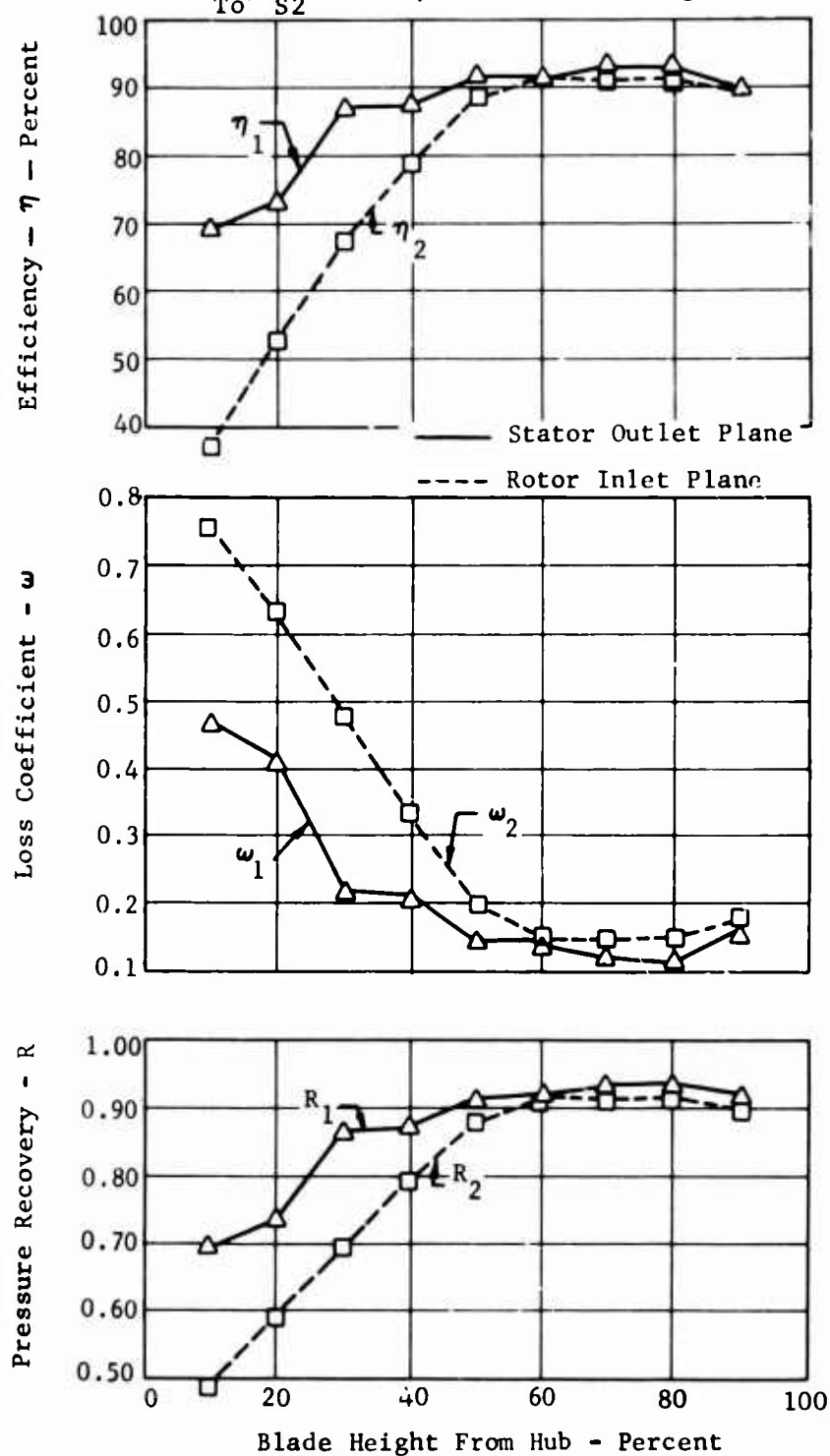


Figure 85. Stator Cascade Test Results.

Run No. 18, Point No. 14
 Average Loss Height = 2.295 Inches

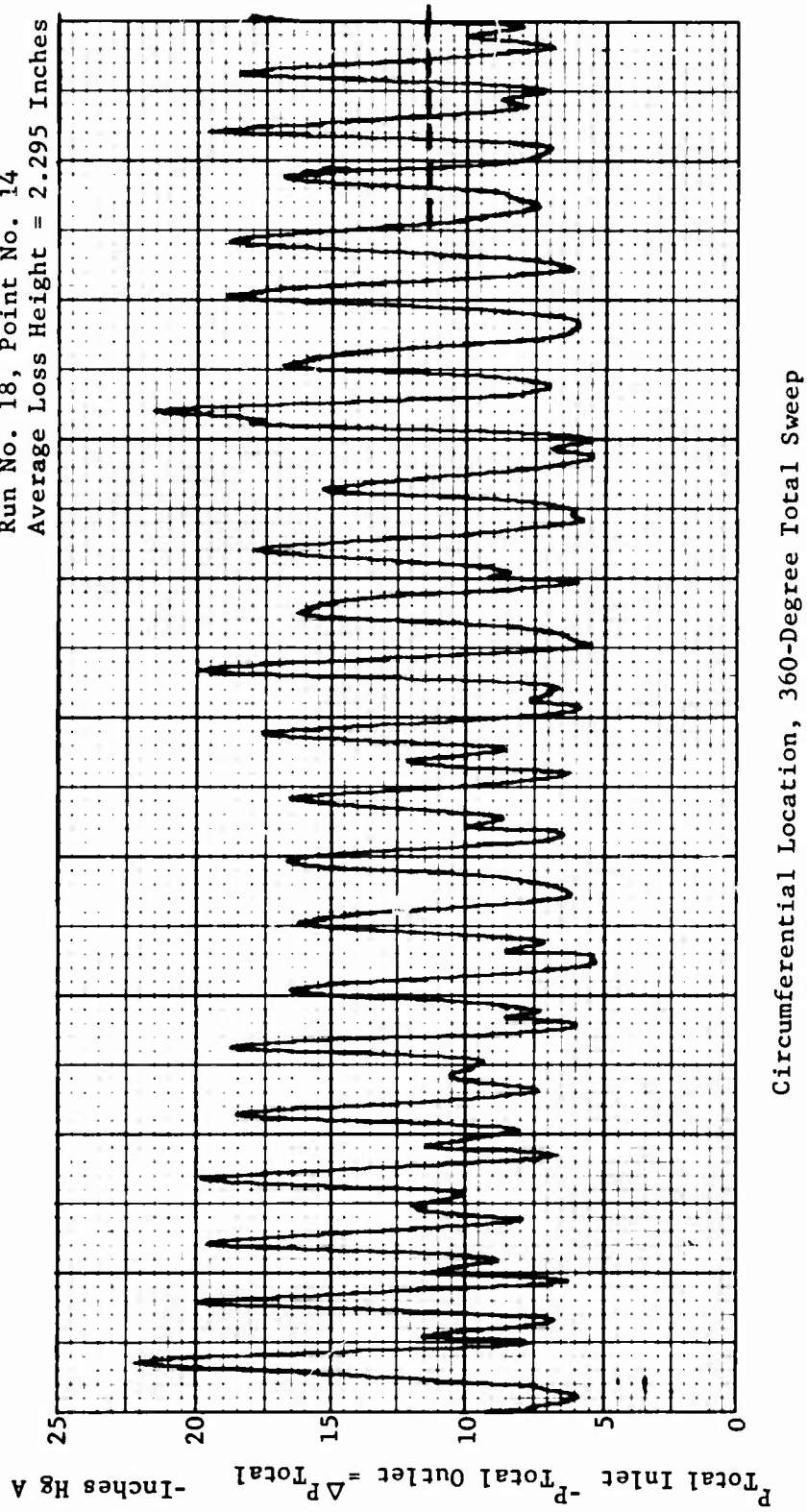
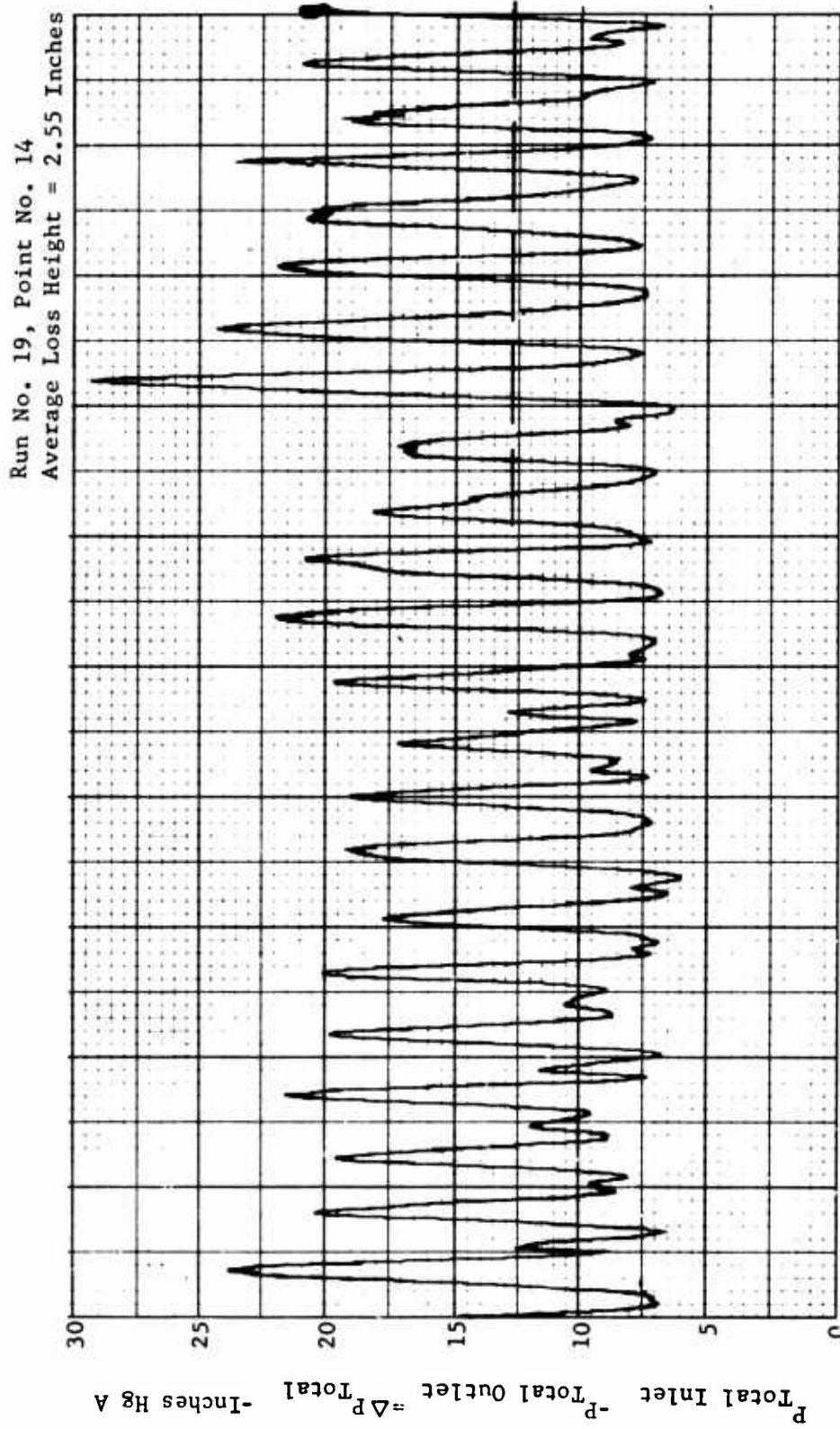
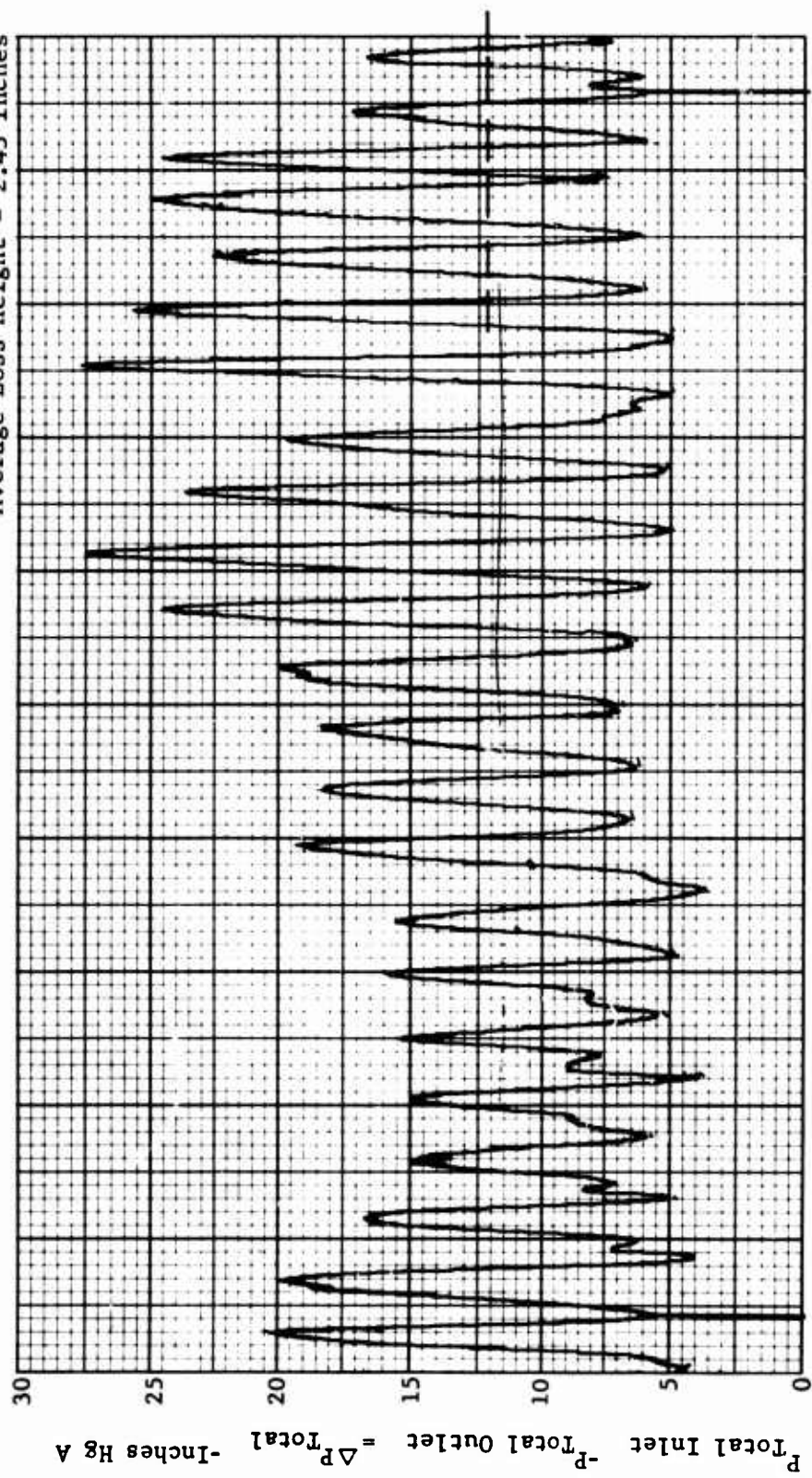


Figure 86. Typical Mid-Height Data Trace - 0-Percent Cooling Air.



Circumferential Location, 360-Degree Total Sweep
Figure 87. Typical Mid-height Data Trace - 4-Percent Cooling Air.

Run No. 7, Point No. 14
 Average Loss Height = 2.43 Inches



Circumferential Location, 360-Degree Total Sweep
 Figure 88. Typical Mid-Height Data Trace - 8 Percent Cooling Air.

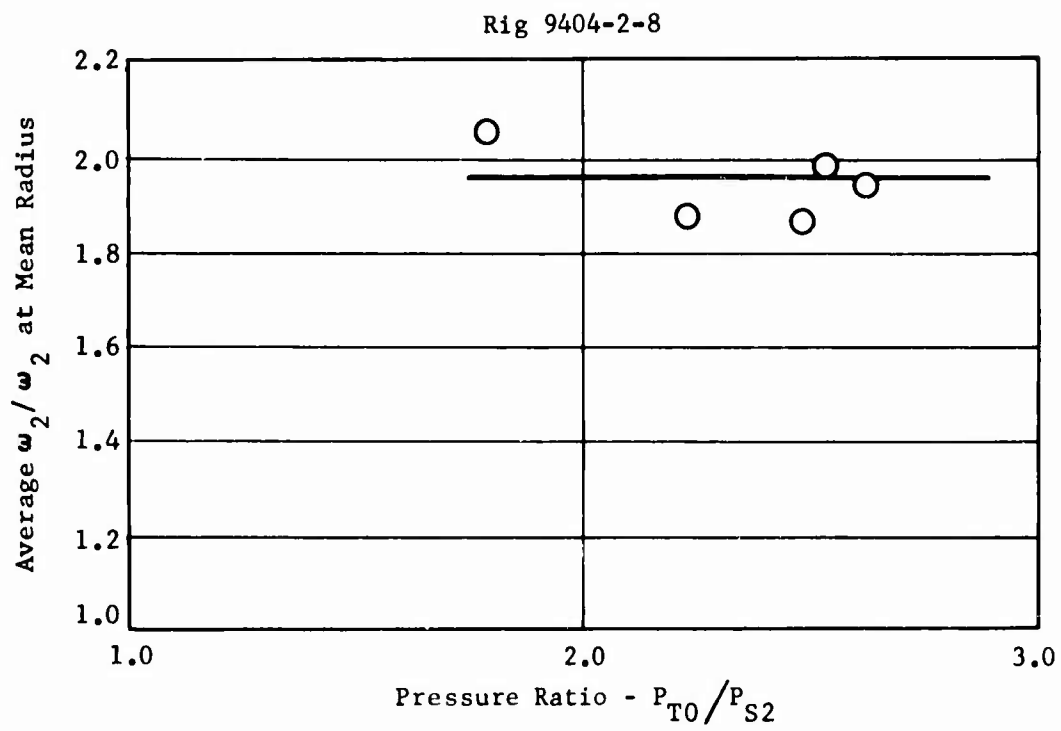


Figure 89. Ratio of Average to Mid-Height Stator Loss Coefficient.

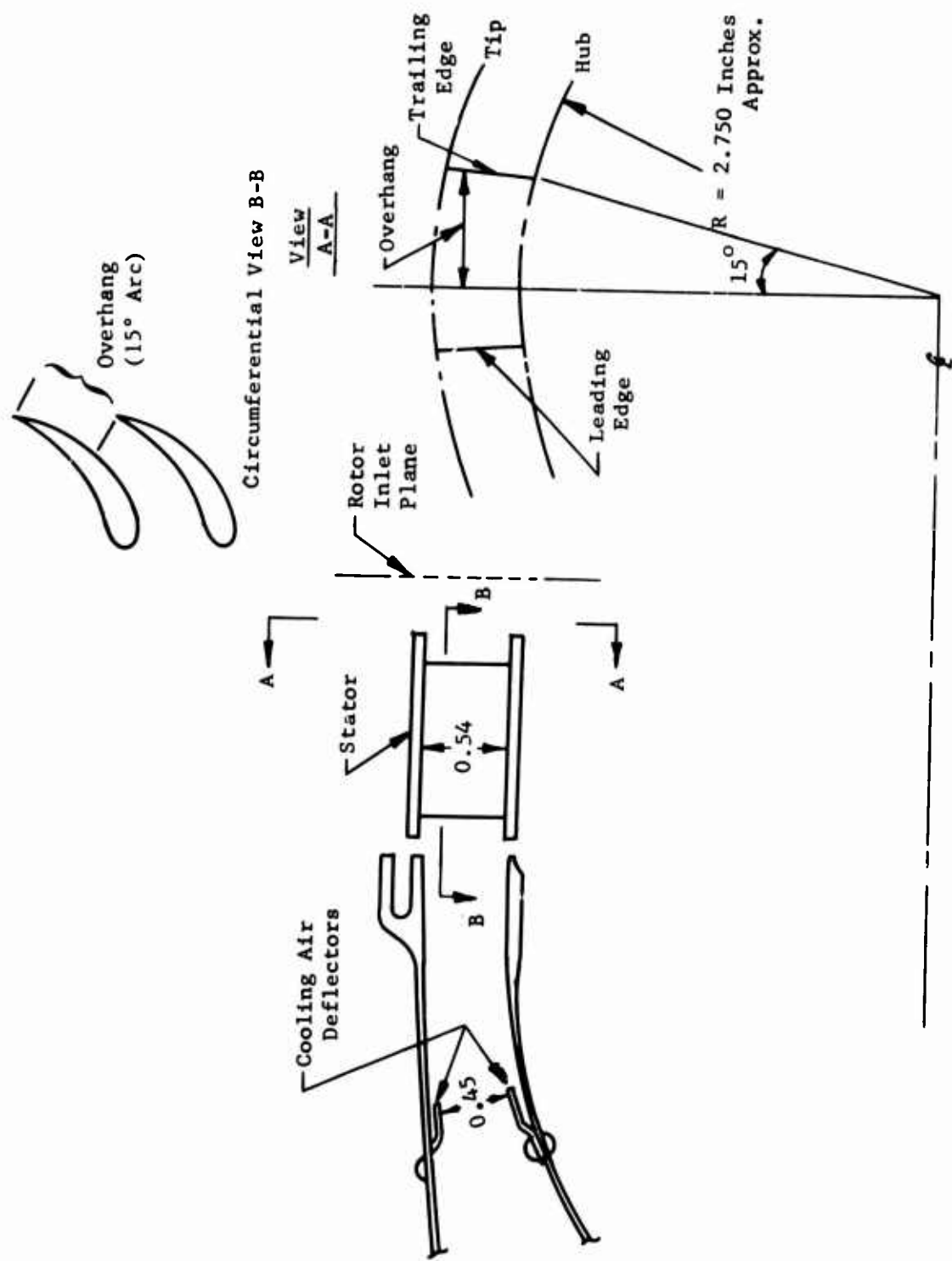


Figure 90. Turbine Stator and Combustor Cooling Air Deflectors.

Rig 9404-2-8, $P_{To}/P_{S2} = 2.5$

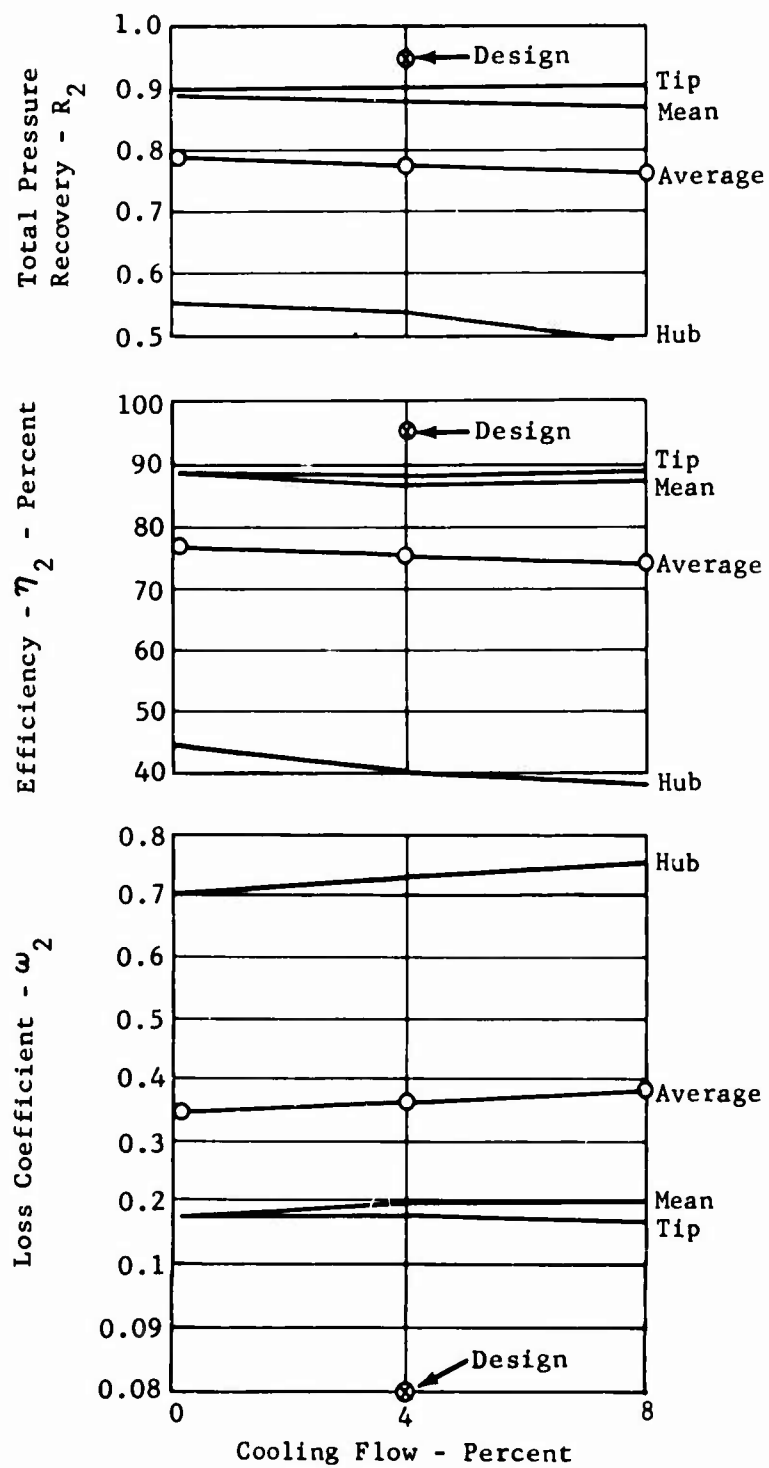


Figure 91. Stator Cascade Test Results.

Rig 9404-8,4 Percent Cooling Air

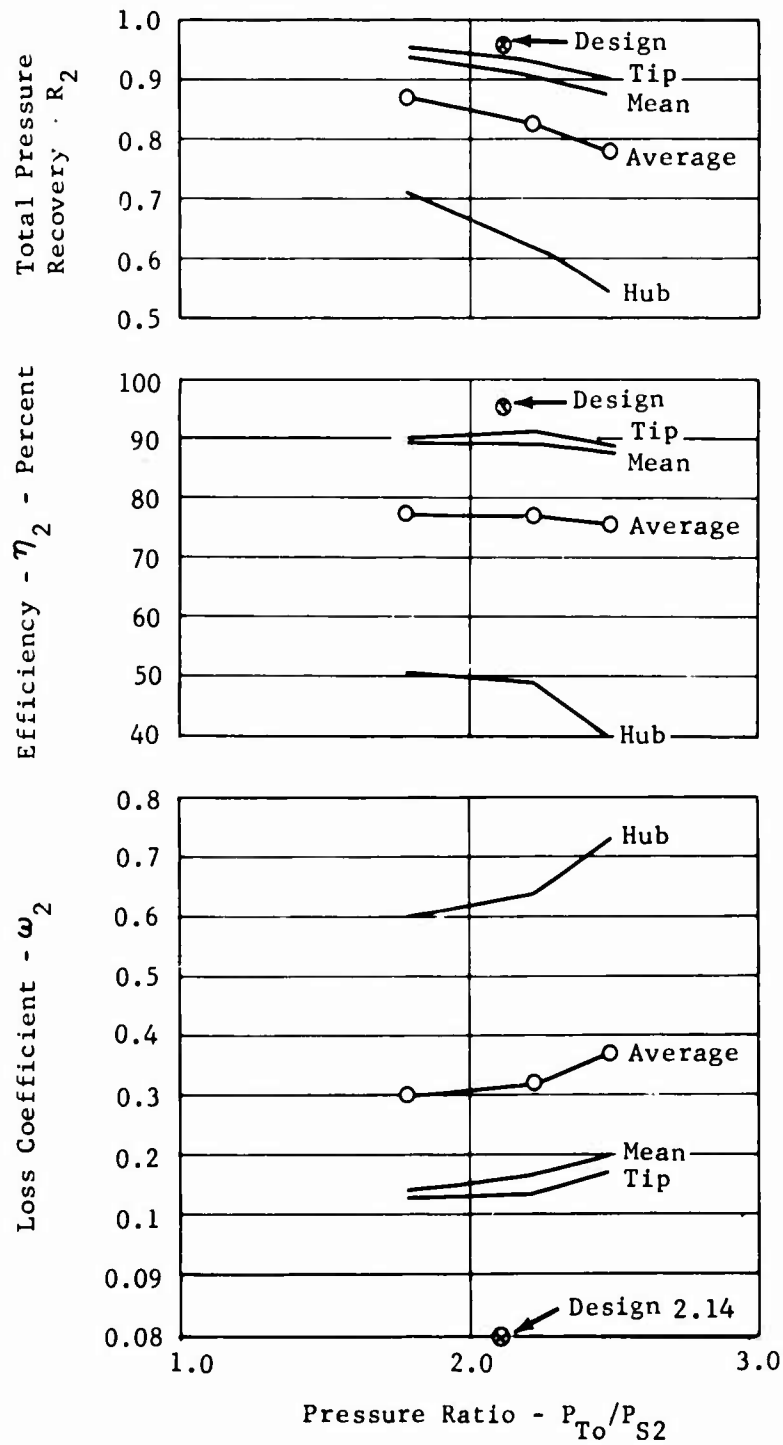


Figure 92. Stator Cascade Test Results.

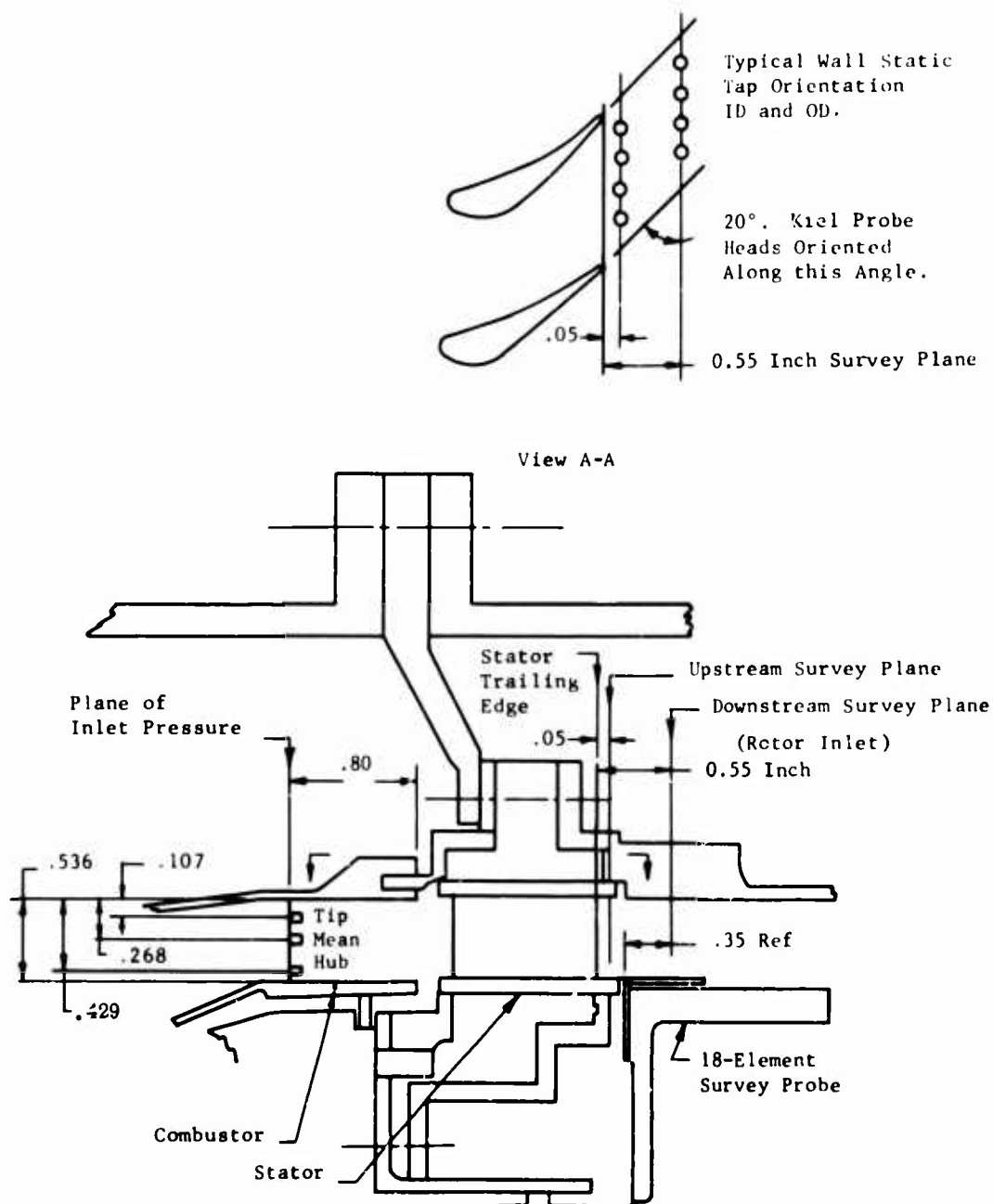


Figure 93. Rig Cross Section - Stator Instrumentation.

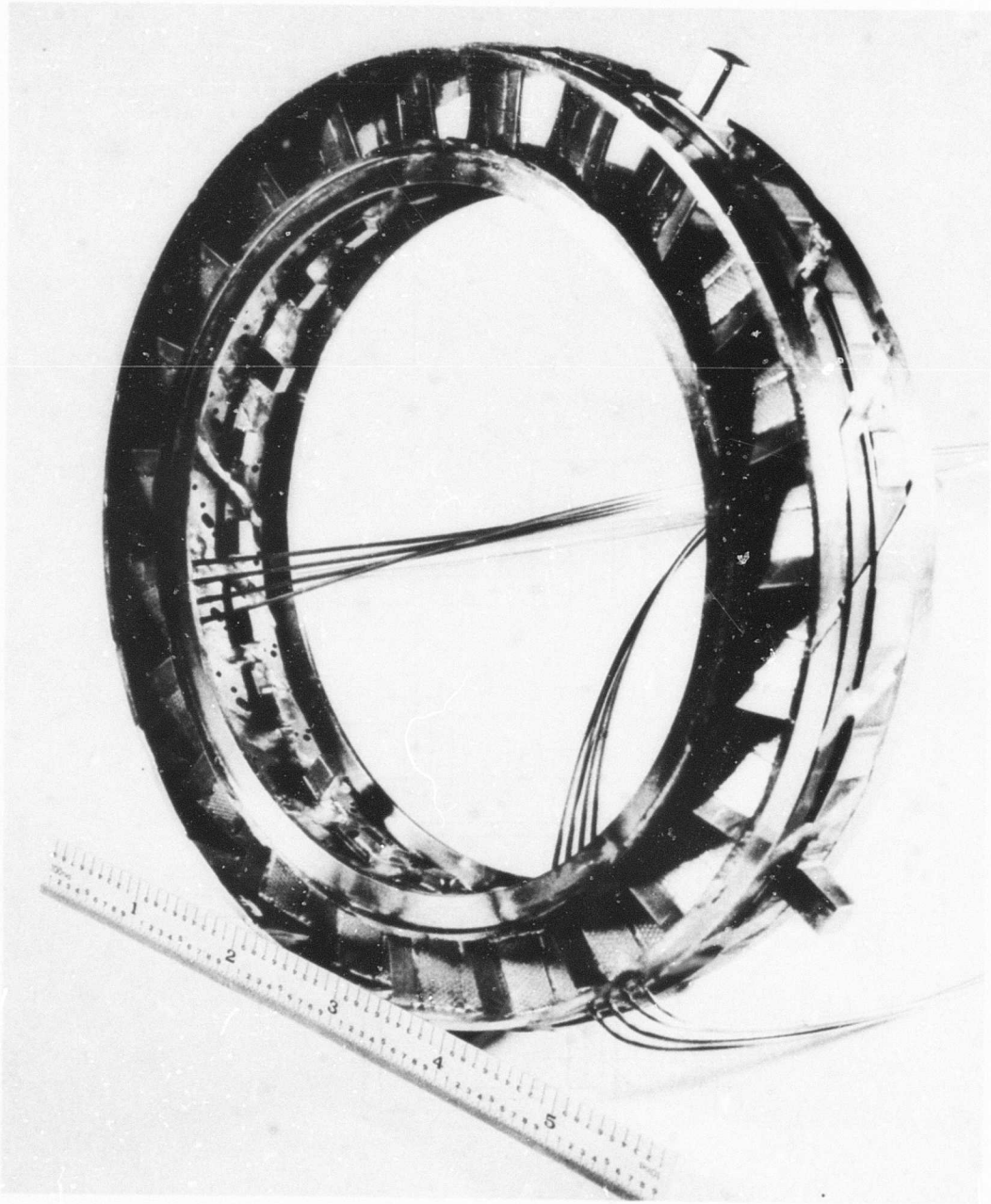


Figure 94. Second Welded Stator Assembly - Rear View Showing Static Pressure Instrumentation.

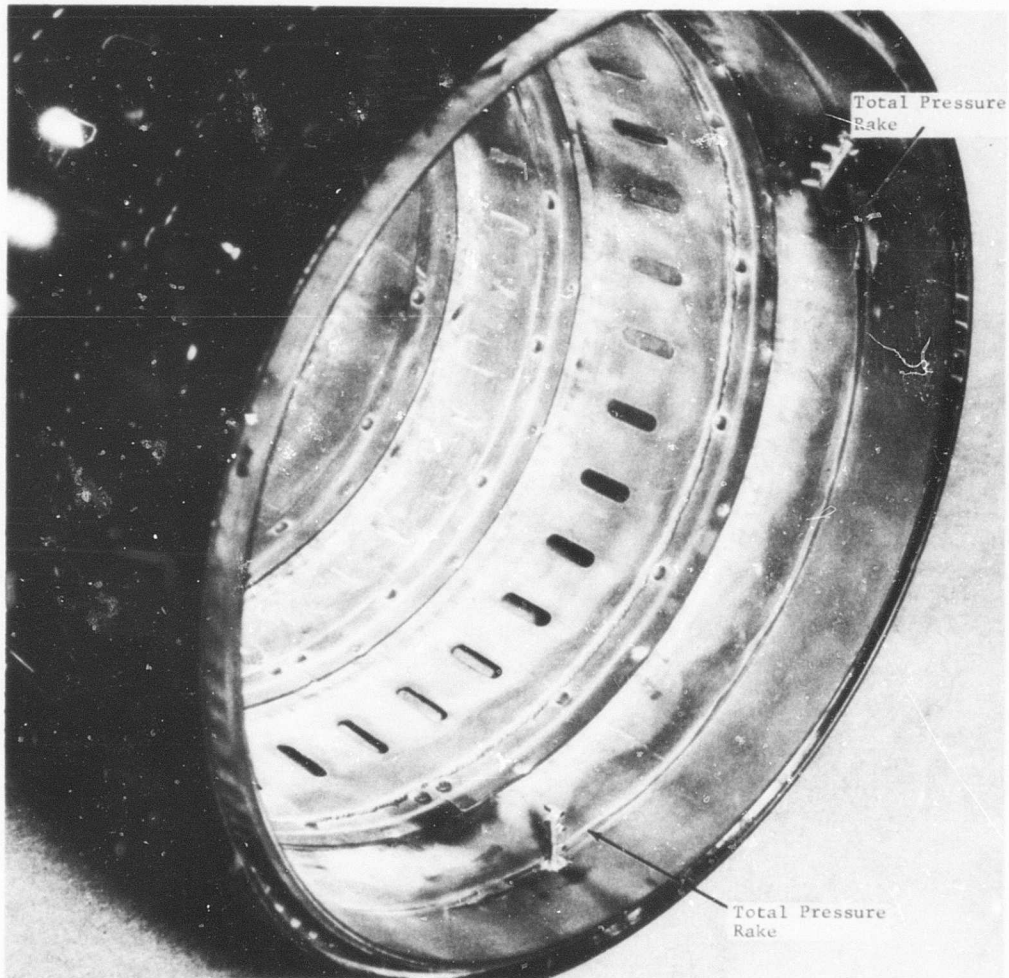


Figure 95. Stator Inlet Pressure Instrumentation.

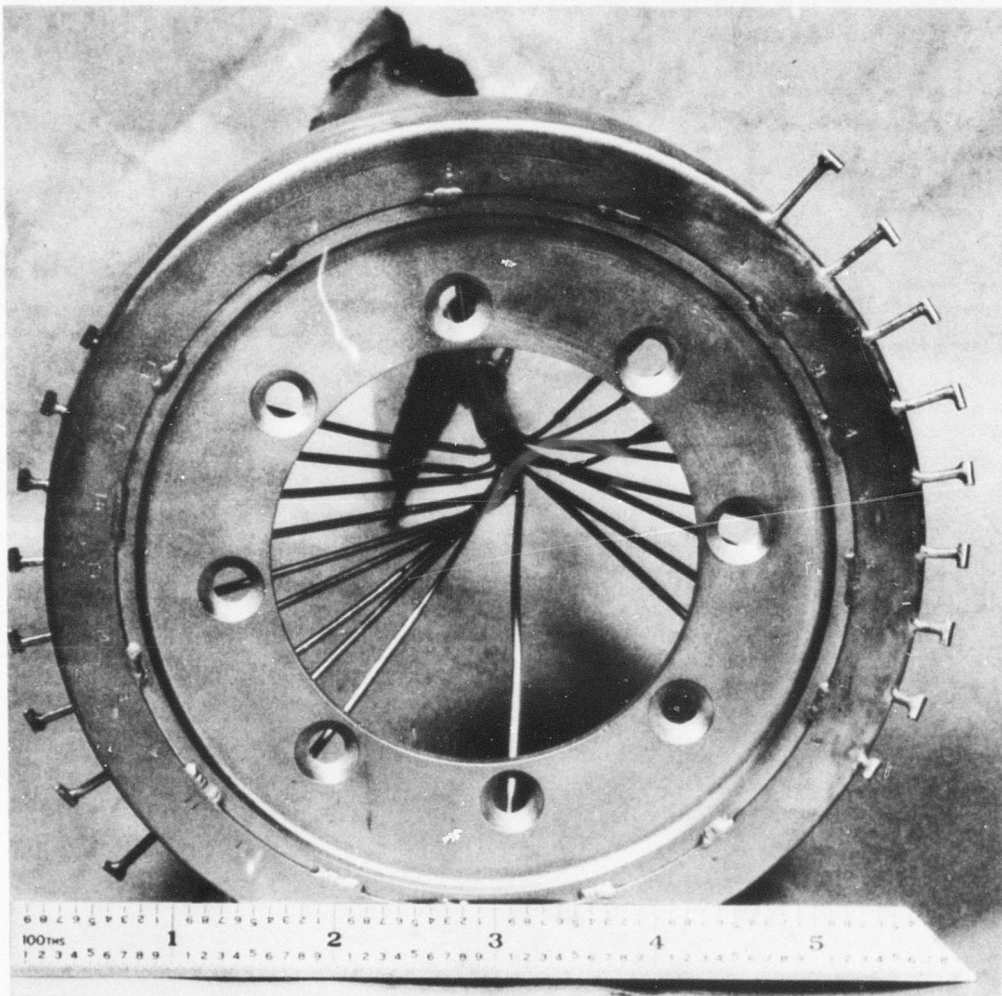


Figure 96. Survey Instrument Showing Fixed Kiel Probes On Rotating Ring.

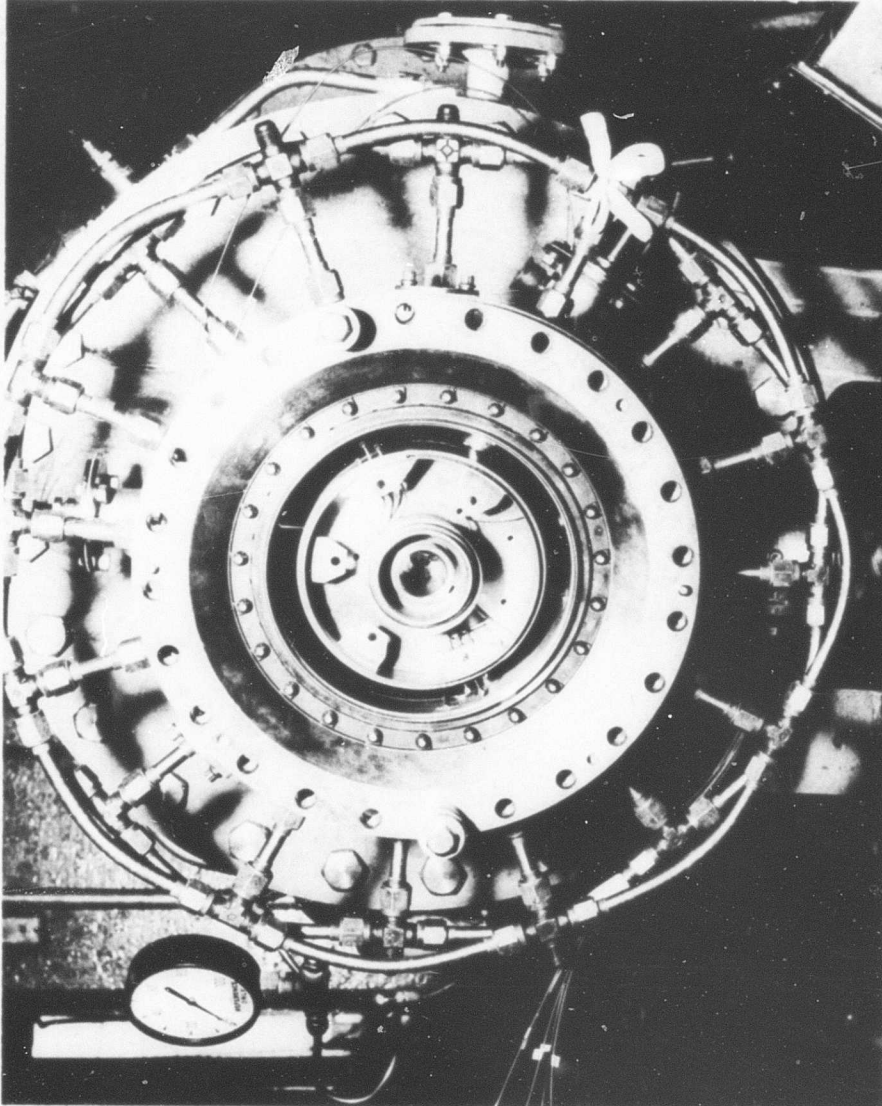


Figure 97. Driving Mechanism for 18-Element Survey Instrument.

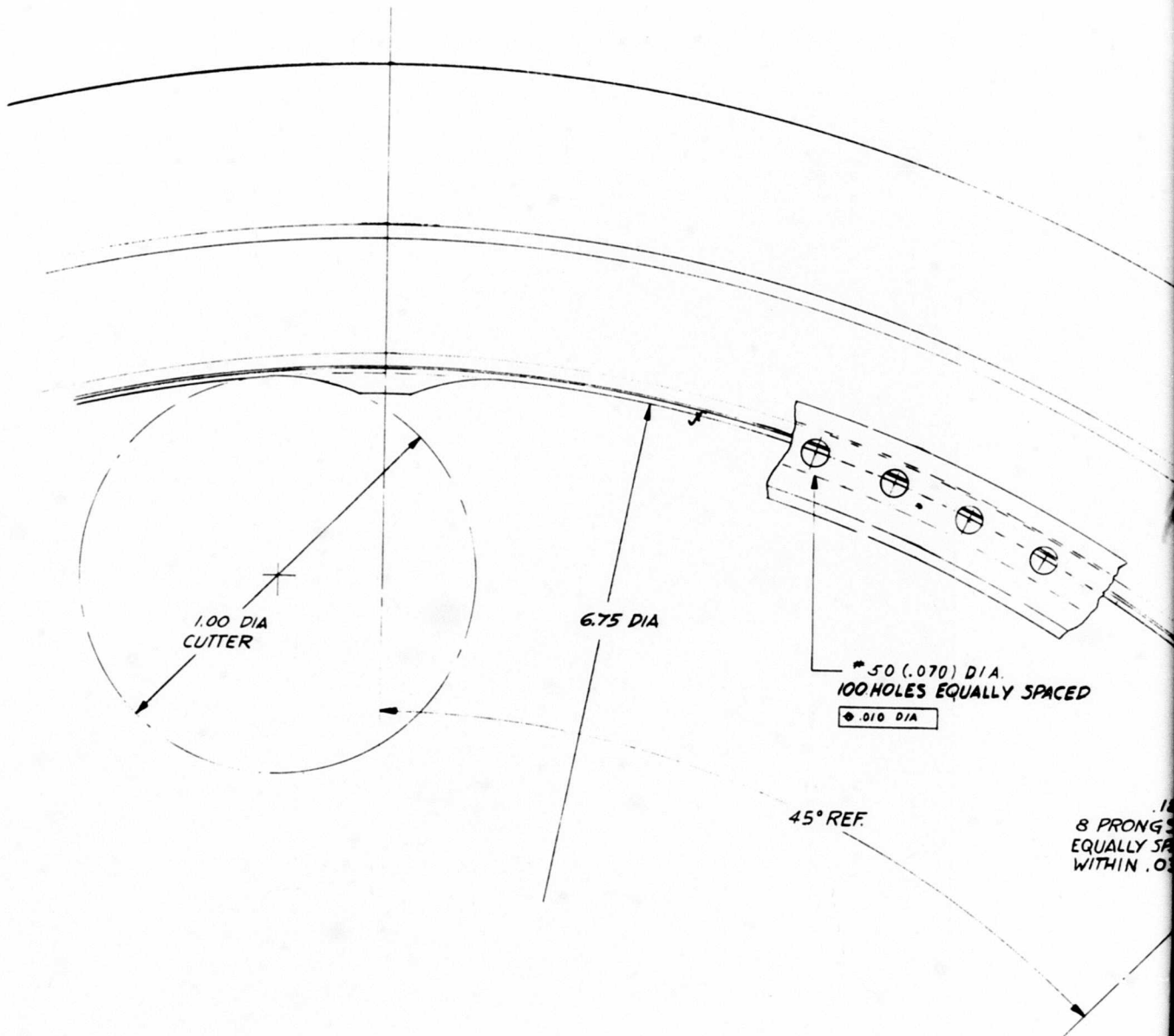
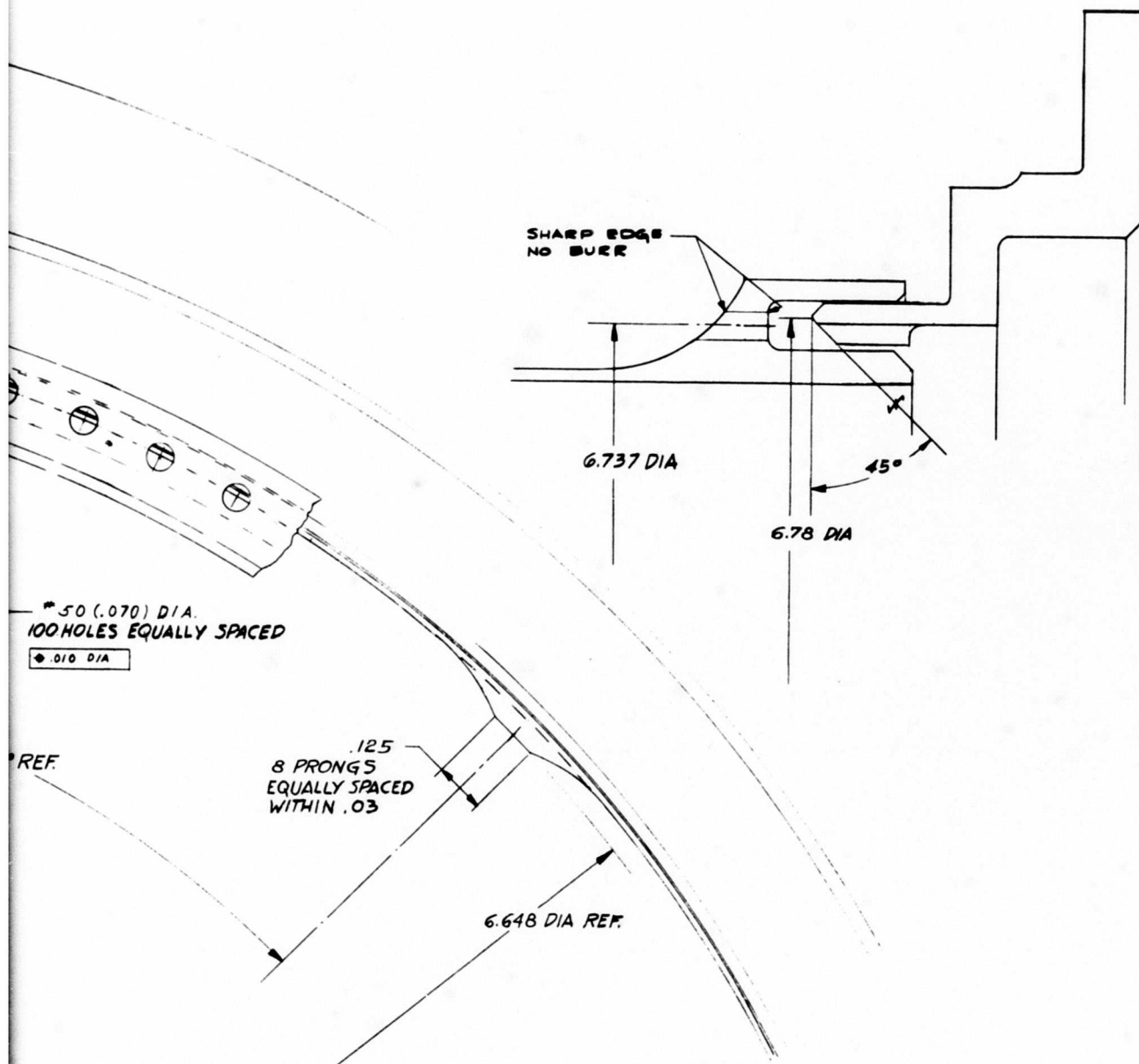


Figure 98. Liner and Support Rework.



B

BLANK PAGE

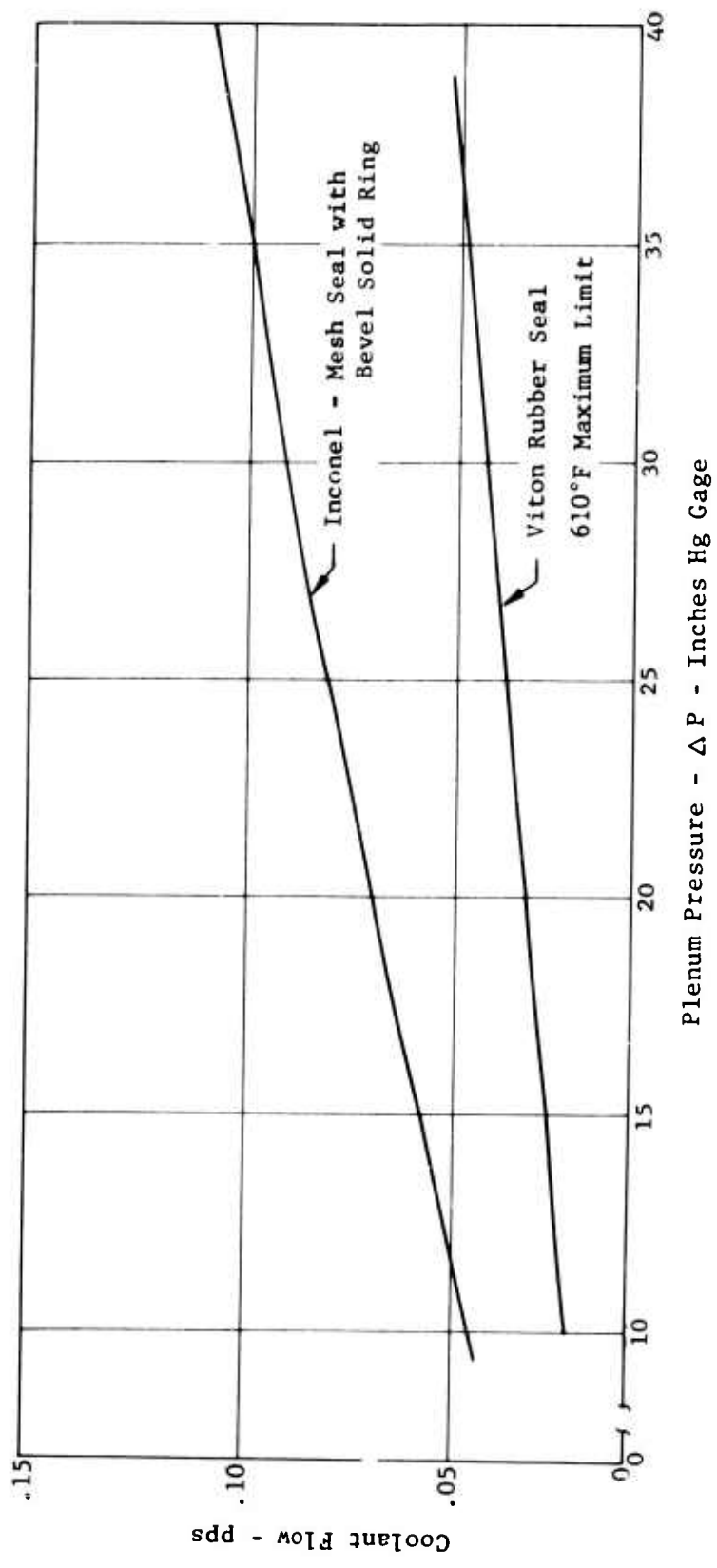


Figure 99. Outer Stator Plenum Flow Characteristic.

expected to show a reduced level of performance. Nevertheless, aerodynamic testing was conducted to provide valuable insight into the inherent performance characteristics of a high work, transpiration cooled blade design of low aspect ratio.

Full-Stage Test Goals Accomplished

Testing of the USAAVLABS small gas turbine engine component under contract was completed February 26, 1968. All contractual objectives were accomplished prior to sustaining rig damage during the final checkpoint run. Table XV lists the technical objectives and accomplishments.

TABLE XV PROGRAM TEST SUMMARY		
Objectives		Accomplishments
1. Turbine Inlet Temperature		2500°F
Target Value:	2338° - 2258°F	
Min Value:	2176° - 2096°F	
Max Value:	2420° - 2500°F	
2. Turbine Work		133 Btu/lb (at 3.05 Pressure Ratio)
Target Value:	133 Btu/lb	
Min Value:	126 Btu/lb	
Max Value:	140 Btu/lb	
3. Rotor Cooling Air		5.0 percent at 2446°F Turbine Inlet Temperature
Target Value:	5.0% at 2420°F	
Min Value:	4.0% at 2420°F	
Max Value:	6.5% at 2420°F	
4. Combustor Rig		
Time - hours	25.0	137.83
Temperature - °F	2500	2500
5. Stator Cascade Rig		
Time - hours	100.0	87.92
Temperature - °F	2500	2650
6. Full-Stage Rig Test Time	Hours	Hours
Below 1600°F	40	89.08
1600° - 2200°F	5	5.42
2200° - 2400°F	4	4.33
2400° - 2500°F	1	2.00

4.3.1 Rotor Blade Cooling Airflow and Leakage Characteristics

As an initial step, each coolant air passage was flow tested. This was done using several blades in order to compare the actual flow in each passage against the design value. Then the complete blade was tested to get the total flow, first without the skin and then with the skin welded in place. The reason for the check without the skin was to allow modification of the orifice hole size in the event of flow to marginal flow. Figure 100 presents the results from a typical blade. As can be seen from the figure, the flow in the individual channels on each side of the trailing edge of the blade was higher than design, whereas the flows of all the other channels were slightly lower.

The single blade total flow is shown in Figure 101. After the skins were installed, a flow check was again made at 30 inches Hg supply pressure.

The flow varied from 29 to 31×10^{-4} pounds per second. This represents a maximum deviation from design of less than 7 percent for each rotor set. As a further check on the single blade total flow, the individual channel flows of Figure 100 were added and plotted on Figure 101. This composite flow is within experimental accuracy of the flow measurement and shows the validity of the two methods.

With the 26 blades welded on the disc, the flow of the complete assembly was checked prior to each full-stage test. Figure 102 shows the flow check of the original rotor blade configuration and the revised configuration for increased leading-edge panel flow and compares them with design. The original configuration is slightly above design possibly because of leakage between blade butts. The revised configuration (Section 4.3.3) shows about a 10-percent increase in total flow at 30 inches Hg supply pressure which is due to increasing the channel flow at the leading-edge pressure side by a factor of three.

The top line of Figure 102 is the total cooling flow with the rotor installed in the rig on the test stand. This flow is higher because of the leakage past the labyrinth seal. The seal area was pressurized by a separate air supply, but this was not sufficient to prevent leakage. Since the leakage is predictable, however, it was a simple matter to adjust the rotor blade coolant flow to compensate for the leakage at any test point.

4.3.2 Aerodynamic Performance

The aerodynamic performance tests of the complete turbine stage were conducted with warm air at an inlet temperature of 610°F and inlet pressures up to 120 inches of Hg. Using the continuity equations, inlet total pressure was calculated from measured static pressure, inlet weight flow, and inlet temperature. Inlet total pressure probes were not installed since their presence in front of the turbine during the latter hot (2500°F) endurance testing would endanger the turbine component.

The work of the turbine was obtained as an average of three values determined from: (1) torquemeter readings, (2) turbine temperature drop, and (3) temperature rise of the water through the water brake. Next, the pumping work done by the rotor on the cooling air was calculated. The cooling air flows through the hollow turbine shaft and into the split disc. Inside the disc it is pumped radially outward by vanes cast integral with the disc. The system is assumed to act as a simple centrifugal compressor with no inlet whirl and with all the cooling air brought up to mean wheel speed. For this case, the work done on the cooling air is U^2/gJ Btu per pound. This work of pumping was added to the average work to get the total work of the turbine. The total work thus obtained was employed in turbine performance determination presented in Figures 103 and 103(a).

The test points shown on Figure 103 were run at 98 percent to 102 percent of design $N/\sqrt{T_{t2}}$ and with total (stator plus rotor) blade cooling flows varying from 7 percent to 13 percent of the rotor inlet flow. It can be seen from the figure that the parameters do not indicate any consistent trend within the scatter with change in cooling flow percentage. Even though the effect of cooling flow cannot be assessed quantitatively because of the scatter, it can be concluded that the effect is small within the tested range of cooling flows.

The comparison of the test performance with the design values in Figures 103(b) 103(c) shows that the flow parameter is essentially the same as design and furthermore is not affected by change in cooling flow percentage. The efficiency and consequently the work are both considerably less than design values shown in Figures 103(a) and 103(c). Because of the low (4 pounds per second) design weight flow, resulting annulus flow areas required were low. Consequently, blade heights were short. The long blade chords required for proper cooling air distribution coupled with short blade heights resulted in low (.5) stator aspect ratio. The unfavorable effects of low aspect ratio are known from uncooled turbine tests. Undesirable secondary flows develop. The compromise in the blade profile aerodynamics further aggravated the secondary flow losses as observed in the cascade tests.

The low stator performance is reflected in the overall drop in stage performance as shown in the comparison of the test vector diagram with the design (Figure 104). As can be seen, the actual stator gas outlet angle, α_{N1} , and Mach No. were less than design. The actual Mach number was subsonic rather than transonic. This resulted in a lower swirl tangential velocity and hence lower overall work.

Recommendations for Performance Improvement

Testing in a turbine cascade rig under an independent research and development program of two different stator profiles, one similar to the USAAVLABS stator and another with symmetric nose and high passage convergence between inlet and throat, indicated the latter shape to have superior performance. Blades similar to the USAAVLABS stator were tested as a cooled (porous airfoil) and a noncooled (solid) configuration to determine the effect of cooling flow and porous airfoil on blade row performance.

The test performance of the improved shape as solid blade is shown in Figure 105 together with that of the USAAVLABS stator. The solid line, which shows the effect of axial aspect ratio, is based on the test data of the improved shape (aspect ratio of 1.8) and the assumption of constant end loss. The dotted line is drawn based on a 3-point drop in efficiency for porous blades of the same shape as obtained by test results of solid and porous blades of identical shapes in a separate rig. As seen from Figure 105, the performance could be improved substantially by utilizing improved blade shape.

Further improvement would result by increasing the aspect ratio of the blades. This may be achieved by increasing the annular height and decreasing the blade chord as shown in Figure 106, resulting in average axial aspect ratio of 1.3 for the stator and .94 for the rotor. The use of decreased chord length is possible due to development testing over the past several years directed towards improved cooled designs and improved shorter chords notwithstanding.

As noted previously (Figure 90), the unguided portion of the suction surface (overhang) of stator blades is long (15 degrees circumferentially) so that the air must also flow unguided both along the overhang and along the hub surface. The latter has a high radius of curvature. This adverse streamline curvature is felt to contribute to the hub flow separation. By modifying the hub wall contour so that it is straight rather than curved at blade outlet (incorporate "flats") the straight inner wall would minimize the adverse hub streamline curvature effects on the suction side which occur for constant hub diameter as shown in Figure 90. Modification to both hub and tip wall curvature as shown in Figure 106 would increase the meridional acceleration and thereby minimize boundary layer growth and consequent secondary flow losses in the stator.

The stator is designed to utilize high energy level gas and to generate transonic velocities. Inefficient operation defeats the intent of the design. Furthermore, NASA research has shown that stator effects continue directly through the rotor. Thus, the principal effect of stator secondary flows lies in the result of core formation on the operation of the rotor. Improved stator performance would result in a more uniform flow leaving the stator, which would minimize mixing loss and incidence loss at the rotor.

The design and test performance of the present design, and the estimated performance of the improved design based on the preceding modifications, are shown in Table XVI.

The stator loss coefficient was obtained from the cascade tests. The rotor loss coefficient was calculated using stator loss coefficient and overall stage performance from turbine rig tests. While the principal factors responsible for the high stator loss were poor blade shape, low aspect ratio and porous skin and cooling flow, the rotor loss was high because of its low aspect ratio, porous skin and cooling flow, and the incidence effects caused by the radial profile in flow introduced by the stator. The rotor loss can be reduced by increasing the aspect ratio from .56 to .94 and by

TABLE XVI IMPROVED DESIGN ESTIMATED PERFORMANCE			
	Present Design	Test	Improved Design (Estimated)
Stator Efficiency	.95	.77	.86
Stator Loss Coefficient	.08	.32	.20
Rotor Loss Coefficient	.17	.29	.22
Turbine Efficiency	.89	.71	.81

providing more uniform flow entering the rotor. The rotor loss coefficient of .22 for the improved design was obtained by adding the effects of cooling and aspect ratio based on stator cascade tests (Figure 105), to conventional high aspect ratio rotor blade losses.

The estimated efficiency of the redesign is still below the original goal because of (1) the effect of secondary flows (3 to 4 points) since the redesign is still a low aspect ratio design, (2) the effect of cooling flow and porous airfoil (3 points), and (3) some compromise in the profile shape of transpirationally cooled blades to meet cooling and structural requirements (1 point).

4.3.3 Durability

The initial assembly of the complete turbine stage was made to check mechanical operation and to obtain aerodynamic performance data. The first series of performance tests indicated that the turbine efficiency was lower than anticipated and prompted the further study of the stator aerodynamic performance undertaken in the aero cascade tests. Testing of the complete stage was terminated upon the failure of the connecting shaft to the test equipment gearbox. Shaft failure analysis is discussed in the Appendix. The rotor was damaged and could not be used for further testing. Prior to this test, the gearbox input side bearings had seized and were replaced by ones with improved lubrication.

A second turbine rotor was then assembled and high temperature testing was initiated. The first two builds in this series of tests were terminated when the rotor blade leading-edge pressure side panels parted on one blade in the first test and on two blades in the second. Six other panels which had not parted showed bulging. As a result, all the leading-edge panels were removed and reworks were performed to provide improved cooling and strength, (discussed later in this section).

The final series of tests showed that the rotor blading and skins were in excellent condition after running at turbine inlet temperatures of 2500°F and at 45,000 revolutions per minute. The final test at 2500°F TIT and

speed of 50,000 revolutions per minute was terminated by failure of the turbine to gearbox connecting shaft. Analysis revealed that the cause of shaft failure was improper nitriding as discussed in the Appendix.

A chronological listing of the full-stage rig testing accomplished is presented in Table XXV.

Time accumulated at various turbine inlet temperatures is shown in Table XVII.

TABLE XVII ACCUMULATED TIME AT TEMPERATURE		
Turbine Inlet Temperature - °F	Time - Hours	
	Target	Actual
Below 1600	40	89.08
1600 - 2200	5	5.42
2200 - 2400	4	4.33
2400 - 2500	1	2.00

As can be seen from the table, the target times were exceeded at all temperature ranges. Metal temperatures of critical parts of the rig were obtained from thermocouples placed at strategic locations. A resume of the design versus actual metal temperatures is shown in Table XVIII for rotor Build 5, test point 19, which is the maximum turbine inlet temperature condition.

TABLE XVIII DESIGN VERSUS TEST METAL TEMPERATURE		
Item	Design °F	Actual °F max/min
Turbine Inlet Gas Temperature, Avg.	2500	2500
Stator Blade Cooling Air	610	650 - 490
Stator Blade Trailing Edge at Tip	1550	1555
Stator Blade Shelf at Tip	1355	1050
Honeycomb Shroud	1550	1470 - 1205
Turbine Exhaust Housing Inner Annulus	1250	1250 - 1205
Turbine Exhaust Housing Outer Annulus	1575	1625 - 1445
Turbine Exhaust Housing Outer Surface	1515	1270

Figures 107 and 108 show further details of temperatures, pressures, and airflows throughout the rig. Figure 107 shows the temperatures listed in Table XVIII in addition to those determined by means of temperature paint. As can be seen, all temperatures are within the design values of Phase I or lower. The pressure levels of Figure 108 were lower than planned to accommodate the pressure drops associated with the test-stand air systems. Consequently, the inlet pressure was reduced from the planned 178.5 inches Hg A to 149.2 inches Hg A.

Stator blade metal temperatures are shown in Table XIX for rotor Build 5, test point 12, in which more of the thermocouples were functioning.

TABLE XIX DESIGN VERSUS TEST METAL TEMPERATURES		
Item	Design °F	Actual °F
Turbine Inlet Gas Temperature, Avg.	2500	2460
Stator Blade Cooling Air	610	645 - 515
Stator Blade Spar Temperature	1220	855
Stator Blade Trailing Edge at Tip	1550	1525 - 1300
Stator Blade Shelf at Tip	1355	1050
Leading-Edge Land	1540	1100
First Pressure Side Land	1240	920
First Suction Side Land	1290	1075

The condition of the rotor and stator was noted as the test progressed. The rig was split at the stator flange to inspect the blading after running points of increased severity. For intermediate inspections, borescope holes were provided and offered an excellent view of the rotor blades. The last full inspection of the rig was made after point 12 (12.58 hours burning time and 1.33 hours at 2400° - 2500°F), and photos were taken (see Figures 109, 110, and 111).

Subsequent testing to 100 percent speed (50,000 rpm) and 2450°F turbine inlet temperature resulted in a rig failure. This failure and condition of parts after this test are discussed in the Appendix.

The major modifications carried out during the full-stage rig testing were made to improve the rotor blade cooling and to improve turbine shroud cooling. Originally, it was felt that the rotor blade skin tearing was due to a faulty land weld; in fact, this was clearly evident in the first instance of failure. However, subsequent testing at 2240°F turbine inlet temperature and at 28,600 revolutions per minute indicated that additional cooling was required.

The need to provide additional stator shroud cooling became clear during the test of the fourth rotor build. Measured shroud temperatures were high, and it was felt that they would rise well above the design value of 1600°F when the turbine was run at the 2500°F inlet temperature points. The resulting fix also reduced the stator tip cooling airflow by minimizing the leakage between the rear stator outer ring and the shroud forward lip.

The detailed discussion of the changes to the rotor blade cooling and turbine shroud cooling is presented in the following sections. Also presented is a detailed discussion of the whirl testing procedure used for the turbine rotor.

Rotor Blade Cooling

Rework of the turbine wheel assembly was required to correct the deficiencies in the airfoil leading-edge porous skin panel. The tearout failures and bulging in the upper two-thirds of the panel occurred as a result of high material temperatures together with high centrifugal loads. The centrifugal load developed in the panel because of its orientation (weave) on the blade surface. Because the elements are not radial, the centrifugal force develops a component normal to the panel surface having an effect equivalent to a large pressure differential. At 50,000 rpm, this component constitutes a major load acting on the panel and was many times greater than that due to the cooling air pressure differential.

The high metal temperatures in the upper portion of the panel were caused by an inadequate supply of cooling air, particularly to the outer two-thirds of the panel. The operating temperatures of the leading-edge panel were estimated to be between 1600°F and 1800°F. This condition was attributed to the unusually low external gas pressure at the hub due to high stator row losses in this section which results in excess cooling airflow effusing through the mesh at the hub section.

Inspection revealed that in seven out of eight failed panels, the skin was attached with the weak direction (weave orientation, Table II) of the skin bridging the gap between the lands, thereby reducing its ability to resist the normal force component tending to bulge it. The weak and strong directions refer to the minimum and maximum mesh strength in tension which coincides with minimum and maximum strength in bending. Mesh strength is determined by the weave pattern during manufacture.

The following revisions were made to the rotor blade leading-edge airfoil panel in order to correct the situation:

1. The coolant-air supply-hole area was increased fourfold from 2.55 to 10^{-4} square inches to 1.02×10^{-3} square inches to reduce the estimated operating skin panel temperature to 1200°F.
2. Cooling air distribution to the upper portion of the panel was improved by masking the lower one-third of the panel, except for the leading edge.

3. The panel skin was replaced with mesh oriented with its stronger direction between lands to better resist the bending loads.

A .023-inch-thick Nichrome V Cb replacement skin was used for the leading-edge panel. In the structural analysis, the skin was considered to be a homogeneous flat rectangular plate with all edges fixed and subject to a uniform load made up of the centrifugal force component and the cooling air pressure differential. The maximum bending stresses and material properties are shown in Table XX.

TABLE XX AIRFOIL MESH MATERIAL PROPERTIES AT 1200°F				
	Material UTS (psi)	Properties .2% YS (psi)	Maximum Bending Stress at Center of Edge (psi)	Margin of Safety
Strong Direction	29,800	18,900	9,390	1.02
Weak Direction	16,400	13,300	4,590	1.90

A summary of the estimated skin temperatures for the leading-edge panel when the base orifice is increased by four times and the lower third is masked is shown in Table XXI.

TABLE XXI AIRFOIL LEADING-EDGE PRESSURE SIDE PANEL TEMPERATURES		
Span	Leading Edge at Stagnation Point (°F)	Average Panel Temperature (°F)
1/6	1300	-
1/2	1320	920
5/6	1165	880

The variation of leading-edge panel skin temperature versus the average transpiration flow rate in pounds per hour per square foot is shown in Figure 112.

Turbine Shroud Cooling

The cooling air path through the shroud support assembly was changed in order to:

1. Include cooling of the back side of the rotor blade shroud segments.
2. Improve cooling of the inner ring on the shroud support box structure.

This was done by adding new holes in the inner and outer rings of the shroud support box structure, cutting a series of slots in the front support rail, and plugging the existing hole in the forward wall. A picture of the modified cooling airflow path is shown in Figure 113.

In addition, a source of air leakage at the forward lip on the shroud support structure was eliminated by installing a wire mesh seal which was squeezed between the gap made with the adjoining retainer.

The requirement for added cooling was determined from temperature paint readings. These indicated that the inner ring on the shroud support assembly and the back side of the rotor blade shroud segments were operating at 1652°F when the gas inlet temperature was 2240°F. The original heat transfer analysis was done for a 2500°F gas inlet temperature and an external cooling air supply separate from the main flow. Predicted inner ring temperature was 1055°F and a shroud segment temperature 1550°F. This trend indicated that the operating temperature of these structures would increase by approximately 260°F over the measured values mentioned above if the rig were operated at a 2500°F gas inlet temperature. In order to preclude any further increase in these temperatures, the coolant air supply was doubled and rerouted through the structure.

A summary of the coolant airflow, pressures, temperatures, and orifice sizes through the shroud support assembly is given in Table XXII. The total airflow supply is .0858 pound per second at 610°F and 68 pounds per square inch pressure. Ten percent of the air is assumed to be lost through the mesh seal as leakage. The remaining .078 pound per second flows through the shroud support assembly and discharges into the main gas stream in front of the turbine rotor blade at a static pressure of 38.6 pounds per square inch.

Each orifice was sized to meet the requirements for flow continuity. A discharge coefficient of .6 was used except between Stations 1 and 2 where a value of .75 was used as determined from test data. The pressure upstream of the discharge slots (Station 4) was set at 39.9 pounds per square inch and the pressure in the shroud support assembly plenum (Station 3) was set at 44.1. Prior to the rework, Station 3 operated at 40.7 pounds per square inch. However, this value was raised slightly to accommodate the flow through the additional orifices.

Disc Whirl Testing

The turbine rotor was an all-welded assembly which consisted of 26 transpirationally cooled blades individually electron beam welded to the disc.

TABLE XXII
AIRFLOW DATA THROUGH SHROUD

Data	Station* 1 - 2	2 - 3	3 - 4	4 - 5
W - lb/sec	.0858	.078	.078	.078
T _t - °F	610	610	610	610
P _T - Upstream-psia	68	66.8	44.1	39.8
P _S - Downstream-psia	66.8	44.1	39.8	36.8
A _{TOT} - sq in.	.4390	.125	.299	.372
No. of Holes	23	24	48	48
Area/Hole - sq in.	.0191	.0035	.000855	.00622
Dia Hole - in.	.156	.067	.033	.089
				.031x.50 Slot
*Refer to Figure 113 for station location.				

No welding was done to join adjacent blades to each other. It was observed after final welding of the first rotor that fine radial cracks existed in the welded joints extending radially inward from some blade butt-to-butt joints (see Section 3.1.2). Figure 28 shows the rotor and cracks. To demonstrate the structural integrity of the finished component, a spin test was conducted.

While the spin pit had the rotative speed capacity, its mechanical characteristics with the rotor assembly installed would not be known; viz, critical speeds of the combination were not considered amenable to analysis. To ascertain the critical speeds and to explore the operating characteristics of the test equipment prior to spinning the actual rotor, a mass-representative, unbladed dummy rotor was designed and tested. Prior to testing, the dummy rotor was dynamically balanced to the close tolerance of .001 ounce-inch.

By means of a periscope, direct visual observation of the rotor during testing was possible; by this means it was noted that the rotor passed through a critical speed between 10,000 and 15,000 revolutions per minute. The complete test consisted of spinning the rotor at 10, 20, 30, 40, 50 and 56 thousand revolutions per minute. The facility was thus judged to be satisfactory for testing the bladed rotor.

To minimize the risk to the actual hardware, the test program for the complete turbine stage specified that the low speed, low temperature testing be carried out before proceeding to the high speed, high temperature, design point testing. The spin testing was scheduled to complement the full-stage testing as follows. First, the actual rotor was spin tested up to 35,000 revolutions per minute. The results of this test were satisfactory, and the rotor was installed in the complete stage and the cold aerodynamic mapping testing was completed up to 35,000-revolution-per-minute mechanical speed. Next, the rotor was removed from the turbine and whirl tested up to 56,000 revolutions per minute. This too proved satisfactory, and the rotor was then installed in the complete stage for hot testing up to 55,000 revolutions per minute.

The overall test approach is as follows. First, the radius to the tip of each blade was measured. Next, the crack lengths were measured radially inward from the underside of the shelf with the aid of a high magnification optical glass. Then the first rotor assembly was tested at each of the following speeds: 20,000, 30,000 and 35,000 revolutions per minute. After 2 minutes at each speed point, the rotor was removed from the pit, and measurements were taken of the radial growth at the blade tip and of any weld joint crack growth. Radial tip growth of approximately .0005 inch occurred up to 30,000 revolutions per minute with no further increase measured after the 35,000-revolution-per-minute test. The maximum weld joint crack growth was .110 inch (.150 to .260 inch) after the 20,000-revolution-per-minute point. No further increase after the higher speed points occurred. It was concluded from this test that the integrity of the rotor was adequate for the initial phase of rig testing.

The rotor was then installed in the complete turbine stage, and the cold, aerodynamic mapping was carried out. This was accomplished without incident. The rotor was removed and returned for spin testing up to 56,000 revolutions per minute. As before, the test consisted of 2 minutes at each prescribed speed followed by shutdown, removal from pit, and repetition of the inspection procedure. The speeds for the test were 20, 30, 40, 45, 50, 52, 54, and 56 thousand revolutions per minute. No significant crack elongation occurred. Operation of this rotor in the test rig was satisfactory with regard to these cracks which did not progress beyond the blade-to-disc weldment.

4.3.4 Test Equipment

Power Absorber

The power absorber used during the full-stage test was the Taylor Hi-Eff Hydraulic Dynamometer (Model D-20-10) shown in Figure 114. The advantage of this particular water brake is that it has 10 discs in separate chambers that can be closed or opened independently for attenuating power absorption capacity.

Speed regulation was stable at all points. The water inlet control valve, however, had to be monitored and adjusted periodically to minimize drift in speed while recording data. With care, speed could be maintained within 250 revolutions per minute (1/2 percent) during a steady-state data recording point. Approximately 100 hours of operation at brake speeds up to 8200 revolutions per minute was achieved with satisfactory mechanical operation.

All high temperature testing was performed with the water discharge from the brake wide open. For the lower power performance testing, the brake discharge valve was partially closed to obtain a large water temperature rise, taking care to avoid the water exit temperature limits. In this way the temperature rise value becomes less sensitive to the individual thermocouple errors which were used to measure water inlet and water outlet temperatures.

Brake power was obtained by measuring the brake load from 15.75-inch lever arm mounted off the case and acting on a strain-gage-type load cell.

An additional check on power was to measure water brake flow (in the range of 10,400 pounds per hour) and water temperature rise (in the range of 70°F). To obtain an accurate temperature rise (ΔT) reading, the water-inlet and water-outlet thermocouples were connected in series, and the output of this circuit was measured in millivolts and then converted to a ΔT reading directly. A separate water-inlet and water-outlet thermocouple was also recorded and showed slight lower ΔT readings.

To allow more passage of water, the water brake was modified prior to the high speed runs to provide additional side clearance between the rotating discs and sidewalls. Two additional water discharge passages were also provided to assure free flow of the water at high speeds.

Analyses of the bearings and rotors of the Taylor dynamometer were made because of the limited operational use this model had at speeds above 6500 revolutions per minute. The rotor shaft bearing calculation indicated satisfactory operation at 9120 revolutions per minute (110 percent of turbine design speed) using its oil mist lubrication system. The calculated DN value (diameter in millimeters times revolutions per minute) for this bearing is 560,000, and the maximum allowable is 750,000.

The analysis of the water brake rotors indicated that they were structurally adequate for operation at 9,120 revolutions per minute. The calculated average tangential stress is 7,400 pounds per square inch; this was well below the 38,000-pound-per-square-inch yield strength of the American Iron and Steel Institute 316 rotor material.

The critical speed of the shaft in flexure with ten rotors was calculated assuming no viscous damping and using an estimated bearing spring rate of 500,000 pounds per inch. The computed critical speed was 9,850 revolutions per minute versus 9,120 revolutions per minute maximum anticipated for a turbine operation at 110 percent of design speed. The normal practice is

to allow a margin and operate at a speed 25 percent lower than the calculated critical speed, i.e., 7,400 revolutions per minute. Not having this margin, vibration pickups were carefully monitored during high speed operation as a precaution. Maximum displacements of 1.2 mils occurred at 6,300 revolutions per minute (38,000 turbine revolutions per minute); all other speeds were below .7 mil.

Reduction Gearbox

The reduction gearbox used between the turbine rotor and the water brake was Model 716-S manufactured by the Cotta Transmission Company. The speed reduction was 6.03 to 1 and was accomplished in a single stage by two back-to-back helical pinions meshing with two mating bull gears. Figure 114 shows an external view of the gearbox mounted in the test stand.

During the first two builds of the turbine rig, the reduction gearbox operated satisfactorily for approximately 50 hours at speeds up to 40,000 revolution per minute. However, the second test was terminated due to gearbox input end bearing seizure. Operation was at relatively low speeds followed by 5 to 10 minutes at 24,000 to 30,000 revolutions per minute.

Examination of the gearbox components disclosed that the failure resulted from seizure of the ball bearings at the input end of the unit. The gearbox used a pair of 25-degree angular contact duplex back-to-back ball bearings at each end of the pinion shaft. The inner races are separated by a .090-inch spacer and the outer races by a wave spring designed to provide a 20-pound preload. A drain between bearings at each end is connected to a single scavenge pump.

The probable cause for the bearing failure, which involved fracture of the cages, was a lubrication breakdown. Due to the advanced stage of the failure, the exact reason for lubrication breakdown could not be established; however, it is considered likely that inadequate oil supply was a major factor. With opposing oil jets and inadequate venting between bearing; by the single scavenge pump, flow of oil into or through the bearing is questionable.

In light of the possible causes for failure, the following changes were recommended by Curtiss-Wright to the gearbox vendor and incorporated into the rebuilt gearbox.

1. Replacement of the 25-degree contact angle bearings with 12-degree contact angle bearings which generate less heat at the inner race contacts.
2. Use of 3/64-inch-diameter oil jets (2 ppm per jet) to provide adequate oil for lubrication and cooling of the bearing.
3. Rework of inside diameter of the gear baffle to be flush with the bearing outside diameter to permit adequate drainage from the inner bearings at each end of the pinion shaft.

4. Machining off of labyrinth seals to the bearing outside diameter to permit adequate drainage from the outer bearings at each end of the pinion shaft.
5. Use of solid spacers between the bearings with an interbearing drain, with inner and outer spacers ground parallel and matched to give the correct preload and the outer spacer slotted to permit oil drainage.

The failure of the high speed end of the reduction gearbox also prompted a review of the critical speed of the connecting shaft drive line which connects the turbine to the gearbox. This review revealed that the connecting shaft had a critical speed at 35,400 revolutions per minute, approximately in the range at which failure occurred. Although it was not known that the critical speed of the connecting shaft was the primary cause of the gearbox failure, it was deemed prudent to redesign the connecting shaft to eliminate the possibility of critical speed being a contributing factor.

A design rework of the existing connecting shaft was made which raised the critical speed to 64,200 revolutions per minute. Two changes were involved: (1) elimination of the bearing and shear pin at the gearbox end, and (2) reduction of the tubular wall thickness to .063 inch. Neither change affected the critical speed of the turbine shaft which remained at 19,500 revolutions per minute.

The margin between 110 percent of turbine design speed and the calculated critical speed of the connecting shaft is 15 percent. Since a margin of 25 percent is normally desired, a Bently pickup located near the gearbox end of the quill shaft was used for monitoring excessive shaft deflection.

For subsequent rig testing, a new single-piece connecting shaft was designed to replace the reworked two-piece design. This new shaft was used throughout the test program. However, the shaft had been nitrided all over by the vendor; this was contrary to the drawing. This nitrided condition precipitated failure of the shaft at the final checkpoint of the test program. A discussion of this failure is found in the Appendix.

Test Cell Installation

The water brake, gearbox, and full-stage rig complete assembly are shown installed in the test cell in Figure 114. This shows the rear view and a close-up of the brake to gearbox coupling, brake torque arm, turbine oil filter, and turbine exhaust duct. The exhaust duct was water-spray cooled and was routed from the rig discharge up through a flexible duct section and then out of the end of the test cell. The turbine discharge could be routed through an ejector to obtain high pressure ratio conditions. Note also in this figure the calibrating load cell in position at the end of the water brake torque arm.

The calibration was done on the whole system as installed to eliminate any installation error. The purpose of the angle iron frame was to take the weight of the exhaust duct off the rig which was bolted to the gearbox through a spool-piece. This figure also shows the radial traversing probe mechanism and the upstream preheater.

Control Room

The control room for rig testing is shown in Figures 115 and 116. The former shows the rig control panel. Note the control knobs on the left for the remote air-actuated valves for water brake flow, main air inlet and exhaust, preheater and main fuel flow, and cooling airflow. The front of the panel contained the fuel flowmeters and switches for fuel pump operation and ignition. Figure 116 shows the manometer banks, X-Y plotters and control for the traversing probe, and the oscilloscopes for recording turbine shaft and turbine to gearbox connecting shaft deflection.

Temperatures were observed on push-button Brown recorders. Pressures were read on gages or manometers. Airflows were obtained from ΔP readings across calibrated orifices; in the case of the main air, an additional pressure drop reading was taken across an inlet bellmouth as a check. Main fuel flow was obtained from pressure drop across calibrated orifices as well as from the flowmeter readings. Turbine power absorption was measured by a torquemeter reading and also by measuring the water flow with a Potter flowmeter and noting the temperature rise. Vibration pickups were placed on the water brake, gearbox, and turbine rig and were recorded on an indicator in the control room.

The rotor and stator cooling air system had electric heaters to adjust the supply temperatures.

Ref EX810003N

P_{ext} - 14.7 psig

T_{air} = 70°F

Skin Permeability = 3.6×10^{-11} in.²
Thickness = .020 in.

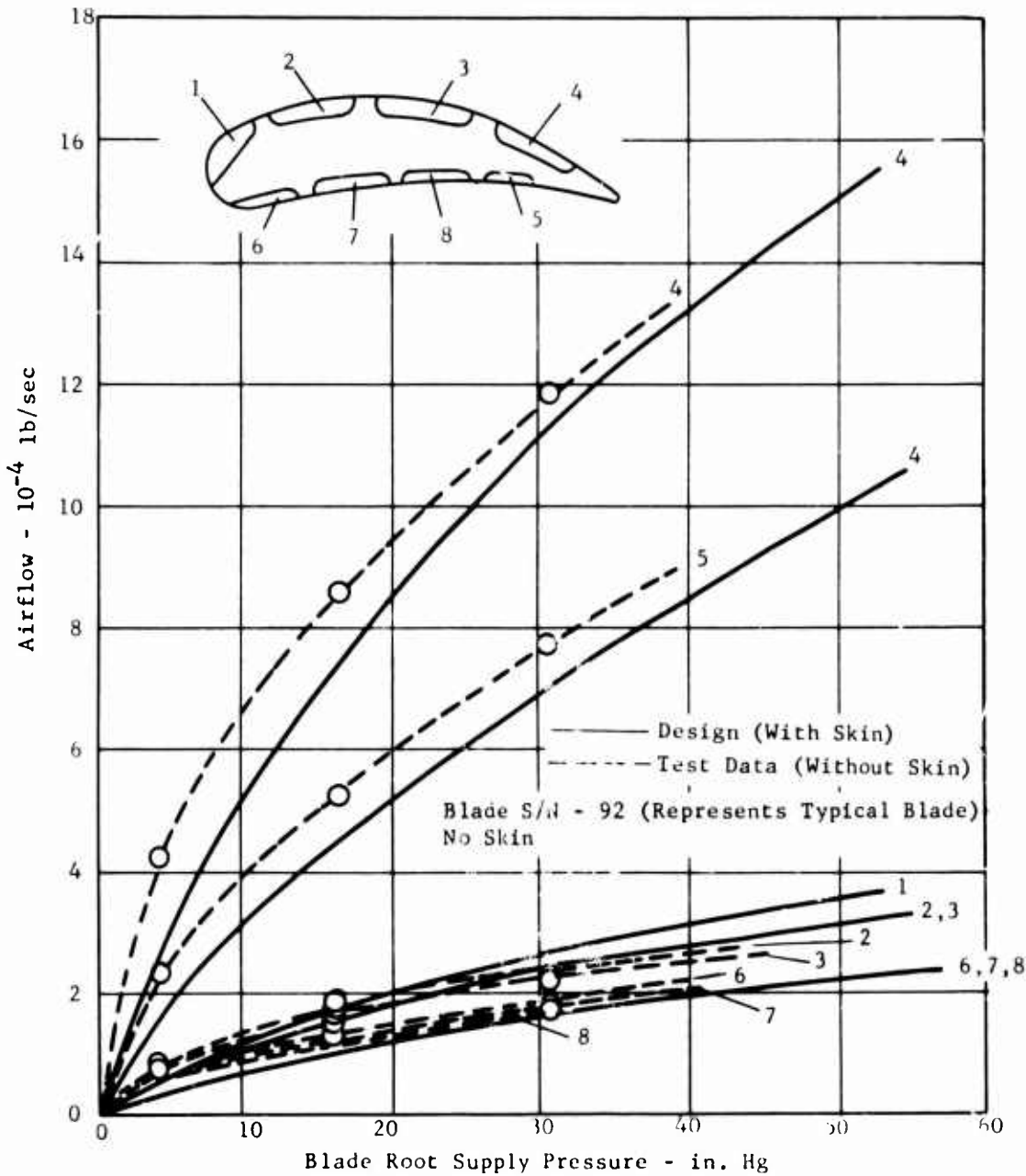


Figure 100. Turbine Rotor Blade - Channel Flow Characteristics for Ambient External Conditions.

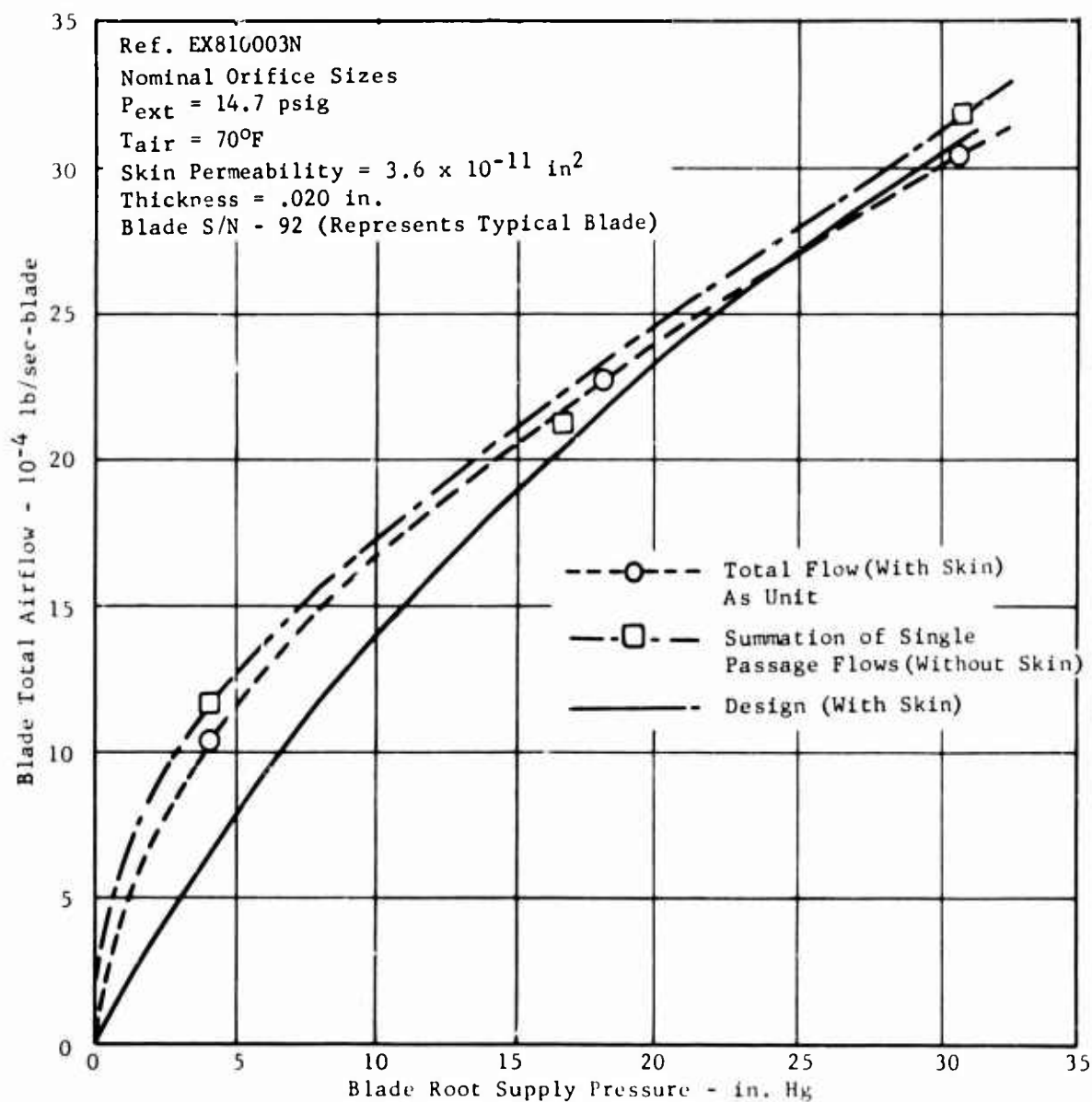


Figure 101. Turbine Rotor Blade - Total Flow Characteristics for Ambient External Conditions - Single Blade

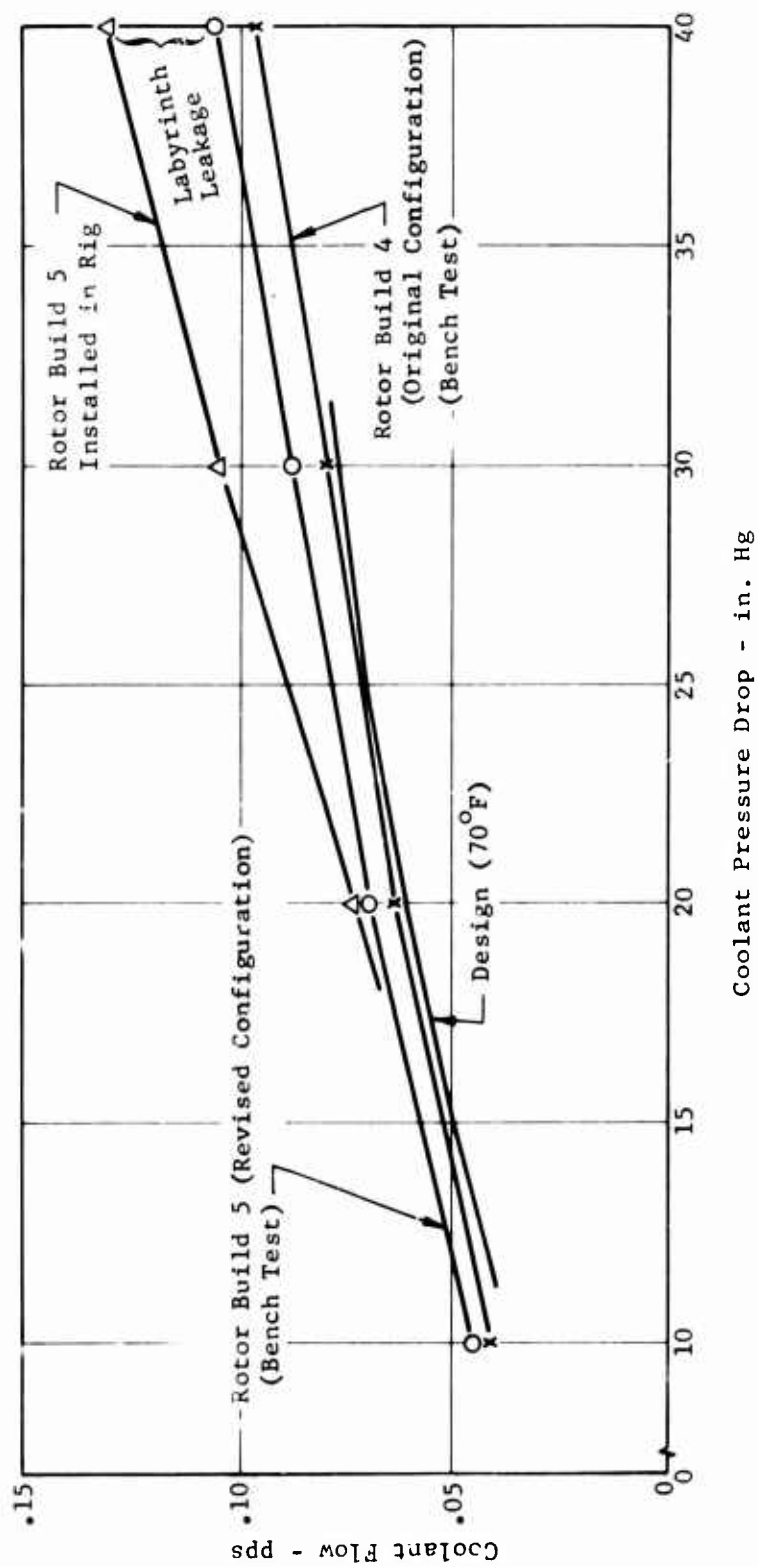


Figure 102. Turbine Totor Cooling Airflow Characteristics - Rotor Build 5.

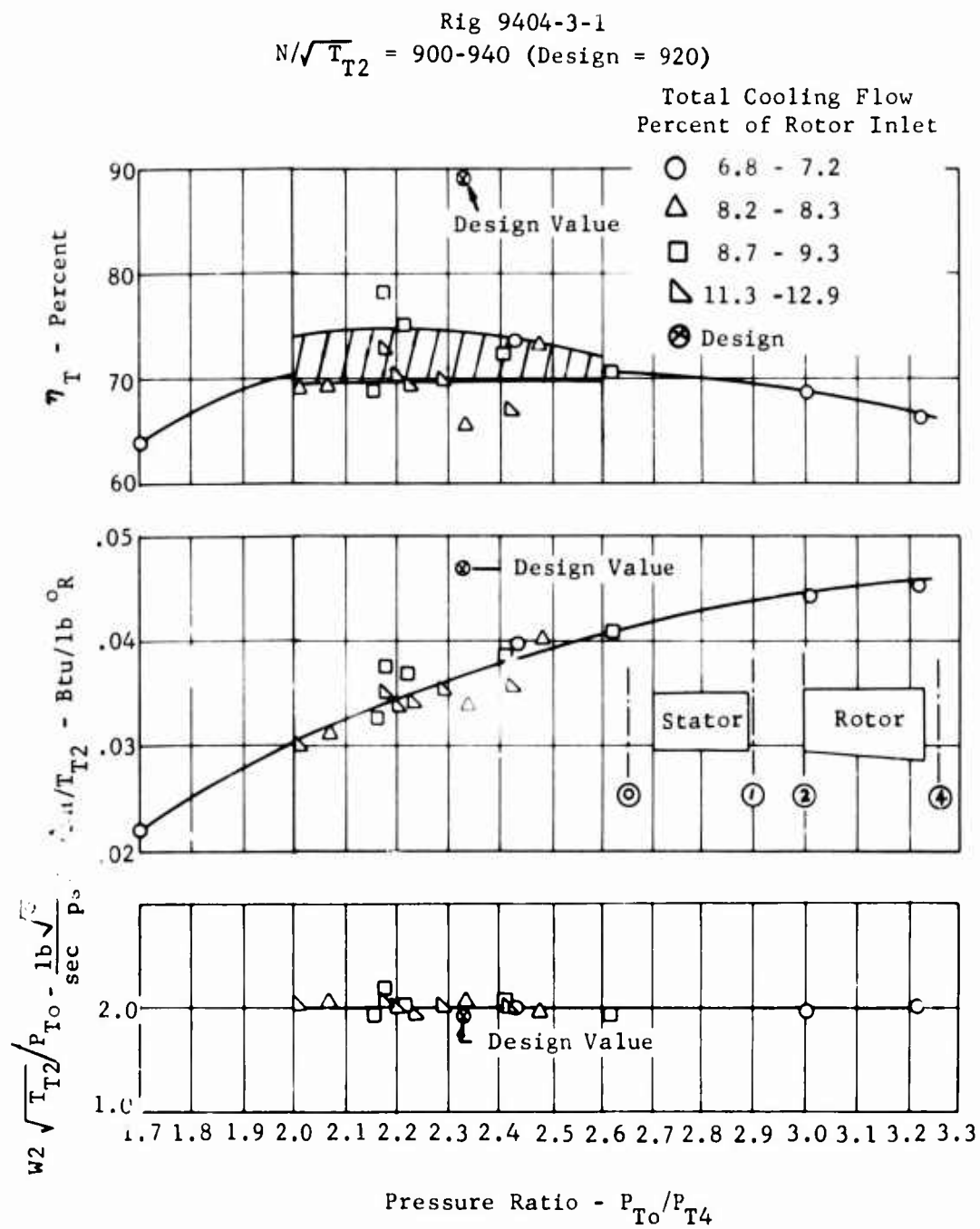


Figure 103. Turbine Performance Test Results.

Design Point Data: Gas Generator Application

Inlet Weight Flow	4.0 lb/sec
Actual Work Output	140 Btu/lb
Inlet Temperature, Rotor	2500° F (Stator Absolute Leaving)
Inlet Pressure	229.9 in Hg A
Gas Gen Rotor Speed	50,000 rpm

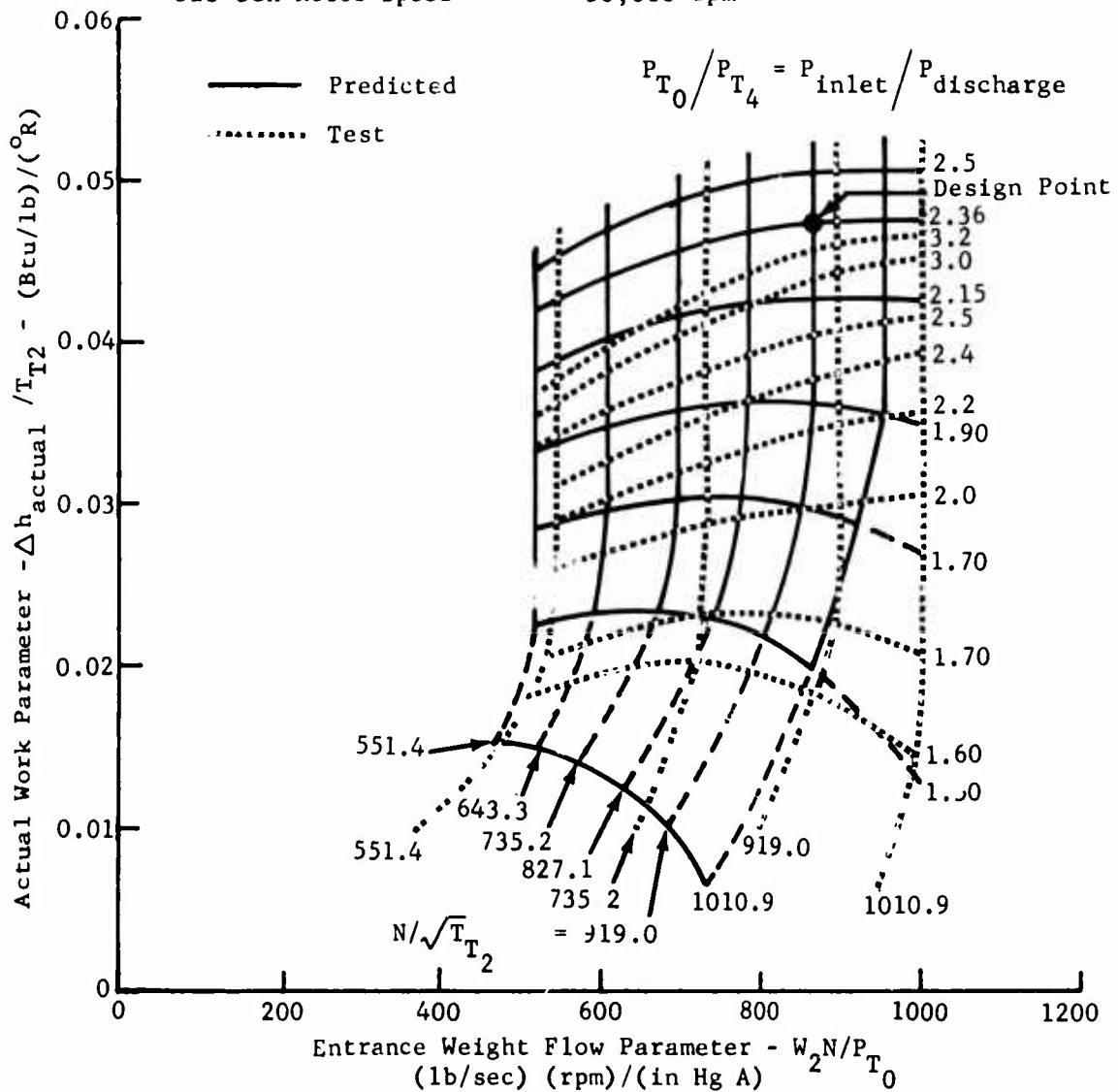


Figure 103 (a). Universal Turbine Map - Comparison of Estimated and Test Performance.

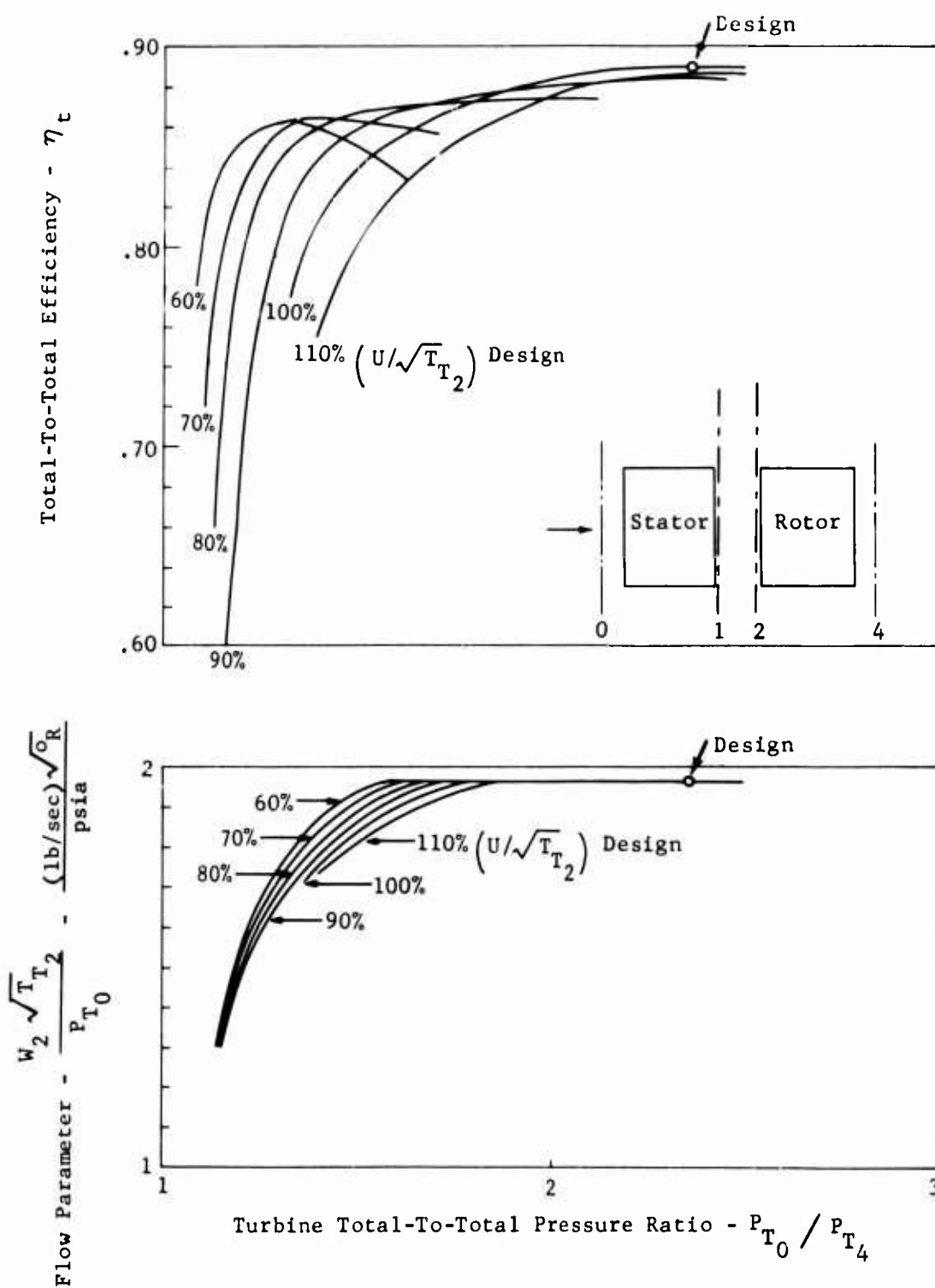


Figure 103 (b). Estimated Overall Turbine Performance Map.

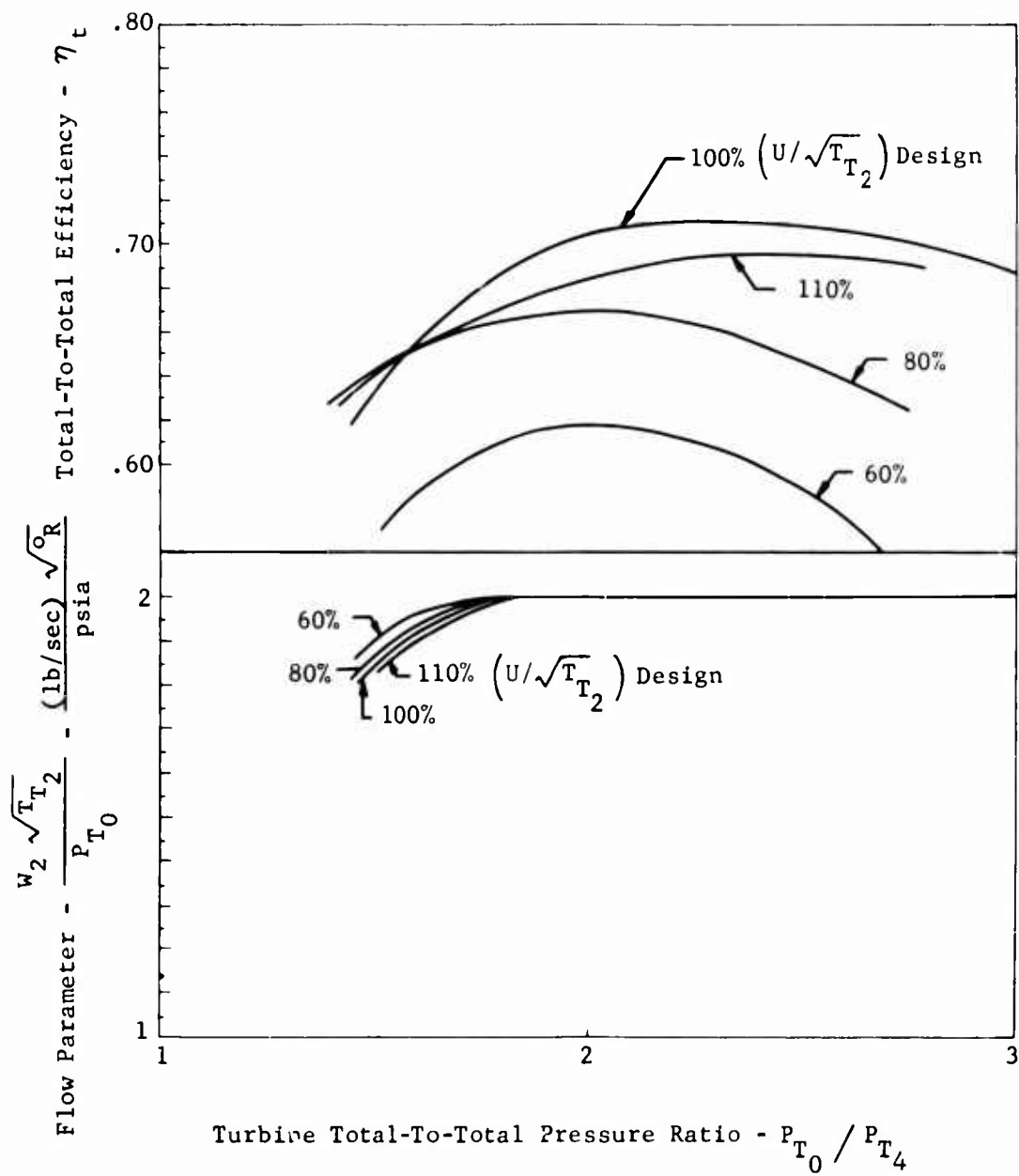


Figure 103 (c). Test Overall Turbine Performance Map

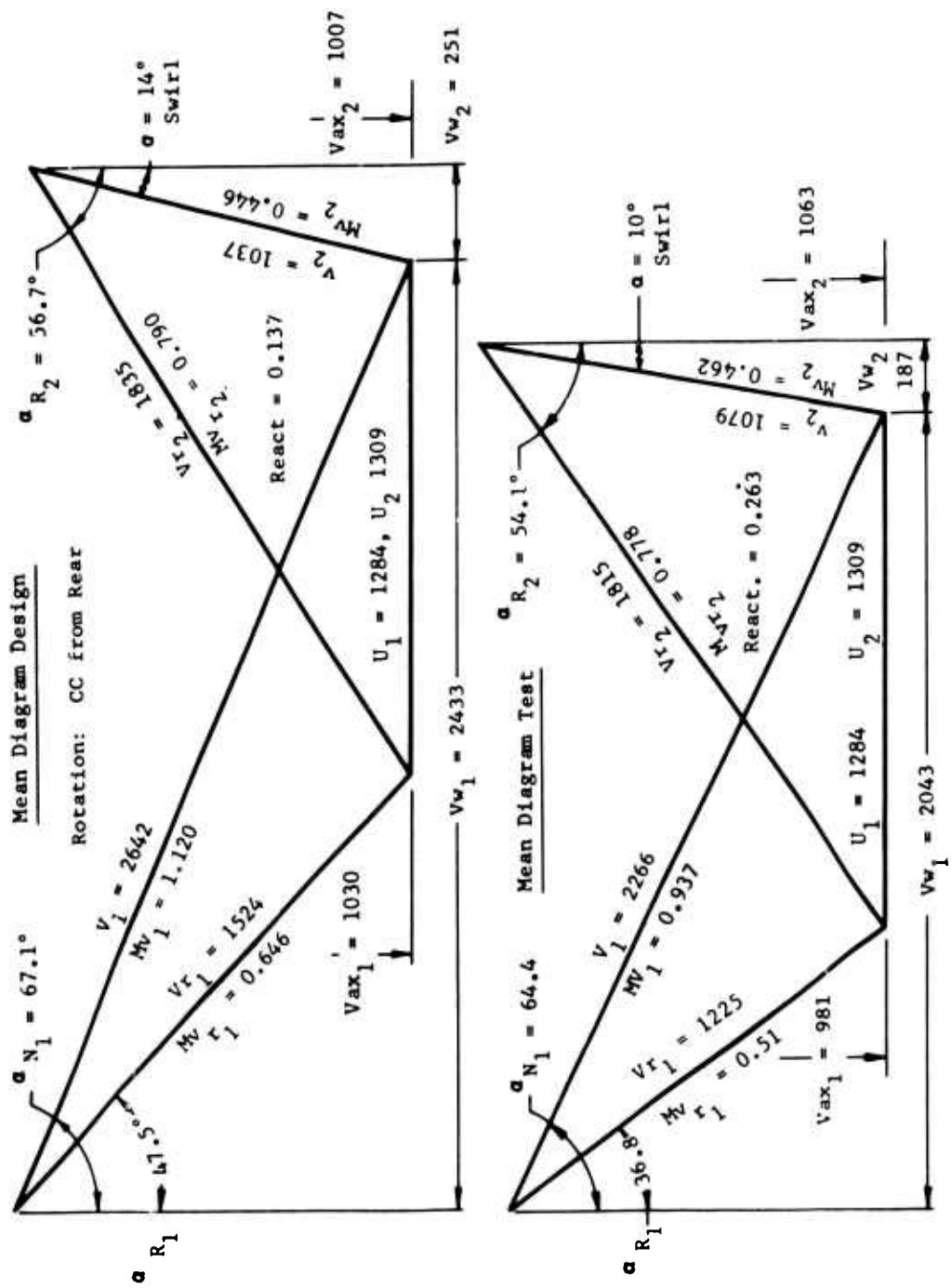


Figure 104. Comparison of Design With Test Vector Diagram.

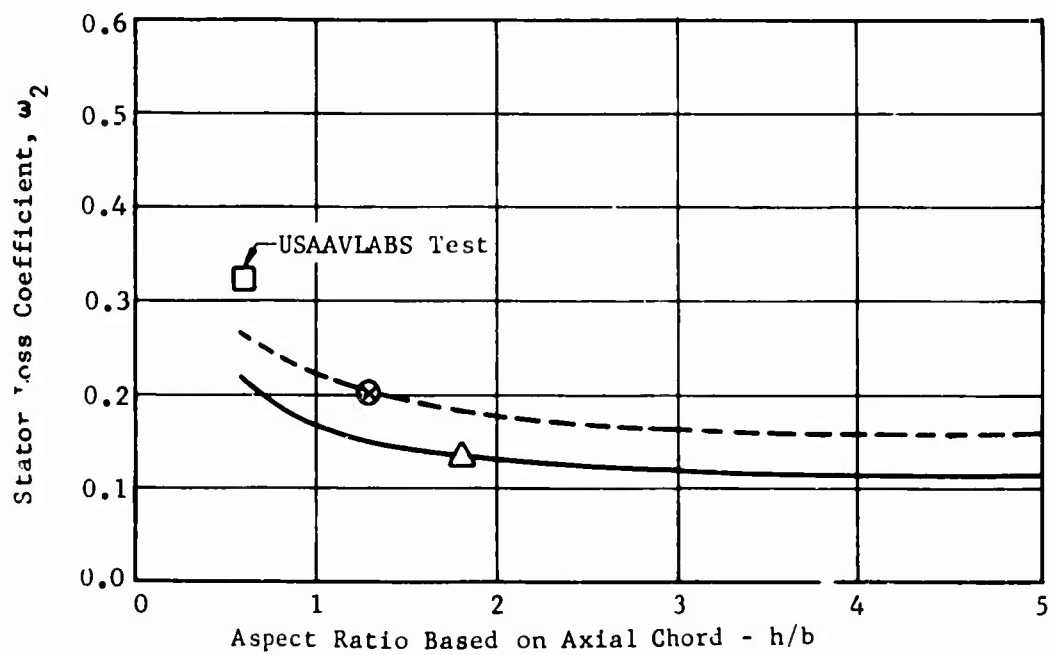
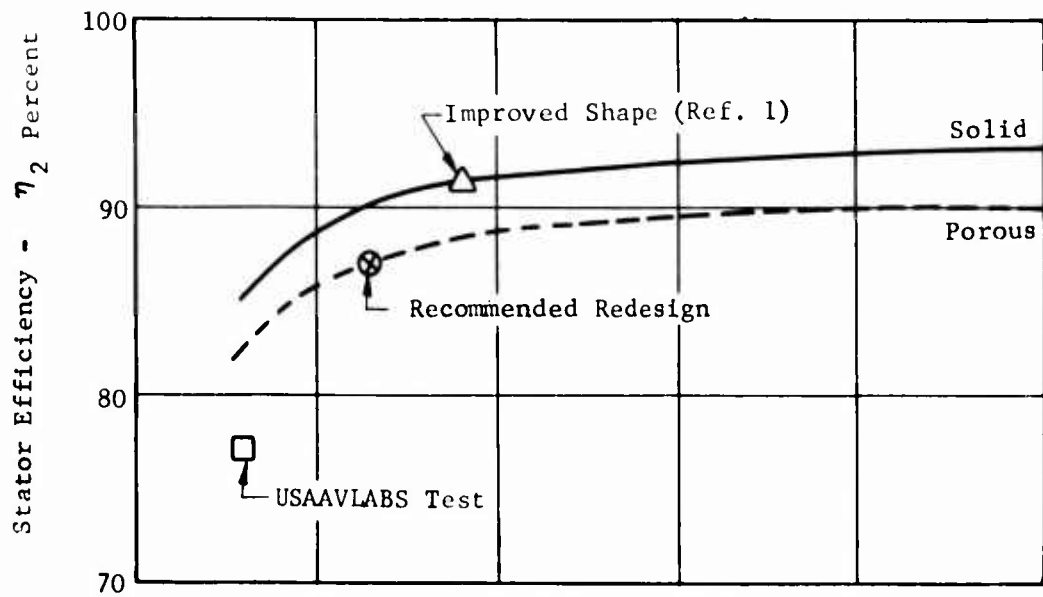


Figure 105. Stator Loss Coefficient and Efficiency Versus Aspect Ratio.

	PRESENT		MODIFIED	
	Stator	Rotor	Stator	Rotor
Average Height, in.	.541	.639	.78	.73
Axial Chord, in.	.938	1.142	.60	.78
Axial Aspect Ratio	.576	.560	1.30	.936

— Present
 - - - Modified

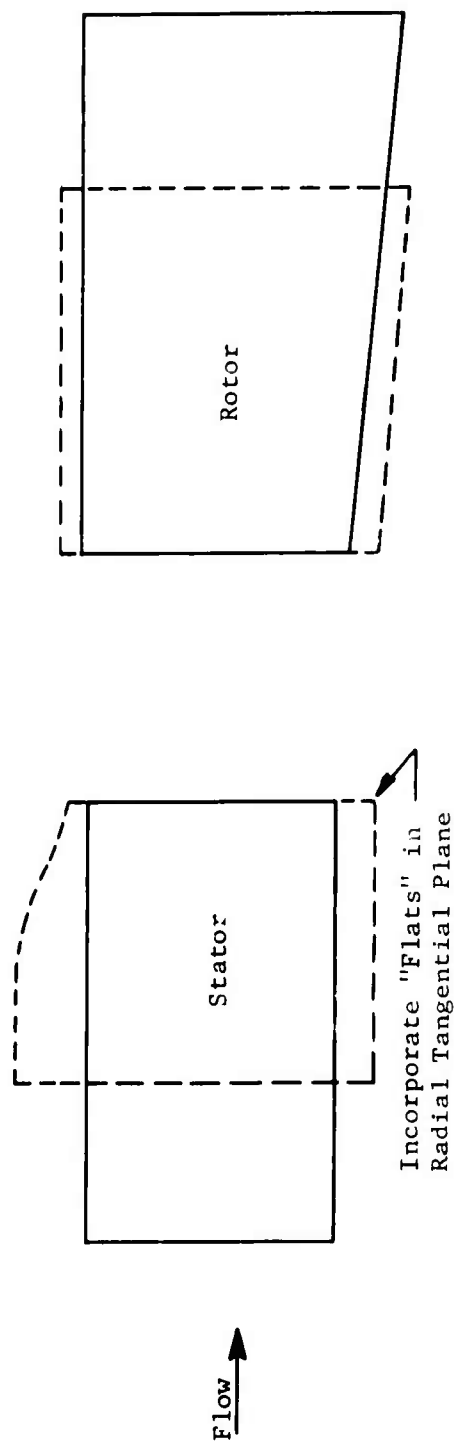


Figure 106. Comparison Between Present USAAVLABS Turbine and Recommended Modified Design.

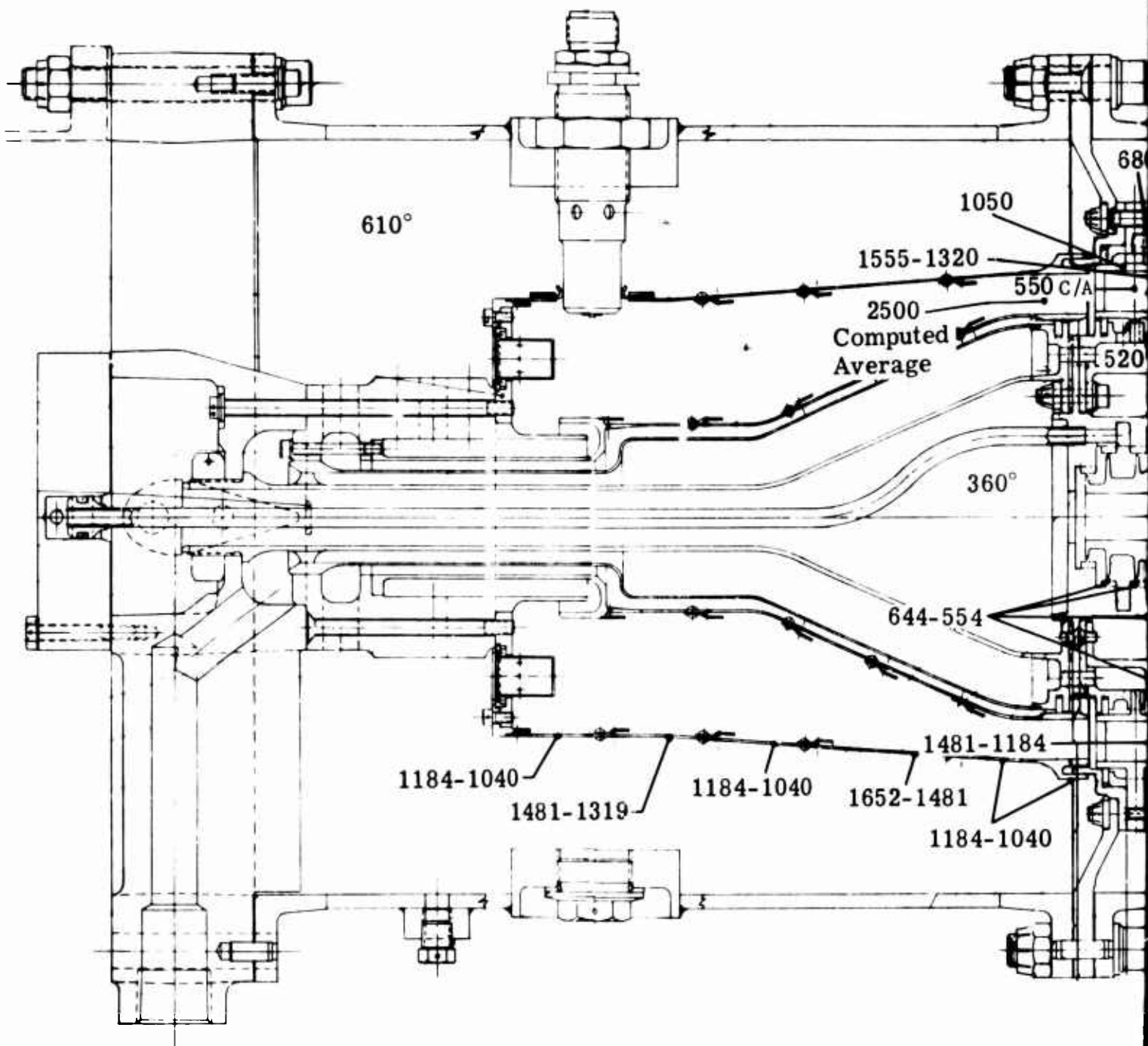
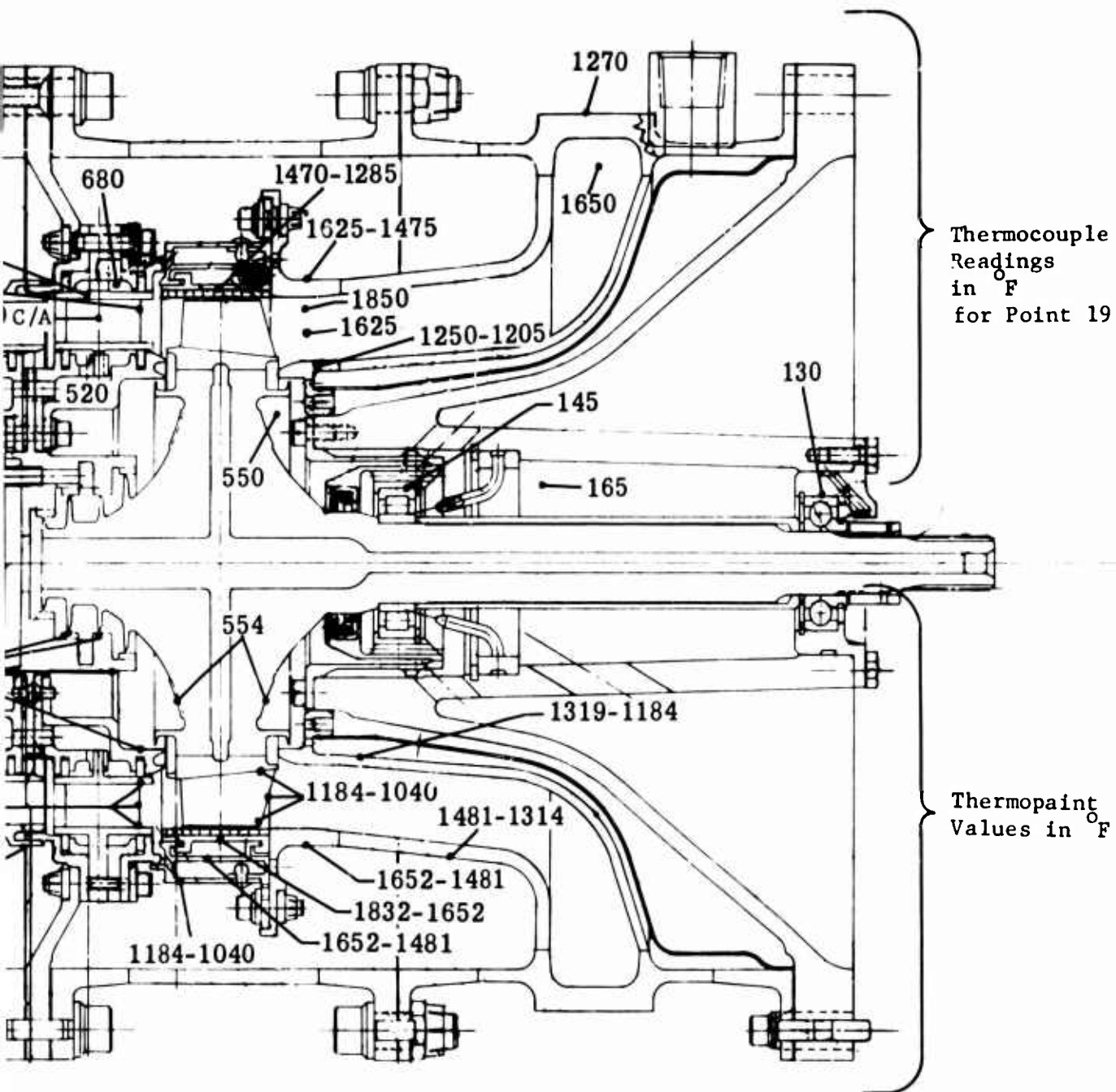


Figure 107. Gas and Metal Temperatures During Test - Rotor Build 5.



Test Point 19 - Tur
All Pressures are s

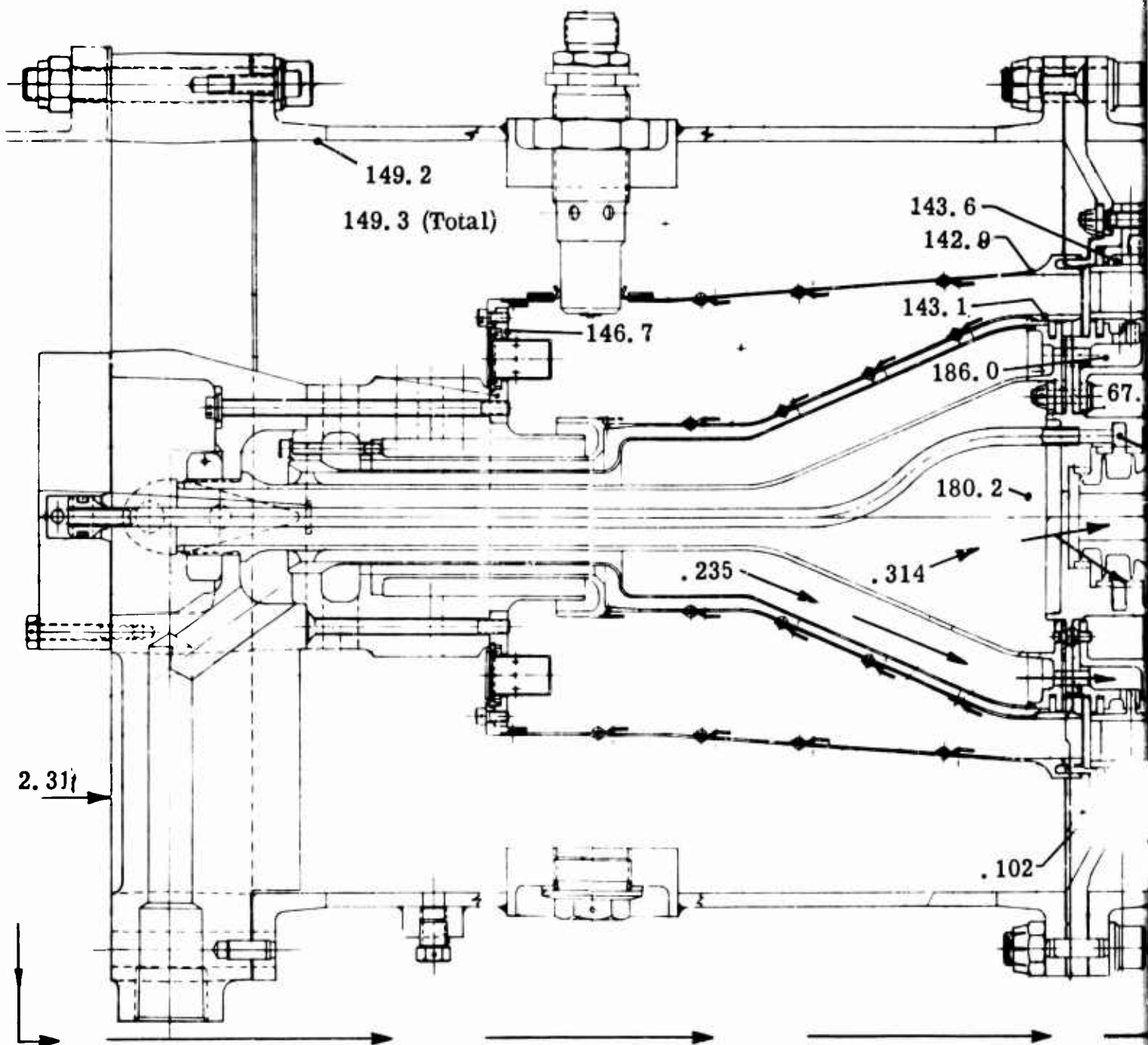
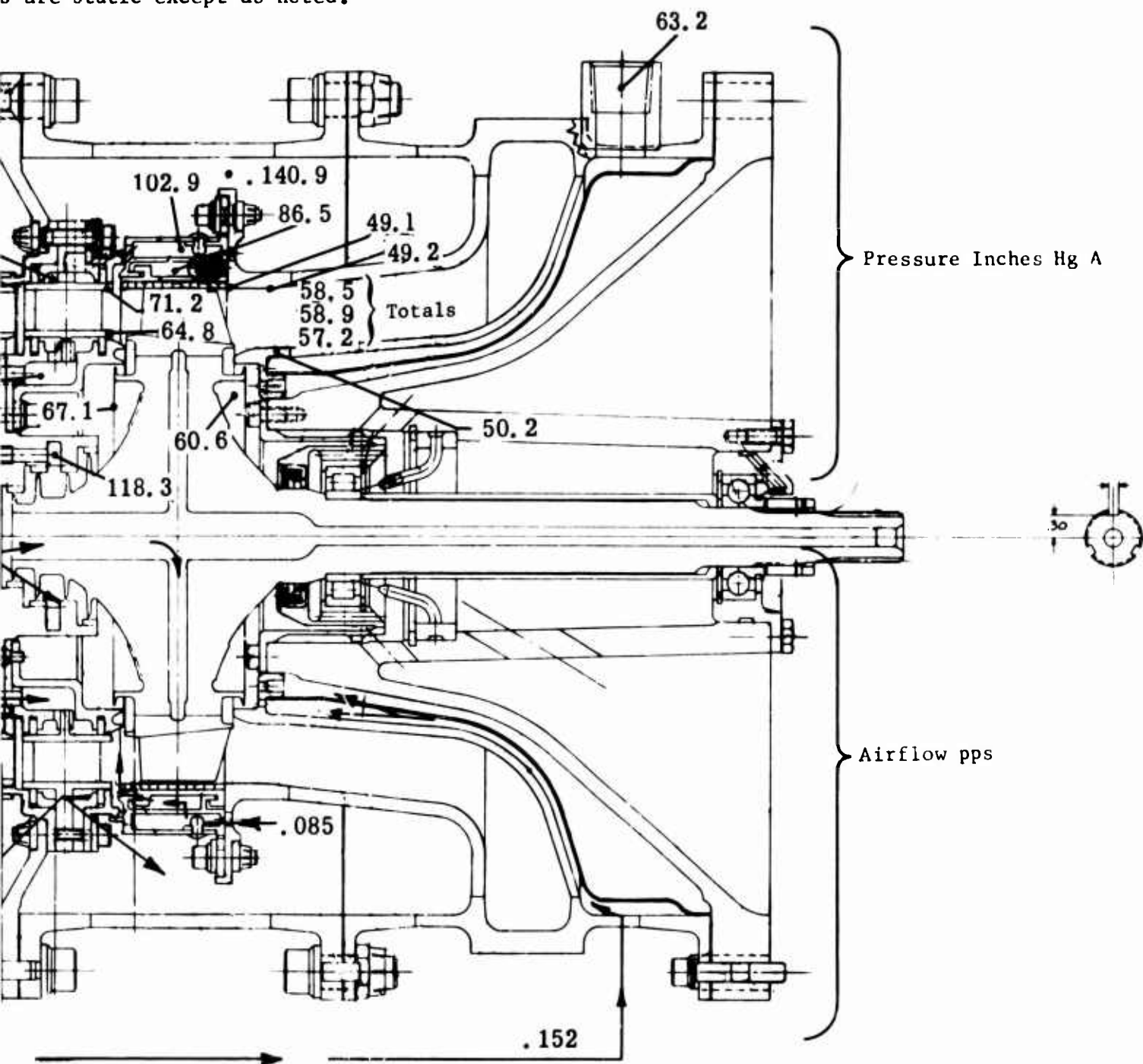


Figure 108. Pressures and Airflow Values During Test - Rotor Build 5.

A

9 - Turbine Inlet Temperature 2500°F

s are static except as noted.



BLANK PAGE

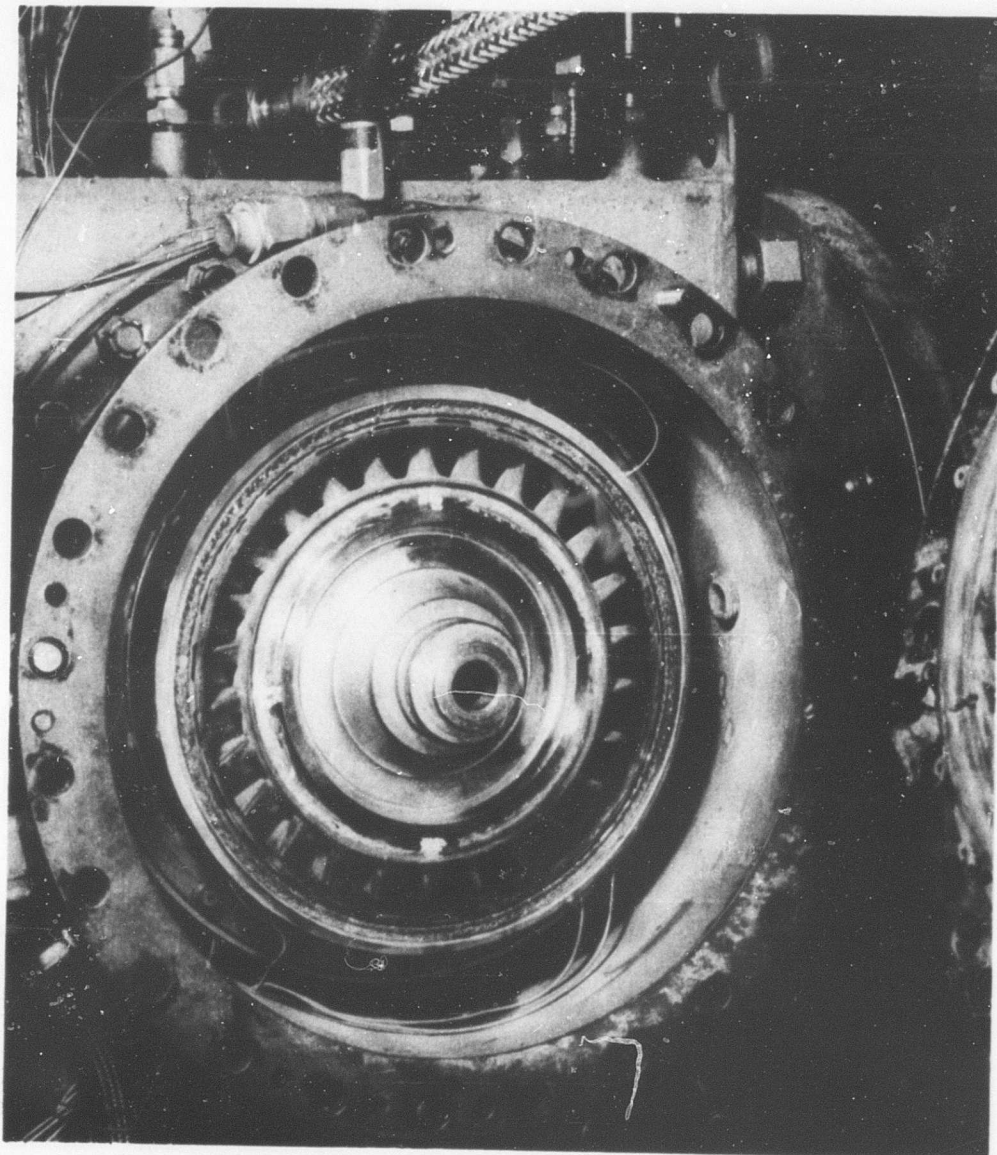


Figure 109. Turbine Rotor.

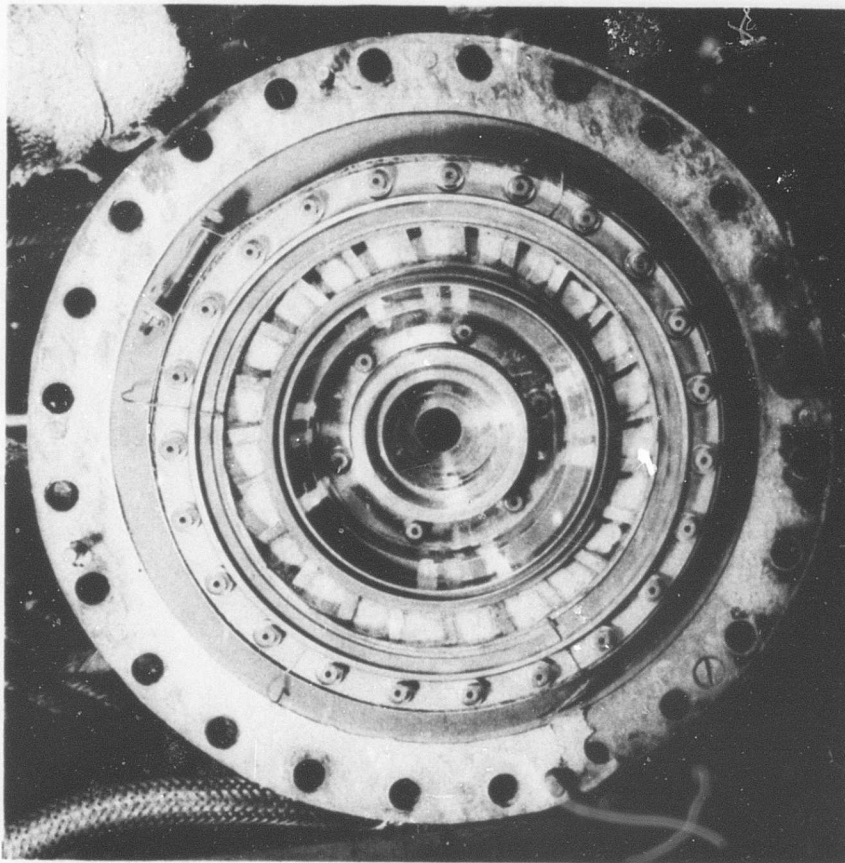


Figure 110. Turbine Stator.

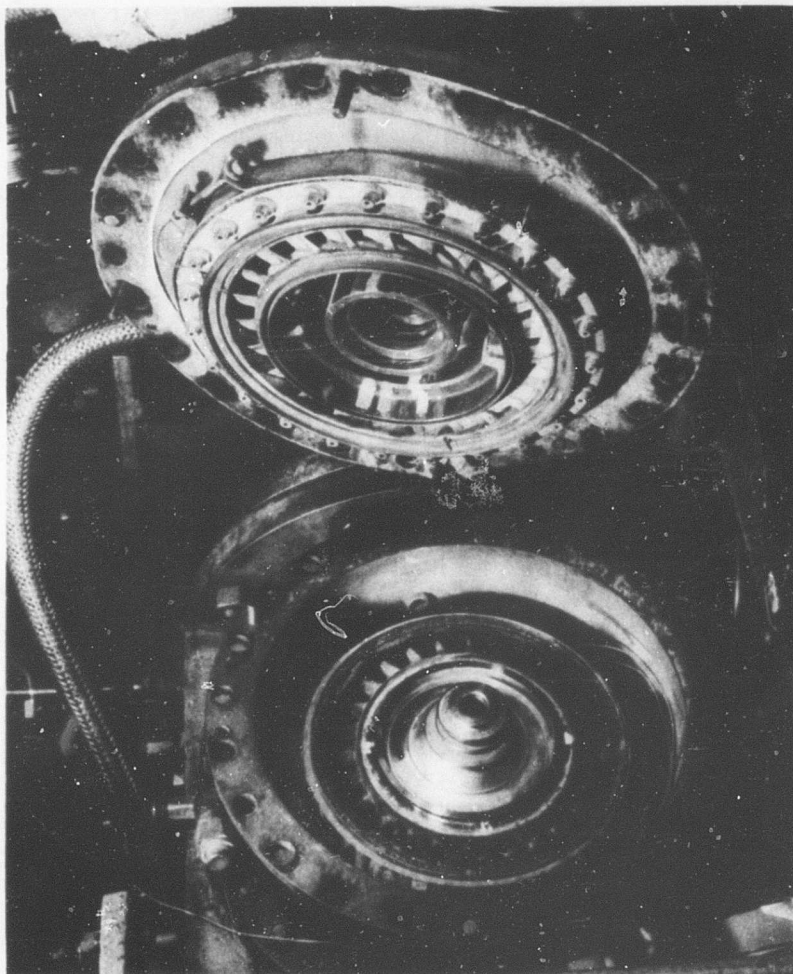


Figure 111. Turbine Rotor and Stator.

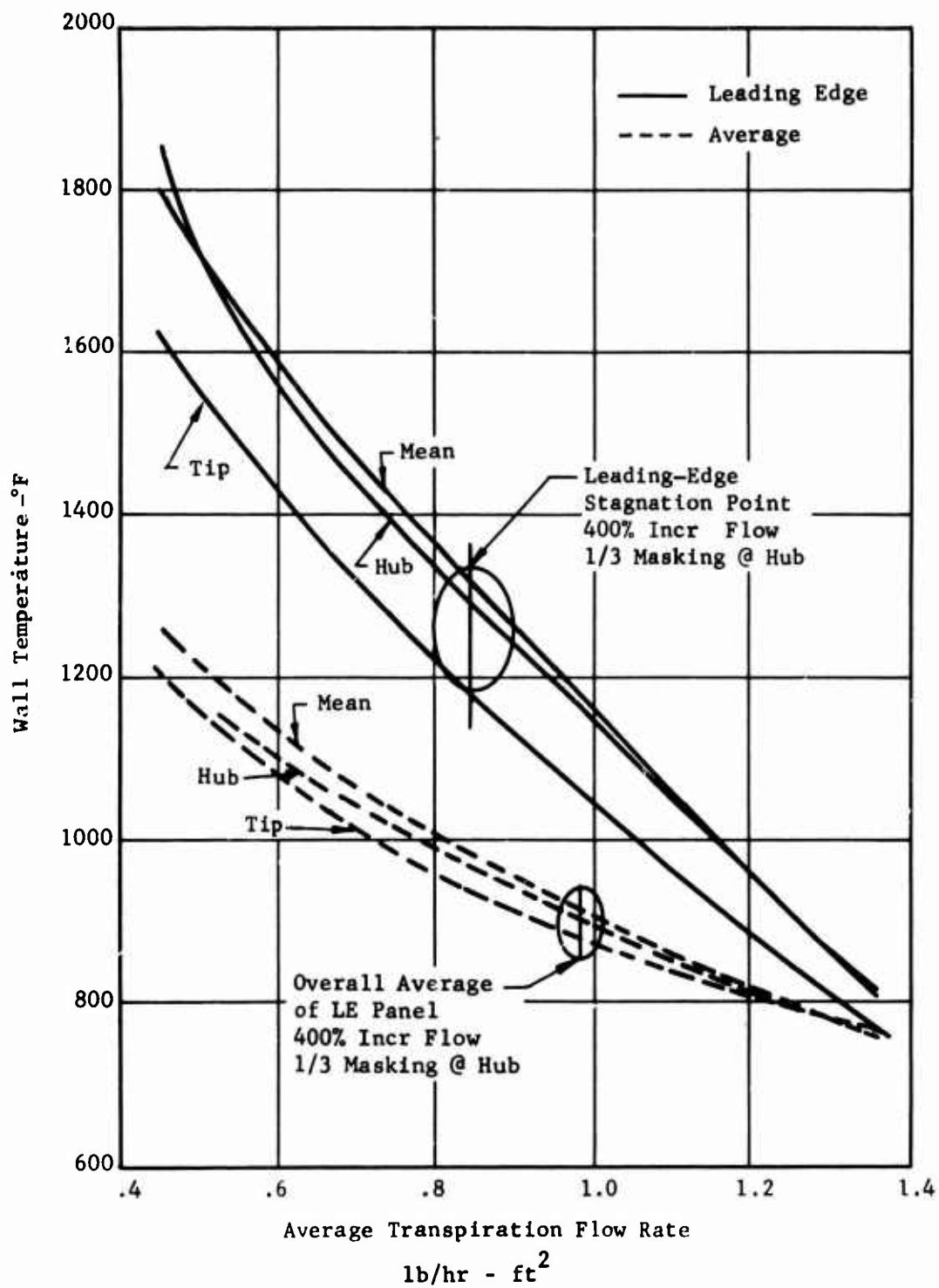


Figure 112. Turbine Rotor Blade Skin Temperature Leading-Edge Pressure Side Channel.

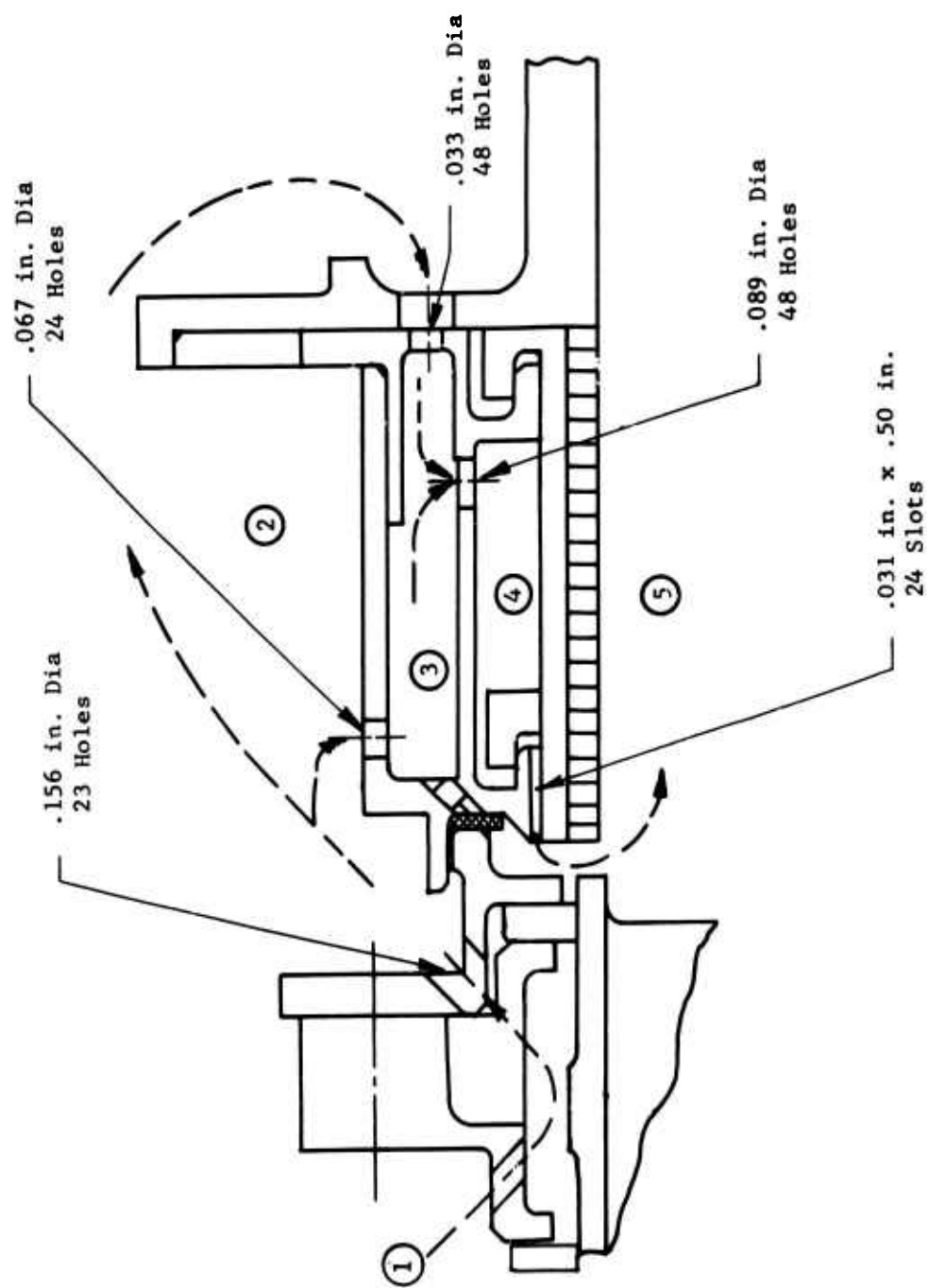


Figure 113. Airflow Path Through Shroud Support Assembly.

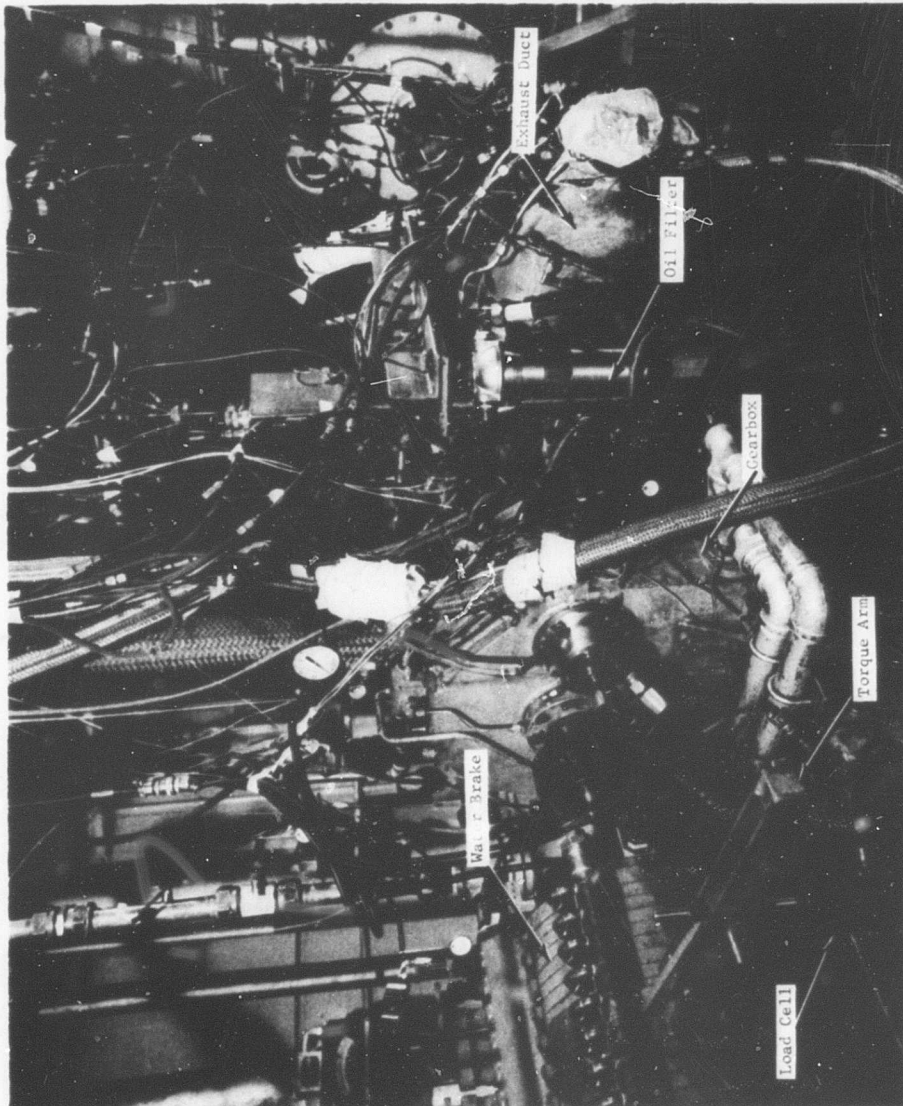


Figure 114. Test Cell Installation - Rear View.

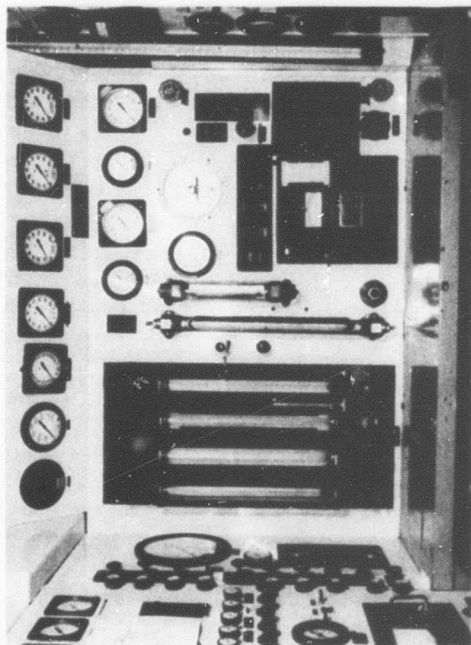


Figure 115. Rig Control Panel.

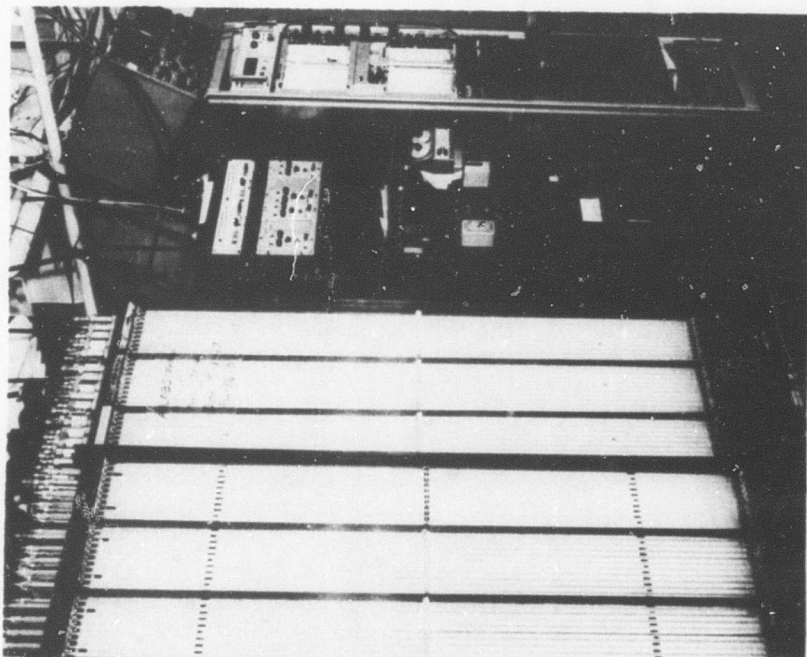


Figure 116. Rig Instrumentation Panel.

CONCLUSIONS

1. The program demonstrated that the advanced technology incorporated in the turbine design relative to blade cooling and turbine mechanical integrity can be applied to the design of advanced small gas turbines for high-performance aircraft.
2. The mechanical and thermal characteristics of the transpiration-cooled turbine blading over a range of gas temperatures up to 2500°F were demonstrated.
3. The transpiration-cooled blading design has sufficient cooling margin to tolerate the local peak gas temperatures of about 3300°F as well as to offer growth potential for operation up to stoichiometric temperature levels.
4. The large change in effusion of cooling air through the surface of the blades produced no significant effect on turbine performance over a wide range of pressure ratios (see Figures 82, 91, and 103).
5. The stator blade aerodynamic profile shape was compromised to achieve proper distribution of the cooling air and by manufacturing limitations. In addition, secondary flow effects associated with low aspect ratio and high works were observed to produce an adverse effect on stage performance.
6. The blade-to-disc attachment of a small, high-temperature, high-work turbine presents a severe structural design problem. Electron beam butt welding of blade to disc employed in this program offers a satisfactory solution provided the weld joint at both faces is accessible for inspection and the welding process can control beam incidence and weld path concentricity.
7. Cooling air leakage was substantially reduced by welding the stator blade assembly into an integral which eliminated the interblade shelf sealing requirements and facilitated the sealing configuration for blade butt and cooling air plenum.
8. The use of rub-tolerant "Nicroseal" fill in the rotor shroud honeycomb offers promise for successful application in high-temperature, low-tip-clearance designs.

9. The annular vaporizing combustor of this program, which operated with high efficiency (99 percent) over a wide range of test conditions (up to 2650°F), offers potential for use in advanced small gas turbines.

RECOMMENDATIONS

1. Continue to develop the application of transpiration-cooled turbines to small gas turbine engines.
2. Investigate the effects of aspect ratio and loading on turbine blade efficiency.
3. Evaluate the aerodynamic and mechanical characteristics of small, high-temperature high-work turbines in order to achieve optimum performance in this type of turbine stage.
4. Investigate methods of rotor blade-to-disc attachment for small turbines.
5. Study advanced blade fabrication techniques with a goal of achieving the minimum compromise in the aerodynamics, thermal, and structural characteristics of the blade.
6. Carry out a design study of air cooling and sealing arrangements for small high-temperature turbines which will provide minimum pressure loss, minimum leakage, and require the least cooling air pumping work.
7. Conduct a cyclic endurance test of a small transpiration-cooled turbine to evaluate the thermal fatigue characteristics of the component.

APPENDIX
TEST PROGRAM SUMMARY

TABLE XXIII
COMBUSTOR TEST CHRONOLOGY

Build No.	Vaporizer Configuration No.	Test Hours		Test Objective	Remarks
		Burn	Cumulative		
1	1	.17	6.08	Combustor cold flow determination. Two-point fuel injection upstream of air swirler plane.	Partial combustion on top portion only.
2	2	4.17	4.33 20.92	Combustor hot and cold performance and ignition sensitivity with two-point fuel injection downstream of air swirler plane.	Checked out rotating probe. Circumferential exit temperature profile showed two high peaks at F/A of .02.
3	3	1.33	5.66 22.58	Combustion performance with two-point fuel injection in line with air swirler plane.	Slight angular displacement of exit temperature profile and lower combustion efficiency at F/A of .02.
4	-	-	-	Combustion performance with circumferential dam.	Not tested at this time since reworks were required to assemble parts.
5	4	6.83 12.5	30.58	Combustion performance with two-point downstream fuel injection and axial dams to spread fuel.	Exit temperature profile at F/A of .02 improved in sections but peaks still evident. Dam location is too sensitive.

TABLE XXIII - Continued

Build No.	Vaporizer Configuration No.	Test Hours		Test Objective	Remarks
		Burn	Cumulative		
6	5	1.25	13.75 32.58	Combustion performance and durability with four-point downstream fuel injection and no dams.	Ran F/A's from .015 to .030; exit temperature profile improved. Burning of inner liner cooling air deflectors and rotating probe deflector as noted and rectified.
7	6	.5	14.25 35.17	Combustion performance using two-point downstream fuel injection with axial instead of swirl primary air.	Unstable burning at F/A of .016.
8	4	1.92	16.18 37.08	Repeat of Build 5 above with axial dams repositioned.	Ran F/A's from .010 to .033. Exit temperature profile high.
9	7	6.08	22.25 43.83	Combustion performance using four-point downstream fuel injection and four axial dams.	Ran F/A's around .020. Rotated combustor parts to check effect on exit temperature profile - negligible effect.
10	8	7.83	30.08 52.75	Combustion performance with four-point downstream fuel injection and circumferential dam.	Ran F/A's of .020 and obtained improved exit temperature profiles. Rotated parts with negligible effect on profile.

TABLE XXIII - Continued

Build No.	Vaporizer Configuration No.	Test Hours		Test Objective	Remarks
		Burn	Cumulative		
11	5 & 8	19.42	49.50	73.00	Comparison of four-point downstream fuel injection with and without the circumferential dam.
12	8	13.42	62.92	97.25	Combustion performance with four-point fuel injection, circumferential dam, and upstream air straightening screen.
13	8	4.17	65.08	109.50	Same as Build 12 with matched fuel injection hole sizes.
14	8	3.58	70.66	119.83	Same as Build 13 with diluent slots moved forward.
15	8	5.50	76.17	132.92	Combustion performance and cold flow pressure drop with four-point fuel injection, circumferential dam, and downstream diluent slot location.
16	8	3.42	79.58	137.83	Same as above.

TABLE XXIV
STATOR TEST SUMMARY

Build No.	Hours Burn	Cumulative Burn	Total	Test Objective	Remarks
1	-	-	9.0	Nozzle performance with and without cooling air	Nozzle characteristic obtained.
2	-	-	15.83	Nozzle exit survey	Exit data obtained.
3	2.5	2.5	29.58	Hot test using fiber glass seal material	Reached max avg turbine inlet temp. of 2040°F at F/A .020.
4	5.25	7.25	36.83	Hot test with improved fiber glass seal configuration	Reached max turbine inlet temp. 2580°F at F/A .032.
5	11.58	19.33	49.08	Hot endurance with improved fiber glass configuration	Burned seal at outer plenum caused test stop. Max F/A = .026
6	6.08	25.42	59.66	Hot test with integral welded stator assembly	Reached max avg turbine inlet temp. 2650°F test terminated because of leaking fuel feed fitting which resulted in torching.
7	-	25.42	69.17	Aero cascade test	Ran 1.3, 1.6, and 2.2 pressure ratio.
8	-	25.42	87.92	Aero cascade test (Deleted defectors at the inlet)	Ran 1.6, 1.9, 2.2, and 2.8 pressure ratio with 4 to 8 percent cooling air.

TABLE XXV
FULL-STAGE RIG TEST SUMMARY

Build No.	Hours Cumulative		Test Objective	Remarks
	Burn	Total		
1	.33	48.33	1. Mechanical integrity 2. Turbine performance 3. Main burner check	Completed test objectives. Disassembled to install high temperature stator outer seals and to instrument for hot testing.
2	-	53.75	1. Turbine performance checkpoint 2. High temperature test	Ran 18,000 rpm performance point, then gearbox bearing seized causing shutdown. Disassembled rig for precautionary inspection. Gearbox repaired.
2b	-	62.17	1. Turbine performance checkpoint 2. High temperature test	Ran 30,000 rpm performance point, then while setting 18,000 rpm point had failure of the connecting shaft to gearbox. Complete disassembly.
3	3.83	74.25	1. Turbine performance checkpoint 2. High temperature test	Rebuilt rig with stator no. 1 and rotor no. 2. Ran 30,000 rpm performance. After hot point at F/A of .026 and 39,000 rpm, one rotor blade leading-edge skin was lost. Repaired rotor, replaced roller bearing inner race which was damaged during ultrasonic cleaning.
4	1.58	77.50	High temperature test	Ran F/A at .026 and 39,000 rpm and lost two rotor blade leading-edge skins. Disassembled rotor and repaired.
5	14.75	100.83	High temperature test	Completed program objectives. Ran at 2500°F. Ran 5 percent rotor cooling flow at 2446°F. Failed interconnecting shaft.

FAILURE ANALYSIS

During the complete stage turbine component tests, failure of the test equipment interconnecting shaft between the turbine rig and reduction gearbox occurred on two occasions. The first occurred during Rebuild 2B at 18,000 rpm and the second during Rebuild 5 at 50,000 rpm. After the first failure, the interconnecting shaft was changed from a two-piece design with a critical speed of 35,400 rpm to a single spool piece with a critical (at 64,500 rpm) above design speed. A vendor fabrication discrepancy in the revised shaft was responsible for its failure.

An analysis of the two failures follows. Posttest failure analysis of the rig hardware after Rebuild 2B failure was carried out. Although the mode of primary failure could not be established at that time from the analysis of available evidence, the following possibilities were suspect and corrective action was taken to ensure improvement in the configuration for the following build:

1. Improper installation of the roller bearing retaining ring permitting bearing displacement and finally causing loss of the bearing for the rotor support - Special engineering inspection of this section of the rig was performed during the rig build-up.
2. Heavy rotor tip rub - Radial clearances were increased above the .008 inch specified minimum.
3. Loss of a blade due to the progression of the electron beam weld shrinkage crack between blades - Subsequent weld trials with new fixturing and revised process techniques produced excellent fusion weld joints on the front and rear sections of the disc. These revisions were incorporated in the welding of the second rotor assembly.
4. Large deflection of the interconnecting drive shaft caused by operation approaching the shaft's critical speed - Progressive unbalance and displacement of the interconnecting shaft bent the gearbox drive shaft. At the same time the interconnecting shaft's large deflections caused it to rub a web in the housing and the shaft failed. Corrective action consisted of providing a one-piece interconnecting shaft with splined adapter ends to the gearbox shaft and turbine. Nitrided splines were specified to assure hardened splined joints for low wear. Shaft wall thickness was chosen to raise the critical speed (64,500 rpm) and put it beyond the turbine's design point of 50,000 rpm.

Posttest analysis of the rig hardware after Rebuild 5 provided the following reconstruction of events. Circumferential cracking developed in the interconnecting shaft approximately 2-3/4 inches from the gearbox spline shoulder as a result of stresses developed from shaft deflection at the 50,000-revolution-per-minute operating speed. Shaft displacement was monitored during the test by means of the Bently pickup, which was located in a

plane about 1/2 inch from the gearbox spline end shoulder. A maximum deflection of $\pm .015$ inch was observed during operation from 48,000 to 50,000 revolutions per minute; normal deflection had been $\pm .005$ inch. The shaft deflection is greater at 2-3/4 inches from the shoulder where the circumferential cracks occurred. This cracking progressed, resulting in unwrapping of the shaft (Figure 117). The interconnecting shaft had been inadvertently nitrided on all surfaces including the inner and outer diameters, resulting in a brittle case on the shaft walls (.015 to .020 inch each side) and a thin core cross section (.025 to .030 inch). The blueprint had specified nitriding only on the shaft's female splines. Nitriding of the shaft produces very high compressive residual stresses in the brittle case. Subsequent shaft deflection results in increasing the compressive stress in the shaft wall inner case and producing a tensile stress which cannot be supported in the brittle case of the outer wall. Furthermore, the flexure load on the shaft wall must be carried out by the reduced section nonbrittle core which results in almost doubling the design stress level in the shaft.

Inspection of the interconnecting shaft revealed that each axial crack in the shaft's inner diameter was interrupted and displaced at the circumferential cracks (Figure 118). This indicates that the circumferential cracks occurred first and the axial cracks subsequently when the shaft unwrapped. Failure of the connecting shaft and resulting unbalance displacement of the gearbox input shaft spline end caused this shaft to bend and fracture.

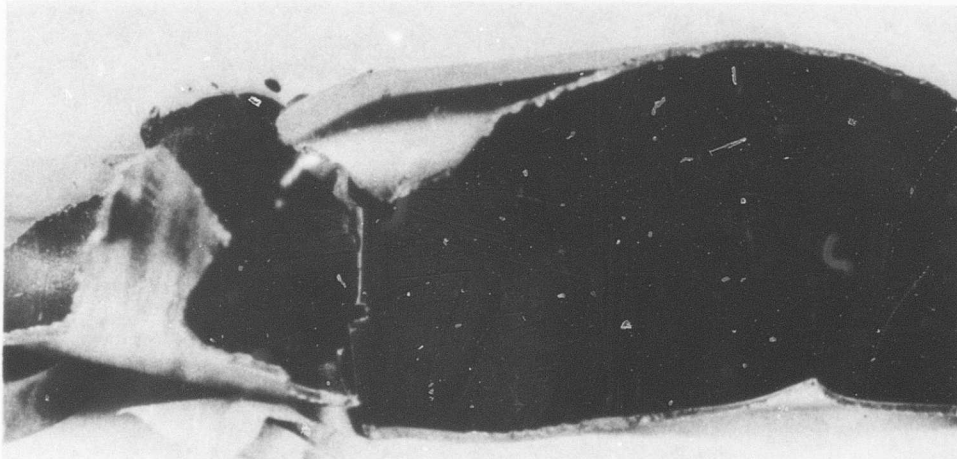
Macroetch examination of the gearbox pinion shaft and spline assembly showed that twisting or torsion did not occur (Figure 119) except in the last stage of fracture.

Failure of the connecting shaft removed the only restraint on the turbine which immediately oversped, with two results:

1. The large out-of-balance load on the turbine shaft spline (with its still-attached section of connecting shaft end) caused the shaft spline end to fracture in bending. No evidence of torsional failure was observed.
2. The higher centrifugal loads on the blades caused the break at the gas shelves at about 150 percent of design speed. Although the electron beam weld at the rotor blade-to-hub rear disc did not provide 100 percent weld attachment of the blade to the rear disc, this was not a factor in the failure (Figure 120). The blade-to-front disc electron beam weld exhibited excellent fusion and attachment.

Reexamination of Rebuild 2B parts was made in the light of the Rebuild 5 failure analysis. The condition of the parts after Rebuild 2B test was found similar to the parts as described in the Rebuild 5 discussion. Figure 121 shows the two-piece interconnecting shaft and the broken spline end from the gearbox.

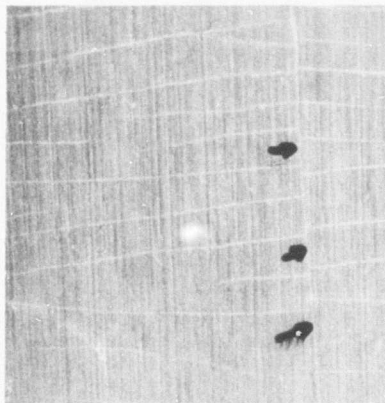
It was concluded that the primary cause of failure was the same in both cases - failure of the interconnecting shaft - and that the reasons 1, 2, and 3 cited as possible primary causes for the Rebuild 2B failure were merely consequences of the interconnecting shaft failure.



Approx 2x

The ID of the interconnecting shaft showing the circumferential cracks (arrows).

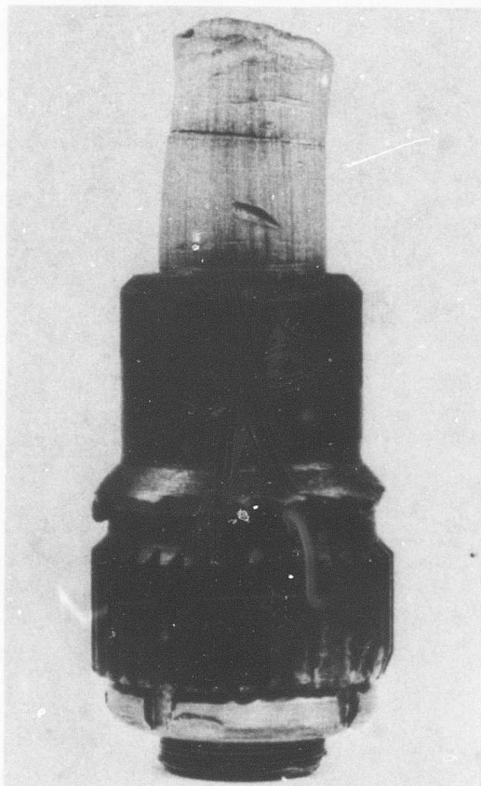
Figure 117. Interconnecting Shaft ID.



Approx 10x

A close-up of the shaft ID showing the axial cracks interrupted and displaced across the circumferential crack, indicating that the circumferential cracks occurred first.

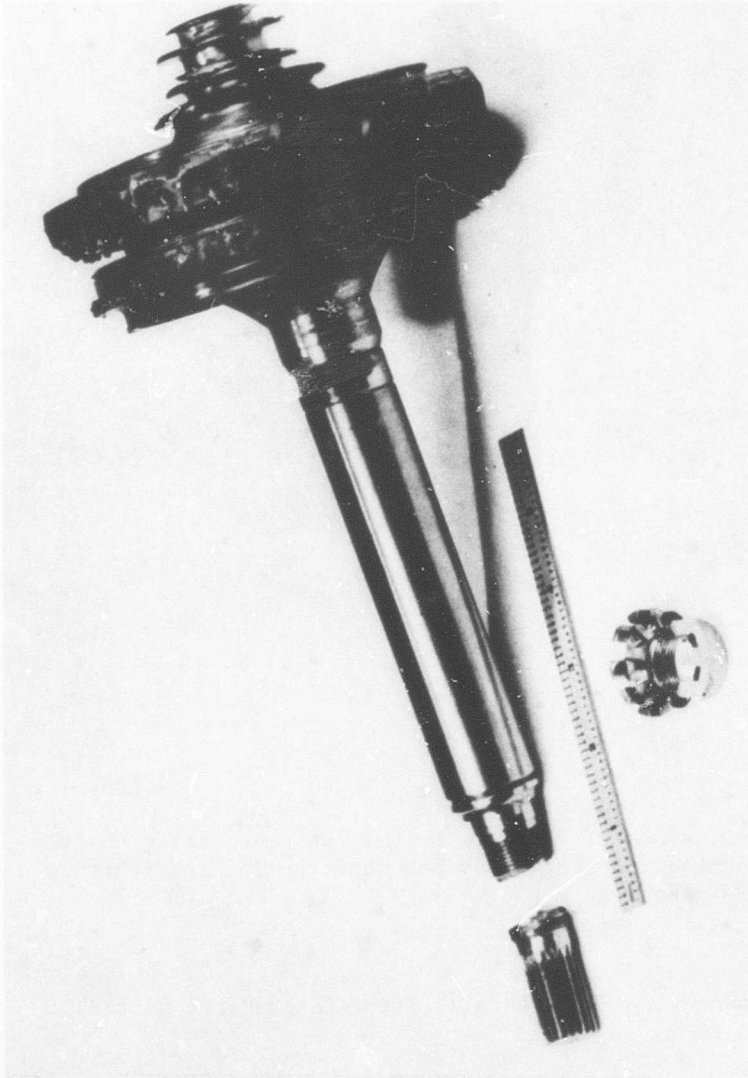
Figure 118. Interconnecting Shaft ID.



Approx 1x

The input pinion gear shaft microetched to show the in-line flow lines indicating that no twisting of the shaft was experienced and that the connected parts had been operating in line at one speed just prior to failure.

Figure 119. Gearbox Input Shaft Spline End After Test - Rotor Build 5.



Approx 1/2 x

A view of the turbine rotor assembly showing the fracture location at the spline end, the fractures through the rotor blade-rear hub mating surfaces and the gas shelves, and the severe rub in the roller bearing inner race.

Figure 120. Turbine Rotor After Test - Rotor Build 5.



Approx 1 x

A photo showing the locations of fracture in the interconnecting shaft (three LH pieces), and the industrial gearbox shaft spline end fracture aft of the splines (RH piece).

Figure 121. Interconnecting Shaft Details After Tests-Rotor Build 2B.

Unclassified

Security Classification

DOCUMENT CONTROL DATA - R & D		
(Security classification of title, body of abstract and indexing annotation must be entered when the overall report is classified)		
1. ORIGINATING ACTIVITY (Corporate author) Curtiss-Wright Corporation Wood-Ridge, New Jersey		2a. REPORT SECURITY CLASSIFICATION Unclassified
		2b. GROUP
3. REPORT TITLE SMALL GAS TURBINE ENGINE COMPONENT TECHNOLOGY - TURBINE VOLUME II - PHASE II SUMMARY REPORT		
4. DESCRIPTIVE NOTES (Type of report and inclusive dates) Final Report		
5. AUTHOR(S) (First name, middle initial, last name) W. Franklin J. Heilbron S. Moskowitz		
6. REPORT DATE August 1968	7a. TOTAL NO. OF PAGES 219	7b. NO. OF REFS 0
8a. CONTRACT OR GRANT NO. DA 44-177-AMC-182(T)	8b. ORIGINATOR'S REPORT NUMBER(S) USAAVLABS Technical Report 68-50B	
9. PROJECT NO. 1G162203D14413		
c.	9b. OTHER REPORT NO(S) (Any other numbers that may be assigned this report)	
d.	R-419-F2	
10. DISTRIBUTION STATEMENT This document has been approved for public release and sale; its distribution is unlimited.		
11. SUPPLEMENTARY NOTES Volume II of a two-volume report		12. SPONSORING MILITARY ACTIVITY US Army Aviation Materiel Laboratories Fort Eustis, Virginia
13. ABSTRACT This report describes the aerodynamic, thermal, and mechanical design and analysis, fabrication, and experimental evaluation of a transpiration cooled, single stage axial-flow turbine component capable of operation at 2500° F average inlet temperature. Combustor design and development and test rig design are described, as well as stator vane hot thermal and cold aerodynamic cascade testing. The objective of the program was to advance and demonstrate high turbine inlet technology for use in a gas generator with a compressor pressure ratio of 8 to 10 and an airflow of 4 pounds per second. Additional objectives included turbine work of 140 Btu per pound of airflow at a high level of turbine efficiency. Phase I report presents the design and analysis and Phase II report gives the details of manufacture and results of test evaluations. One hundred hours of complete stage testing were accomplished with 2 hours at 2500° F. The cascade rig was tested for 87 hours which included 1.2 hours at 2650° F. All blading was in excellent condition after the tests and confirmed the efficacy of the thermal design and transpiration cooling as applied to small size blading. A work of 133 Btu per pound was achieved at a low level of efficiency, attributable to stator profile shape and low aspect ratio. One hundred thirty-seven hours of combustor testing at an average exit temperature of 2500° F was accomplished with operating characteristics consistent with the turbine requirements. It was concluded that the advanced technology incorporated in the turbine design relative to blade cooling and turbine mechanical integrity are practical and can be applied to the design of advanced small gas turbines.		

DD FORM 1473

REPLACES DD FORM 1473, 1 JAN 64, WHICH IS OBSOLETE FOR ARMY USE.

Unclassified

Security Classification

Unclassified

Security Classification

14.	KEY WORDS	LINK A		LINK B		LINK C	
		ROLE	WT	ROLE	WT	ROLE	WT
	Axial Flow Turbine Aerodynamic Design Mechanical Design Test, Development Analysis Cascade Test Combustor Design Thermal Design and Test Cooling, Transpiration High Temperature High Work Manufacture Rig Design Performance Stator Vanes Rotor Blades Efficiency Turbine Map Temperature Profile Blade Profile Dynamometer Test Equipment						

Unclassified

Security Classification

9528-68